UNIVERSITY OF BIRMINGHAM

Exploring Applications of Liquid Metals in Robotic Systems

by

Timothy Cole

A thesis submitted to the University of Birmingham for the degree of

DOCTOR OF PHILOSOPHY

Department of Mechanical Engineering

School of Engineering

College of Engineering and Physical Sciences

The University of Birmingham

September 2024

ABSTRACT

Current robotic systems are typically made using all rigid materials. This causes them to have precise, fast control. However, all-rigid robots face difficulty handling delicate objects and interacting with people, who may get injured by them. Additionally, if the robot gets unexpectedly caught on an obstruction, it can get stuck and damage its motors. The introduction of controllable soft elements using low melting point alloys can eliminate these problems. For example, the phase change of liquid metal (between liquid and solid) can provide an extreme change in stiffness to help a robot pass by an obstruction. For grasping delicate objects and interacting with people, soft robots can be used instead of rigid. Typically, soft robots utilise a pump to change the pressure in a liquid, or high voltage to compress a fluid enclosed within a shell. However, the use of external pumps and high voltages limits their usefulness. Using liquid metal as the fluid, it is possible to create soft robots actuated using low voltages without using external pumps. This thesis therefore aims to solve problems in robotics using the unique properties of liquid metals.

Firstly, a smart stiffness changing elastomer made using a non-toxic low melting point alloy − Field's metal (melting point 62 °C) − is created. This elastomer composite exhibits unconventional and tuneable mechanical and electrical properties that change with temperature and strain. Its resistance decreases by orders of magnitude when compressed or stretched. The electrical and mechanical properties are first investigated with variations in applied stress and temperature. Afterwards, its smart ability to change stiffness and resistance upon a combination of mechanical and electrical stimuli is demonstrated. It is then used in two proof of concept demonstrations − to make a variable stiffness compliance module for robotic grippers, and a resettable fuse.

Secondly, a capillary liquid metal muscle is created, which utilises the giant, switchable change in interfacial tension of eutectic gallium indium liquid metal to generate force and movement. The theory behind the working of the muscle is first explored, and the estimated force output for capillary size and overall diameter is calculated. The design is then optimised for maximum force and stroke. Tests were done on force change for various frequencies, movement of the muscle for different mass payloads, and the effect of different electrolytes on the performance of the muscle. The force output of the muscle and its position during movement is able to be controlled using feedback control. Finally, designs with extra small capillary slit widths are fabricated and tested, showing further increased force change.

Overall, this thesis explores two different ways that liquid metals can be used to improve robotic systems.

Acknowledgements

Firstly, I would like to thank Dr. Shiyang Tang for introducing me to this field and guiding me throughout my PhD, as well as for giving me the freedom to try out new ideas.

I would also like to thank Prof. Yi Wang for his supervision and support during the latter stages of my PhD.

To group members past and present: Yuxin Zhang, Jiahao Zheng, Bayinqiaoge, Yi-Wen Wu and Guolin Yun. Your presence and help made the whole journey much more fun, thank you. Additional thanks go to Bayinqiaoge for printing parts for me and Prof. Xing Ma for use of the Boston Microfluidics printer.

Thanks also to my family for their support throughout the years.

Finally, to my partner, Arlene Domingo, thank you for everything.

Table of Contents

List of Publications

Publications included in this thesis

T. Cole, S-Y. Tang, Liquid metals as soft electromechanical actuators, Mater. Adv., 2022, 3, 173-1852022

G. Yun, T. Cole et al., Electro-mechano responsive elastomers with self-tunable conductivity and stiffness, Sci. Adv. 2023, 9, eadf1141

T. Cole, J. Zheng, J. Shu, Bayinqiaoge, Y. Zhang, Y-W. Wu, M. D. Dickey, Y. Wang, S-Y. Tang, Capillary Liquid Metal Muscle (preparing for publication)

Other publications contributed to during PhD

T. Cole, Liquid metal engineering impact. In: Handbook of Liquid Metals, Springer, 2024

T. Cole, K. Khoshmanesh, S-Y. Tang, Liquid Metal Enabled Biodevices, Adv. Intell. Syst., 3: 2000275

List of Figures

List of Tables

1. Introduction

1.1 Background

The unique properties of liquids, including interfacial tension, viscosity, and reconfigurability, present the potential to create radically different robotic systems, with innovative designs and capabilities not possible using standard components.

Low melting point alloys, particularly Gallium based liquid metals (LMs) such as Eutectic Gallium Indium (EGaIn, 75.5% Gallium, 24.5% Indium), are a remarkable family of functional fluidic materials that are inherently fluidic at or near room temperature [1]. They also possess high thermal (>20 W m^{-1} K^{-1}) [1] and electrical (>6×10^6 S m^{-1}) conductivities [2]. Most importantly, they can actuate electrically for realising mechanical functions, offering many potential benefits to electromechanical systems [3]. Such actuators are simple, highly responsive, highly controllable, and reversible, which has led to the creation of useful devices such as reconfigurable antennas [4], artificial muscles [5, 6], electrical switches [7], and soft robots [8], just to name a few.

Field's metal is another low melting point metal with atypical properties. It is an alloy of bismuth (32.5 wt%), indium (51 wt%) and tin (16.5 wt%), and has a low melting point of 62 °C [9]. Therefore, it can transition between solid and liquid with a relatively low amount of heat applied in comparison to most other metals. This low phase change temperature makes Field's metal very useful for stiffness change applications, as the variation in stiffness between solid and liquid states is much larger than that achieved using alternatives, such as vacuum jamming of particles [10].

1.2 Motivation, Aim and Objectives

The motivation for this research stems from the need to explore low melting point alloys as a solution to challenges in both conventional robotics and soft robotics. These materials offer unique properties such as flexibility, high conductivity, reconfigurability, electrical controllability, and ease of fabrication, making them ideal for addressing limitations in traditional rigid robotics, as well as enhancing the integrity and functionality of soft robotic systems. By leveraging these alloys, this research aims to bridge the gap between structural rigidity and mechanical compliance, creating more versatile and innovative robotic applications.

One issue faced by conventional rigid robotics is that during operation, its end effector can often become slightly misaligned from its optimal position [11]. This may be due to the target object being inaccurately placed or it shifting from its original position. This misalignment can cause damage to both the robot and the target object or cause it to perform its task inaccurately (such as milling). Additionally, the robot may be unexpectedly blocked (such as in telerobotics applications where there may be a slight time delay, and the operator may not be aware of obstacles outside their field of vision [12]), which may also cause damage. Adding variable stiffness elements that can transform from rigid to soft can help the robot avoid damage by softening a joint so it can correct for slight misalignments or move around an unexpected obstacle. The variable stiffness element can then become more rigid again afterwards. Therefore, one objective was to create a variable stiffness material utilising the phase change at low temperature of Field's metal.

Soft robots are designed to be used to interact with delicate objects or for safer human-robot interaction. Actuating the soft robot can be done in many different ways, such as by using pumps

or compressors to inflate a diaphragm, using shape memory polymers which change shape when heated, or using high voltage to pull electrodes together for movement. However, each of these methods have drawbacks, such as slow speed, use of bulky compressors/pumps, or safety concerns due to high voltage. Alternatively, the unusual variable interfacial tension of LM can be used to generate force and movement for soft robotic systems. EGaIn's interfacial tension varies from 500 mN/m (~9 times that of water) to ~0 mN/m, based on its oxidative state [13]. This has previously been used to make LM droplet type robots which rise up and down with the change in energy state [5, 6, 14], however, the force and stroke of these muscles are relatively low. One of the objectives of the thesis is to create and test a new design of LM muscle, using the high change in interfacial energy to generate force. This would then be used to make proof-of-concept application demonstrations, such as in a soft robotic gripper and finger.

The overall aim of the thesis is therefore to use low melting point alloys to create improved rigid and soft robots.

1.3 Thesis Structure

Chapter 1: Introduction

This chapter outlines the general field for the research, motivations, and the key themes and ideas explored

Chapter 2: Literature Review

This chapter is a detailed literature review, previously published as 'Liquid Metals as Soft Electromechanical Actuators'. It describes the different ways that LM can be actuated and the many ways this has been used.

Chapter 3: Electro-Mechano Responsive Elastomers with Tunable Conductivity and Stiffness

This chapter describes a variable stiffness elastomer made with Field's metal. The elastomer is able to change in conductivity with applied strain, as well as change in stiffness when heated. The elastomer's electrical and mechanical properties are tested, and then it is used in two proof of concept applications in robotics and electronics which utilise its mechanical and electrical properties. Note that experimental details for this chapter and the next are included at relevant locations within the text. Therefore, there is no dedicated experimental details chapter.

Chapter 4: Liquid Metal Capillary Muscle

This chapter describes a new type of actuator, which uses the variable interfacial tension of EGaIn LM to generate force. The theoretical force change of the muscle is first derived. The design of the muscle is then optimised, and its properties are tested. Control of force and position of the muscle is also achieved. It is used in various applications, including as a variable damper and in a soft robotic finger and gripper.

Chapter 5: Conclusion and Future Work

This chapter summarises the findings of the work conducted and describes future work which could improve and expand upon that achieved here.

1.4 References

1. Dickey, M.D., et al., *Eutectic Gallium-Indium (EGaIn): A Liquid Metal Alloy for the Formation of Stable Structures in Microchannels at Room Temperature.* Advanced Functional Materials, 2008. **18**(7): p. 1097-1104.
2. Zrnic, D. and D.S. Swatik, *On the resistivity and surface tension of the eutectic alloy of gallium and indium.* Journal of the Less Common Metals, 1969. **18**(1): p. 67-68.
3. Eaker, C.B. and M.D. Dickey, *Liquid metal actuation by electrical control of interfacial tension.* Applied Physics Reviews, 2016. **3**(3): p. 031103.

4. Wang, M., et al., *A reconfigurable liquid metal antenna driven by electrochemically controlled capillarity.* Journal of Applied Physics, 2015. **117**(19).
5. Liao, J. and C. Majidi, *Soft actuators by electrochemical oxidation of liquid metal surfaces.* Soft Matter, 2021. **17**(7): p. 1921-1928.
6. Shu, J., et al., *A Liquid Metal Artificial Muscle.* Adv Mater, 2021. **33**(43): p. e2103062.
7. Wissman, J., M.D. Dickey, and C. Majidi, *Field-Controlled Electrical Switch with Liquid Metal.* Adv Sci (Weinh), 2017. **4**(12): p. 1700169.
8. Zhao, R., H. Dai, and H. Yao, *Liquid-metal magnetic soft robot with reprogrammable magnetization and stiffness.* IEEE Robotics and Automation Letters, 2022. **7**(2): p. 4535-4541.
9. Idrus-Saidi, S.A., et al., *Liquid metal core–shell structures functionalised via mechanical agitation: the example of Field's metal.* Journal of Materials Chemistry A, 2019. **7**(30): p. 17876-17887.
10. Le, H.M., et al., *A temperature-dependent, variable-stiffness endoscopic robotic manipulator with active heating and cooling.* Annals of Biomedical Engineering, 2020. **48**: p. 1837-1849.
11. Xu, P., et al., *Stiffness modeling of an industrial robot with a gravity compensator considering link weights.* Mechanism and machine theory, 2021. **161**: p. 104331.
12. Marinho, M.M., et al., *Dynamic active constraints for surgical robots using vector-field inequalities.* IEEE Transactions on Robotics, 2019. **35**(5): p. 1166-1185.
13. Khan, M.R., et al., *Giant and switchable surface activity of liquid metal via surface oxidation.* Proc Natl Acad Sci U S A, 2014. **111**(39): p. 14047-51.
14. Liao, J. and C. Majidi, *Muscle-Inspired Linear Actuators by Electrochemical Oxidation of Liquid Metal Bridges.* Advanced Science, 2022. **9**(26): p. 2201963.

2. Literature Review

This has been published as T. Cole, S-Y. Tang, Liquid metals as soft electromechanical actuators, Mater. Adv., 2022, 3, 173-1852022

2.1 Introduction

Transformable soft actuators constituting highly deformable materials with low moduli, such as polymers, gels, and fluids play an important role in actuating robotic systems, particularly for those with soft moving bodies.[1, 2] These actuators generate motions and forces upon the application of external stimuli, such as electric/magnetic fields,[3-8] pressure/temperature changes,[9-12] light,[13-15] and chemicals.[16, 17] Unlike their rigid counterparts, soft actuators can easily deform and adapt to dynamic conditions in changing environments.

Electromechanical soft actuators transduce electrical energy into mechanical motions or deformation. Among all stimuli, electrical signals have numerous advantages; for example, they allow for easy control of magnitude, frequency, and phase. Additionally, components for generating electrical stimuli are compatible with conventional electronics and therefore, could be readily integrated and powered by batteries. The design, synthesis, and integration of non-ionic (e.g., dielectric elastomers, electrostrictive polymers, liquid crystal elastomers, etc.)[4, 13, 18-20] and ionic (e.g., ionic conducting polymers and their composites, ionic gels, etc.)[21-23] electro-responsive polymers, as well as fluids that can change viscosity, surface tension, and pressure upon electrical stimulation[5, 24-27] have been extensively explored to make soft actuators over the past decade.

Liquid enabled soft actuators are able to make use of the inherent advantages of fluidic systems. For example, fluids can deform freely without mechanical constraints to movement and are naturally self-healable. Thus, incorporating electro-responsive fluids in solid materials, or using fluids themselves as actuators minimises mechanical fatigue and heals electrical breakdown.[3] Moreover, interfacial tension of fluids can be readily tuned electrically using the electrowetting effect, making fluid actuators an attractive alternative in small-scale robotic systems.[2, 25]

Gallium-based liquid metals (GaLMs) provide many unique properties that make them particularly suited for usage in soft actuators. For instance, GaLMs have the highest surface tension (> 600 mN/m) among all liquids and have a negligible vapour pressure even at a high temperature (> 500 °C).[28] They are also immiscible to aqueous and organic fluids. More importantly, their metallic properties enable many extraordinary effects that cannot be reproduced using conventional fluids, such as electrochemical oxidation/reduction, continuous electrowetting, and the induction of the Lorentz force. These effects have enabled unparalleled actuation methods that have been harnessed for making innovative electromechanical soft actuators, and eventually lead to the construction of more complex systems for various applications (Figure 2.1).

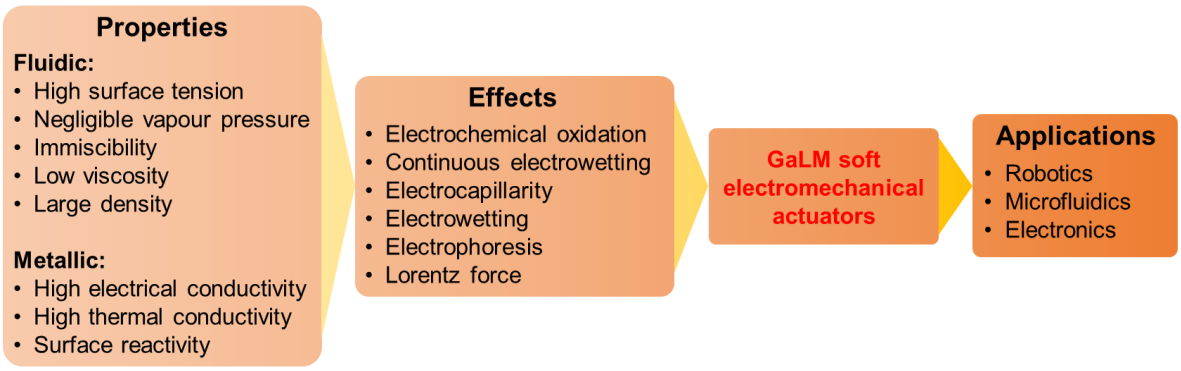

Figure 2.1 The properties, effects, and applications of Gallium based liquid metals. The unique properties of GaLMs can be harnessed for realising various effects, enabling the formation of numerous soft electromechanical actuators and eventually lead to applications in more complex systems.

This chapter seeks to summarise and highlight the fundamental principles and applications of GaLM enabled electromechanical actuators. First, there is a brief discussion on the unique properties of GaLMs that can be harnessed for realising electromechanical effects. After this, the different electronically controlled actuation methods are described, alongside examples of its various uses in robotic, electronic, and microfluidic systems. Finally, there is a perspective on the opportunities and challenges for the future development of such GaLM-based electromechanical actuators.

2.2 Brief summary of the properties of gallium-based liquid metals

GaLMs includes alloys such as eutectic gallium indium (EGaIn, 75 wt% Ga, 25 wt% In)[29] and Galinstan (68% wt% Ga, 22 wt% In, 10 wt% Sn).[28] Pure Ga has a melting point of 29.8˚C,[29] slightly above room temperature, whereas EGaIn and Galinstan have melting points of 15.7˚C and ~11˚C respectively.[29, 30] In contrast to mercury, GaLMs have a very low toxicity.[31] They also have a negligible vapor pressure,[28, 29] meaning there is no danger of accidental inhalation. Another feature of GaLMs is its oxide layer ‘skin’ which quickly forms

in air with a thickness of between 0.7-3 nm.[32] Oxide formation occurs even at very low concentrations of oxygen (~few ppm).[32] The oxide layer reduces the surface tension from >600 mN/m for bare GaLMs[33, 34] to ~350 mN/m.[35] Interfacial tension is also reduced when GaLM is immersed in electrolyte (down to 415 mN/m in 1 M sodium hydroxide, NaOH)[36] due to electrical double layer formation. The oxide layer can be removed chemically by using acid or base, or electrochemically.[37, 38] With the oxide layer present, the LM has increased adhesion, which can be used for patterning the LM.[39] However, the stabilizing effect and adhesion of the oxide also stops the bulk metal from flowing, so in some circumstances the oxide layer has to be continuously removed, or a surface coating applied to prevent the oxide sticking.[40] GaLMs also readily alloy with some metals, such as copper,[41] and aggressively corrodes some aluminium alloys.[42] Other metals it has been shown to be non-corrosive towards however.[42] A comprehensive review on the properties of GaLMs can be found elsewhere.[32, 43-45]

The high conductivity and fluidity of GaLM, and its oxide layer mean that it can be actuated using various electrically based means. As the focus of this chapter is on electrically based actuation, other ways to actuate GaLM (such as by utilizing the redox reaction between GaLM and aluminium in a NaOH solution)[46] will not be discussed. See two recent review papers for more information on these other actuation regimes.[47, 48] In this chapter, the focus is on GaLMs. Both of the terms ‘LM’ and ‘GaLM’ are used, but should be understood to refer to GaLMs only. See elsewhere[49] for a review that discusses actuation by interfacial tension modulation of both mercury and GaLMs.

2.3 Interfacial tension modulation by electrochemical oxidation and reduction

GaLMs exhibit a huge change in interfacial tension from >400 mN/m to ~0 mN/m under certain conditions.[38] This change happens in under 1 s, is reversible, and only requires a small voltage (~1 V). The interfacial tension reduction is achieved by electrochemically oxidising the LM droplet while in electrolyte, making an oxide layer grow. If the electrolyte used is an acid or base that removes the oxide layer, then the oxide is continually removed as it is formed. This means the LM has no impedance to its spreading, and with such a low interfacial tension, it flattens and forms random shapes (Figure 2.2A).[50] The interfacial tension can be increased back to its maximum value of >400 mN/m by removing the oxidative potential if in acid or base, or by applying a reductive potential. This makes the droplet reform its spherical shape. The interfacial tension change arises from the oxide layer acting as a surfactant and compressive stresses resulting from oxidation.[50, 51] This speed and repeatability of this effect have been showcased by using it to make droplets that jump over 5 mm in electrolyte (Figure 2.2B),[52] and a beating heart gallium droplet that is capable of 610 beats per minute.[53]

The shape of LM in 2D can be controlled electrochemically using oxidation and the Marangoni effect.[54] The Marangoni effect is when liquid flows from regions of low interfacial tension to regions of high interfacial tension. To achieve the shape control, a LM droplet was placed in a round dish with an anode touching it, immersed in a NaOH electrolyte, and with cathodes at the edge of the dish. By applying a potential, oxide forms preferentially where the LM side is facing a cathode. This reduces its interfacial tension locally, and results in Marangoni flow towards where the LM has a higher interfacial tension at the centre of the dish. This makes the LM spread towards the cathodes (Figure 2.2C). The LM could be spread to up to three different

cathodes. The minimum angle between two protrusions was 30˚. Using a feedback control system, the LM stayed in position for up to 12 s.

A switch that makes use of oxidation and reduction to coalesce and split LM droplets has also been made.[55] The switch consists of electrolyte encapsulating two LM droplets wetted on two copper electrodes, with two additional outer electrodes on either side. The LM preferentially wets the copper by alloying,[41] preventing the LM moving off it. When the switch is off, the droplets are separate. To turn the switch on, an oxidative potential is applied to one droplet and a reductive potential to the outer electrode on the far side. This causes one droplet to oxidise and spread out, merging with the second droplet (Figure 2.2D). To split the droplets, a positive potential is applied to one outer electrode and a negative potential is applied to the other outer electrode. This causes one side of the merged droplet to oxidise, and one side to be reduced, which makes the droplet unstable and splits.

Soft artificial muscles have been made that make use of the change in surface tension of LM.[56-58] As LM preferentially wets copper by alloying, two copper pads can be used to hold the droplet in place for actuation (Figure 2.2E). The droplet is then immersed in an electrolyte, with a periodically oscillating potential applied to it. The electrolyte is usually a caustic acid or base to increase the speed at which the oxide layer is removed, although an alternative electrolyte (such as sodium chloride solution) has been shown to work if a reductive potential removes the oxide layer.[56] With the LM droplet pinned from above and below, the force generated can result in either pushing or pulling of the pads, depending on the configuration.[56] Artificial muscle droplets can be used in parallel to increase the force or in series to increase the stroke (Figure 2.2F). The artificial muscle droplets are unstable if the distance between the pads becomes too great, as this causes the LM droplet to be pulled apart

during actuation. Maximum distance between the pads is ~2-4mm for a 1mm radius LM droplet muscle, depending on its oxidation/reduction state and load force.[57] Another issue is that electrolysis of the electrolyte during electrochemical reactions causes hydrogen to be formed as an unwanted by-product. The gas generation can degrade the performance of the actuator. If the voltage used is too high (~8 V) the amount of bubbles generated can block the actuation.[56] Gas build-up would be a major issue in sealed contractile units, and requires release valves to be used, or an alternative electrolyte that does not create a gaseous by-product. The artificial muscles are able to actuate with strains up to 87%, with negligible response time.[56] Voltages typically used for actuation were from 4 V to –0.5 V. The artificial muscle was able to actuate repeatedly at 0.5 Hz for 2 hours with no loss of performance. LM artificial muscle was used to make an untethered swimming fish (Figure 2F), a bimodal display, cargo carrier and reconfigurable optical reflector.[56] The work density of such LM muscles created with 1 mm diameter droplets is ~100 kJm^{-3}[57] (c.f work density natural muscles: 8 kJ m^{-3}; dielectric elastomer: 150 kJ m^{-3}; shape memory alloy: 10 MJ m^{-3})[59]. Reducing the size of the droplets will result in a greater work density due to an increase in the surface area to volume ratio. Note that interfacial tension scales linearly with length (L), whereas forces such as electrostatic and magnetic scale as L^2 and L^3 respectively.[2] This means that interfacial tension forces dominate at small scales. A droplet size of 2 μm will result in a theoretical work density of 10^3 kJm^{-3}, greater than that of dielectric elastomers and equal to that of shape memory alloys.[57]

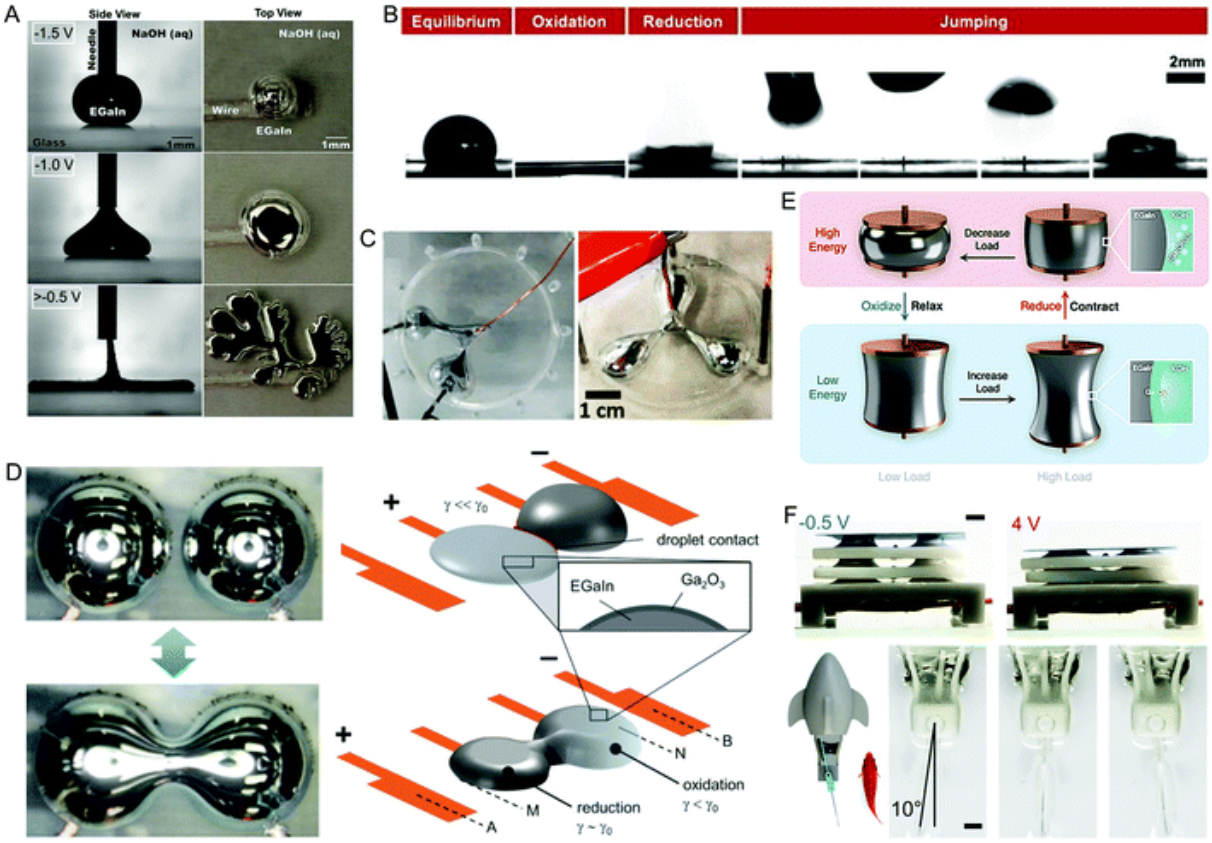

Figure 2.2 Actuators enabled by oxidation and reduction of LM.
(A) Oxidation of LM immersed in a NaOH solution causes its interfacial tension to reduce significantly, resulting in flattening and spreading of the LM. Reproduced with permission.[38] Copyright 2014, National Academy of Sciences. (B) A LM droplet jump over 5 mm high due to oxidation and reduction. Reproduced with permission.[52] Copyright 2021, American Institute of Physics. (C) LM shape control using electrochemistry. Reproduced with permission.[54] Copyright 2019, MDPI. (D) Merging and separation of LM used as an electrical switch. Reproduced with permission.[55] Copyright 2017, Wiley-VCH. (E) A LM artificial muscle with copper pads on either side to pin the LM. Contraction and relaxation of the LM artificial muscle can be achieved upon oxidation or reduction. Reproduced with permission.[57] Copyright 2021, Royal Society of Chemistry. (F) Actuation of a 3-layer stack LM artificial muscle and using a LM artificial muscle to swing the caudal fin of an untethered bionic robotic fish. Scale bars are 2 mm. Reproduced with permission.[56] Copyright 2021, Wiley-VCH.

2.4 Continuous electrowetting

2.4.1 Continuous Electrowetting Theory

When a LM droplet is immersed in an electrolyte, it gains a net surface charge. For example, when in a NaOH solution, chemical reactions result in formation of $[Ga(OH)_4]^-$ on the LM

surface. An electrical double layer (EDL) is then formed around the droplet as oppositely charged ions in the electrolyte are attracted towards it (Figure 2.3A).[60] The interfacial tension varies with the potential across it. The Young-Lippman equation describes the variation of the interfacial tension, γ:

$$\gamma = \gamma_0 - \frac{1}{2} C V_{EDL}^2 \tag{2.1}$$

where γ_0 is the maximum interfacial tension at the point of zero charge, C is the capacitance per unit area of the EDL, and V_{EDL} is the voltage across the EDL [61]. When a potential is applied across a LM droplet in an electrolyte, the low electrical conductivity of the electrolyte means that there is a potential drop along the channel. The LM, however, has a high conductivity, so its potential can be regarded as the same at all points on the droplet. Therefore, the potential difference across the EDL is higher at one side of the droplet than the other. This results in a non-uniform interfacial tension. With no external applied potential, the interfacial tension everywhere on the droplet is still uniform.

2.4.2 LM Droplet Manipulation Using Continuous Electrowetting

When there is an interfacial tension gradient across the LM droplet, this results in the generation of Marangoni flows along the surface to drive the droplet towards the anode (Figures 2.3A-B). It also results in flow of electrolyte from the lower interfacial tension side of the droplet to the higher interfacial tension side. This type of LM actuation is known as continuous electrowetting (CEW). CEW offers a large degree of control over the movement of the LM droplet. LM can be controlled in two dimensions,[62] and even made to travel up a slope.[63]

Accurate manipulation of multiple LM droplets in 2D has been achieved using infrared lasers to selectively trigger phototransistors.[64] The experimental set up used contains a grounded

graphite electrode, which surrounds a circuit board immersed in NaOH solution, with a phototransistor and copper electrode array on it. A transparent epoxy is coated on the circuit board, with only the tips of the electrodes exposed, meaning the LM droplets are able to move freely. When a laser is shone onto a phototransistor, the appropriate copper electrode is activated, and a LM droplet is actuated towards it by CEW. This can be used to control the position of multiple LM droplets concurrently. It can also be used to merge droplets by moving them at speed towards one another. If the laser is left on a phototransistor while the LM is situated on its electrode, the LM is oxidised, flattens and spreads. Removing the laser stops the oxidation, and the NaOH solution causes the oxide to be removed, beading the LM back up to a spherical shape. The LM can be split into two droplets during this process if it spreads enough during its oxidation.

The electrolyte used affects the actuation of the LM. For example, using a hydrochloric acid (HCl) solution rather than NaOH results in the LM surface becoming positively charged[65] (it is negatively charged in NaOH solution). An EDL then forms has a reversed polarity compared with that made in NaOH solution. This causes the LM to travel to the cathode rather than the anode. The LM also moves slower and needs a greater potential however (25 V minimum for actuation compared with 2 V).[66] The worse performance is due to the low surface activity of chloride ions.[36] Using an acidified (0.1 M HCl) potassium iodide (KI) solution generates a higher surface charge density on the EDL due to iodide ion adsorption.[36] This gives improved electrical actuation in an acidic electrolyte, and it even exhibits better performance than when using NaOH electrolyte. The actuation required a lower voltage (4 V rather than 9 V) and droplets moved faster.[36]

When immersed in a NaOH solution, LM droplet speed initially increases with greater potential applied.[67] Once a maximum droplet speed is reached however, an increased potential does not result in greater interfacial tension difference on the LM droplet, and hence its speed is not increased. If the potential applied is large enough, it can cause oxidation of LM, making its interfacial tension gradient in the opposite direction, causing the droplet to travel towards the cathode rather than the anode.[67]

A surface coating applied to the LM can also affect its actuation behaviours. Micro- or nanoparticles can coat the surface of GaLM droplets to form LM marbles.[68] For LM marbles with semiconductive nanoparticle coatings, a n-type nanomaterial coating (e.g., tungsten trioxide, WO_3) induces actuation in a way similar to that of bare LM droplets in a NaOH solution – the marble moves towards the anode upon the application of an external potential gradient.[66] However, a p-type nanomaterial coating (e.g., cupric oxide, CuO) induces more complex actuation behaviours – the marble elongates and actuates towards the cathode while the nanoparticles migrate to form a dense cluster tail.[69] The tail eventually falls off and then the LM droplet abruptly changes the direction of actuation towards the anode.

Although the voltages used for LM CEW actuation are relatively low (~few volts usually), the potential difference is still large enough for electrolysis to occur (>1.2V required for H_2 generation). However, bubble generation has been shown to have only a very slight impact on the actuation of the LM.[66] This was achieved by comparing the actuation of stainless steel beads and LM in electrolyte solution with a potential difference across them. The bead actuation was caused only by bubble generation, whereas LM actuation was caused by both bubble generation and the surface tension gradient. The beads moved very slowly in HCl solution (<0.2mm/s), and didn't move at all in NaOH solution. In contrast, LM actuation was much

faster – up to 67mms^{-1} in NaOH solution and 33mms^{-1} in HCl solution. This shows that the surface tension gradient has a much greater effect on LM actuation than bubble generation.

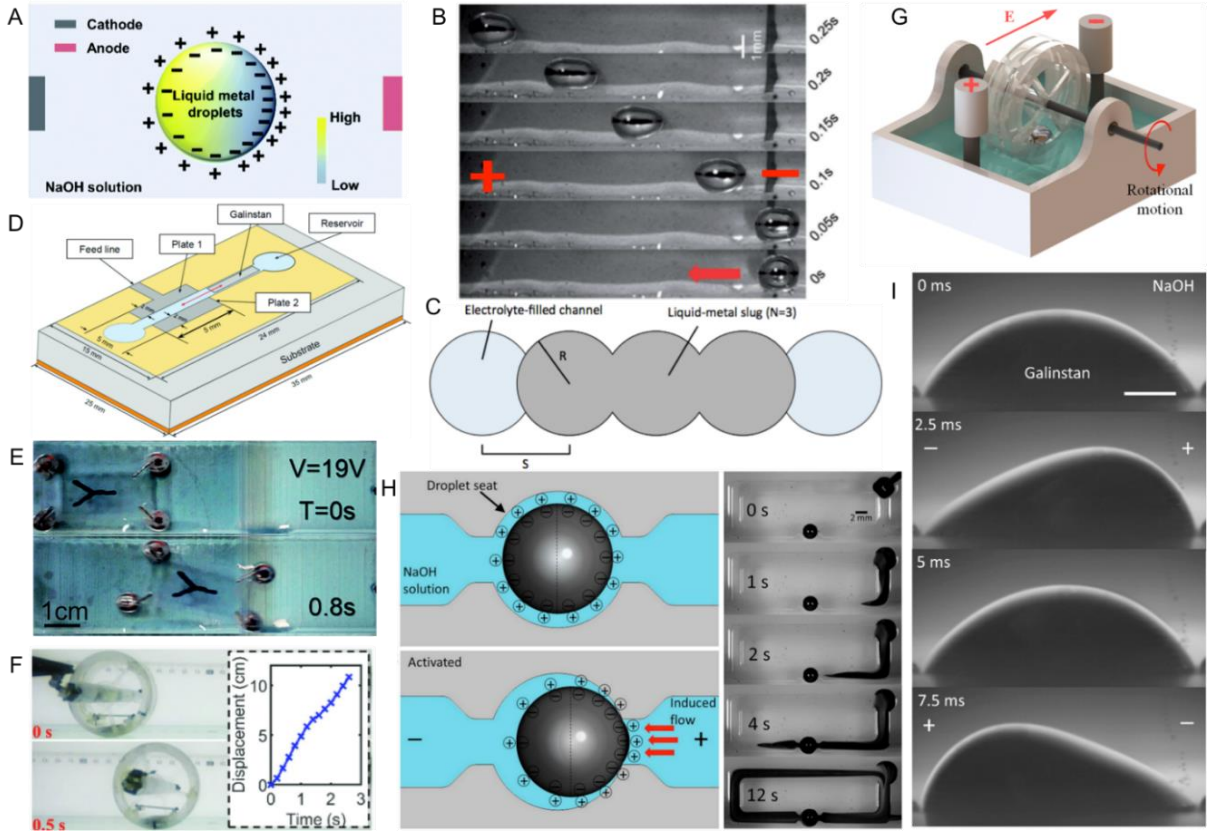

Figure 2.3 Actuators enabled by the CEW effect of LM.
(A) Distribution of the EDL on LM immersed in NaOH solution with an applied potential across it. Reproduced with permission.[67] Copyright 2021, Royal Society of Chemistry. (B) LM moving in a channel, from the cathode towards the anode, due to CEW. Adapted with permission.[66] Copyright 2013, Royal Society of Chemistry. (C) Shape of a channel to cause minimum energy states of LM, keeping it in the desired position. Reproduced with permission.[70] Copyright 2014, IEEE. (D) Diagram of a variable parallel-plate capacitor. Reproduced with permission.[71] Copyright 2021, IEEE. (E) A small vehicle with LM 'wheels'. Reproduced with permission.[72] Copyright 2016, Royal Society of Chemistry. (F) Side view of a wheeled robot driven by a change in centre of gravity moving outside of electrolyte. Reproduced with permission.[73] Copyright 2018, Wiley-VCH. (G) A universal mechanical module that is converts the flow caused by LM CEW into mechanical work. Reproduced with permission.[74] Copyright 2021, Royal Society of Chemistry. (H) A LM pump. Reproduced with permission.[75] Copyright 2014, National Academy of Sciences. (I) An AC potential applied across LM causes it to oscillate. Reproduced with permission.[76] Copyright 2014, Wiley-VCH.

2.4.3 Variable Electronic Components Using LM Continuous Electrowetting

The high conductivity and fluidity of LM means it is particularly useful in making reconfigurable antennas.[77] The LM can be moved to different positions to change the properties of the antenna. Accurate positioning of the LM is important for radio frequency applications; however, this is difficult to achieve when actuating LM using CEW due to the inertia of the LM and low friction between LM and the channel.[70] Also, the motion of the LM can create a pressure differential between the electrolyte at either side of it. After actuation, the pressure differential could cause the LM to move from its desired position.[70] One method to improve the accuracy of positioning of LM is to shape the channel to create minimum energy states for the LM droplet.[70] An example of this is a series of rounded indentations (Figure 2.3C). The high surface tension of LM means that it will try to minimise its surface area. Therefore, after actuation, it will stay within a set position. This results in a discrete number of positions of the droplet and corresponding radio frequency properties.

A radio frequency shunt switch has also been made which makes use of CEW of LM.[78] For the switch, a signal line is placed across a channel, and LM is actuated into a position over the signal line to complete the connection to ground. If no LM is above the signal line, then the connection to ground is removed. The use of electrolyte in radio frequency devices can introduce unwanted losses, however. In this case, when the electrolyte is above the signal line, it absorbs the radio frequency signal. In order to use CEW while reducing the losses due to electrolyte, the switch design used a bubble trapped in the channel, and capillary troughs to carry the electrolyte to either side of the main channel. The capillary troughs gave a continuous path in the electrolyte for the CEW to function. The troughs were smaller than the channel containing the LM, preventing the LM from moving into the troughs as this would increase its

surface area. A bubble was positioned between two LM droplets, it stayed in position due to capillary action of the electrolyte preferentially bringing the electrolyte into the trough rather than the bubble. This design reduced the losses caused by the electrolyte.

CEW of LM can also be used for tuneable capacitors.[71] The tuneable parallel-plate capacitor comprises a copper bottom layer with dielectric above it, and a top conductor made of two stainless steel plates with a gap separating them, with a channel placed between the plates (Figure 2.3D). The channel is filled with electrolyte and a LM slug. Actuating the LM slug by CEW to bridge the gap between the two stainless steel plates causes the effective area of the plates to be increased, resulting in a higher capacitance. The capacitance varied from 9.76pF with the LM slug not contacting the plates to 10.34pF with the slug fully between the plates.

2.4.4 Continuous Electrowetting Driven LM Robots

LM droplets can be used to propel vehicles by using the droplets as soft 'wheels' in electrolyte (Figure 2.3E).[72, 79] By building a platform around the droplets, cargo can be carried, and the droplets are steered by CEW to a specified location. Alternatively, the LM droplet itself can be used as the vehicle.[80] For example, as LM preferentially wets copper, LM was used to encapsulate a hollow copper-coated sphere. The hollow sphere contained three cabins – the driving, counterweight, and cargo cabins. The driving cabin contained magnetic particles to aid in moving the droplet in addition to using CEW. The counterweight was used to keep the correct position of the sphere within the droplet. The cargo cabin was filled with the payload, and was sealed with wax, which could be melted with a laser. The droplet was successfully actuated using CEW and magnets before unloading its payload.

LM soft robots are interesting but have a major drawback – they are only able to move in an electrolyte, which limits their real-world applications. It is possible to use LM to actuate robots

outside of an electrolyte, however. This has been achieved by encasing a channel with a LM droplet, electrolyte, electrodes and a battery within an untethered wheeled robot.[73] The LM position changes depending on the potential applied, which in turn causes the centre of gravity of the wheel to alter, making the wheeled robot move (Figure 2.3F).

A similar, alternative approach is to create a LM universal mechanical module, which is inspired by a water wheel (Figure 2.3G).[74] CEW of LM drives the spinning of the wheel, which is then used to generate rotational motion outside of the solution. Aluminium flakes were also added to the LM, which created a greater negative charge on the LM due to the galvanic reaction between aluminium, EGaIn and NaOH. The greater charge is then utilised to generate a stronger Marangoni flow with the applied potential. This in turn creates a larger force from the module.

Another device that uses LM to do mechanical work is a LM motor.[81] The motor contains a rotor with multiple LM actuating units.[81] Each of the actuating units contained a LM droplet immersed in a NaOH electrolyte, controlled with a pair of electrodes. The actuating units work together to generate a continuous output torque that is greater than that made by a single LM droplet. LM was also used as the electric brush between the rotor and stator, making use of its high conductivity and low viscosity. This reduced friction and prevents wear and sparks. The motor was used to successfully drive an untethered vehicle and boat.

2.4.5 LM Pumps and Mixers Driven by Continuous Electrowetting

When a LM droplet is trapped within an electrolyte filled chamber with an applied electric potential across it, it functions as a pump.[75] The surface tension gradient causes Marangoni flow around the droplet, but as the droplet is trapped, it cannot move out of the chamber. Therefore, the electrolyte is pumped by the droplet (Figure 2.3H). The applied potential may cause an oxide layer to form on the more anodic pole of the droplet after a few seconds. This

would then stop the pumping due to the reduction in the surface tension on that side (as that was the side with the highest surface tension previously). Oxidation can be prevented by using an AC potential difference with a DC offset.[75] The optimum frequency (~200 Hz) ensures surface charges can be accumulated and released, preventing oxidation and allowing pumping to continue. Too low of a frequency results in gradual oxidation. Too high of a frequency means that the ions in the EDL do not have time to redistribute, reducing the pressure difference across the droplet and the lowering the pumping rate. Under optimum conditions, the LM pump exhibited a high flow rate with low power consumption. It was shown to work with a range of electrolytes including solutions of NaOH, NaCl, and phosphate buffered saline. It could also pump a liquid made by mixing glycerol and deionised water, which had a viscosity of $0.209 Nsm^{-2}$ (~230 times water viscosity). LM pumps have been used as cooling systems,[82] and have also been shown to be able to pump an ionic liquid.[83] Using ionic liquid offers an advantage over using NaOH as electrolyte due to an increased interfacial ion adsorption, which results in a higher pumping rate.

In addition to pumping of liquid, mixing is also important for flows at low Reynolds numbers. Mixing can be achieved by applying an AC electric potential in electrolyte to a LM droplet wetting on a copper pad, causing the Marangoni flow generated at the surface of the LM to oscillate back and forth (Figure 2.3I).[76] The oscillating potential causes the interfacial tension on different parts of the surface to vary rapidly with time, and LM wetted onto the copper pad prevents the bottom layer of the droplet moving. Mixing can also be achieved without the use of a copper pad.[84] By using a DC biased AC potential with a greater potential variance, this induces chaotic advection between the neighbouring laminar flow.

2.5 Electrocapillarity

The flow of LM in capillaries can be achieved by using electrochemical and electrowetting techniques- both of which will be elaborated on here.

Electrochemically controlled capillarity (or 'recapillarity') involves removing the oxide layer of GaLM, causing LM to retreat from a channel (Figure 2.4A).[85] This prevents the oxide layer from sticking to the walls of the channel (which can occur if the LM is pumped out). A non-caustic electrolyte such as sodium fluoride (NaF) is used for electrochemically controlled capillarity, as it does not remove the oxide without a reducing potential. Applying a reducing potential to the LM causes a current to flow and the LM to move out of the channel due to removal of the oxide and its increase in interfacial tension. Removing the potential stops the current and the LM flow, because oxide that formed on the sidewalls of the channel needs to be removed for the LM to flow out. Speeds of up to 0.3 ms^{-1} have been achieved using a high concentration of electrolyte (1 M NaF). Localised reduction of planar GaLM is also able to 'write' by removing LM near an electrode (Figures 2.4B and C).[86]

Electrowetting based control of LM in capillaries is similar in principle to CEW. By applying a positive potential to the electrolyte relative to the LM, a surface tension gradient is generated on the LM.[60] For the case of LM in a reservoir connected to a channel, the point of the LM with the lowest interfacial tension is at the entrance to the channel. The interfacial tension gradient results in Marangoni flow along the channel, which acts as a conveyor belt to pull the LM out of the reservoir. If this force is greater than the capillary pressure, the LM is pulled into the channel.[60] Small capillary side-channels can be used in addition to the main channel to ensure LM does not block the flow of electrolyte.

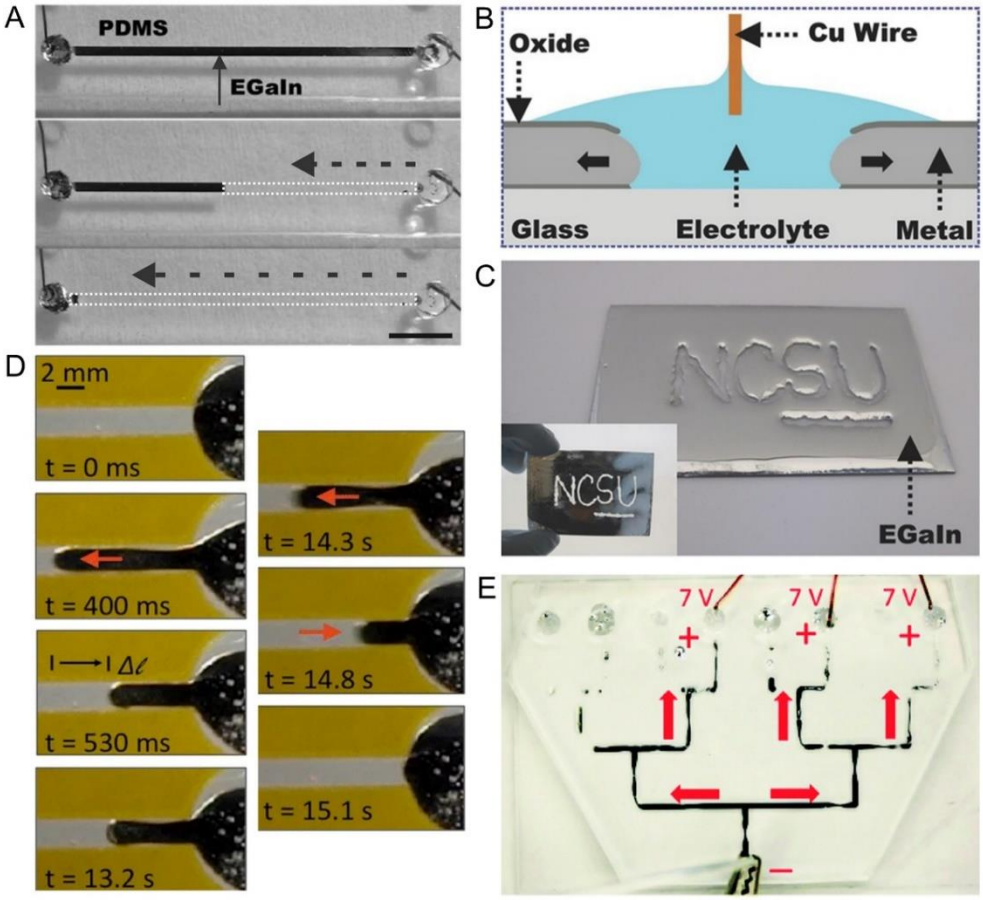

Figure 2.4 Actuators enabled by electrocapillarity flow of LM.

Fig. 2.4 Actuators enabled by electrocapillarity flow of LM. (A) Recapillarity-reduction of LM in a channel causes it to flow out. Reproduced with permission.[85] Copyright 2015, Wiley-VCH. (B) In-plane recapillarity schematic. (C) Writing using in-plane recapillarity. Reproduced with permission.[86] Copyright 2016, Wiley-VCH. (D) Electrocapillarity causes LM to flow out of a reservoir. The potential is then flipped and the LM is oxidised to keep it in place. After this, the potential is reversed again, reducing the oxide and the LM retreats to the reservoir. Reproduced with permission.[60] Copyright 2015, Springer. (E) Directing LM flow to three end points in branching channels. Reproduced with permission.[87] Copyright 2015, Royal Society of Chemistry.

Alternatively, applying a negative potential to the electrolyte relative to the LM causes oxidation of the LM[60]. This also causes LM to move along the channel from the reservoir due to interfacial tension reduction and Marangoni flow. The potential used dictates how far the LM will travel along the channel, as when the LM gets closer to the negative electrode and the resistance decreases, the current increases, which leads to more rapid oxide growth. This can eventually stop the LM actuation. The oxide growth has been used to make LM retain its shape

in a channel after actuating it to a desired position (Figure 2.4D).[60] Reducing the oxide will then quickly bring the LM back to the reservoir.

Electrocapillarity is also able to steer LM as it is pumped along branching microchannels.[87] Applying a positive potential to an electrolyte relative to LM in one of two branching channels causes LM to flow preferentially to the channel with the applied potential, as that requires less energy (Figure 2.4E). Alternatively, applying a high (~5 V) oxidative potential to the LM in electrolyte causes a thick oxide layer to form as it nears the negative electrode. This blocks the channel, making the LM travel along the other channel.[87]

LM has been used in reconfigurable antennas that use electrocapillary actuation.[88, 89] One antenna design varied its polarization by making LM move into 5 discrete states by filling different channels that were connected to a central reservoir. There were also notches at the end of the channels to create a minimum energy state for the LM, keeping it in position without having to use any power.[88] Another design combined electrocapillarity and CEW of LM in a reconfigurable LM pixel array.[89]

2.6 Electrowetting on dielectric (EWOD)

Electrowetting on dielectric is a widely used technique to modify the surface wetting properties of conductive liquid droplets.[90] A droplet placed on a dielectric surface, with an electrode beneath it and an electric potential applied, causes a redistribution of charges towards the droplet-surface interface. The charge accumulation on the surface of the droplet reduces its surface tension and hence its wetting angle. Surface tension varies according to the Young-Lippman equation, which here is written to show how the angles change based on the applied voltage:

$$\cos\theta = \cos\theta_\gamma - \frac{\varepsilon_r \varepsilon_0}{2d\gamma_{LV}}(V - V_0)^2 \quad (2.2)$$

where θ is the contact angle, θ_γ is the Young's contact angle under zero applied potential, ε is the relative permittivity of the dielectric used, ε_0 is the permittivity of free space, d is the dielectric layer thickness, and γ_{LV} is the interfacial tension between the liquid and vapor phases.[90]

Using LM for EWOD has some challenges associated with it. For example, the oxide layer adheres well to most surfaces and can impede the actuation of the LM. One solution is to prevent the oxide layer forming by reducing the oxygen concentration <1 ppm.[28] However, this is not feasible for most applications. Alternatively, infiltrating a silicone oil with HCl results in an acidic oil that is electrically insulating and removes the oxide layer.[91] Also, the very high surface tension of LM means that a high voltage (>1 kV) is required to be able to change the surface tension appreciably. This high voltage, coupled with the thin dielectric layer means it nears or is greater than the dielectric breakdown limit for some materials. To reduce the voltage required, the shape of the channel can be changed so that the LM droplet is actuated with a lower electrostatic pressure. This technique was applied to actuate LM in acidic silicone oil using EWOD, with grooved channels in order to reduce the difference in electrostatic pressure required to merge the droplets (Figure 2.5A).[91] The shape of the grooves also meant the droplets separated when the voltage was removed (Figure 2.5B). The LM EWOD device was used as an electromagnetic polarizer with a low switching time of ~12 ms.

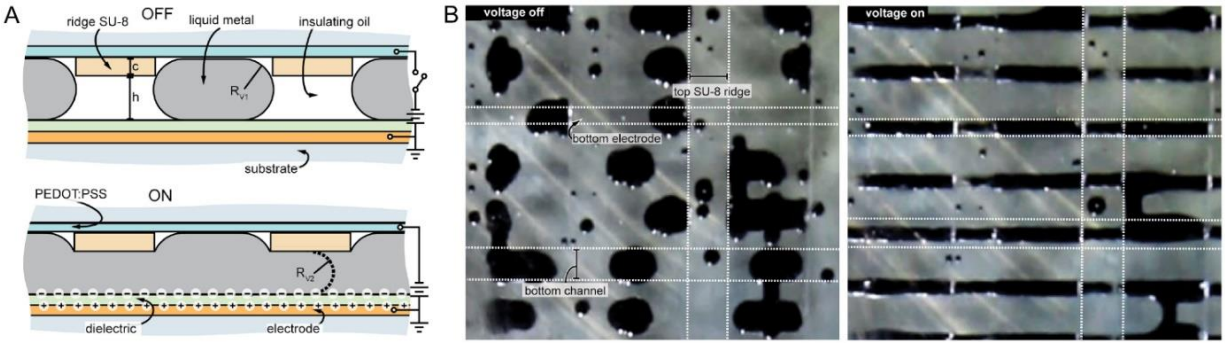

Figure 2.5 Actuators enabled by EWOD.
(A) Schematic of EWOD LM polarizer. The ridges cause the pressure differential between the two states to be reduced and break the LM apart after the voltage is removed. (B) Picture of the LM polarizer with voltage off and voltage on. Reproduced with permission.[91] Copyright 2017, IOP.

2.7 Electrostatic

Electrostatic forces have also been used to successfully actuate non-spherical LM particles electrophoretically.[92] The particles were created using shear forces to pinch off LM flow out of a capillary tube. The silicone oil used as the fluid was saturated with oxygen to ensure rapid oxidation of the LM. The oxide layer stabilised the non-spherical shape formed by the shearing forces. Various morphologies were created, such as an ellipsoid, single tail, double tail and rod, and had a size of ~250 μm. The particles were actuated using a high potential difference (~few kV) with needle electrodes. Bringing a charged electrode towards a particle and contacting it caused it to be charged. It then was repelled due to electrostatic forces (Figure 2.6A). Placing the positive and the negative electrode opposite each other made the particle move between the electrodes. At first the LM particle is positively charged and moves towards the negative electrode, then it becomes negatively charged and moves the other way (Figure 2.6B). The period of the oscillation reduces with increasing potential difference between the electrodes, from a 148ms period at 2.4kV potential difference, to 55ms at 3.6kV. The thinner tails of the

particles line up with the applied electric field due to uneven charge distribution. Multiple particles line up in series between the two electrodes (Figure 2.6C), and can form a short-lived electrical connection, which is destroyed as a result of the high voltage causing rapid electrolysis.

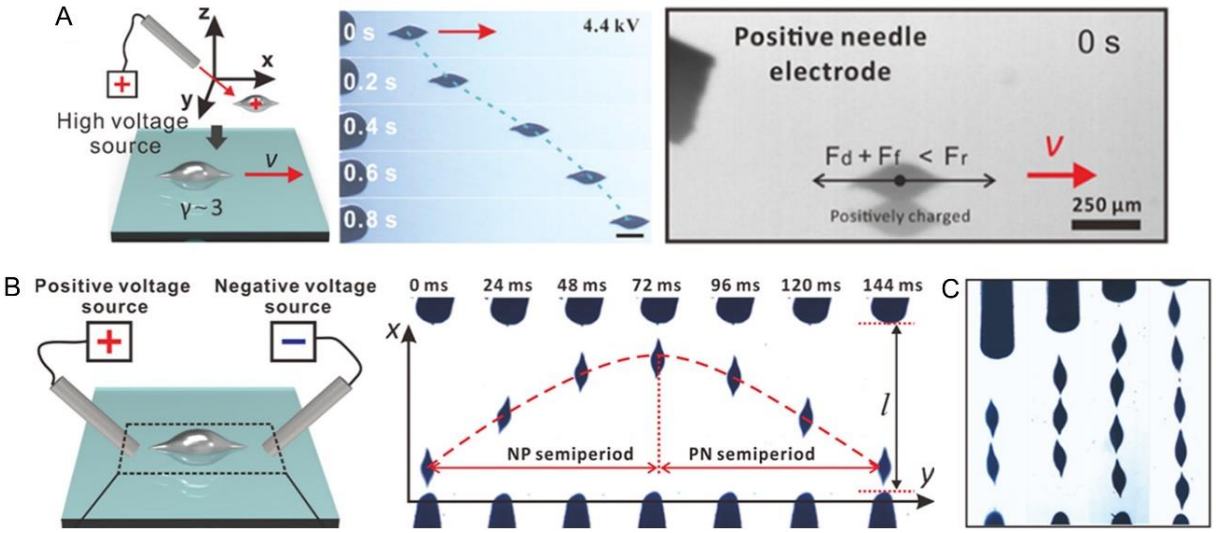

Figure 2.6 Electrostatic actuation of LM.
(A) Repelling a LM droplet from a high voltage probe. (B) Oscillating movement of LM between two probes. (C) LM droplets lining up along the electric field. Reproduced with permission.[92] Copyright 2021, ACS.

2.8 Magnetic

The high conductivity of LMs means that a changing magnetic field is able to induce a large enough eddy current for Lorentz forces to move a LM droplet in a NaOH solution.[93] The alkaline solution is required to remove the oxide layer to prevent the LM droplet sticking to the container. Interestingly, the LM droplet moves in the opposite direction to solid gallium and copper spheres under the same conditions (Figure 2.7A). The Lorentz forces experienced by solid metal spheres result in a horizontal force (which is in the same direction as the moving magnet), and a torque that makes it rotate towards the opposite direction. The slip layer on LM

acts as a lubricant, preventing it rolling. Therefore, LM moves in the opposite direction to solid spheres, which roll due to the applied torque.

Rotating magnetic fields have been shown to induce surface patterns in large LM droplets (Figure 2.7B).[94] The setup used comprises a LM droplet in NaOH electrolyte, with graphite electrodes in the centre and around the outside. With a rotating magnetic field and a low potential applied (2.5 V), the LM rotates around the inner electrode due to Lorentz forces. With an increased potential (4 V), the LM stops rotating, and displays the folding and rippling patterns. The combination of the applied potential and the rotating magnetic field causes variations in interfacial tension to generate the patterns.

A ferromagnetic LM alloy has been made that is able to be actuated electrically by CEW and using magnetic fields.[95] LM was mixed with copper-iron nanoparticles in HCl solution to create the ferromagnetic LM. The HCl solution removed the oxide on the LM and on the nanoparticles. A galvanic cell is also formed between the Ga and the copper-iron nanoparticles in HCl solution, oxidising the Ga and preventing the nanoparticles from dissolving in the HCl solution. Mixing for 30 minutes resulted in the LM gaining a thick solid shell composed of various oxides and alloys. CEW could be used to separate the more fluidic LM core from the solid shell. The resultant fluidic, ferromagnetic LM had a greater weight content of copper-iron with larger amount of nanoparticles added initially. LM alloys with a higher weight content of copper-iron had increased viscosity, which resulted in slower actuation speed during CEW and a reduced pumping flow rate, but had greater magnetic sensitivity.

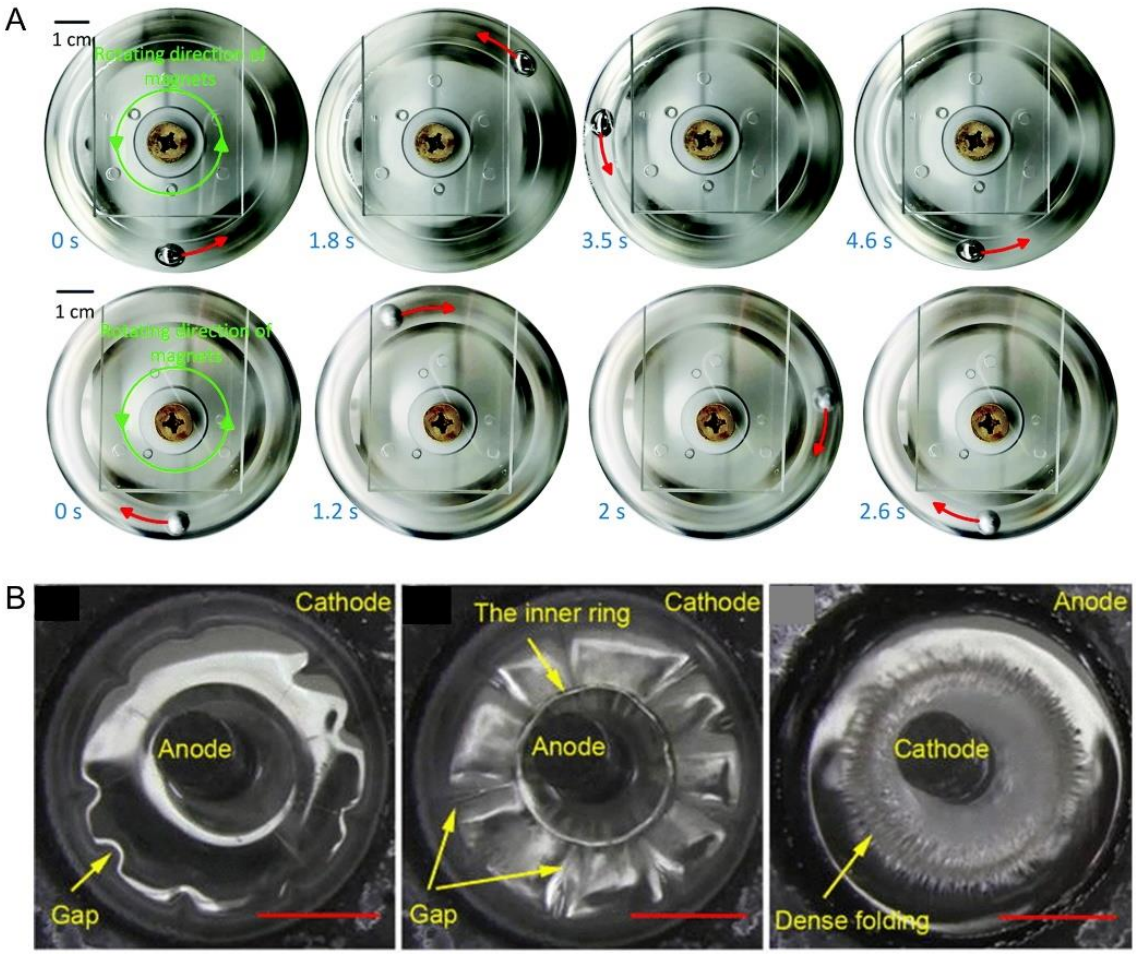

Figure 2.7 Magnetic based actuation of LM.
(A) Lorentz forces cause rotation of LM in the opposite direction to a solid gallium sphere due to the slip layer on LM. Reproduced with permission.[93] Copyright 2018, Royal Society of Chemistry. (B) A rotating magnetic field causes rippling and folding patterns on LM. Reproduced with permission.[94] Copyright 2016, American Institute of Physics.

Table 2.1 Details of the different LM actuation types

Actuation Type	Voltage	Scale	Uses	Observed Performance	References
Oxidation/ reduction	~Few V	mm	Artificial muscle Switch	Max force: 43 mN (6 × 2 mm diameter droplets in parallel)[56] Estimated force to volume ratio: 850 NL^{-1} Estimated force to mass ratio: 0.14 Ng^{-1} Up to 4 Hz Frequency Estimated work density for 2 µm droplets: 10^3 kJ m^{-3} [57]	[38, 50, 52-58]
CEW	~Few V	mm-cm	Reconfigurable antennas Tuneable capacitors Radio frequency shunt switch Soft robot Pump Mixer	LM wheeled robot speed of up to 150 mm s^{-1} [79] Pumping rate for a 3 mm diameter droplet: 28.1 mL min^{-1} [82]	[36, 62-64, 66-84]
Electrocapillarity	~Few V	mm-cm	Reconfigurable antenna	Max speed: 0.3 m s^{-1} [85]	[60, 85-89]
EWOD	300 V	mm	Switchable electromagnetic polariser	Switching speed for polariser: 12 ms	[91]
Electrostatic	2.4-4.4 kV	µm-mm	-	Frequency of oscillation between two electrodes: 7-18 Hz	[92]
Magnetic	N/A	mm-cm	-	Speed of droplets: 90 mm s^{-1} [93]	[93-95]

2.9 Summary

In this review, the electrical methods to actuate LMs have been discussed, along with the many different applications for this, such as in reconfigurable antennas, pumps, switches, motors, and artificial muscles (Table 2.1). It is certain that the unique and beneficial properties of LM means that it offers great advantages to a range of technologies. However, there are still some challenges that must be overcome in order for LM enabled electromechanical actuator-based devices to become widely accepted and even commercially viable.

For example, electrolyte is needed for most of the LM actuation types- to continuously remove the oxide, for electrochemical reactions to be able to occur, and for EDL manipulation. This LM-electrolyte system has to be carefully sealed and is difficult to get useful work out of. Electrolyte is especially unwanted in radio frequency devices, where it introduces additional losses. Moreover, electrochemical oxidation/reduction and CEW effects for GaLMs work best in a strong basic solution or acidified KI solution; this compromises the performance and limits the applications of LM actuators in neutral, other acidic, and non-ionic liquids. Instead of using electrolyte and electrical based actuation, pressure can be used in conjunction with a non-wetting coating. However, this introduces additional components and doesn't use one of the benefits of LM (low voltage electrical actuation). An acidic silicone-based oil has been shown to remove the oxide layer for EWOD, however, this is a corrosive liquid and is electrically insulating, so cannot be used for CEW or oxidation/reduction.

Electrolysis is another issue. Bubbles of hydrogen are generated at the cathode during electrochemical reactions in aqueous solutions when the potential difference used is >1.2 V. The bubble generation can impact the performance of the LM actuator itself (for example by blocking the actuation of LM artificial muscle). Electrolysis also reduces the efficiency of the actuation. Using an ionic liquid rather than a NaOH solution is one potential remedy, as LM has been shown to be able to pump an ionic liquid. Finding an ionic liquid that is safe to use, doesn't generate gas bubbles at the potential voltages needed and able to be used for oxidation/reduction and CEW would be of great benefit.

Another challenge is how best to induce larger forces with LMs? The actuation methods mentioned in this review mainly use interfacial tension modulation to induce motion. The artificial muscles created were only able to lift ~1 g, whereas for most real-world applications

the forces required will be >100 times greater. Decreasing the size of LM droplets would increase the surface area to volume ratio, which scales with the inverse of the droplet radius. This would result in actuators with a greater power density. However, this could also be more complex to make and to get work out of the system.

A gap in the literature is therefore increasing the work density of LM muscles by decreasing the droplet size below ~1 mm radius, or using an alternative design which also increases the force generated. This gap will be addressed within the thesis in chapter 4, by confining LM to small channels to dramatically increase the resultant force, with it capable of lifting a 1 kg mass.

2.10 References

1. El-Atab, N., et al., *Soft Actuators for Soft Robotic Applications: A Review.* Advanced Intelligent Systems, 2020. **2**(10): p. 2000128.
2. Hines, L., et al., *Soft Actuators for Small-Scale Robotics.* Adv Mater, 2017. **29**(13): p. 1603483.
3. Rothemund, P., et al., *HASEL Artificial Muscles for a New Generation of Lifelike Robots-Recent Progress and Future Opportunities.* Adv Mater, 2021. **33**(19): p. e2003375.
4. Duduta, M., et al., *Realizing the potential of dielectric elastomer artificial muscles.* Proc Natl Acad Sci U S A, 2019. **116**(7): p. 2476-2481.
5. Cacucciolo, V., et al., *Stretchable pumps for soft machines.* Nature, 2019. **572**(7770): p. 516-519.
6. Kim, Y., et al., *Ferromagnetic soft continuum robots.* Sci Robot, 2019. **4**(33): p. 1-15.
7. Hu, W., et al., *Small-scale soft-bodied robot with multimodal locomotion.* Nature, 2018. **554**(7690): p. 81-85.
8. Tang, S.Y., et al., *Versatile Microfluidic Platforms Enabled by Novel Magnetorheological Elastomer Microactuators.* Advanced Functional Materials, 2018. **28**(8): p. 1705484.
9. Tang, Y., et al., *Leveraging elastic instabilities for amplified performance: Spine-inspired high-speed and high-force soft robots.* Sci Adv, 2020. **6**(19): p. eaaz6912.
10. Walker, J., et al., *Soft Robotics: A Review of Recent Developments of Pneumatic Soft Actuators.* Actuators, 2020. **9**(1): p. 3.
11. Kim, H., et al., *Shape morphing smart 3D actuator materials for micro soft robot.* Materials Today, 2020. **41**: p. 243-269.
12. Lu, H., et al., *Reversible Underwater Adhesion for Soft Robotic Feet by Leveraging Electrochemically Tunable Liquid Metal Interfaces.* ACS Appl Mater Interfaces, 2021. **13**(31): p. 37904-37914.

13. Bisoyi, H.K. and Q. Li, *Light-Driven Liquid Crystalline Materials: From Photo-Induced Phase Transitions and Property Modulations to Applications.* Chem Rev, 2016. **116**(24): p. 15089-15166.
14. Liu, Y., et al., *Sequential self-folding of polymer sheets.* Sci Adv, 2017. **3**(3): p. e1602417.
15. Park, S.J., et al., *Phototactic guidance of a tissue-engineered soft-robotic ray.* Science, 2016. **353**(6295): p. 158-62.
16. Bartlett, N.W., et al., *SOFT ROBOTICS. A 3D-printed, functionally graded soft robot powered by combustion.* Science, 2015. **349**(6244): p. 161-5.
17. Shepherd, R.F., et al., *Using Explosions to Power a Soft Robot.* Angewandte Chemie-International Edition, 2013. **52**(10): p. 2892-2896.
18. Kotikian, A., et al., *Innervated, Self-Sensing Liquid Crystal Elastomer Actuators with Closed Loop Control.* Adv Mater, 2021. **33**(27): p. e2101814.
19. Ford, M.J., et al., *Size of liquid metal particles influences actuation properties of a liquid crystal elastomer composite.* Soft Matter, 2020. **16**(25): p. 5878-5885.
20. Pan, C., et al., *A Liquid-Metal-Elastomer Nanocomposite for Stretchable Dielectric Materials.* Adv Mater, 2019. **31**(23): p. e1900663.
21. Hao, M.Y., et al., *A Compact Review of IPMC as Soft Actuator and Sensor: Current Trends, Challenges, and Potential Solutions From Our Recent Work.* Frontiers in Robotics and Ai, 2019. **6**: p. 129.
22. Carrico, J.D., et al., *3D-Printing and Machine Learning Control of Soft Ionic Polymer-Metal Composite Actuators.* Sci Rep, 2019. **9**(1): p. 17482.
23. Morales, D., et al., *Electro-actuated hydrogel walkers with dual responsive legs.* Soft Matter, 2014. **10**(9): p. 1337-48.
24. Nagaoka, T., et al., *ECF (electro-conjugate fluid) finger with bidirectional motion and its application to a flexible hand.* Smart Materials and Structures, 2019. **28**(2): p. 025032.
25. Kedzierski, J., et al., *Microhydraulic Electrowetting Actuators.* Journal of Microelectromechanical Systems, 2016. **25**(2): p. 394-400.
26. Kedzierski, J. and H. Chea, *Multilayer microhydraulic actuators with speed and force configurations.* Microsystems & Nanoengineering, 2021. **7**(1): p. 22.
27. Tonazzini, A., A. Sadeghi, and B. Mazzolai, *Electrorheological Valves for Flexible Fluidic Actuators.* Soft Robotics, 2016. **3**(1): p. 34-41.
28. Liu, T., P. Sen, and C.-J. Kim, *Characterization of Nontoxic Liquid-Metal Alloy Galinstan for Applications in Microdevices.* Journal of Microelectromechanical Systems, 2012. **21**(2): p. 443-450.
29. Dickey, M.D., et al., *Eutectic Gallium-Indium (EGaIn): A Liquid Metal Alloy for the Formation of Stable Structures in Microchannels at Room Temperature.* Advanced Functional Materials, 2008. **18**(7): p. 1097-1104.
30. Lin, Y., J. Genzer, and M.D. Dickey, *Attributes, Fabrication, and Applications of Gallium-Based Liquid Metal Particles.* Adv Sci (Weinh), 2020. **7**(12): p. 2000192.
31. Wang, X., et al., *Printed Conformable Liquid Metal e-Skin-Enabled Spatiotemporally Controlled Bioelectromagnetics for Wireless Multisite Tumor Therapy.* Advanced Functional Materials, 2019. **29**(51): p. 1907063.
32. Dickey, M.D., *Emerging applications of liquid metals featuring surface oxides.* ACS Appl Mater Interfaces, 2014. **6**(21): p. 18369-79.
33. Zrnic, D. and D.S. Swatik, *On the resistivity and surface tension of the eutectic alloy of gallium and indium.* Journal of the Less Common Metals, 1969. **18**(1): p. 67-68.

34. Handschuh-Wang, S., et al., *Analysis and Transformations of Room-Temperature Liquid Metal Interfaces - A Closer Look through Interfacial Tension.* Chemphyschem, 2018. **19**(13): p. 1584-1592.
35. Handschuh-Wang, S., et al., *Surface Tension of the Oxide Skin of Gallium-Based Liquid Metals.* Langmuir, 2021. **37**(30): p. 9017-9025.
36. Handschuh-Wang, S., et al., *Electric Actuation of Liquid Metal Droplets in Acidified Aqueous Electrolyte.* Langmuir, 2019. **35**(2): p. 372-381.
37. Chung, Y. and C.-W. Lee, *Electrochemistry of Gallium.* Journal of Electrochemical Science and Technology, 2013. **4**(1): p. 1-18.
38. Khan, M.R., et al., *Giant and switchable surface activity of liquid metal via surface oxidation.* Proc Natl Acad Sci U S A, 2014. **111**(39): p. 14047-51.
39. Gozen, B.A., et al., *High-density soft-matter electronics with micron-scale line width.* Adv Mater, 2014. **26**(30): p. 5211-6.
40. Ma, J., et al., *Metallophobic Coatings to Enable Shape Reconfigurable Liquid Metal Inside 3D Printed Plastics.* ACS Appl Mater Interfaces, 2021. **13**(11): p. 12709-12718.
41. Ozutemiz, K.B., et al., *EGaIn-Metal Interfacing for Liquid Metal Circuitry and Microelectronics Integration.* Advanced Materials Interfaces, 2018. **5**(10): p. 1701596.
42. Deng, Y.-G. and J. Liu, *Corrosion development between liquid gallium and four typical metal substrates used in chip cooling device.* Applied Physics A, 2009. **95**(3): p. 907-915.
43. Handschuh-Wang, S., F.J. Stadler, and X.C. Zhou, *Critical Review on the Physical Properties of Gallium-Based Liquid Metals and Selected Pathways for Their Alteration.* Journal of Physical Chemistry C, 2021. **125**(37): p. 20113-20142.
44. Tang, S.Y., et al., *Gallium Liquid Metal: The Devil's Elixir.* Annual Review of Materials Research, Vol 51, 2021, 2021. **51**: p. 381-408.
45. Daeneke, T., et al., *Liquid metals: fundamentals and applications in chemistry.* Chem Soc Rev, 2018. **47**(11): p. 4073-4111.
46. Zhang, J., et al., *Self-fueled biomimetic liquid metal mollusk.* Adv Mater, 2015. **27**(16): p. 2648-55.
47. Xu, S., et al., *Self-fueled liquid metal motors.* Journal of Physics D-Applied Physics, 2019. **52**(35): p. 353002.
48. Wang, X., R. Guo, and J. Liu, *Liquid Metal Based Soft Robotics: Materials, Designs, and Applications.* Advanced Materials Technologies, 2018. **4**: p. 1800549.
49. Eaker, C.B. and M.D. Dickey, *Liquid metal actuation by electrical control of interfacial tension.* Applied Physics Reviews, 2016. **3**(3): p. 031103.
50. Eaker, C.B., et al., *Oxidation-Mediated Fingering in Liquid Metals.* Phys Rev Lett, 2017. **119**(17): p. 174502.
51. Song, M.Y., et al., *Interfacial Tension Modulation of Liquid Metal via Electrochemical Oxidation.* Advanced Intelligent Systems, 2021. **3**(8): p. 2100024.
52. Song, M.Y., et al., *Jumping liquid metal droplets controlled electrochemically.* Applied Physics Letters, 2021. **118**(8): p. 081601.
53. Yu, Z., et al., *Discovery of a Voltage-Stimulated Heartbeat Effect in Droplets of Liquid Gallium.* Phys Rev Lett, 2018. **121**(2): p. 024302.
54. Li, M., et al., *Automatic Morphology Control of Liquid Metal using a Combined Electrochemical and Feedback Control Approach.* Micromachines (Basel), 2019. **10**(3): p. 209.
55. Wissman, J., M.D. Dickey, and C. Majidi, *Field-Controlled Electrical Switch with Liquid Metal.* Adv Sci (Weinh), 2017. **4**(12): p. 1700169.

56. Shu, J., et al., *A Liquid Metal Artificial Muscle.* Adv Mater, 2021. **33**(43): p. e2103062.
57. Liao, J. and C. Majidi, *Soft actuators by electrochemical oxidation of liquid metal surfaces.* Soft Matter, 2021. **17**(7): p. 1921-1928.
58. Russell, L., J. Wissman, and C. Majidi, *Liquid metal actuator driven by electrochemical manipulation of surface tension.* Applied Physics Letters, 2017. **111**(25): p. 254101.
59. Liao, J. and C. Majidi, *Muscle-Inspired Linear Actuators by Electrochemical Oxidation of Liquid Metal Bridges.* Advanced Science, 2022. **9**(26): p. 2201963.
60. Gough, R.C., et al., *Rapid electrocapillary deformation of liquid metal with reversible shape retention.* Micro and Nano Systems Letters, 2015. **3**(1): p. 4.
61. Junghoon, L. and K. Chang-Jin, *Surface-tension-driven microactuation based on continuous electrowetting.* Journal of Microelectromechanical Systems, 2000. **9**(2): p. 171-180.
62. Dacuycuy, S.J., W.A. Shiroma, and A.T. Ohta, *Two-Dimensional Actuation of Liquid-Metal Droplets for Hot-Spot Cooling*, in *2021 20th IEEE Intersociety Conference on Thermal and Thermomechanical Phenomena in Electronic Systems (iTherm)*. 2021. p. 1262-1267.
63. Sarabia, K.J., et al., *Out-of-plane continuous electrowetting actuation of liquid metal.* Electronics Letters, 2017. **53**(25): p. 1635-1636.
64. Ren, H., et al., *Light-controlled versatile manipulation of liquid metal droplets: a gateway to future liquid robots.* Mater Horiz, 2021. **8**(11): p. 3063-3071.
65. Kosmulski, M., *Chemical properties of material surfaces*. Vol. 102. 2001: CRC press.
66. Tang, S.Y., et al., *Electrochemically induced actuation of liquid metal marbles.* Nanoscale, 2013. **5**(13): p. 5949-57.
67. Ye, J., et al., *A new hydrodynamic interpretation of liquid metal droplet motion induced by an electrocapillary phenomenon.* Soft Matter, 2021. **17**(34): p. 7835-7843.
68. Sivan, V., et al., *Liquid metal marbles.* Advanced Functional Materials, 2013. **23**(2): p. 144-152.
69. Sivan, V., et al., *Influence of semiconducting properties of nanoparticle coating on the electrochemical actuation of liquid metal marble.* Applied Physics Letters, 2014. **105**(12): p. 121607.
70. Gough, R.C., et al., *Continuous Electrowetting of Non-toxic Liquid Metal for RF Applications.* Ieee Access, 2014. **2**: p. 874-882.
71. Sahara, M.W., et al., *A Tunable Parallel-Plate Capacitor Using Liquid-Metal Actuation*, in *2021 IEEE Texas Symposium on Wireless and Microwave Circuits and Systems (WMCS)*. 2021. p. 1-6.
72. Yao, Y.Y. and J. Liu, *Liquid metal wheeled small vehicle for cargo delivery.* Rsc Advances, 2016. **6**(61): p. 56482-56488.
73. Wu, J., et al., *A Wheeled Robot Driven by a Liquid-Metal Droplet.* Adv Mater, 2018. **30**(51): p. e1805039.
74. Xue, R., et al., *Small universal mechanical module driven by a liquid metal droplet.* Lab Chip, 2021. **21**(14): p. 2771-2780.
75. Tang, S.Y., et al., *Liquid metal enabled pump.* Proc Natl Acad Sci U S A, 2014. **111**(9): p. 3304-9.
76. Tang, S.Y., et al., *Liquid Metal Actuator for Inducing Chaotic Advection.* Advanced Functional Materials, 2014. **24**(37): p. 5851-5858.
77. Zhang, G.B., et al., *An Electrically Actuated Liquid-Metal Gain-Reconfigurable Antenna.* International Journal of Antennas and Propagation, 2018. **2018**: p. 1-7.

78. Moorefield, M.R., et al., *An Electrically Actuated DC-to-11-GHz Liquid-Metal Switch.* Ieee Access, 2018. **6**: p. 1261-1266.
79. Li, X.X., et al., *A Controllable Untethered Vehicle Driven by Electrically Actuated Liquid Metal Droplets.* Ieee Transactions on Industrial Informatics, 2019. **15**(5): p. 2535-2543.
80. Li, F.X., et al., *Liquid metal droplet robot.* Applied Materials Today, 2020. **19**: p. 100597.
81. Wang, E., et al., *Liquid metal motor.* iScience, 2021. **24**(1): p. 101911.
82. Zhu, J.Y., et al., *An Integrated Liquid Cooling System Based on Galinstan Liquid Metal Droplets.* ACS Appl Mater Interfaces, 2016. **8**(3): p. 2173-80.
83. Xue, R., et al., *Pumping of Ionic Liquids by Liquid Metal-Enabled Electrocapillary Flow under DC-Biased AC Forcing.* Advanced Materials Interfaces, 2020. **7**(14): p. 2000345.
84. Hu, Q.M., et al., *Fluid Flow and Mixing Induced by AC Continuous Electrowetting of Liquid Metal Droplet.* Micromachines, 2017. **8**(4): p. 119.
85. Khan, M.R., C. Trlica, and M.D. Dickey, *Recapillarity: Electrochemically Controlled Capillary Withdrawal of a Liquid Metal Alloy from Microchannels.* Advanced Functional Materials, 2015. **25**(5): p. 671-678.
86. Khan, M.R., J. Bell, and M.D. Dickey, *Localized Instabilities of Liquid Metal Films via In-Plane Recapillarity.* Advanced Materials Interfaces, 2016. **3**(23): p. 1600546.
87. Tang, S.Y., et al., *Steering liquid metal flow in microchannels using low voltages.* Lab Chip, 2015. **15**(19): p. 3905-11.
88. Zhang, G.B., et al., *A Liquid-Metal Polarization-Pattern-Reconfigurable Dipole Antenna.* Ieee Antennas and Wireless Propagation Letters, 2018. **17**(1): p. 50-53.
89. Elassy, K.S., et al., *Toward the Design of a Reconfigurable Liquid-Metal Pixel Array*, in *2021 IEEE 21st Annual Wireless and Microwave Technology Conference (WAMICON)*. 2021. p. 1-4.
90. Mugele, F. and J.C. Baret, *Electrowetting: From basics to applications.* Journal of Physics-Condensed Matter, 2005. **17**(28): p. R705-R774.
91. Diebold, A.V., et al., *Electrowetting-actuated liquid metal for RF applications.* Journal of Micromechanics and Microengineering, 2017. **27**(2): p. 025010.
92. Wang, S., et al., *Generation of Nonspherical Liquid Metal Microparticles with Tunable Shapes Exhibiting an Electrostatic-Responsive Performance.* ACS Appl Mater Interfaces, 2021. **13**(14): p. 16677-16687.
93. Shu, J., et al., *Unconventional locomotion of liquid metal droplets driven by magnetic fields.* Soft Matter, 2018. **14**(35): p. 7113-7118.
94. Wang, L. and J. Liu, *Liquid metal folding patterns induced by electric capillary force.* Applied Physics Letters, 2016. **108**(16): p. 161602.
95. Li, F.X., et al., *Magnetically- and Electrically-Controllable Functional Liquid Metal Droplets.* Advanced Materials Technologies, 2019. **4**(3): p. 1800694.

3. Electro-mechano responsive elastomers with self-tunable conductivity and stiffness

This work has been published as G. Yun, **T. Cole**, Y. Zhang, J. Zheng, S. Sun, Y. Ou-yang, J. Shu, H. Lu, Q. Zhang, Y. Wang, D. Pham, T. Hasan, W. Li, S. Zhang, S-Y. Tang, Electro-mechano responsive elastomers with self-tunable conductivity and stiffness, Sci. Adv. 2023, 9, eadf1141

Author contributions: Conceptualization: G.Y., T.H., and S.-Y.T. Data curation: G.Y. and **T.C.** Formal analysis: G.Y., **T.C.**, and S.-Y.T. Funding acquisition: G.Y., T.H., W.L., S.Z., and S.-Y.T. Investigation: G.Y., **T.C.**, Y.Z., J.Z., and S.-Y.T. Methodology: G.Y., H.L., Q.Z., T.H., and S.-Y.T. Resources: **T.C.**, S.S., Y.O.-y., J.S., S.Z., and S.-Y.T. Supervision: T.H., W.L., S.Z., and S.-Y.T. Writing (original draft): G.Y. and S.-Y.T. Writing (review and editing): **T.C.**, Y.W., D.P., T.H., W.L., and S.-Y.T

3.1 Introduction

Electrical conductivity and mechanical stiffness are two fundamental properties of any material system. These properties are usually not tunable, with materials and overall design chosen to satisfy the functional criteria defined by specific applications. However, an increasing number of emerging applications in robotics, structural engineering, and consumer wearable electronics would benefit from materials whose properties can be actively tuned [1-6]. These smart materials that can respond to changes in their environment are revolutionising products and devices. For instance, materials with switchable conductivity show promising applications in electronic switches [7], optoelectronics [8], random access memory [9, 10], and reconfigurable electronics [11]. In addition, materials with variable stiffness offer exciting opportunities in soft

robotics and manipulators [12, 13], automotive and aerospace engineering [14, 15], and surgical and rehabilitation devices [16, 17]. Metal-polymer conductive elastomers offer such tunable electrical or mechanical properties [18-20]. Among them, conductive elastomers filled with low–melting point alloys [LMPAs; such as eutectic gallium (Ga)–indium and Field's metal (FM, melting point: 62 °C): eutectic tin–bismuth–indium] have recently become attractive because their resistance and stiffness can be changed by varying the temperature [21-23].

LMPAs have high electrical/thermal conductivity and high deformability after melting [24]. The solidification of LMPAs can induce volume expansion, thereby contacting adjacent particles to transform an insulating composite into a conductor [22]. Alternatively, melted LMPAs can fill the microgaps in conductive networks as the temperature rises, making the composite conductive [21]. In addition, the melting of LMPA particles can reduce the stiffness of the composites by up to two orders of magnitude [25, 26]. However, LMPA-filled elastomers demonstrated to date suffer from significant limitations [27]. On one hand, composites filled only with LMPA fillers can only switch between conductive and insulating states. Therefore, they are not competent for more complex applications requiring continuous resistance changes, such as sensors. On the other hand, LMPA-filled elastomers usually require external control systems to change their temperature, such as liquid nitrogen immersion [22] or adjusting the applied electrical current [23, 25]. Existing works have not attempted to combine variable resistance and stiffness properties and investigate their synergistic effects to achieve independence from external control.

Herein, a stretchable FM-filled hybrid elastomer (FMHE) comprising hybrid fillers of FM and spiked nickel (Ni) microparticles dispersed in a polydimethylsiloxane (PDMS) matrix is created. The use of FM avoids the extremely low solidifying temperature (below −30 °C, caused

by supercooling) required for Ga-based LMPAs [28, 29]. It is also biocompatible as it contains only indium, bismuth, and tin without lead or cadmium [30]. The use of spiked metal particles as the secondary filler gives high strain sensitivity and improves microstructural strength and mechanical stability [31, 32]. The FMHE exhibits not only reversibly switchable stiffness but also tunable electrical properties. Harnessing these effects synergistically, a self-triggered variable stiffness compliance compensator for robotic manipulators, with 10 times improved compensation capabilities than the best commercial products is demonstrated. In addition, a highly compact (>one order of magnitude smaller), self-recovering, resettable, current-limiting fuse with >10 times faster response than state-of the-art resettable fuses is created.

3.2 Preparation and Imaging of the FMHE

3.2.1 Preparation of the FMHE

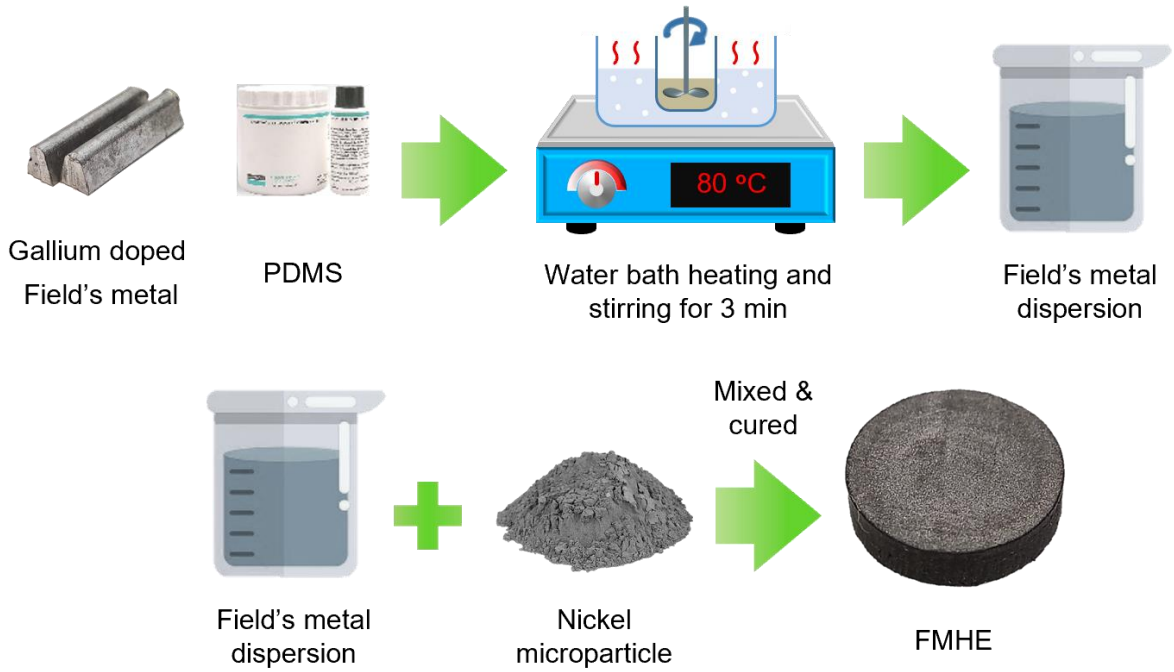

Figure 3.1 Procedure for preparing the FMHE.

The overall procedure for making FMHE is shown in Figure 3.1. The first step for fabrication is to prepare FM alloy. Indium (51 wt %), bismuth (32.5 wt %), and tin (16.5 wt %) were cut into pieces less than 3 mm in size and placed in a glass beaker on a hot plate to melt at 220 °C for 1 hour. The melted metal was stirred with a glass rod with continued heating for 5 mins. As the molten metal has a viscosity similar to water, mixing by hand for a short period is sufficient to ensure the Field's metal alloy is fully mixed. Then the molten Field's metal was left to cool at ambient temperature for 5 min, before being poured into a deionized water tank to obtain a FM alloy block as it rapidly cools and solidifies. 1 wt % of Ga was added into molten FM at 100 °C to prepare Ga-doped FM alloy (its melting point is ~60 °C). The Ga-doped FM and PDMS were put into a glass beaker placed in an 80 °C water bath with a volume ratio of 1:1 (the PDMS used is a mixture of 90 wt % of SYLGARD 184 silicone elastomer base and 10 wt % of SYLGARD 184 silicone elastomer curing agent). They were mixed using a high-speed electric stirrer (rotating speed of 300 rpm) for 5 min. The electric stirrer was equipped with a flat mixing stick with a cross section of 2 mm by 5 mm. The obtained FM-PDMS dispersion was then mixed with Ni microparticles (2-5 μm diameter, APC Pure) for 4 min at a rotating speed of 200 rpm using the electric stirrer. Different FMHE samples had differing Ni: PDMS mass ratios of 0/0.5/1/2/3:1, denoted as $FMHE_{0/0.5/1/2/3}$. The volume ratio of PDMS/FM/Ni in $FMHE_3$ is 1:1:0.34. The mixtures were then degassed in a vacuum chamber for 20 min to remove air bubbles. Last, it was poured into 3D printed polyurethane moulds and cured at 75 °C for 12 hours to obtain the FMHE samples (Figure 3.2). Prepared samples were cubic (8 mm by 8 mm by 8 mm) for compression testing and bar-shaped (2 mm by 5 mm by 30 mm) for stretch testing.

Consistency between samples was ensured by using the same mixing parameters for all samples, as mixing speed has a large impact on the average metal droplet size and the resistivity

of the final elastomer [33]. The electric stirrer used was always equipped with the same size mixing stick (cross section of 2 mm by 5 mm), and mixing was done using consistent rpm and length of time across all samples (rotating speed of 300 rpm for 5 min to make the FM-PDMS dispersion, and 4 min at a rotating speed of 200 rpm after Ni was added). 5 samples were made in the same batch if multiple samples were required for testing.

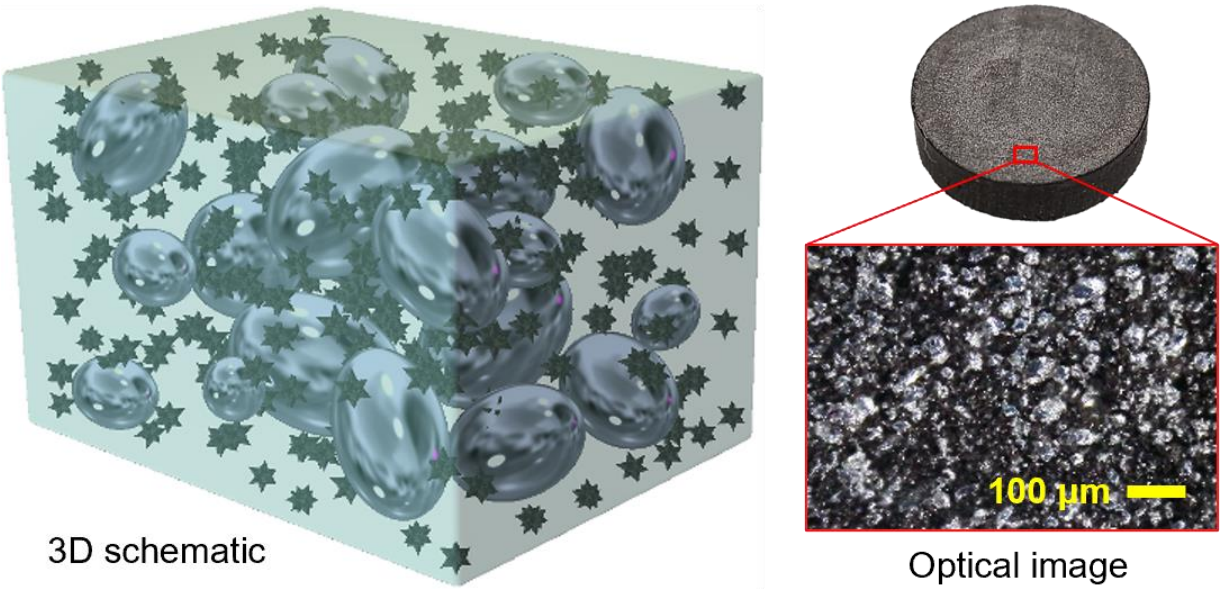

Figure 3.2 3D schematic of the composition and optical microscope image showing the surface structure of the FMHE.

Ga was added to FM because it forms a Ga oxide layer on the surface of the FM droplet as it can provide the lowest Gibbs free energy [34, 35]. This prevents the coalescence of FM microdroplets during mixing and provides better control over the droplet size.

3.2.2 SEM and EDS Imaging of FMHE

A Gemini SEM 500 field emission scanning electron microscope was used to obtain scanning electron microscopy (SEM) and energy-dispersive X-ray spectroscopy (EDS) images of FMHE (Figure 3.3 and Figure 3.4). The diameter of the FM particles in $FMHE_0$ is 15~30 μm. Due to their high (50%) volume fraction, these FM particles are in close contact with one another with nanometre-wide gaps in between. The EDS image (Figure 3.3A) shows the elemental distribution of gallium, indium and silicon in $FMHE_0$. The distribution area of gallium overlaps with that of indium, showing the gallium oxide layer on the surface of the FM particles (also visible in SEM images (Figure 3.3A and Figure 3.4A). Gallium oxide usually forms on the surface of gallium based liquid metals. For the gallium-doped FM in this work, the formation of the gallium oxide layer is due to the fact that this can provide the lowest Gibbs free energy of the FM droplet [34]. Note that FM particles also existed in the red dotted circles, but they are attached to the other cross-section of the sample after fracture, as evidenced by the pits in the red circles in the SEM image (Figure 3.3A). In addition, the residual Ga oxide skin in the white circles in the EDS image (Figure 3.3B) corresponds to the pits in the SEM image, which further proves the existence of FM particles in the circles.

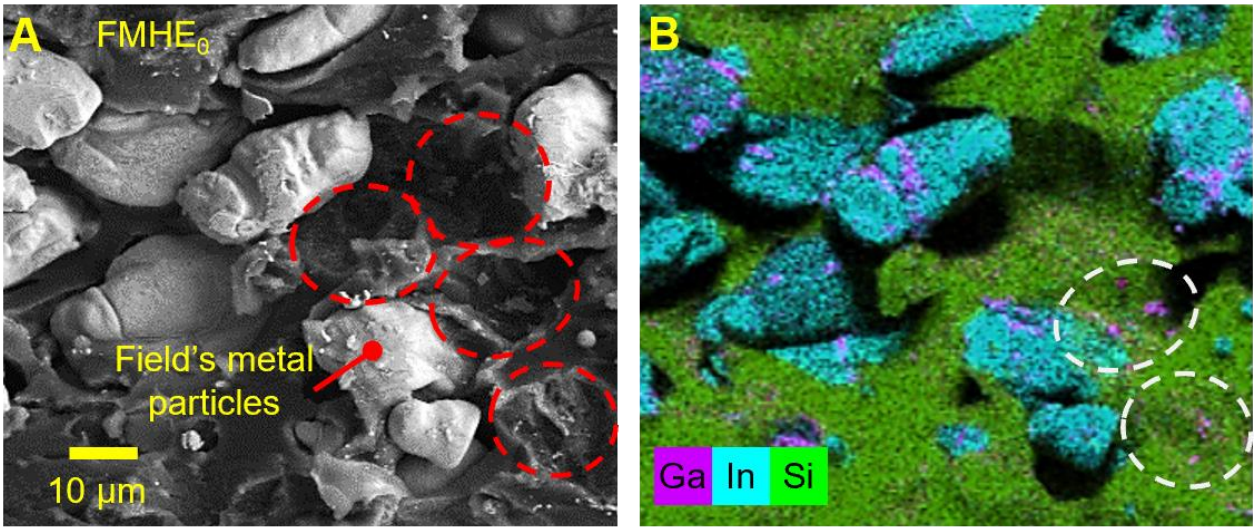

Figure 3.3 (A) Scanning electron microscopy (SEM) and (B) energy dispersive spectroscopy (EDS) images of the cross-section of $FMHE_0$.
The pits in the red circles are formed by the removal of FM particles.

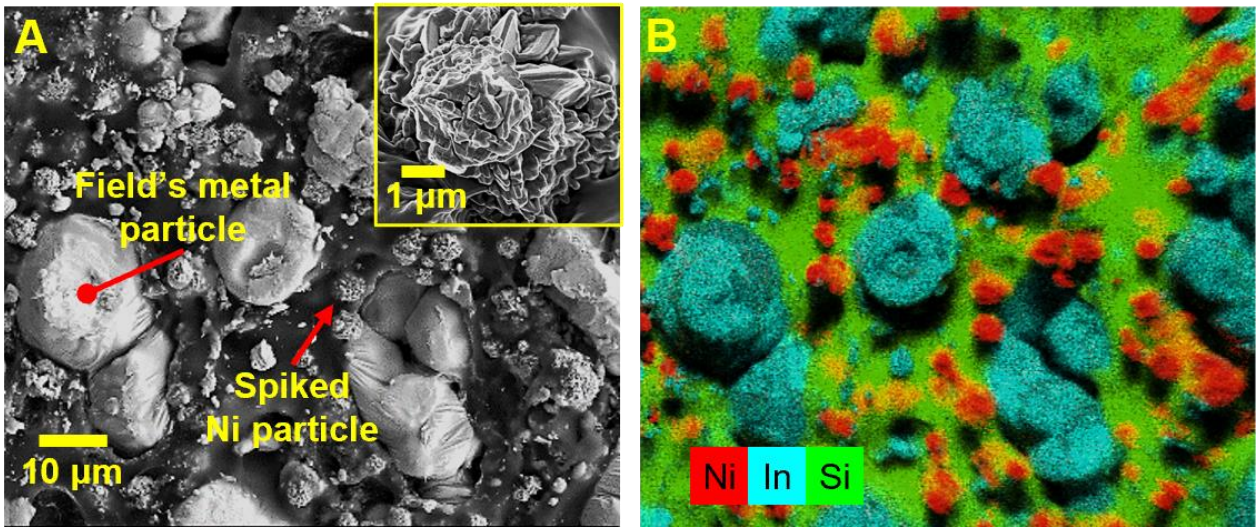

Figure 3.4 (A) SEM and (B) EDS images of the cross section of the $FMHE_3$ sample.
The distribution of Ni, FM and PDMS are represented by their characteristic elements of Ni, In and Si. The inset shows a close-up SEM image of a spiked Ni particle.

The diameter of the FM particles in $FMHE_3$ is 10 to 20 μm. The spiked Ni microparticles increase the total volume of the FMHE composite and thus reduce the volume fraction of FM particles from 50 to 42.8%. They also separate FM particles to prevent them from contacting,

as indicated by the thick PDMS layer between adjacent FM particles. This is in contrast with the FM particles in $FMHE_0$, which are in close contact with nanometer-wide gaps in between because of the absence of the Ni microparticles (Figure 3.3). Because of the presence of the nickel microparticles, the $FMHE_3$ is expected to have a higher electrical resistivity at zero strain than that of the $FMHE_0$. The inset in Figure 3.4 shows the microstructure of an individual Ni particle with numerous spikes on the surface. The low–melting point FM and spiked Ni particles impart variable electromechanical properties and unconventional electrical strain response to FMHEs. Ni was chosen as the solid conductive filler as it has been shown to have a much higher change in conductivity ratio per percentage strain than for iron and copper particles (5 orders of magnitude greater and 7 orders of magnitude greater, respectively) [33].

3.3 Electrical Properties of the FMHE

3.3.1 Experimental Set-up for Electrical Testing of the FMHE

The electrical properties of the FMHE were tested under mechanical deformation at different temperatures. A Single Column Mechanical Testing Machine (YK-Y0026, Dongguan Yaoke Instrument Equipment Co. Ltd., China) was used to compress block samples and stretch bar samples at a speed of 5% min^{-1}. The block samples were heated using a Thermoelectric Peltier chip (TEC1-12706), and the bar samples were heated using an induction heater (dc: 5 V, 12 A). A Voltcraft temperature-measuring instrument (PL-125-T2USB) was used to record temperature data, with the thermometer probe attached to the surface of the FMHE sample. A FLUKE 8845A digital multimeter with a resistance range of 100 mega ohms was used to measure the resistance and current, with data being recorded through Flukeview forms software. The multimeter leads were first connected with no sample in between, then the multimeter was set to relative mode to remove the lead resistance from measurements. The resistance

measurement resolution of the multimeter as per the data sheet was 100 micro ohms, with accuracy of measurement of 0.01%. See Figure 3.5 for pictures of the experimental setup.

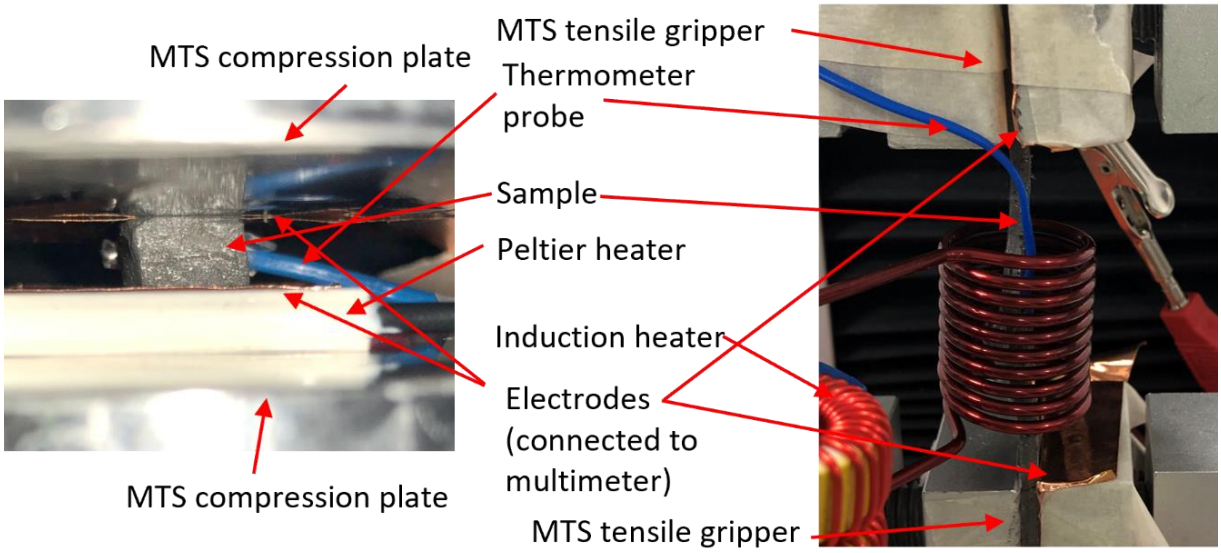

Figure 3.5 Experimental set up for compression and tensile testing of FMHE.
The thermometer probe was attached to the surface of the samples using stretchable tape. The grippers and compression plates of the MTS were covered in tape to prevent electrical connection between the MTS and the samples.

3.3.2 Measured Electrical Properties of the FMHE

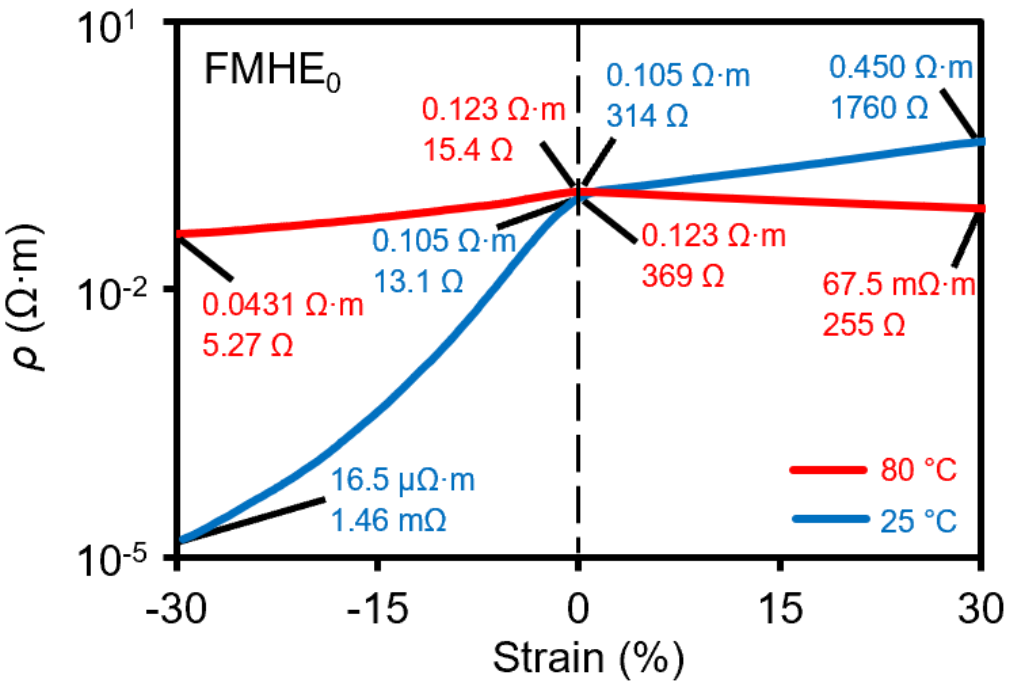

Figure 3.6 Resistivity-strain curve of $FMHE_0$ at 25 °C and 80 °C.
A negative value of strain represents compression.

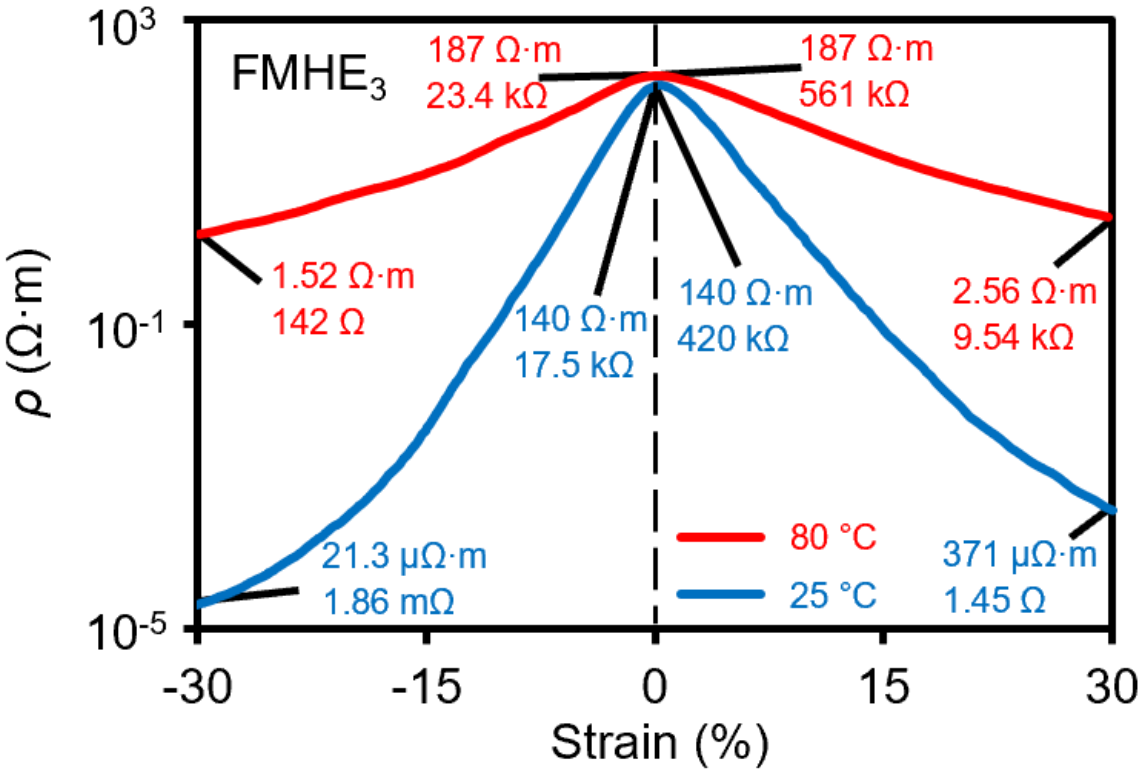

Figure 3.7 Resistivity-strain curve of $FMHE_3$ at 25 °C and 80 °C.
A negative value of strain represents compression.

Figure 3.6 and Figure 3.7 show the resistivity-strain curves of $FMHE_0$ and $FMHE_3$ at 25 °C (FM is solid) and 80 °C (FM is liquid), respectively. Resistivity of the samples, ρ, was calculated according to the equation

$$\rho = \frac{Rl}{A} \tag{3.1}$$

where R is the measured resistance of the sample, l is the length, and A is the cross-sectional area. Testing used block samples for compressive measurements and bar samples for tensile measurements, therefore the resistance for each of the types of sample differs due to their different cross-sectional area and length.

The $FMHE_0$ has an initial resistivity of 0.105 ohm·m at 25 °C. Under compression, the FM particles are brought into contact, leading to an exponentially enhanced conductivity. For $FMHE_3$, the Ni particles serving as spacers increase the initial resistivity to 140 ohm·m. The reduction in its resistivity under compression is more obvious than that of $FMHE_0$, indicating an improved strain sensitivity. During stretching, the $FMHE_0$ resistivity increases because of the separation of the FM particles (positive piezoresistivity). Conversely, Ni particles reverse the piezoresistivity of $FMHE_3$ to negative when stretched. It has previously been shown that this effect is due to the hybrid conductive particle network and the spiked shape of Ni particles [36, 37]. Note that although the elastomer studied in this work exhibits the negative piezoresistive effect previously reported, the presented electro-mechano responsive property and the self-triggered tunability have not been found before, as elaborated in the following sections.

The resistivity of the composite mainly depends on the number of electrical connection pathways in the conductive filler network. Because of its positive Poisson's ratio, $FMHE_3$ is always compressed in a certain direction under any mechanical load, including stretching. The FM and Ni particles in $FMHE_3$ then squeeze each other along the compression direction, leading to a sharp increase in the number of electrical connections, thereby reducing the resistivity [36]. Furthermore, the protruding spikes of Ni particles allow the fillers to be in contact with a higher probability when $FMHE_3$ is deformed [31]. As a result, the conductivity of $FMHE_3$ increases during deformation, showing a much higher strain sensitivity compared with $FMHE_0$.

At 80 °C, the FM particles melt, increasing the initial resistivity and greatly reducing the strain sensitivity of the FMHE. The melted FM microdroplets deform along with the PDMS matrix

under strain, avoiding their close contact under compression and separation under stretching. The optical microscope images in Figure 3.8 clearly demonstrate the space changes between FM particles during compression and stretching, as well as their deformation upon melting. $FMHE_3$ still shows better strain sensitivity than $FMHE_0$ as solid Ni particles can squeeze PDMS layers and form conductive paths.

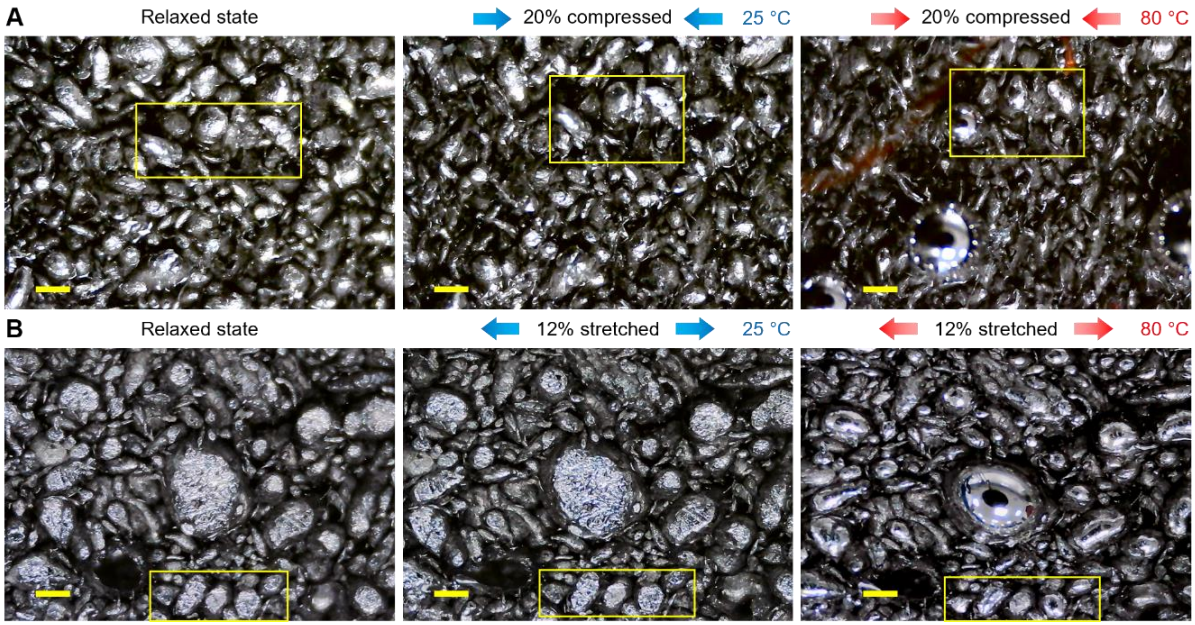

Figure 3.8 Microscope images of the surface of $FMHE_0$ showing the space change between FM particles and their deformation upon melting under (A) compression and (B) stretching.
Scale bars are 20 μm. The yellow rectangles highlight a small section of the FMHE to more easily see the shape change of selected particles during compression and stretching.

Figure 3.9 depicts the filler network changes in $FMHE_3$ during compression at different temperatures. At 25 °C, the thickness of the PDMS layers along the conductive pathways (red curves in Figure 3.9) decreases sharply when compressed, leading to a rapid decrease in resistivity. At 80 °C, FM melts into droplets, while solid Ni particles can still squeeze PDMS

layers and form conductive paths. Therefore, the resistivity of $FMHE_3$ gradually decreases during compression, showing a lower strain sensitivity than that at 25 °C.

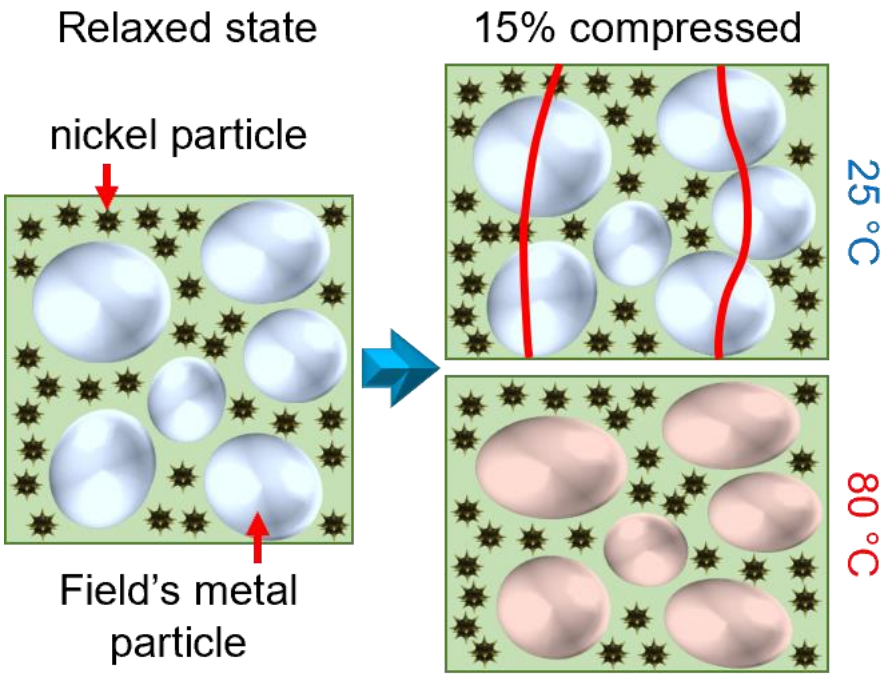

Figure 3.9 Diagram of the change in the filler network of $FMHE_3$ under compression at 25 °C and 80 °C.

The gauge factor of $FMHE_0$ and $FMHE_3$ was calculated for temperatures of 25 °C and 80 °C, as shown in Figure 3.10. Gauge factor ($GF = \Delta\rho/\rho\varepsilon$, where ρ and ε are the electrical resistivity and strain, respectively) quantifies the strain sensitivity of an electrical component. A higher GF value indicates higher sensitivity, and a positive GF indicates a positive piezoresistive effect. At 25 °C, $FMHE_0$ shows a maximum GF of 34.1 at 5% compressive strain. In contrast, $FMHE_3$ exhibits a higher strain sensitivity with a maximum GF of 70.5. In addition, the negative GF of $FMHE_3$ during stretching shows its special negative piezoresistive effect. At 80 °C, the melting of FM significantly reduces the strain sensitivity of FMHEs, as indicated by their low GF. The GFs of $FMHE_0$ during compression and stretching are only 3.6 and −1.6, respectively. The

strain sensitivity of $FMHE_3$ also drops sharply after FM melts but remains high. Its GF under 5% compressive and tensile strain is 18.4 and −13.4, respectively, which is much higher than that of $FMHE_0$.

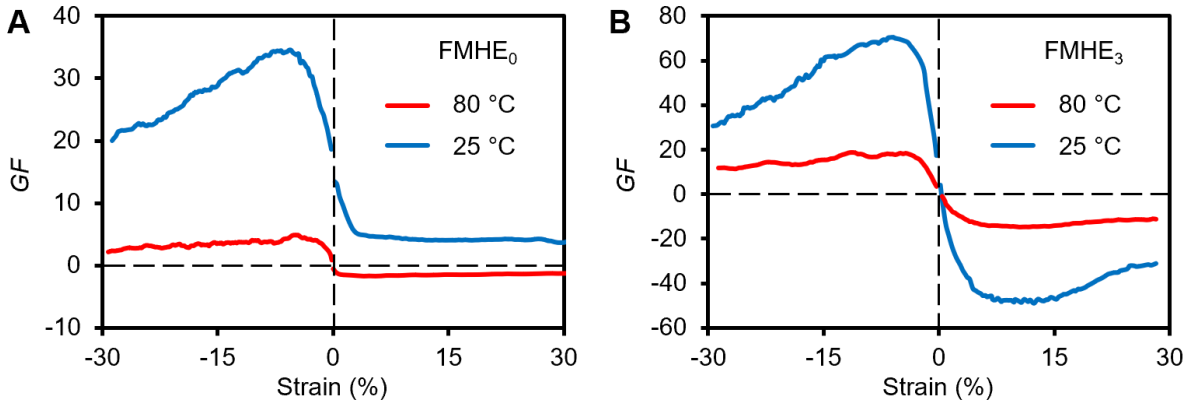

Figure 3.10 Gauge factor-strain curves of (A) $FMHE_0$ and (B) $FMHE_3$ at 25 °C and 80 °C.

3.3.3 Simulation of Resistivity of FMHE

Simulations of FMHE resistivity were done to compare with the experimental results. (See Table 3.1 and Figure 3.11). COMSOL Multiphysics 5.2 finite element software was used to simulate the resistivity of the $FMHE_0$ and $FMHE_3$ 2D models (150×150 μm) during a compression process at 25 °C and 80 °C. The thickness of the model was set at 1 μm. The models were established based on the SEM images. The sizes of the Ni (2~5 μm) and FM (15~30 μm) particles are equal to those in the actual composites. An electrical-mechanical-thermal coupled multifield model was used to simulate the mechanical deformation and resistivity of the model. The material parameters of the fillers and PDMS matrix (mainly including the elastic modulus, Poisson's ratio, conductivity, dielectric constant, and coefficient of thermal expansion) are consistent with the COMSOL material library. The FM used material parameters corresponding to the solid or liquid state at 25 °C or 80 °C, respectively. In the

simulation model, the gallium oxide layer on the surface of the melted FM droplet was omitted. This is because the thickness of the gallium oxide film is only 1~3 nm [35], which is much smaller than the diameter of FM droplets (10~20 μm). Such a thin oxide layer does not affect the mechanical deformation of the FM droplets. Additionally, since the conductivity of both the FM droplet and the gallium oxide is much higher than that of the PDMS matrix, this extremely thin oxide layer also does not affect the simulation for the resistivity of the composite. The mechanical deformation and microstructure change of the model were simulated by applying a fixed displacement load to the upper side of the model. Figure 3.11 shows the boundary conditions in the simulation. The left and right sides of the 2D model were electrically insulated, the lower side was grounded, and the current density through the upper side was fixed at 100 $A \cdot m^{-2}$. The resistivity of the FMHE model can be calculated based on the drop in electrical potential.

Table 3.1 Details of the COMSOL simulation

Software	COMSOL Multiphysics 5.2
Model type	Electrical-mechanical-thermal coupled multifield
Dimensions	150 μm width 150 μm height 1 μm thickness
Materials	Ni FM (solid or liquid depending on temperature) PDMS
Size of particles	Ni: 2-5 μm FM: 15 – 30 μm (based on SEM image)
Ni properties	Electrical conductivity: 13.8×10^6 S m^{-1} Coefficient of thermal expansion: 13.4×10^{-6} K^{-1} Young's modulus: 219×10^9 Pa Poisson's ratio: 0.31
FM properties	Electrical conductivity: 1.9×10^6 S m^{-1} Coefficient of thermal expansion: 3×10^{-4} K^{-1} Young's modulus: 9.25 $\times 10^9$ Pa (solid); N/A (liquid) Poisson's ratio: 0.44 (solid); 0.5 (liquid)
PDMS properties	Coefficient of thermal expansion: 9×10^{-4} K^{-1} Relative permittivity: 2.75 Young's modulus: 750 kPa Poisson's ratio: 0.49
Simulation boundary conditions	Top side: 100 A m^{-2} current density Bottom side: grounded Left and right side: electrically insulated Temperature: 25°C and 80°C
Measurement	Drop in electrical potential between top and bottom

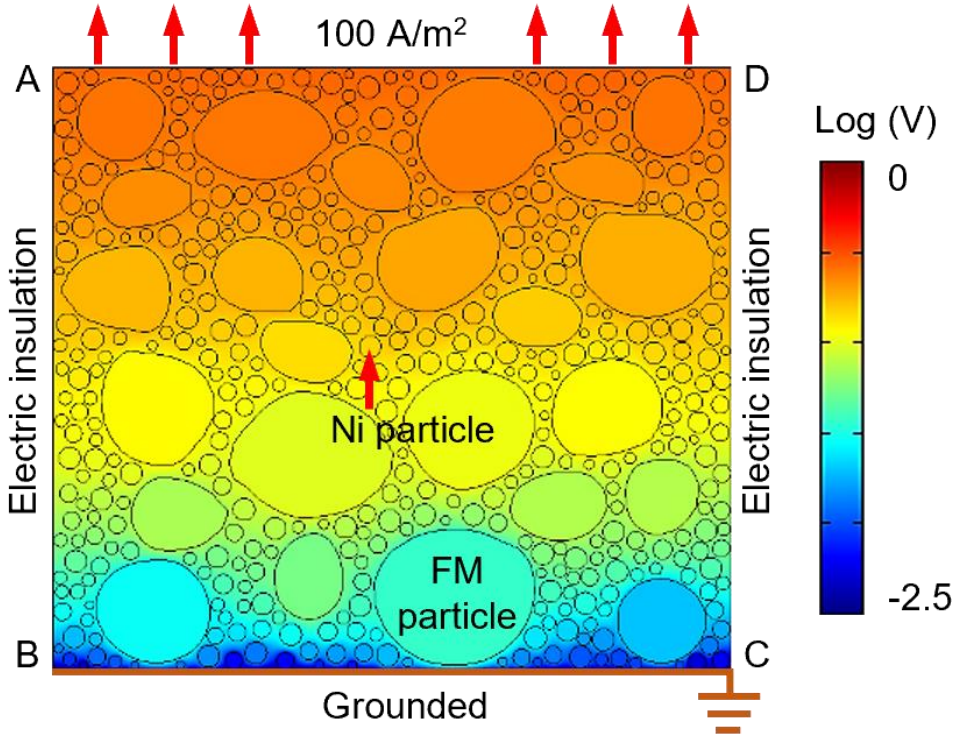

Figure 3.11 COMSOL simulation set up to determine the resistivity of FMHE.
Labels show the FM particles and Ni particles, with sizing and positioning determined by a SEM image. The bottom side was grounded, with the top side having a current density of 100A·m^{-2} set to pass through it. The left and right side were electrically insulated. Thickness of the model was set to 1 μm. The colour shows the voltage drop across the simulation.

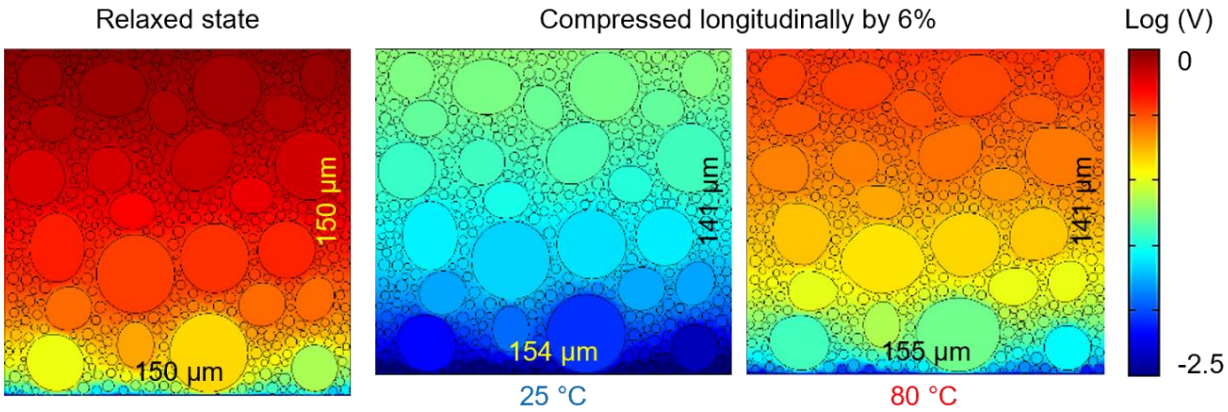

Figure 3.12 Simulation results of the electrical potential distribution of FMHE$_0$ at different strains and temperatures.

A 2D simulation was chosen to do rather than 3D as it is simpler to set up and compute, however it has some limitations due to its lack of a third dimension. In a 2D simulation, the material is assumed to be uniform throughout the whole slice. For example, if there is a Ni or FM particle on the surface, it is assumed in the simulation to continue through the whole thickness of the slice, with the same shape and dimensions. This is inaccurate as the metal particles are roughly spherical, so their cross-sectional area will change with depth. Also, in the simulation, where there is PDMS on the surface, it is assumed to be PDMS in that section through the whole thickness. This is inaccurate as there may be Ni or FM just below the surface of PDMS. The depth of the simulation was set to 1 μm to try to minimise the effect of the assumptions and get as accurate as possible simulation results. However, doing a full 3D simulation would give the most accurate simulation results. Only compression simulation was done because the FMHE behaved in a similar manner for strain due to compression and tension.

The 2D model can show the microstructural changes and predict the sensitivity of FMHE at different temperatures (Figure 3.12). The deformation of FM droplets at 80 °C is evident. The simulated resistivity-strain curves given in Figure 3.13 show higher initial resistivity and lower sensitivity of $FMHE_3$ at 80 °C, which is consistent with the experimental results.

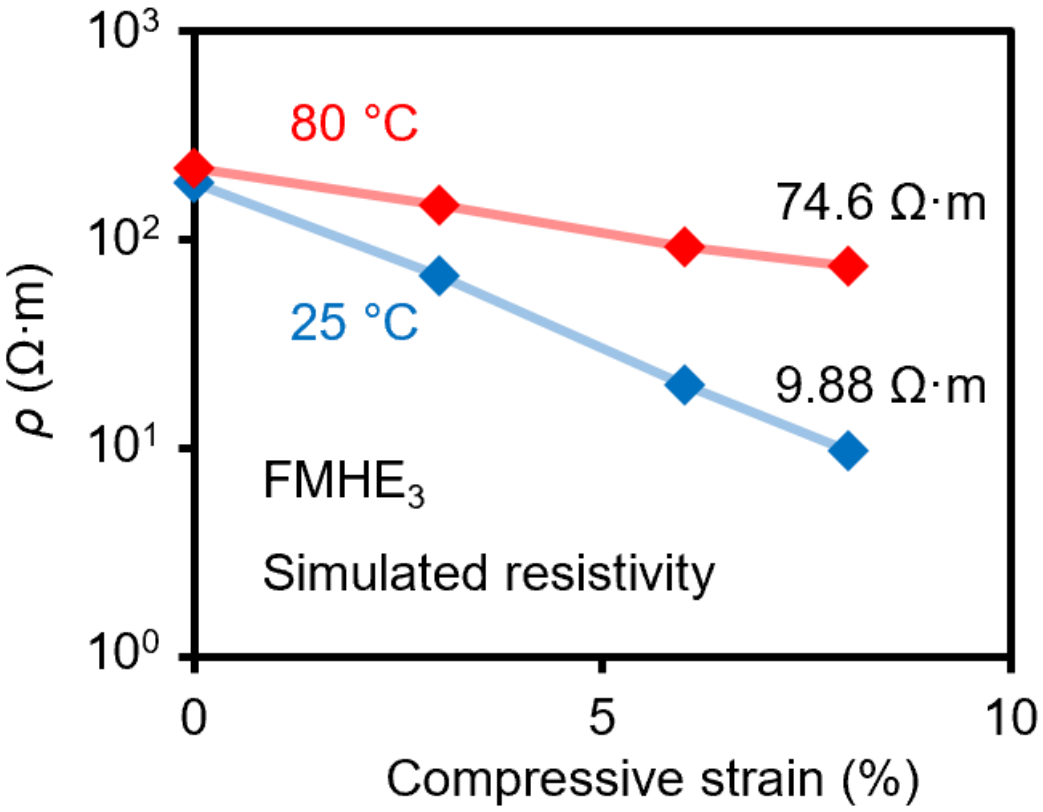

Figure 3.13 COMSOL simulation resistivity-strain curves of FMHE$_3$ at 25 °C (blue) and 80 °C (red).

The simulations on FMHE$_0$ are also in line with the experimental results. Figure 3.14 shows the microstructure and electrical potential distribution of FMHE$_0$ compressed at 25 °C and 80 °C. The potential drop when FMHE$_0$ is compressed by 8% at 80 °C is similar to that in the relaxed state, reflecting the relatively stable resistivity when FM melts. In contrast, the voltage drops at 25 °C are very small, corresponding to low resistivity and high strain sensitivity. The resistivity change in the simulated resistivity–strain curves given in Figure 3.15 is also consistent with the experimental results.

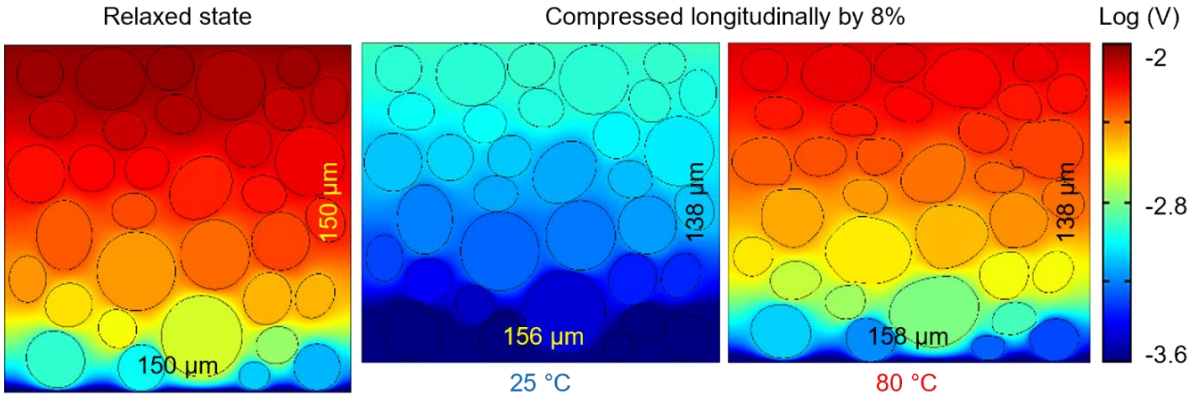

Figure 3.14 Simulation results of the electrical potential distribution of $FMHE_0$ at different strains and temperatures.

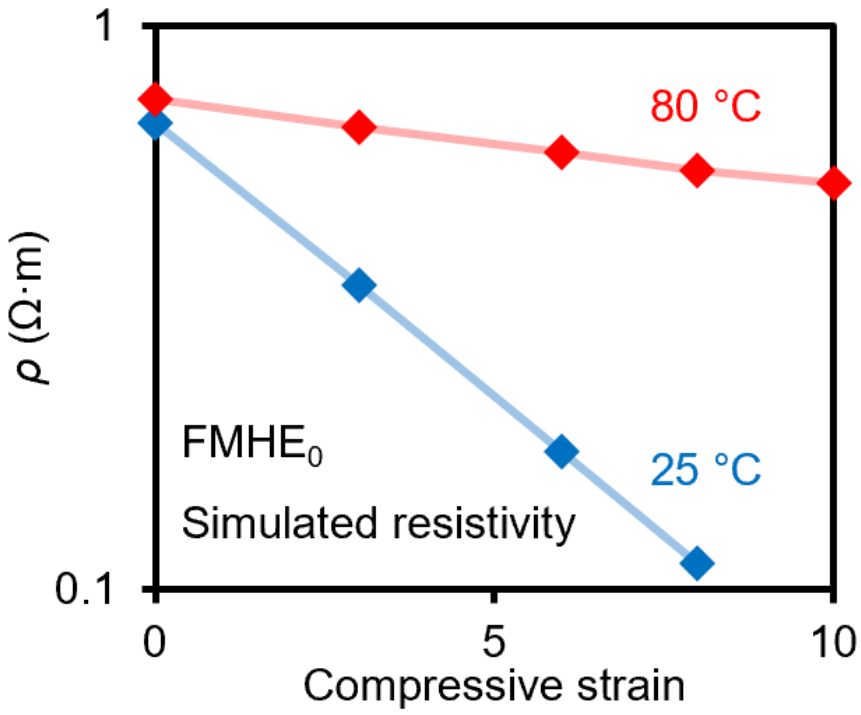

Figure 3.15 COMSOL simulation resistivity-strain curves of $FMHE_0$ at 25 °C (blue) and 80 °C (red).

3.3.4 Influence of Conductive Fillers on Electrical Properties of FMHE

The effect of Ni filler content on the electrical properties of FMHE was investigated. This was done by measuring the resistivity of $FMHE_{0/0.5/1/2/3}$ samples at 25 °C and 80 °C (Figure 3.16). The initial resistivity and strain sensitivity of the FMHE increase significantly with increasing Ni content. In addition, the resistivity of $FMHE_{0.5}$ decreases by 80% when stretched by 10%, proving that FMHE can exhibit a negative piezoresistivity during stretching even with only a small amount of Ni particles. However, Ni particles will also slightly reduce the stability of the FMHE resistivity, as indicated by the relatively large error bars in Figure 3.16A. Figure 3.16B compares the resistivity of $FMHE_{0/0.5/1/2/3}$ samples at strains of −10%, 0% and 10% when the FM particles melt. Melting of FM particles shows little influence on the initial resistivity of the FMHE samples but greatly increases their resistivity under mechanical deformation (i.e., reduces their strain sensitivity). When compressed by 10% at 80 °C, the conductivity of $FMHE_{0/0.5/1/2/3}$ increases by 0.6, 1.1, 2.7, 4.2, and 7 times, respectively.

Interestingly, as Ni content increases, the unstrained resistivity of FMHE increases but conversely, the strained resistivity decreases. FMHE with increases Ni filler content have increased resistivity at 0% strain as each of the Ni particles is surrounded by PDMS so do not have an overall conductive path. Also the increased Ni content increases overall volume of the FMHE, so the percentage volume of the larger FM particles (which help lower the resistivity due to their large size and high conductivity), is reduced. When strained, the FMHE with higher Ni content are more easily able to form conductive paths as there are more Ni particles and less PDMS between them.

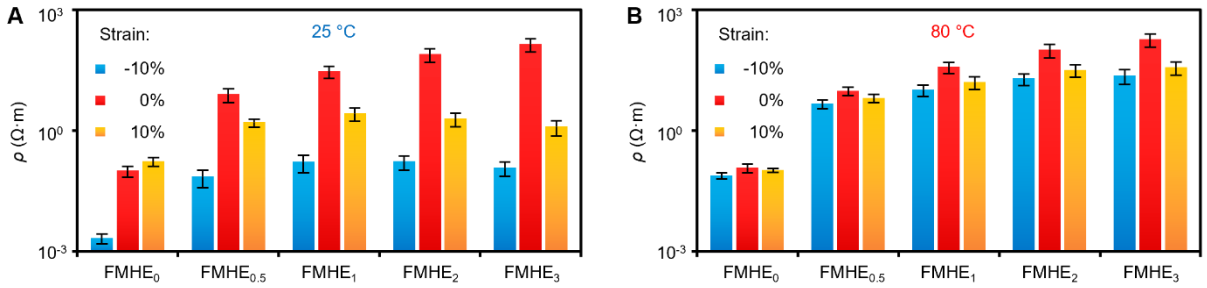

Figure 3.16 Resistivity of the FMHE with different Ni contents at (A) 25 °C and (B) 80 °C. The values of the error bars are the standard deviation of the measurement of resistivity of 5 different samples fabricated in the same batch.

FM particle size and volume fraction will also have a large impact on the electrical properties of FMHE. To investigate this, a set of $FMHE_3$ samples with different average FM particle sizes and FM contents were made, and their initial resistivities at 25 °C and 80 °C were measured. The average particle size was measured under a microscope. The results are shown in Figure 3.17. According to Figure 3.17A, the resistivity of $FMHE_3$ will decrease by >10 times when the average FM particle size is doubled. However, the large particle size also leads to lower resistivity stability. The FM content also has a significant influence on the electrical conductivity of FMHE. From Figure 3.17B, when the volume of FM increases by 10%, the resistivity of $FMHE_3$ can be reduced by approximately 30 times. Increasing the size of the FM particles and a higher FM volume fraction both lead to an increased opportunity to form conductive pathways, which is why the resistivity decreases. For all $FMHE_3$ samples, the melting of FM particles increases their resistivity by 20~40%.

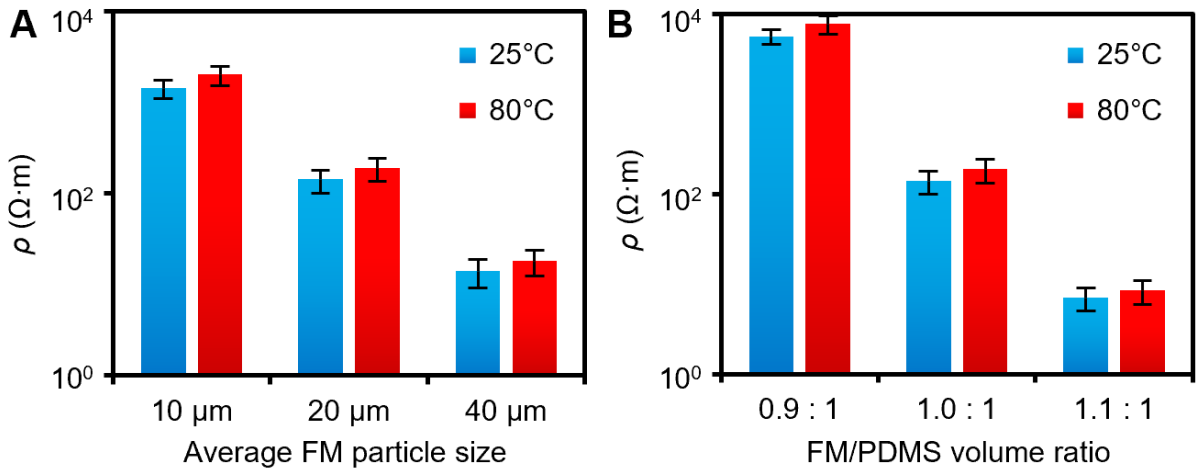

Figure 3.17 Resistivity of FMHE$_3$ samples with different FM (A) particle sizes and (B) contents at 25 °C and 80 °C.
The values of the error bars are the standard deviation of the measurement of resistivity of 5 different samples fabricated in the same batch.

3.3.5 Cyclic Testing

The stability of electrical properties of FMHE was tested by cyclic testing of the resistance with 0-20% compression applied 10 times at 25 °C and 80 °C (Figure 3.18). In each compression cycle, the resistance of FMHE$_3$ decreases steadily and basically returns to the initial value. After 10 cycles, the initial resistance increases by approximately 10%. Resistance was continuously measured and recorded every second using Fluke 8845a digital multimeter and Flukeview forms software.

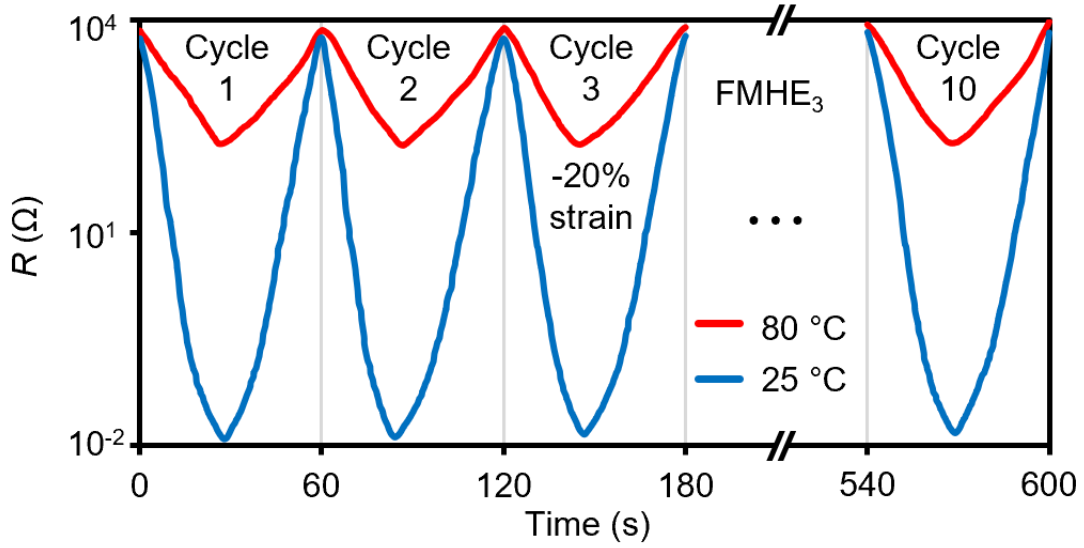

Figure 3.18 Resistance-time curves of FMHE$_3$ over 10 cycles during cyclic loading tests at 25 °C and 80 °C.

3.3.6 Resistance Variation with Temperature

The resistance variation of FMHE with temperature was also investigated, for both heating and cooling of the block samples (Figure 3.19). As in previous experiments, heating was done with a thermoelectric chip. To avoid the hysteresis of the sample temperature increase relative to the chip temperature increase, the chip temperature was increased by about 1 °C for each measurement, then the sample resistance was taken ~10s after the temperature stabilized.

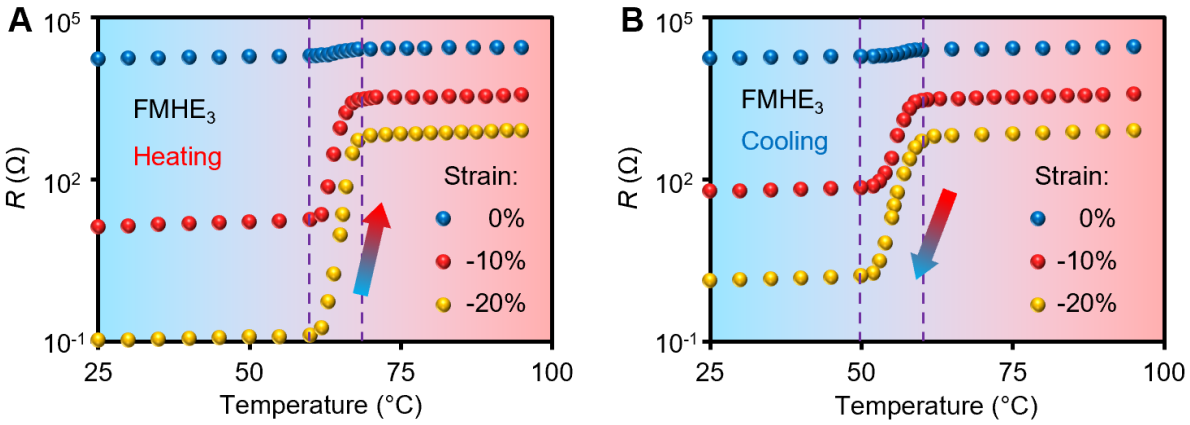

Figure 3.19 Resistance-temperature curves of the $FMHE_3$ sample under different strains during (A) heating, (B) cooling.

Mainly because of the thermal expansion of PDMS (expansion rate of 0.034% $°C^{-1}$) [38], the resistance of $FMHE_3$ samples increases by 20 to 30% when the temperature rises from 25° to 60 °C (Figure 3.19A). As the samples are further heated, the FM particles gradually melt and deform under pressure, leading to their separation from surrounding conductive particles to induce a sharp increase in resistivity. The resistance stabilizes when all FM particles are melted. This resistance change mainly depends on the temperature and is not significantly related to the heating rate or external mechanical manipulation. The resistance curve of the $FMHE_3$ during cooling shows a decrease in resistance at a lower temperature compared to that shown during heating. This is because of a lower solidifying temperature of FM due to supercooling [28, 39]. Under compression, the resistance of the $FMHE_3$ cannot return to its initial value after the FM resolidifies, as shown by the resistance-temperature curves in a heating-cooling cycle under 10% compressive strain (Figure 3.20). Because the $FMHE_3$ sample is compressed, the FM droplets will solidify in a deformed shape during cooling. This increases the distance between conductive particles, leading to a higher initial resistance at 25 °C.

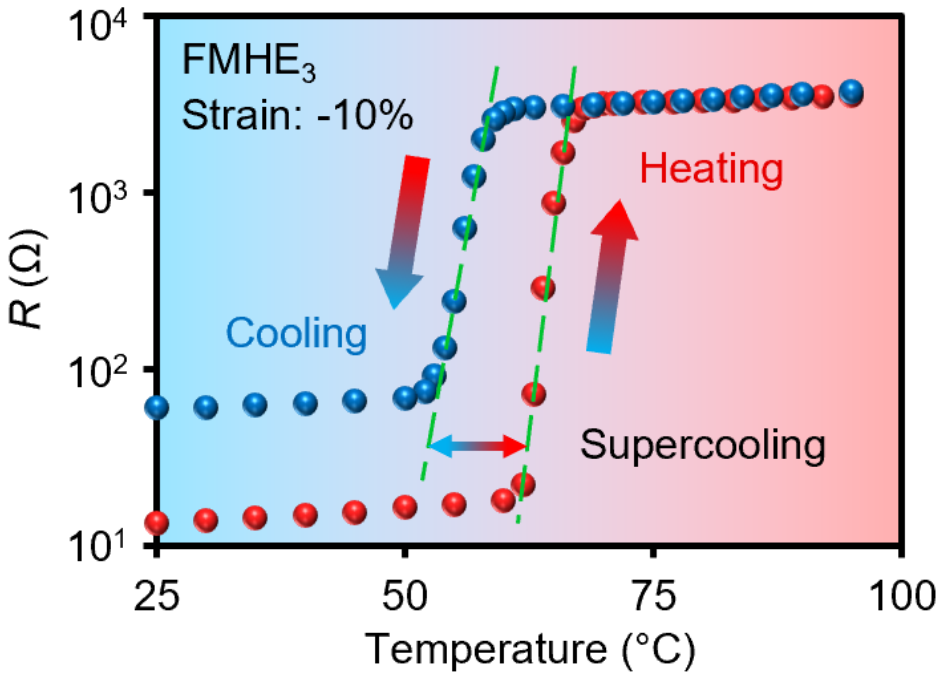

Figure 3.20 Resistance-temperature curves of the $FMHE_3$ sample under 10% compressive strain during heating and cooling.

For comparison, Figure 3.21 gives the resistance-temperature curves for $FMHE_0$, which shows a similar shaped curve, with a sharp increase in resistivity when FM melts, and a slight increase with temperature when the FM is solid or liquid.

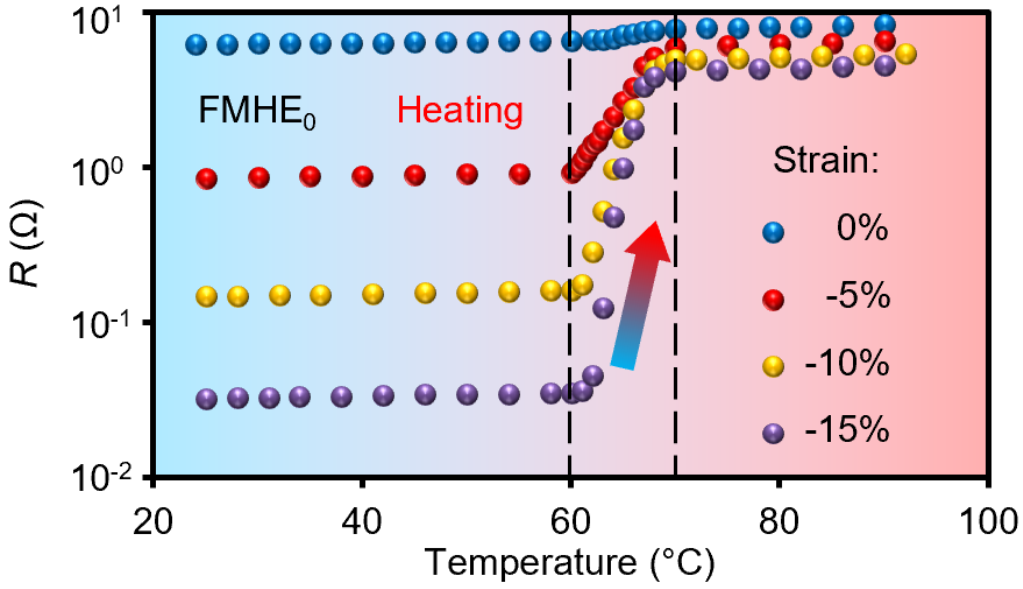

Figure 3.21 Resistance-temperature curves of the FMHE$_0$ sample under different strains during heating

Due to the significant thermal expansion of polymer matrices, most conductive elastomers exhibit a positive temperature coefficient, that is, their resistance increases with temperature. The thermal expansion rate of PDMS is 0.034% °C^{-1} [38]. As a result, the FMHE$_3$ samples in this work expand by around 0.8% when heated from 25 °C to 60 °C. In metal-polymer conductive composites, their resistance depends on the contact resistance between metal microparticles, i.e., the electron tunnelling probability between them, which is extremely sensitive to particle spacing [31]. Therefore, even an expansion of 0.8% can also lead to the separation of metal particles in the FMHE and a significant increase (>20%) in electrical resistance. When a FMHE$_3$ sample is placed in a copper mould to prevent its expansion, its resistance increases by only <3% when heated to 60 °C. This proves that the resistance increase of FMHE during heating mainly corresponds to the expansion of PDMS. Furthermore, the electrical resistance of metal fillers in FMHE increases by about 14% when heated to 60 °C due

to their positive temperature coefficient of ~0.004/°C. However, the resistance of FMHE mainly depends on the contact resistance between the conductive particles rather than the very low resistance of the metal particles themselves. Therefore, this is not the main factor affecting the resistance change of FMHE during heating.

3.3.7 Measurement of Supercooling

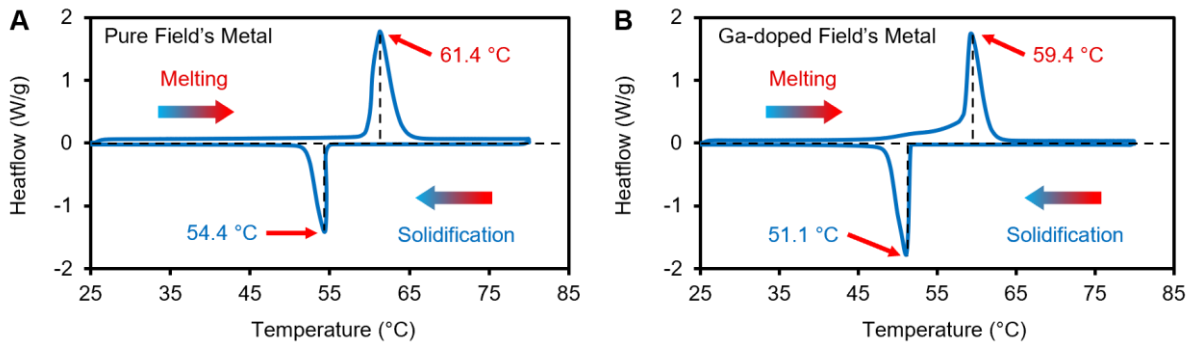

Figure 3.22 Differential scanning calorimetry (DSC) curve of the (A) pure FM alloy and (B) Ga (1 wt%)- doped FM alloy

Supercooling is the lowing the temperature of a liquid below its melting point without it solidifying [40], with supercooling degree the degrees temperature below the melting point the liquid reaches before it solidifies. To measure the supercooling of Field's metal, a differential scanning calorimeter (DSC3+ Mettler Toledo) was used to measure the melting and solidification temperatures. Measurement was done from 25 °C to 80 °C, and heating and cooling rates were both set to 5 °C per minute. According to the DSC curve (Figure 3.22), the melting and freezing points of pure FM are 61.4 and 54.4 °C, respectively, showing a supercooling degree of 7 °C. As a comparison, the melting and freezing points of Ga-doped FM are 59.4 and 51.1 °C, respectively, showing a lower phase transition temperature and a more pronounced supercooling effect (supercooling degree of 8.3 °C).

3.4 Mechanical and Electromechanical Properties of the FMHE

3.4.1 Measurement of Mechanical and Electromechanical Properties of FMHE

In addition to the temperature-dependent electrical properties, the FMHE samples also exhibit variable mechanical properties. The MTS was used to compress or stretch the block or bar FMHE samples at a speed of 3% min^{-1}, with heating applied and temperature measured as in previous experiments. Block samples for compression were heated using a Peltier module, bar samples for tensile testing were heated using an inductive heater. The temperature of the samples was measured using a digital thermometer with measurement probes contacting the surface of the FMHE. The FMHE samples were compressed or stretched at 25 °C, then heated to 80 °C while strained, then compressed or stretched again. Heating from 25 °C to 80 °C took ~1 minute for the block sample and ~2 minutes for the bar sample. Figure 3.23 and Figure 3.24 presents the stress-strain curves for the $FMHE_3$ at different temperatures, showing stress softening of ~67% when FM melts.

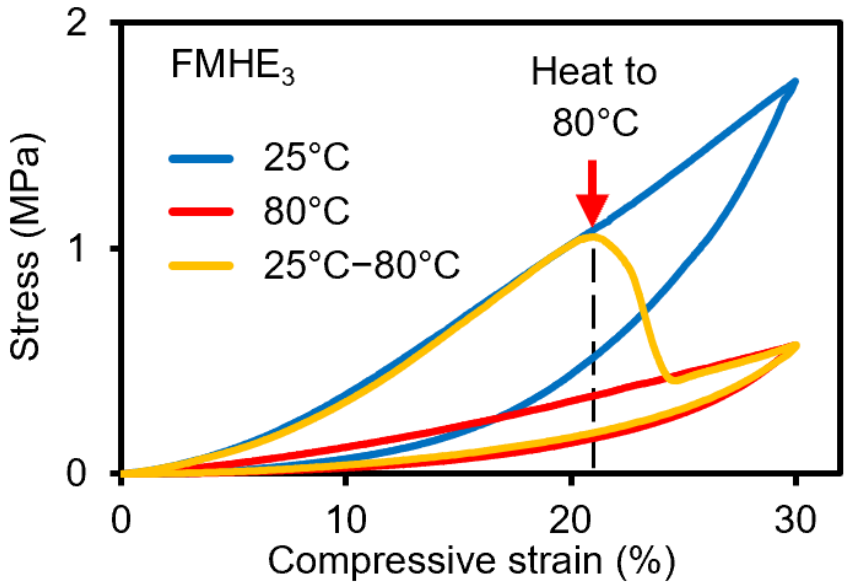

Figure 3.23 Stress-strain curves of the $FMHE_3$ at different temperatures during compression.

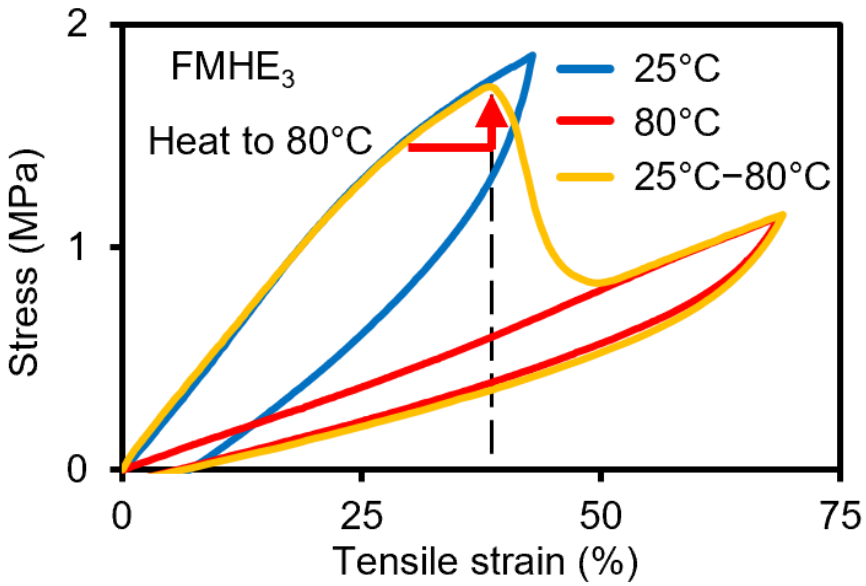

Figure 3.24 Stress-strain curves of the $FMHE_3$ at different temperatures during stretching.

During the experiment, the sample is heated to 80 °C while it is under stress. After the FM particles melt, the stress curve immediately moves to overlap the stress-strain curve at 80 °C. The stress-strain curves demonstrate that $FMHE_3$ exhibits elastic hysteresis behaviour in both tension and compression. The elastic hysteresis is lower at 80 °C due to reduced frictional energy losses. [41].

The stress-strain curves of $FMHE_0$ (Figure 3.25) indicate its similar variable stiffness effect; however, it can be an order of magnitude softer at 80 °C. As the temperature increases from 25 °C to 80 °C, its stress at 30% compressive and tensile strain drops by 89.8% and 86.8%, respectively. When heated during compression/stretching, the stress curves before and after FM melting also overlap with its stress curves at 25 °C and 80 °C, respectively.

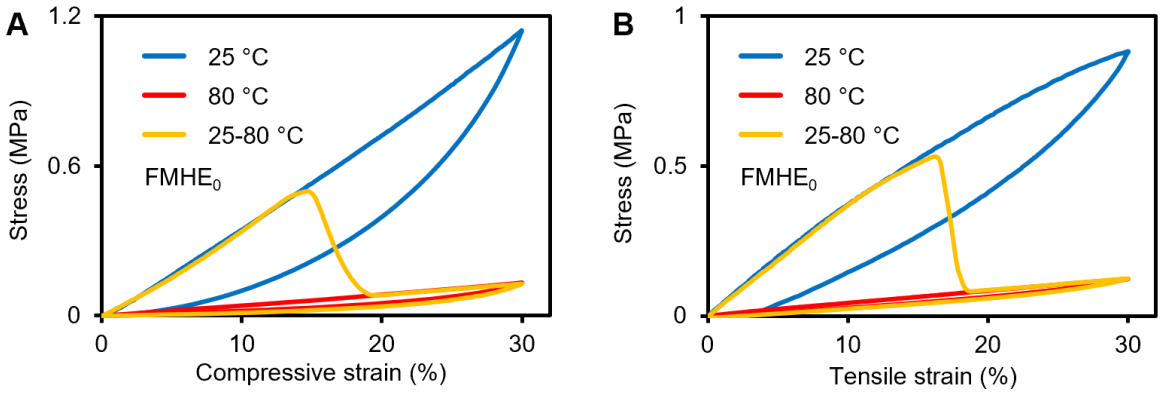

Figure 3.25 Stress-strain curves of $FMHE_0$ at different temperatures during (A) compression and (B) stretching.

To study the mechanical stability of $FMHE_3$ under cyclic loads, cyclic compression/stretching was performed on $FMHE_3$ samples at 25 °C and 80 °C for 6 cycles. Strain rate was 3% min^{-1}, and maximum strain was 20% compressive and 30% tensile (Figure 3.26). Each graph shows more obvious elastic hysteresis in the first cycle (larger elastic hysteresis loop). Their stress curves closely overlap in the subsequent cycles, exhibiting good mechanical stability. After changing the temperature, the curves also overlap after the first cycle. In addition, when FM melts at 80 °C, the elastic hysteresis of $FMHE_3$ is significantly weakened, indicating lower energy dissipation. When loaded at 25 °C, the deformation of the filler network in the FMHE composite results in a position change of the non- deformable solid FM particles. During this process, friction between solid particles as well as between particles and the polymer matrix results in significant energy losses [41]. On the other hand, when loaded at 80 °C, the liquid FM droplets can deform along with the matrix with almost no frictional energy loss. In addition, the deformation of the FM droplet also relieves the actual strain in the polymer matrix, thereby reducing the internal friction loss of the matrix. Overall, $FMHE_3$ shows a high degree of mechanical stability at both low and high temperatures.

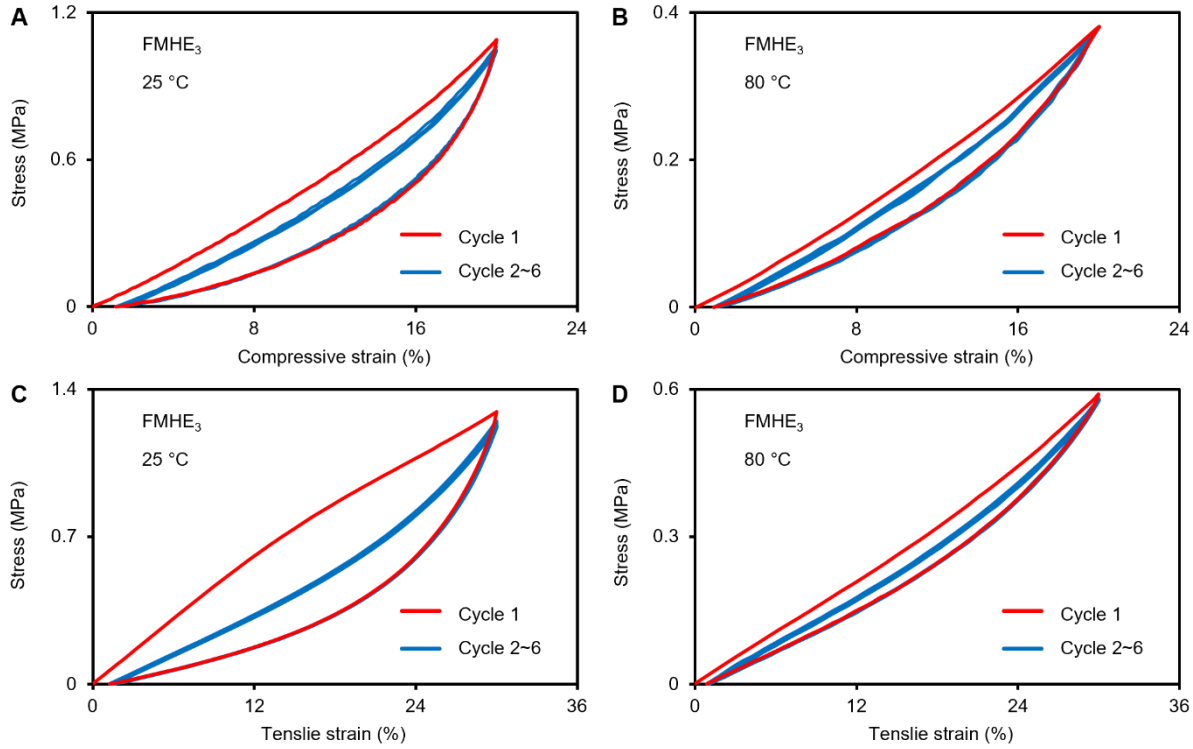

Figure 3.26 Cyclic stress-strain curves of $FMHE_3$ under different conditions.
(A) compression at 25 °C; (B), compression at 80 °C; (C) stretching at 25 °C; (D) stretching at 80 °C.

3.4.2 Simulation of Mechanical Properties

A COMSOL simulation of the mechanical properties of $FMHE_0$ and $FMHE_3$ was done to compare with the experimental results. The simulation settings were the same as previously described (see Table 3.1 and Figure 3.11), additionally another boundary condition was added to compress the FMHE longitudinally by 10%. The stress distribution was calculated at 25°C and 80°C. The results are shown in Figure 3.27.

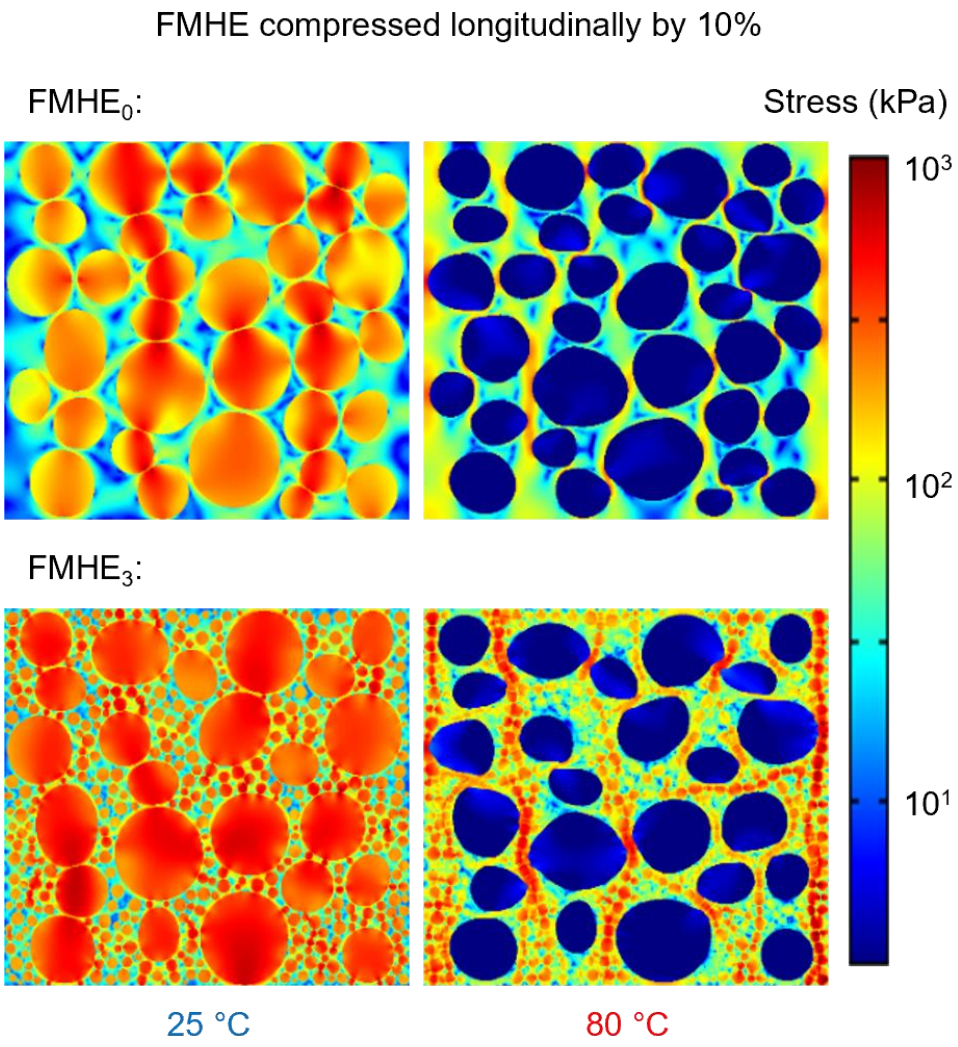

Figure 3.27 Simulation results of the stress distribution of the $FMHE_0$ and $FMHE_3$ compressed by 10% at 25 °C and 80 °C.

Under compression at 25 °C, the stress is primarily distributed in solid FM particles (red colour). At 80 °C, FM melts into droplets with the internal stress approaching zero (blue colour)—this explains the corresponding stress reduction.

The compressive modulus of FMHE was calculated using the roughly linear section of the slope of the stress-strain data for compression during cycles 2-6 (Figure 3.26A and B). The simulated

stress distribution also gives a simulated compressive modulus. The measured and simulated modulus of $FMHE_{0/3}$ at 25 °C and 80 °C are shown in Figure 3.28.

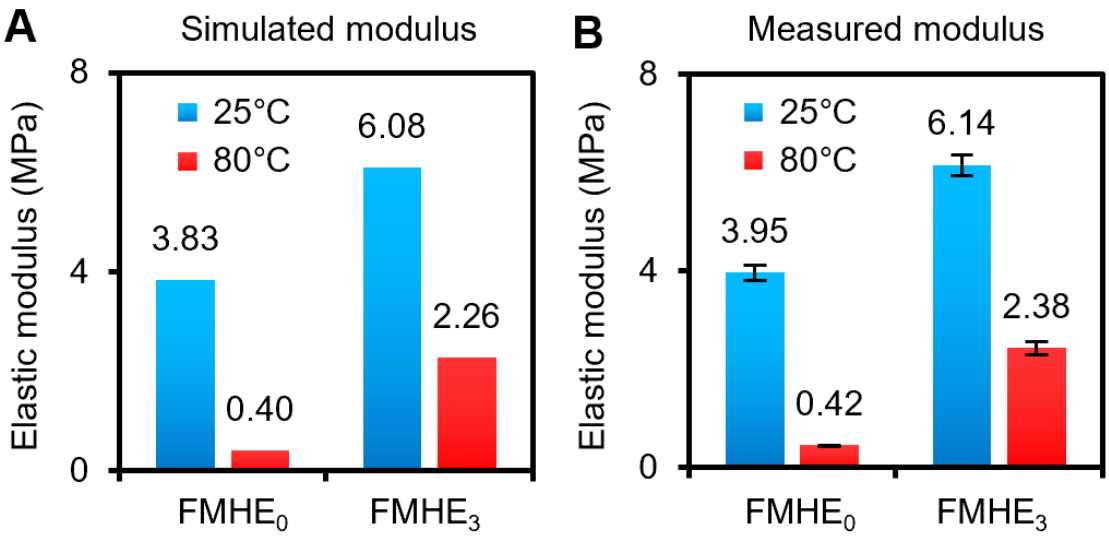

Figure 3.28 (A) Simulated and (B) measured compressive modulus of $FMHE_0$ and $FMHE_3$ at 25 °C and 80 °C.
The values of the error bars are the standard deviation of the modulus for the same sample for five measurements.

The simulation results are very similar to the experimental results, showing a difference in value of less than 5%. After FM melts, the modulus of the $FMHE_0$ and $FMHE_3$ decrease by 89 and 62%, respectively, indicating a more pronounced stiffness reduction in $FMHE_0$.

3.4.3 Ni only Elastomer

To verify that the variable stiffness effect of the FMHE results from the phase transition of FM when the temperature changes, elastomers with Ni particles only (no FM) were prepared, denoted as NiE_3. The mass ratio of Ni particles to the PDMS matrix of these samples was 3:1, which is consistent with that of $FMHE_3$. Compression and stretching at different temperatures were performed at 3% strain min^{-1}. The stress-strain curves for NiE_3 at 25° and 80 °C are only

marginally different (Figure 3.29), indicating that the variable stiffness effect of FMHE is independent of the Ni particles and the PDMS matrix, and that it is caused by the phase transition of FM.

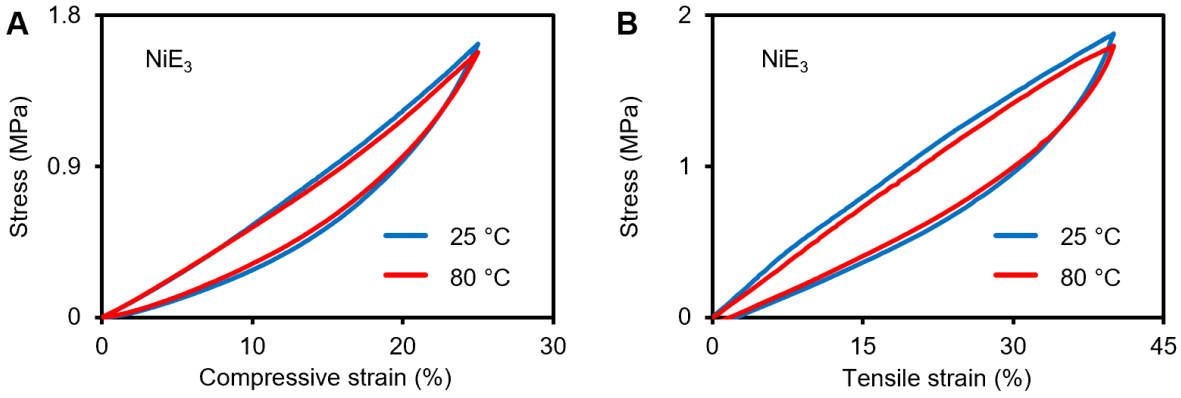

Figure 3.29 Stress-strain curves of NiE_3 at 25 °C and 80 °C during (A) compression and (B) stretching.

3.4.4 Ni Effect on Mechanical Properties

To investigate the influence of Ni particles on the variable mechanical properties of the FMHE, the elastic modulus and tensile limits of the FMHE with different Ni contents was measured at 25 °C and 80 °C. The elastic modulus of the FMHE can be calculated from the roughly linear part of the slope of its stress–strain curve. For tensile limit testing, 5 bar samples of each type were stretched at 5% min^{-1} until break.

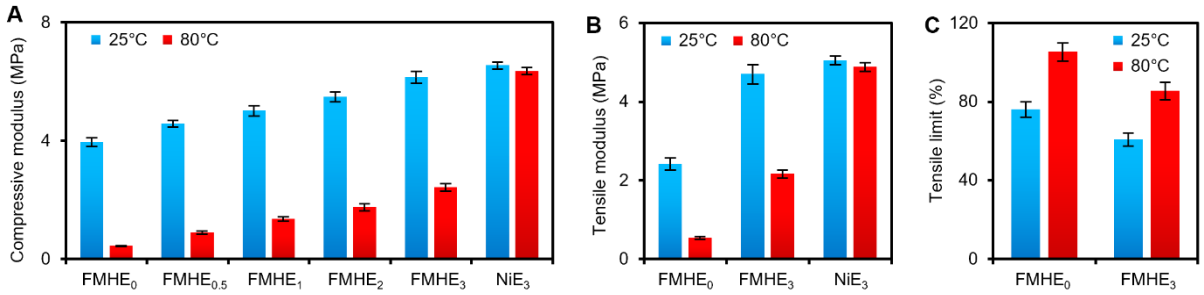

Figure 3.30 The (A) compressive modulus, (B) tensile modulus, and (C) tensile limit of the FMHE with different Ni contents at 25 °C and 80 °C.
The values of the error bars for the compressive and tensile modulus are the standard deviation of the modulus for the same sample for five measurements. The values for the error bars for the tensile limit are for 5 samples fabricated in the same batch.

Figure 3.30A shows the compressive modulus of $FMHE_{0/0.5/1/2/3}$ and NiE_3 at 25 °C and 80 °C. At room temperature, the compressive modulus of the FMHE increases with Ni content from 3.95 MPa ($FMHE_0$) to 6.14 MPa ($FMHE_3$) because of the increase in the solid filler volume fraction. When FM melts, the FMHE with a lower Ni content shows a more significant softening effect upon heating. For instance, the compressive modulus of $FMHE_0$ decreases by 9.5 times to only 418 kPa at 80 °C, which is even lower than that of the PDMS matrix used (~1.0 MPa). In contrast, the compressive modulus of $FMHE_3$ decreases by only 61% when FM melts because Ni particles increase the stiffness of the FMHE at both low and high temperatures. For NiE_3, its compressive modulus at 25 °C and 80 °C differs by only 2.8%, which again proves that the variable stiffness effect of the FMHE is independent of the PDMS matrix and Ni particles. For the tensile modulus shown in Figure 3.30B, with increasing Ni content, the FMHE shows an increased modulus and weakened variable stiffness effect. The tensile modulus of $FMHE_0$ and $FMHE_3$ at 25 °C is 4.7 and 2.3 times that at 80 °C, respectively. Furthermore, the melting of FM can also improve the stretchability of the FMHE. From Figure 3.30C, the $FMHE_0$ bar will break at an average tensile strain of 76% at room temperature. After FM melts, it can

be stretched by up to 110%. With the increase in Ni content, the stretchability of the FMHE decreases but can still be improved at a high temperature. The average tensile limit of $FMHE_3$ is 60.8% at 25 °C and can increase to 85.4% at 80 °C.

3.4.5 Effect of FM Particle size and Volume Fraction on Mechanical Properties

The effect of FM particle size and volume fraction on the mechanical properties of FMHE were also measured. The previously made $FMHE_3$ samples with different average FM particle sizes and FM contents were used again. Their compressive moduli at 25 °C and 80 °C were measured and compared, as shown in Figure 3.31. The elastic modulus of $FMHE_3$ increases with the FM particle size and content at 25 °C but shows the opposite trend at 80 °C. This means that $FMHE_3$ with a larger FM particle size and higher FM content has a more obvious variable stiffness effect.

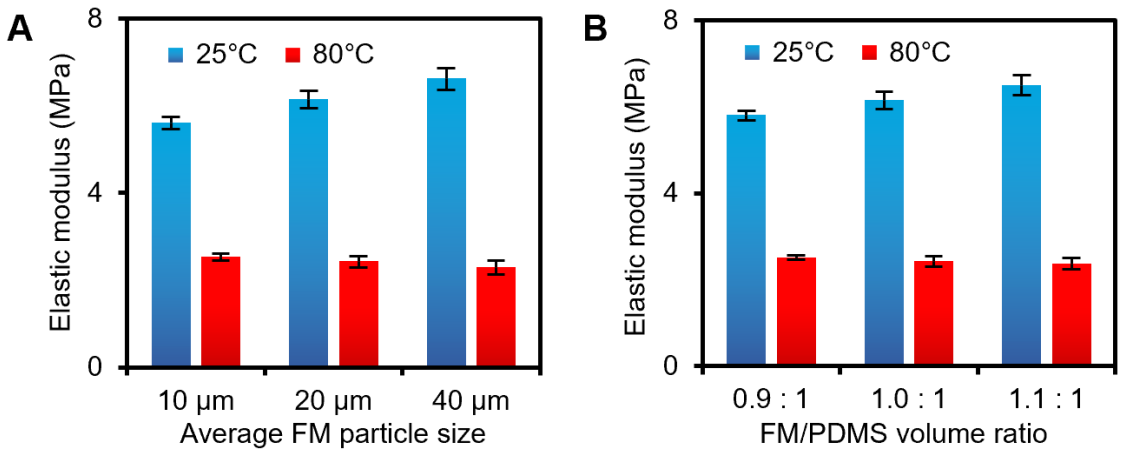

Figure 3.31 Elastic modulus of $FMHE_3$ samples with different FM (A) particle sizes and (B) contents at 25 °C and 80 °C.
The values of the error bars are the standard deviation of the modulus for the same sample for five measurements.

3.4.6 Self-Responsive Stiffness Tuning

The unusual electromechanical properties of the FMHE can be harnessed to achieve a self-responsive stiffness tuning effect. When a DC voltage is applied across the FMHE and it is compressed, its conductivity increases with compression, so the current passing through it increases too. The current passing through it causes its temperature to increase by Joule heating, which can cause the FM to melt. Testing was done with 5V and fast compression (12% min^{-1}) or 3V and slower strain (6% min^{-1}). A $FMHE_3$ sample with dimension of 8 mm x 10 mm x 10 mm was used. The experimental setup is shown in Figure 3.32. Figure 3.33 gives the measured stress-strain curves for the two conditions. Figure 3.34 shows changes of current through the sample and its temperature for the two cases.

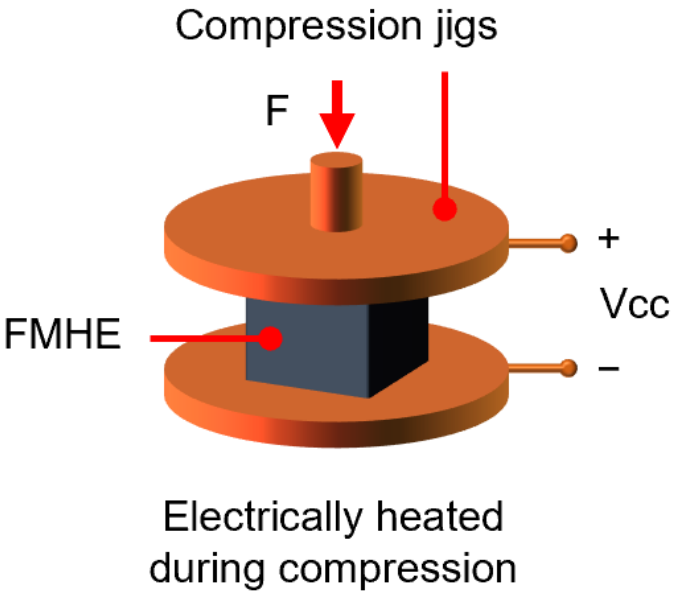

Figure 3.32 Experimental setup for applying a fixed voltage on an $FMHE_3$ sample during compression.

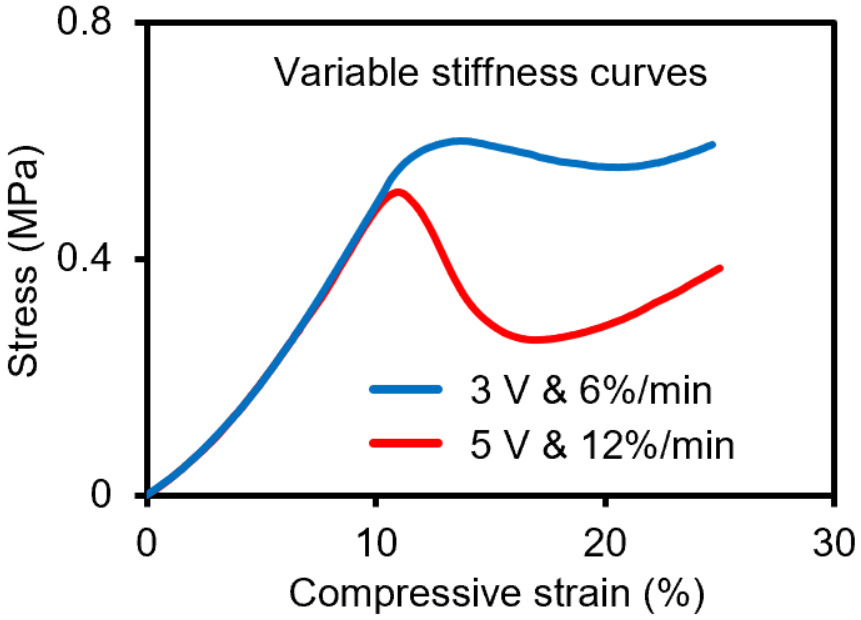

Figure 3.33 Variable stiffness stress-strain curves of the FMHE$_3$ powered by a fixed voltage during compression.

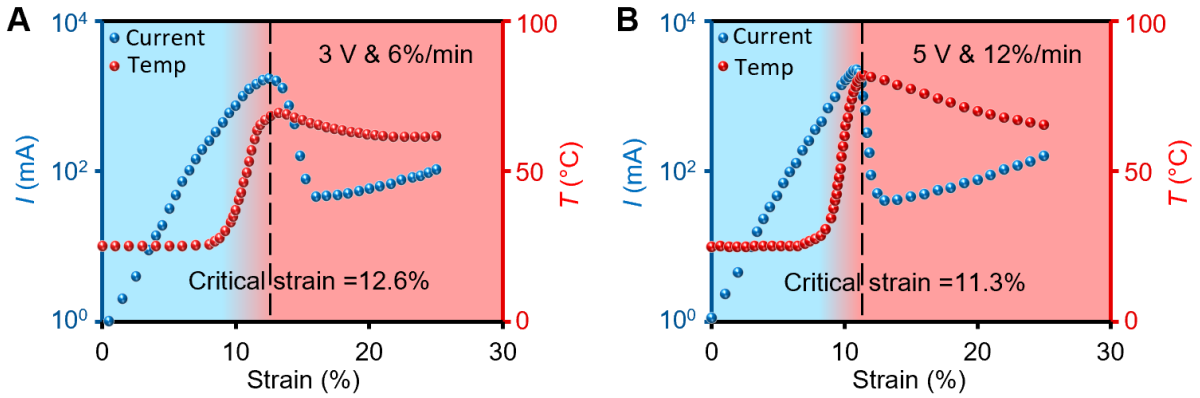

Figure 3.34 Current-strain and temperature-strain curves of the FMHE$_3$ powered by a fixed voltage during compression with different voltages and compression speeds of (A) 3V and 6% min^{-1} and (B) 5V and 12% min^{-1}.
The blue and red shaded regions correspond to the solidification and melting state of FM, respectively.

At low strain, the current passing through the sample is low because of its high resistance. With an increase in strain, the resistance decreases until the current is high enough to melt the FM.

This then causes a sharp decrease in stiffness and a rapid fall of stress. Figure 3.19A shows that melting the FM causes the resistance to increase, reducing the current and preventing a further rise in temperature. Under further compression, the current increases slowly again to maintain the melting of FM. The timing and speed of stiffness reduction of FMHE samples can be controlled by voltage and compression speed applied to them, as shown in Figure 3.34. A higher voltage can reduce the required strain for melting FM, as reflected by the earlier softening indicated by the red curve given in Figure 3.33 and the lower critical strain shown in Figure 3.34B. A fast compression speed will accelerate the stiffness change process. Due to the lag of the temperature rise of the sample relative to its resistance increase, a faster compression speed can lead to a higher current and heating power before FM starts melting, leading to a higher temperature of FMHE samples. This is shown in the comparison of maximum temperatures at different voltages and compression speeds; see Figure 3.35. The maximum temperature of the sample compressed at 6% min^{-1} is 69.3 °C, while that of the sample compressed at 12% min^{-1} is 80.7 °C. Higher temperatures can melt FM particles faster, resulting in a rapid reduction in stiffness, as indicated by the rapidly decreasing red stress curve given in Figure 3.33.

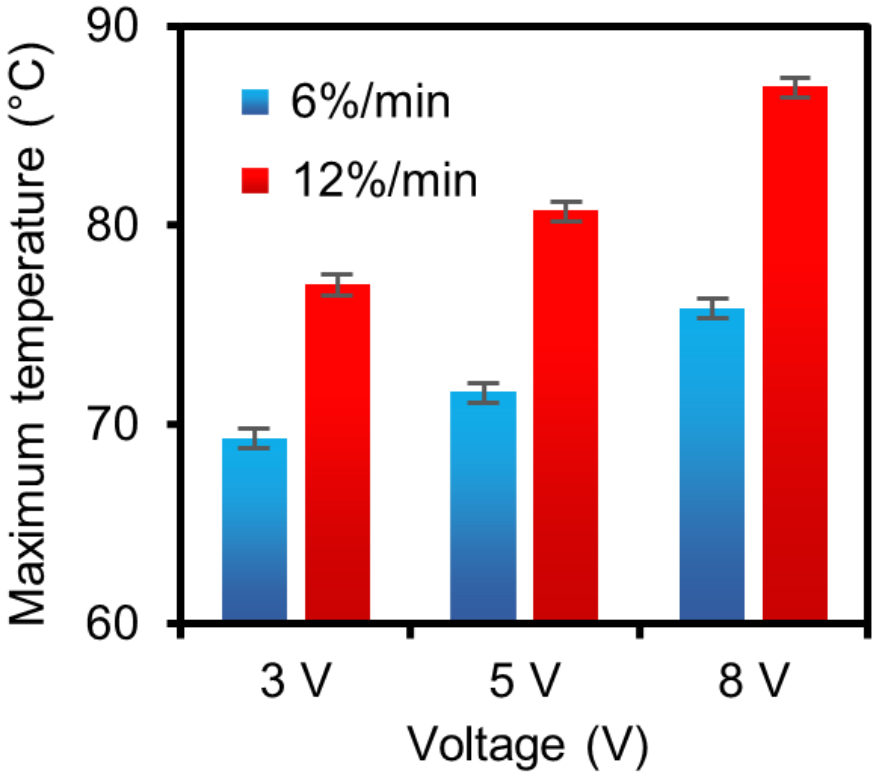

Figure 3.35 The maximum temperatures of $FMHE_3$ samples powered by a fixed voltage during compression with different voltages and compression speeds.
Error bars are given by the error on temperature measurement for the digital thermometer used.

3.5 Applications of the FMHE

3.5.1 Compliance Unit

The unconventional electromechanical properties of the FMHE can solve many practical engineering challenges. To demonstrate its capabilities, its self-triggered variable stiffness property was used to develop a compliance compensation unit. Such a device could help a robotic manipulator to compensate for positional errors through its deformation, thereby preventing damage to tools or workpieces in tasks involving uncertain operational environments and complex contact scenarios. This is the key to robotic manipulation requiring a high-level dexterity where motions and positions must be compensated on multiple axes [42,

43]. However, state-of-the-art devices cannot provide adjustable stiffness and therefore have limited compensation ability. The FMHE variable stiffness compensator can realize compression, bending, and torsion with variable and adjustable stiffness, overcoming limitations of previous designs. Figure 3.36 illustrates the structure of this device and a robotic manipulator equipped with it (see Figure 3.37 for the detailed structure).

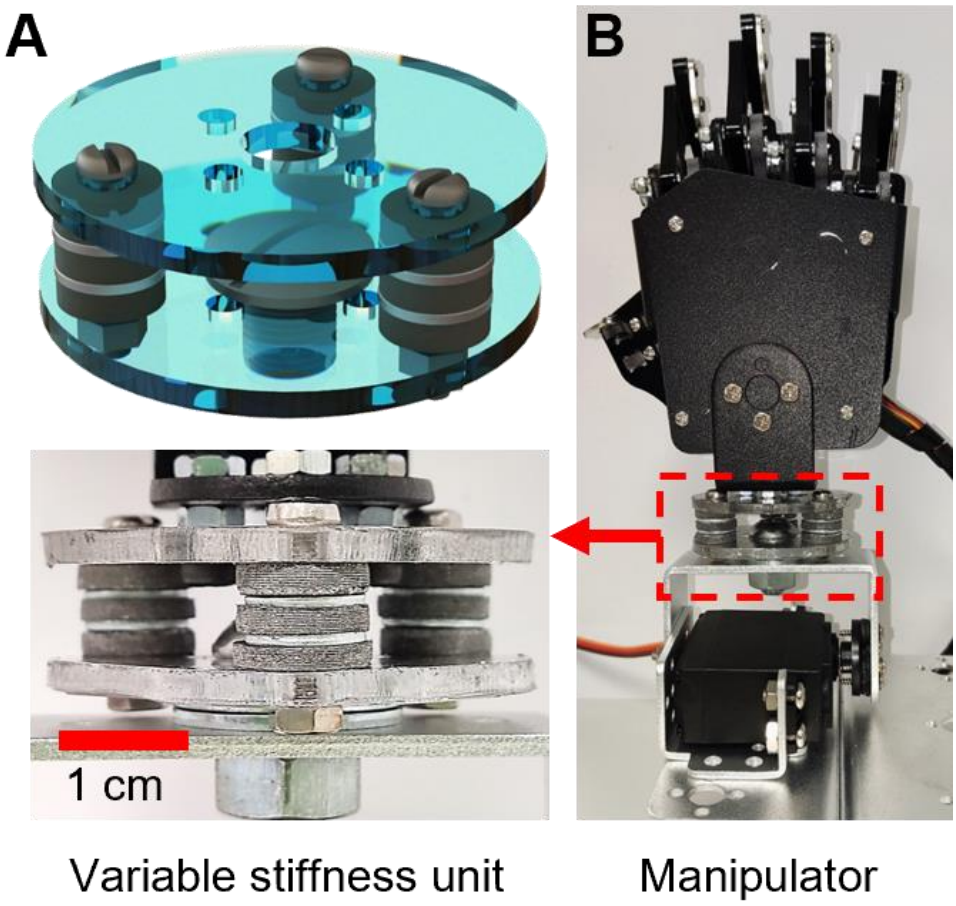

Figure 3.36 (A) Schematic diagram and optical image of the FMHE compensation unit. (B) Photograph of the servomotor-driven manipulator equipped with a compensator.

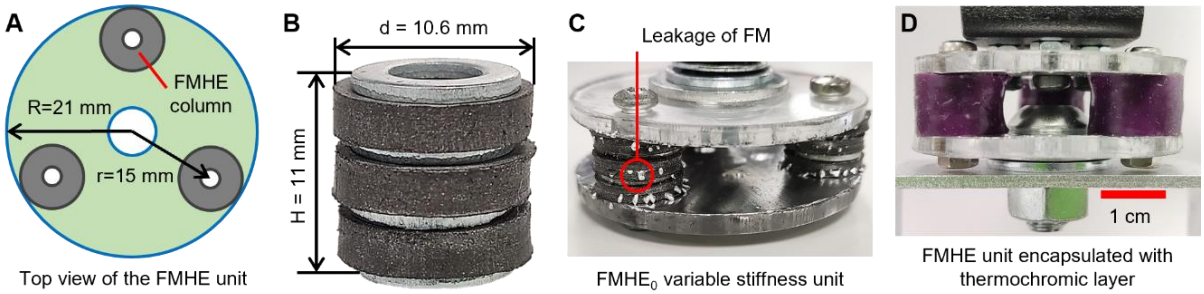

Figure 3.37 Compensation unit diagram and pictures.
(A) Top view of the FMHE variable stiffness unit, showing the positions of the three FMHE columns. (B) Optical image of the FMHE column. (C) FM leakage of the $FMHE_0$ variable stiffness unit after being compressed by 60% at 80 °C. (D) The FMHE variable stiffness unit encapsulated with a thermochromic Ecoflex layer.

Figure 3.37, A and B shows the distribution and size of the $FMHE_3$ columns. Three $FMHE_3$ columns (Φ10.6×11 mm) are arranged in an equilateral triangle and sandwiched between two electrode plates which are used to apply voltages. Each FMHE column consists of three pieces of $FMHE_3$ samples of ~3mm thickness with two alternately stacked gaskets. During fabrication of solid filler elastomer composites, sedimentation of solid fillers can occur due to their greater density during elastomer curing [44]. Thinner samples lessens the thickness of elastomer with reduced filler content if any sedimentation occurs- this is why the FMHE column had 3 pieces of 3 mm thickness.

The structure of the robotic manipulator equipped with the FMHE variable stiffness compensation unit is shown in Figure 3.36B. From top to bottom are the manipulator, the FMHE variable stiffness unit and a digital servo motor (DSSrevo DS3230), with a blocked-rotor torque of 3 N·m. According to Figure 3.28B, $FMHE_0$ has a more significant variable stiffness effect than $FMHE_3$. Theoretically, the variable stiffness unit based on $FMHE_0$ can obtain a higher blocked-rotor angle. However, $FMHE_3$ was chosen to use because of the FM leakage of $FMHE_0$ during compression at a high temperature. As shown in Figure 3.3, the

PDMS layer between adjacent FM particles in $FMHE_0$ is very thin. At a high temperature, these thin PDMS layers can rupture at a compressive strain of > 55%, causing leakage of melted FM (see Figure 3.37C). In contrast, the PDMS layer in $FMHE_3$ is much thicker, so there is almost no FM leakage during deformation.

A thermochromic Ecoflex layer was encapsulated on the $FMHE_3$ columns in the variable stiffness unit, as shown in Figure 3.37D. This encapsulation layer can not only avoid FM leakage but also indicate the working state of the FMHE compensation unit, showing its high/low stiffness state by different colours. The thermochromic elastomer is Ecoflex filled with thermochromic powder. Ecoflex was used as the matrix because of its high stretchability and compliance. The thermochromic powder is composed of spherical particles with a diameter of 2 to 7 μm. Its colour changes when the temperature rises above the activation temperature and reversibly changes back to its original colour when the temperature recovers. The thermochromic powder used in this work is purple below 49 °C, blue between 49 °C and 60 °C, and white above 60 °C. The thermochromic powder was mixed into Ecoflex with a mass fraction of 2.5%, and the mixture was degassed in a vacuum chamber for 20 min. Ecoflex is a mixture of Ecoflex part A and part B with a mass ratio of 1:1. The FMHE column was immersed in a mould filled with the mixture and cured at room temperature for 3 hours to form a thermochromic Ecoflex encapsulation layer on the surface. The thickness of the thermochromic encapsulation layer was about 0.5 mm.

The FMHE self-triggered variable stiffness compensation unit was tested under compression and bending. It was compressed at a speed of 0.4 $mm \cdot min^{-1}$ (using the MTS) and bent at a speed of 2° min^{-1} (using the servo). The FMHE compensation unit was powered by 5V. It was first tested with the power off (no heating or stiffness change). It was then tested with the 5V power

on to change in temperature with strain. It was also tested when preheated to 80 °C. A CAT S60 FLIR infrared thermal camera was used to measure the temperature.

Figure 3.38 shows the results of the variable stiffness compensation unit tests. At room temperature (with heating power off), its compression force basically increases linearly with compression distance to 286 N at 1.5 mm, with a stiffness coefficient of 191 $kN \cdot m^{-1}$. At 80 °C, the force at 1.5 mm drops to 130 N, showing a lower stiffness coefficient of 86.7 $kN \cdot m^{-1}$. With 5 V supplied to the FMHE compliance unit during compression, its stiffness automatically decreases under critical deformation because of the melting of FM. The initial resistance of the compensation unit is ~100 ohm. As the force increases to 83 N at 0.6 mm, its resistance drops to 2.5 ohm, and its temperature reaches 60 °C. Its stiffness then decreases with the melting of FM, as shown in the yellow force–distance curve in Figure 3.38A. As the compression distance increases from 0.7 mm to 1.5 mm, the compensation unit maintains a temperature of ~75 °C and a low stiffness coefficient of 44 $kN \cdot m^{-1}$. For the case of bending (Figure 3.38B), the compensation unit also shows a similar variable stiffness phenomenon. It has bending stiffness coefficients of 0.413 N·m/° and 0.193 N·m/° at 25 °C and 80 °C, respectively. When powered by a 5 V supply during bending, its temperature rises to 75 °C at a bending degree of 3.7°. After that, its bending moment increases slightly, showing a bending stiffness close to 0. After the bending angle reached 7.3°, its bending moment curve intersects and overlaps with the curve at 80 °C. If the ambient temperature is higher or lower than 25 °C, then the time the FMHE takes to heat up to 80 °C or cool down is affected slightly. For lower ambient temperatures, FMHE cooling is faster, but it takes slightly longer to reach 80 °C. For higher ambient temperatures, FMHE is quicker to reach 80 °C when heated but cools down a little slower.

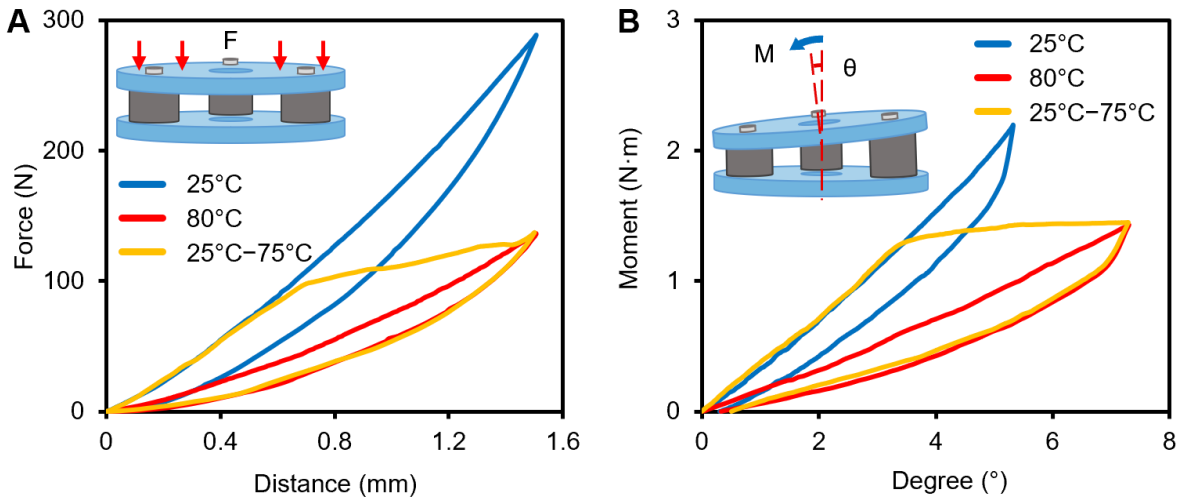

Figure 3.38 (A) Force-distance curves of the compensation unit at different temperatures during compression. (B) Moment-degree curves of the compensation unit at different temperatures during bending.

The FMHE compensation unit was mounted on the wrist of a robotic manipulator driven by a digital servomotor to enable multiaxis compliance (Figure 3.36B). The axis of the servo motor is perpendicular to the compensation unit axis. Therefore, the manipulator swings back and forth when the servo motor is activated. A manipulator without the FMHE unit will get stuck when encountering obstacles during its swing, causing an immediate blocked rotor and damage to the servo motor. This will lead to high internal mechanical stress and overheating of the servo motor, which will cause damage. After being equipped with the flexible FMHE compensation unit, this problem can be solved. When no voltage is applied to the compensation unit, the torque–time and current–time curves of the servo motor after the manipulator is stuck are shown in Figure 3.39. The servo motor rotates at a constant speed of $0.54°\cdot s^{-1}$ with an initial working current of 0.17 A at 0 s. Since the temperature of the FMHE unit remains unchanged, its bending stiffness is constant at 0.413 N·m/°. With the rotation of the servo motor, the bending angle and moment of the FMHE unit increase, resulting in an increase in the torque and current of the

servo motor. At 13.5 s, its torque reaches the blocked-rotor torque of 3 N·m, and the current increases to 2 A, showing a bending compensation angle of 7.3°.

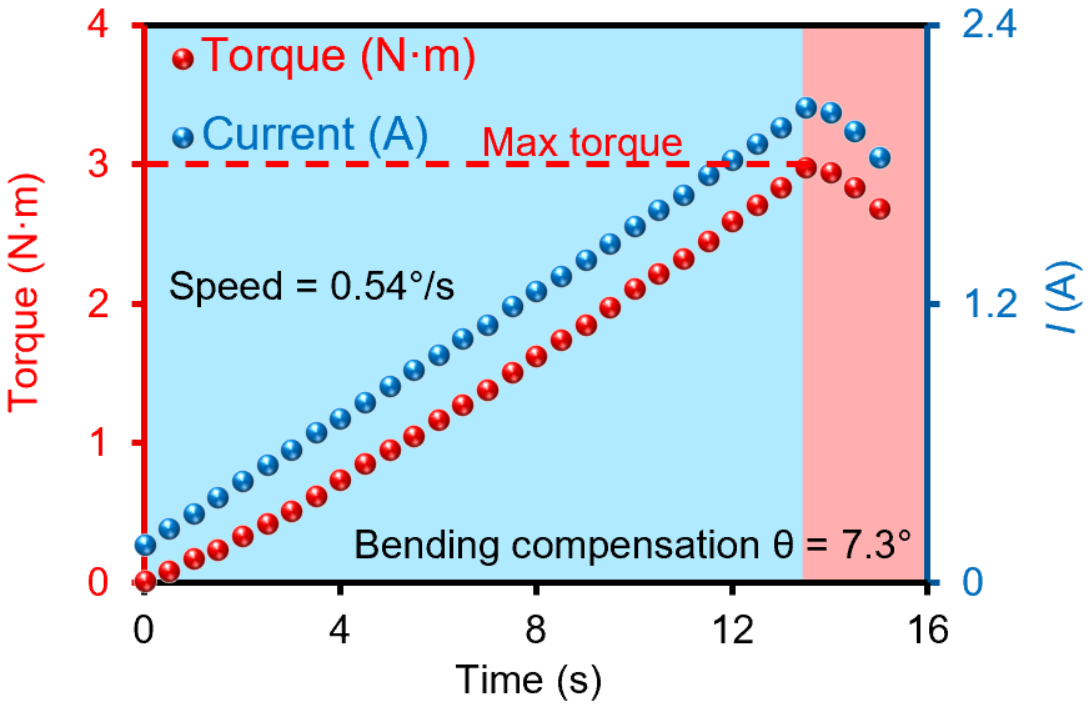

Figure 3.39 Torque-time and current-time curves of the digital servomotor that drives a robotic manipulator equipped with the compensation unit, when the manipulator is stuck, the compensation unit is powered by 0 V.
The blue and red shaded regions correspond to the normal operation and blocked rotor state (the servomotor is blocked due to excessive torque) respectively.

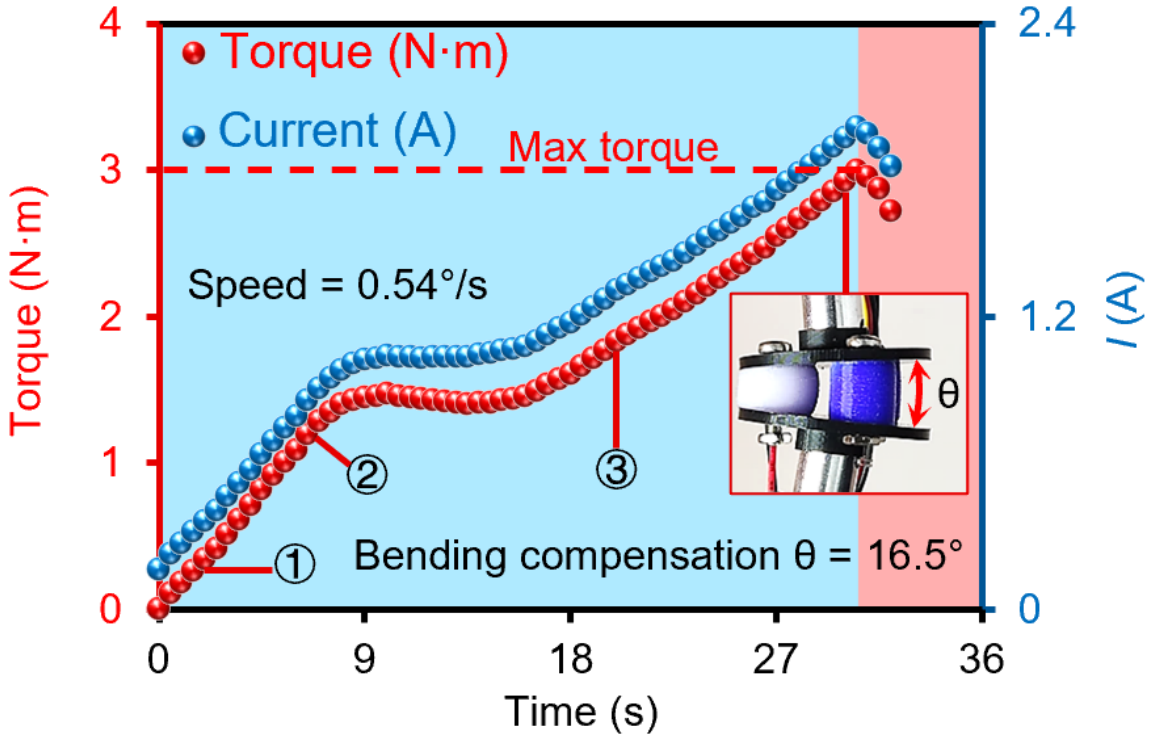

Figure 3.40 Torque-time and current-time curves of the digital servomotor that drives a robotic manipulator equipped with the compensation unit, when the manipulator is stuck, the compensation unit is powered by 5 V.
The blue and red shaded regions correspond to the normal operation and blocked rotor state (the servomotor is blocked due to excessive torque) respectively. The inset shows a photo of the bent compensation unit.

When powered by a 5 V supply, the compensation unit softens at a bending angle of 4.9°, delaying the time for the servo motor to reach the blocked-rotor torque. This thereby further increases the bending compensation angle of the compensation unit to 16.5° (see Figure 3.40). The thermochromic elastomer encapsulation layer on the $FMHE_3$ columns can indicate the working state of the compensation unit. The colours of the encapsulation layer at < 49 °C, 49~60 °C and > 60 °C are purple, blue, and white, respectively. From Figure 3.40 and Figure 3.41, the initial temperature of the FMHE unit is 26 °C with a purple encapsulation layer. At 6 s, the encapsulation layer turns blue, indicating that the FMHE columns have been heated and FM is

about to melt. From 7 s to 16 s, the torque of the servo motor is basically unchanged, corresponding to the 0-stiffness section of the yellow bending moment curve given in Figure 3.38B. After that, the torque increases slowly with the angle of the servo motor, and the encapsulation layer remains white, indicating that the FMHE unit is in the low stiffness state. At 30.5 s, the servo motor stops rotating at a blocked-rotor angle of 16.5°.

Figure 3.41 Photographs of the thermochromic elastomer-encapsulated FMHE compensator at different temperatures.
The thermochromic pigment in the elastomer changes colour with temperature. It is purple below 49 °C, blue between 49 °C to 60 °C, and white above 60 °C. Scale bars are 1 cm.

Compared to state-of-the-art rubber-based compensators, the FMHE-based units show an order of magnitude improved capability (bending angle of 16.5° over 1.1° of existing commercial

systems, e.g., Schunk FUS unit). To illustrate this advantage, the FMHE compensator is shown to prevent the manipulator from damage in complex operational environments (see Figure 3.42). When a manipulator with no FMHE compensator encountered an obstacle (the red metal block in the lower left corner of photos) during operation, it immediately got stuck. This can cause damage to the drive servo motor due to the surge of current (Figure 3.42A). After installing a FMHE compensator, the compensator gradually bends to avoid jamming the manipulator (Figure 3.42B). As its bending angle increases, the compensator self-triggers to reduce its stiffness. It then bends further to allow the manipulator to go around the obstacle.

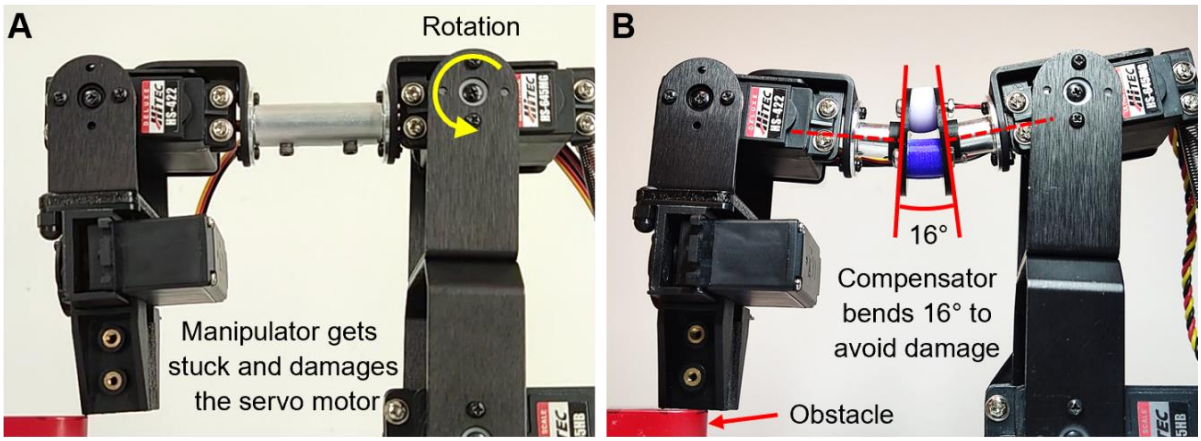

Figure 3.42 Photos of a robotic manipulator installed (A) without and (B) with an FMHE compensator when it is blocked by an obstacle (the red metal block) during operation.

Critically, in addition to bending, the FMHE compensator can also compensate for compressive and torsional movements. Such a multiaxis unit with self-adjusting stiffness and a large compensation range can bring unprecedented flexibility to robotic manipulators, greatly reducing hardware and software costs.

3.5.2 FMHE Resettable Fuse

Additionally, a highly compact, resettable, current-liming fuse based on the FMHE is presented. The fuse utilises the variable resistance of FMHE. In many electronic devices, electrical current rapidly increases in case of a short-circuit or component fault, resulting in overheating and damage to the device. Traditional current-limiting fuses are usually not reusable. State-of-the-art resettable fuses, such as dielectrophoresis-operated fuses [45], liquid metal fuses based on the pinch effect [46], or polymeric positive temperature coefficient (PPTC) fuses [47], have very limited application scopes because of their complex structure, large size (>10 mm), or long response time (>1 s). The FMHE fuse design addresses all these drawbacks. As shown in Figure 3.43, the main structure of the fuse is a 3D printed polycarbonate holder with a trapezoidal groove that attaches two copper electrodes on both sides. An $FMHE_3$ block larger than the trapezoidal groove is then squeezed into the groove with adjustable compressive strain to achieve different initial resistances and adjustable fusing currents from 0.1 to 10 A. Last, the device is encapsulated by a layer of thermochromic elastomer to enhance the structural durability and visually indicate the working state.

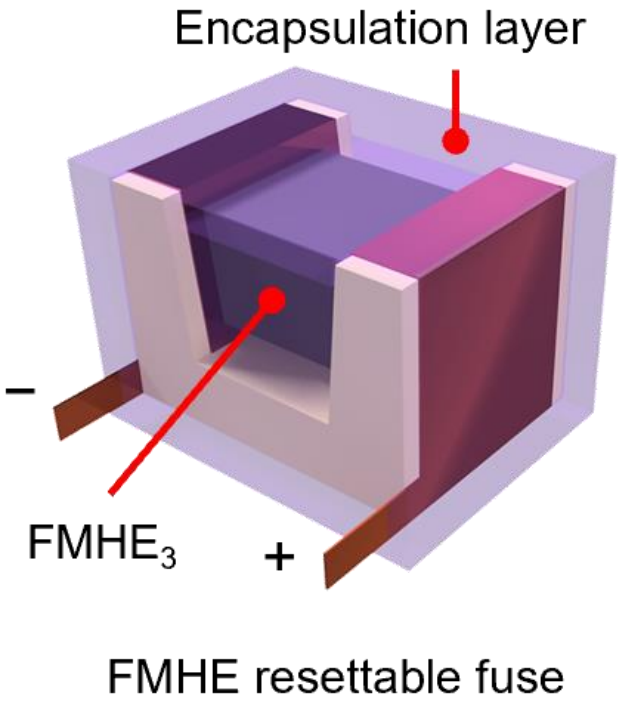

Figure 3.43 Schematic diagram of the FMHE resettable fuse

A servomotor was used as a case study. A FMHE fuse (2 mm by 3 mm by 3 mm) was connected in series with the servomotor with a circuit voltage of 6 V. The compressive strain of the $FMHE_3$ block was set to 25% to adjust the fusing current to ~1 A. Before use, the FMHE fuse was heated and cooled three times to achieve stable resistance-temperature behaviour (see Figure 3.44).

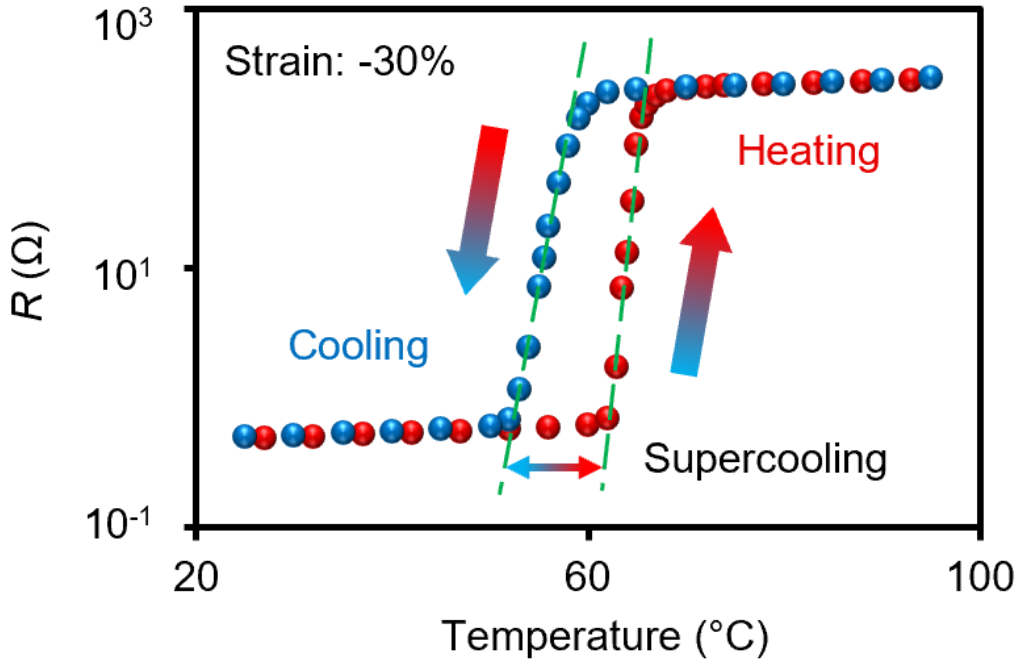

Figure 3.44 Resistance-temperature curve of the FMHE fuse in a heating-cooling cycle.

The resistance was 0.51 ohm at 25 °C and reversibly increased to 255 ohms when heated to 70 °C. Figure 3.45 shows the current passing through the FMHE fuse and its temperature change over time. The temperature for the fuse to blow cannot be changed as it depends on the melting point of Field's metal.

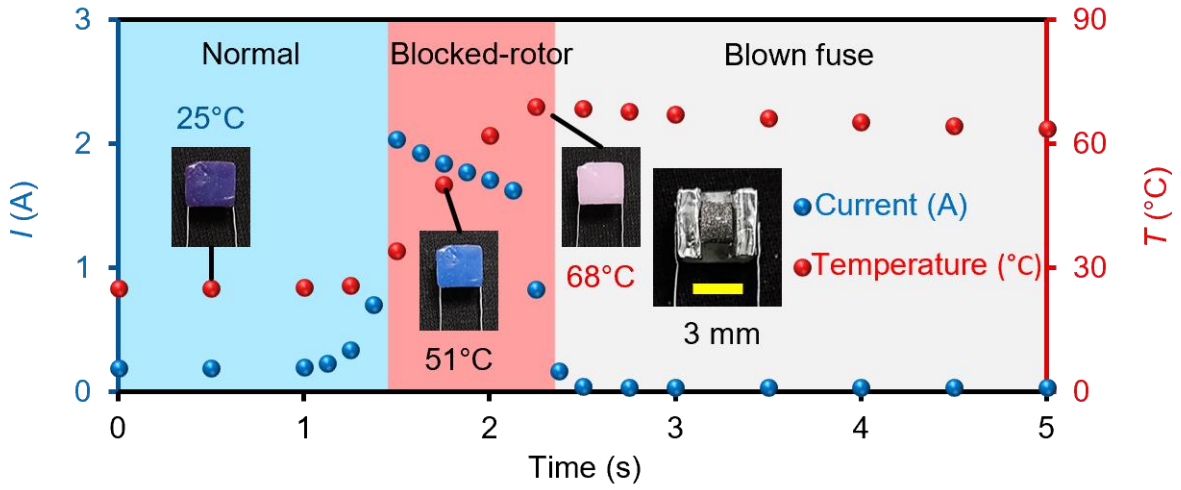

Figure 3.45 Current-time and temperature-time curves of the FMHE fuse during operation/after the blocking of the servomotor. The fourth inset shows a photo of a FMHE fuse without the encapsulation layer.

At first, the servomotor worked normally with a circuit current of 0.17 A. At 1.5 s, the servomotor was manually blocked from rotating, raising the current to 2 A. The FMHE fuse then rapidly heated up at an initial rate of ~60 °C·s^{-1} because of its low volumetric heat capacity (2.06 J·cm^{-3}·K^{-1}) and high heating power (2 W) (see calculation below). The colour of the thermochromic encapsulation layer changed to blue to warn the user. After reaching 69 °C at 2.3 s, the fuse resistance rapidly increased by 500 times. The encapsulation layer turned white, indicating the blown fuse state, while the corresponding current dropped rapidly to 23 mA to protect the servomotor. When the FMHE fuse cooled back to <50 °C, the encapsulation layer turned purple, indicating that it can be used again. As the fuse therefore allows high current to flow through it again, a secondary switch would be required in real world applications to prevent a situation where the fuse is repeatedly blown then cooled.

The volumetric heat capacity describes the ability of a unit volume of a material to store internal energy when undergoing a given temperature change (without undergoing a phase transition).

It is the product of the material density and the specific heat capacity. The volumetric heat capacity of the FMHE is equal to the volume-weighted average of the volumetric heat capacities of the individual components (see Table 3.2). The volume ratio of PDMS, Ni particles and FM in $FMHE_3$ is 1:0.337:1. According to the density and specific heat capacity of each material in the following table, the volumetric heat capacity of $FMHE_3$ is calculated to be 2.06 $J \cdot cm^{-3} K^{-1}$. The heating rate of the FMHE fuse when the servo motor is blocked can also be calculated. In Figure 3.45, the current passing through the FMHE fuse is 2.0 A after blocking. Since the resistance of the FMHE fuse is 0.51 ohm, its initial heating power will be 2.04 W ($P = R \cdot I^2$). According to the size of the FMHE block in the FMHE fuse (2×2×3 mm), it will be heated at a theoretical rate of ~82.5 $°C \cdot s^{-1}$ (2.04 W/[(0.012 cm^3)·(2.06 $J \cdot cm^{-3} \cdot K^{-1}$)]). Due to the heat dissipation through the copper electrodes and current reduction, the actual heating rate between 1.5 s and 2 s is about 50 $°C \cdot s^{-1}$ (Figure 3.45).

Table 3.2 Density, specific heat capacity and volumetric heat capacity of raw materials for $FMHE_3$.

	PDMS	Ni	In	Bi	Sn	Ga	Field's Metal
Density (g cm^{-3})	1	8.9	7.3	9.8	7.28	5.9	7.90
Specific heat capacity (J $g^{-1} K^{-1}$)	1.46	0.447	0.23	0.3	0.228	0.37	0.255
Volumetric heat capacity (J $cm^{-3} K^{-1}$)	1.46	3.98	1.679	2.94	1.66	2.18	2.01

Figure 3.46 and Figure 3.47 compares the current/temperature change of the blocked servomotor equipped with the FMHE fuse and a commercial PPTC-resettable fuse (Littelfuse 1206L050 resettable PPTC fuse; maximum voltage: 6 V; trip current: 1.0 A). The infrared thermal camera was used to measure the temperature.

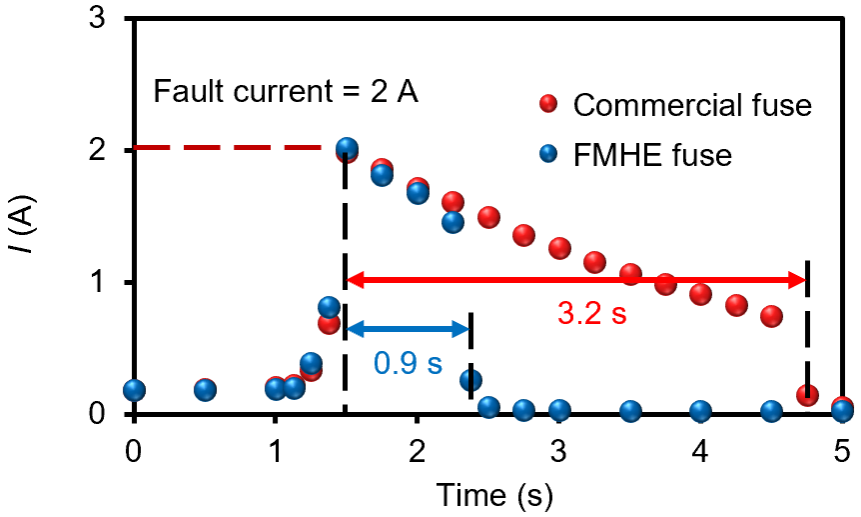

Figure 3.46 Current-time curve of the servomotor equipped with the FMHE fuse and a commercial PPTC fuse after the servomotor is blocked

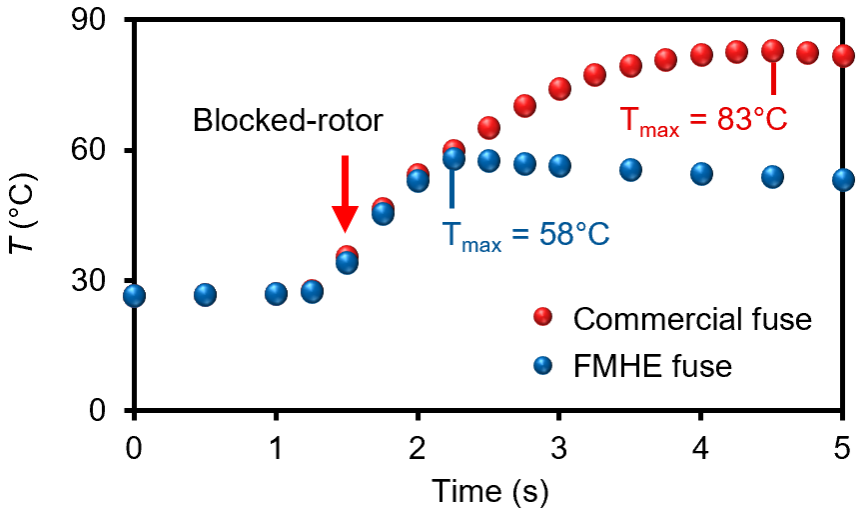

Figure 3.47 Casing temperature-time curves of the servomotor equipped with the FMHE fuse and a commercial PPTC fuse after the servomotor is blocked.

The commercial resettable fuse took 3.2 s to blow. The casing temperature of the servomotor rose to 83 °C during this period, causing irreversible damage. When the FMHE fuse was used,

the current was limited to <100 mA in 0.9 s after the fault, limiting the casing temperature to 58 °C. Such a quick response effectively protects the servomotor from any damage.

To demonstrate the reusability of the FMHE fuse, a 20-cycle fuse blow test was undertaken. Its current-time and temperature-time curves are shown in Figure 3.48. In each cycle, the FMHE fuse was blown within 1 s after the servomotor is blocked. It cools to 50 °C under ambient temperature in ~14 s, with its resistance recovering to ~0.6 ohm to reconnect the circuit (corresponding to the blue shaded region in Figure 3.48). This cyclic test shows the fast response and recovery speed of the FMHE-resettable fuse and its excellent cyclic stability.

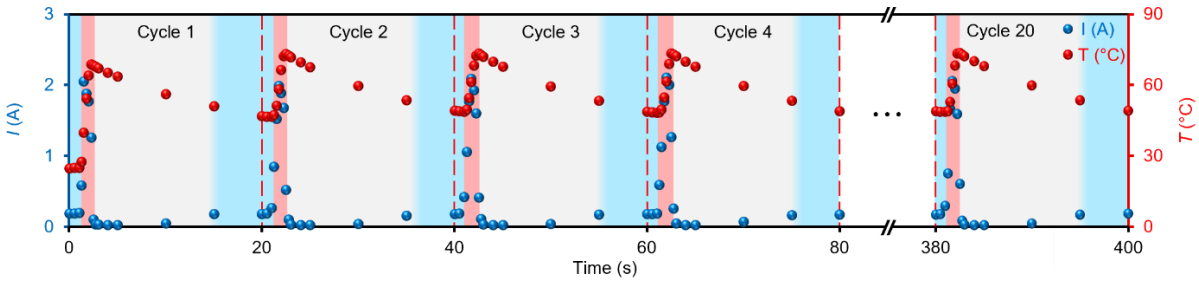

Figure 3.48 Cyclic testing of a FMHE fuse.

By reducing the size of the FMHE resettable fuse, its heating rate during short circuit can be significantly improved due to its higher heating power per unit volume, resulting in a faster response. To demonstrate this, a smaller FMHE fuse with FMHE block size of 1×1×1 mm was created. The FMHE block was pre-compressed by 30% to obtain an initial resistance of ~0.4 ohm and a high fusing resistance of >800 ohm. Figure 3.49A shows its current-time curve at blowing. The FMHE fuse was connected in series in a circuit with a working voltage of 6 V and a working current of 0.18 A. At 60 ms, the circuit is manually short-circuited with a fault current of 2 A. With a volumetric heat capacity of 2.06 $J \cdot cm^{-3} \cdot K^{-1}$ and a heating power of 1.6 W, the FMHE fuse is heated rapidly at a theoretical rate of 0.75 $°C \cdot m\ s^{-1}$. At 145 ms, the

resistance of the FMHE fuse increases by 2000 times and the current is limited to <10 mA, showing a response time of only 85 ms. Such a fast response speed outperforms state-of-the-art commercial and laboratory prototype PPTC resettable fuses. According to Figure 3.49B, the response time of commercial chip resettable fuses with the same working voltage (6 V) and fusing current (1 A) as FMHE fuses is above 1 s. Some reported thermoresponsive fuses can achieve fast response <1s [47, 48], but their size is much larger than that of FMHE fuses. In conclusion, the FMHE resettable fuse in this work exhibits 10 times faster response and >10 times smaller dimension than state-of-the-art products.

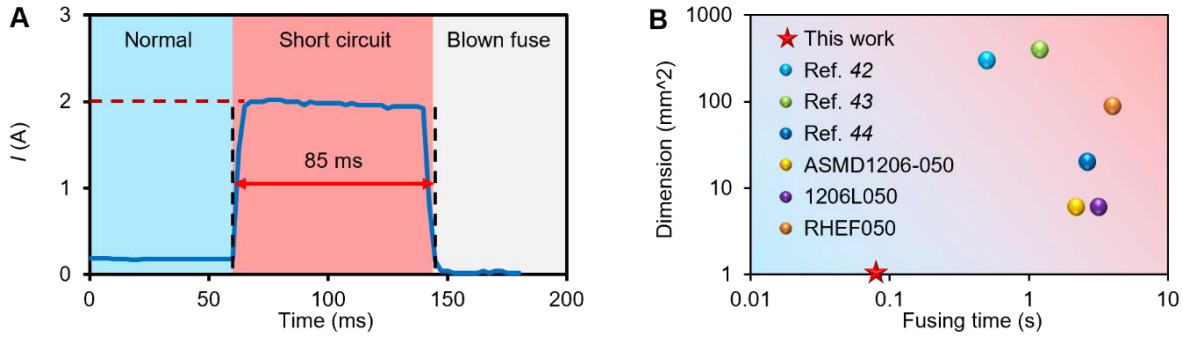

Figure 3.49 A smaller FMHE3 resettable current-limiting fuse.
(A) Current-time curve of the small FMHE fuse at blowing. The blue, red and grey areas correspond to the normal, short circuit and blown fuse states respectively. (B) Response time and the dimension of the small FMHE fuse compared to other reported [47-49] and commercial (JDTFUSE™ ASMD1206-050, Littelfuse™ 1206L050, Littelfuse™ RHEF050) resettable fuses. The dimension on the y-axis refers to the area of these chip fuses. The short circuit current during the test is twice the fusing current of each fuse.

Crucially, the unique mechano-responsive property of the FMHE fuse enables a wide range of adjustable fusing currents on the same device, offering vast versatility and functionality that has never been possible before.

3.6 Summary

In summary, a new type of electro-mechano responsive elastomer, FMHE, has been created that exhibits variable electromechanical properties. Its unconventional negative piezoresistivity, tunable resistivity, strain sensitivity, and stiffness is showcased through experiments and numerical simulations. By combining the high strain sensitivity and variable resistance/stiffness of the FMHE, a variable stiffness compensation unit is developed that can deform to protect a robotic manipulator from excessive compressive, bending, and torsional movements. The unit can adjust its stiffness under deformations without external control, offering an order of magnitude wider protection range than previous state-of-the-art. To underscore the broad applicability of the design, a FMHE resettable fuse that offers adjustable fusing currents while significantly outperforming state-of-the-art solutions in terms of compactness, range of operating current, and response speed is also demonstrated. This material family shows great potential in next-generation intelligent and resilient robotics and electronics.

3.7 References

1. Faber, J.A., A.F. Arrieta, and A.R. Studart, *Bioinspired spring origami.* Science, 2018. **359**(6382): p. 1386-1391.
2. Rus, D. and M.T. Tolley, *Design, fabrication and control of soft robots.* Nature, 2015. **521**(7553): p. 467-75.
3. Zhong, Q., et al., *Tunable stiffness enables fast and efficient swimming in fish-like robots.* Science Robotics, 2021. **6**(57): p. eabe4088.
4. Firouzeh, A. and J. Paik, *Grasp mode and compliance control of an underactuated origami gripper using adjustable stiffness joints.* Ieee/asme Transactions on Mechatronics, 2017. **22**(5): p. 2165-2173.
5. Lanza, M., et al., *Memristive technologies for data storage, computation, encryption, and radio-frequency communication.* Science, 2022. **376**(6597): p. eabj9979.
6. Lv, J., et al., *Printable elastomeric electrodes with sweat-enhanced conductivity for wearables.* Science advances, 2021. **7**(29): p. eabg8433.
7. Ogihara, N., N. Ohba, and Y. Kishida, *On/off switchable electronic conduction in intercalated metal-organic frameworks.* Science advances, 2017. **3**(8): p. e1603103.

8. Yu, X., T.J. Marks, and A. Facchetti, *Metal oxides for optoelectronic applications.* Nature materials, 2016. **15**(4): p. 383-396.
9. Yoo, E.J., et al., *Resistive Switching Behavior in Organic-Inorganic Hybrid CH3 NH3 PbI3-x Clx Perovskite for Resistive Random Access Memory Devices.* Advanced Materials (Deerfield Beach, Fla.), 2015. **27**(40): p. 6170-6175.
10. Yao, Z., et al., *Simultaneous implementation of resistive switching and rectifying effects in a metal-organic framework with switched hydrogen bond pathway.* Science Advances, 2019. **5**(8): p. eaaw4515.
11. Talin, A.A., et al., *Tunable electrical conductivity in metal-organic framework thin-film devices.* Science, 2014. **343**(6166): p. 66-69.
12. Wei, Y., et al., *A novel, variable stiffness robotic gripper based on integrated soft actuating and particle jamming.* Soft Robotics, 2016. **3**(3): p. 134-143.
13. Jadhav, S., et al., *Variable stiffness devices using fiber jamming for application in soft robotics and wearable haptics.* Soft Robotics, 2022. **9**(1): p. 173-186.
14. Yang, J., et al., *A novel magnetorheological elastomer isolator with negative changing stiffness for vibration reduction.* Smart materials and structures, 2014. **23**(10): p. 105023.
15. Sun, S., et al., *A compact variable stiffness and damping shock absorber for vehicle suspension.* IEEE/ASME Transactions on Mechatronics, 2015. **20**(5): p. 2621-2629.
16. Loeve, A., P. Breedveld, and J. Dankelman, *Scopes too flexible... and too stiff.* IEEE pulse, 2010. **1**(3): p. 26-41.
17. Ranzani, T., et al., *A bioinspired soft manipulator for minimally invasive surgery.* Bioinspiration & biomimetics, 2015. **10**(3): p. 035008.
18. Rogers, J.A., T. Someya, and Y. Huang, *Materials and mechanics for stretchable electronics.* science, 2010. **327**(5973): p. 1603-1607.
19. Wang, B. and A. Facchetti, *Mechanically flexible conductors for stretchable and wearable e-skin and e-textile devices.* Advanced Materials, 2019. **31**(28): p. 1901408.
20. Joo, H., et al., *Material design and fabrication strategies for stretchable metallic nanocomposites.* Small, 2020. **16**(11): p. 1906270.
21. Liu, H., et al., *Stimuli-Driven insulator–conductor transition in a flexible polymer composite enabled by biphasic liquid metal.* Advanced Materials, 2021. **33**(43): p. 2104634.
22. Chen, S., et al., *Generalized way to make temperature tunable conductor–insulator transition liquid metal composites in a diverse range.* Materials Horizons, 2019. **6**(9): p. 1854-1861.
23. Schubert, B.E. and D. Floreano, *Variable stiffness material based on rigid low-melting-point-alloy microstructures embedded in soft poly (dimethylsiloxane)(PDMS).* Rsc Advances, 2013. **3**(46): p. 24671-24679.
24. Lin, Y., J. Genzer, and M.D. Dickey, *Attributes, Fabrication, and Applications of Gallium-Based Liquid Metal Particles.* Adv Sci (Weinh), 2020. **7**(12): p. 2000192.
25. Piskarev, E., et al., *Lighter and Stronger: Cofabricated Electrodes and Variable Stiffness Elements in Dielectric Actuators.* Advanced Intelligent Systems, 2020. **2**(10): p. 2000069.
26. Tonazzini, A., et al., *Variable stiffness fiber with self-healing capability.* Advanced Materials, 2016. **28**(46): p. 10105.
27. Hao, Y., et al., *Low melting point alloys enabled stiffness tunable advanced materials.* Advanced Functional Materials, 2022. **32**(25): p. 2201942.

28. Briggs, L.J., *Gallium: thermal conductivity; supercooling; negative pressure.* The Journal of chemical physics, 1957. **26**(4): p. 784-786.
29. Tang, S.-Y., et al., *Phase separation in liquid metal nanoparticles.* Matter, 2019. **1**(1): p. 192-204.
30. Chen, S., et al., *Toxicity and biocompatibility of liquid metals.* Advanced Healthcare Materials, 2023. **12**(3): p. 2201924.
31. Lee, D., et al., *Highly Sensitive, Transparent, and Durable Pressure Sensors Based on Sea-Urchin Shaped Metal Nanoparticles.* Advanced Materials (Deerfield Beach, Fla.), 2016. **28**(42): p. 9364-9369.
32. Stassi, S. and G. Canavese, *Spiky nanostructured metal particles as filler of polymeric composites showing tunable electrical conductivity.* Journal of Polymer Science Part B: Polymer Physics, 2012. **50**(14): p. 984-992.
33. Yun, G., et al., *Liquid metal-filled magnetorheological elastomer with positive piezoconductivity.* Nat Commun, 2019. **10**(1): p. 1300.
34. Zavabeti, A., et al., *A liquid metal reaction environment for the room-temperature synthesis of atomically thin metal oxides.* Science, 2017. **358**(6361): p. 332-335.
35. Plech, A., et al., *In situ x-ray reflectivity study of the oxidation kinetics of liquid gallium and the liquid alloy.* Journal of Physics: Condensed Matter, 1998. **10**(5): p. 971.
36. Yun, G., et al., *Liquid metal composites with anisotropic and unconventional piezoconductivity.* Matter, 2020. **3**(3): p. 824-841.
37. Yun, G., et al., *Hybrid-filler stretchable conductive composites: from fabrication to application.* Small Science, 2021. **1**(6): p. 2000080.
38. Müller, A., M.C. Wapler, and U. Wallrabe, *A quick and accurate method to determine the Poisson's ratio and the coefficient of thermal expansion of PDMS.* Soft Matter, 2019. **15**(4): p. 779-784.
39. Çınar, S., et al., *Mechanical fracturing of core-shell undercooled metal particles for heat-free soldering.* Scientific reports, 2016. **6**(1): p. 21864.
40. Frank, F.C., *Supercooling of liquids.* Proceedings of the Royal Society of London. Series A. Mathematical and Physical Sciences, 1952. **215**(1120): p. 43-46.
41. Cantournet, S., R. Desmorat, and J. Besson, *Mullins effect and cyclic stress softening of filled elastomers by internal sliding and friction thermodynamics model.* International Journal of Solids and Structures, 2009. **46**(11-12): p. 2255-2264.
42. Zhang, Y., et al., *Peg–hole disassembly using active compliance.* Royal Society open science, 2019. **6**(8): p. 190476.
43. Lee, M.A., et al., *Making sense of vision and touch: Learning multimodal representations for contact-rich tasks.* IEEE Transactions on Robotics, 2020. **36**(3): p. 582-596.
44. Pan, C., et al., *Ultrastretchable, Wearable Triboelectric Nanogenerator Based on Sedimented Liquid Metal Elastomer Composite.* Advanced Materials Technologies, 2020. **5**(11): p. 2000754.
45. Ohtsuka, S., H. Suetomi, and M. Hikita. *Fundamental properties of OFF-ON resistance of a new type self-recovering fuse operated by dielectrophoresis*. in *Conference Record of the 2006 Twenty-Seventh International Power Modulator Symposium*. 2006. IEEE.
46. Niu, C., et al., *A novel liquid metal fault current limiter based on active trigger method.* IEEE Transactions on Power Delivery, 2020. **36**(6): p. 3619-3628.
47. Chen, Z., et al., *Fast and reversible thermoresponsive polymer switching materials for safer batteries.* Nature Energy, 2016. **1**(1): p. 1-2.

48. Wang, S., et al., *Conductive vitrimer nanocomposites enable advanced and recyclable thermo-sensitive materials.* Journal of Materials Chemistry C, 2020. **8**(34): p. 11681-11686.
49. Yang, R., et al., *Low-temperature fusible silver micro/nanodendrites-based electrically conductive composites for next-generation printed fuse-links.* Acs Nano, 2017. **11**(8): p. 7710-7718.

4. Capillary Liquid Metal Muscles

4.1 Introduction

There is a growing interest in artificial muscles as an alternative to electric motors for force/movement in various devices. This is due to the unique, bioinspired form factors that are possible using artificial muscles over conventional motors. Such artificial muscles include those made with coiled nylon fishing wire [1], pneumatic braided mesh [2], shape memory alloy [3], shape memory polymer [4] and high voltage electrostatic actuators [5]. However, each of these has drawbacks (such as slow response time, large pumps/compressors required, thermal heating, and high operating voltage), reducing their potential for more widespread use.

Liquid based muscles are a particularly compelling option for soft robotic devices due to liquid's inherent deformability and its ability to transfer pressure effectively. Fluid based actuation options include pumping of liquid- such as for electro conjugate fluid pumps, which uses high voltage to pump a dielectric fluid [6, 7]. Alternatively, electrowetting on dielectric can also be used to pump a liquid in microhydraulic systems [8]. Another approach is to compress a dielectric liquid between electrodes attracted by a high voltage, as for hydraulically amplified, self healing actuators (HASEL) [5, 9].

Recently, another type of liquid based artificial muscle has been characterised, made using a non-toxic liquid metal (LM) alloy of eutectic gallium indium (EGaIn). This LM artificial muscle utilises the unusual variable interfacial tension of EGaIn to generate force [10-12]. Without oxide on its outer layer, LM has a interfacial tension of ~600 mN/m [13] (~10 times that of water), which is the largest among all natural liquids at room temperature. When an oxidative voltage is applied to LM immersed in an electrolyte (particularly sodium hydroxide

solution), it causes an oxide layer to dynamically form and dissolve, making the interfacial tension effectively lowered to ~0 mN/m to flatten the droplet [13]. The LM droplet regains its spherical shape upon the application of a reductive voltage to remove the oxide skin, allowing for the recovery of its large interfacial tension to generate force. Previous works used ~1 mm radius droplets of LM as artificial muscles, characterising their force output and even making a swimming fish robot [10]. An alternative design uses bridges of LM droplets alloyed between copper pads [11]. However, the force generated by these designs is quite low (~mN). Decreasing the size of the LM droplets would increase the surface area, which enhances both force and work density; however, this would be challenging to achieve and would result in a small stroke. To date, no prior work has successfully utilised the exceptionally large surface energy of LM to develop artificial muscles capable of delivering both high force and large stroke.

In this work, capillary liquid metal muscles (CLMM) are developed, which utilise a channel-based design to increase the force output by an order of magnitude over previous LM droplet muscles. The force change is fast (in just tens of ms), the muscle itself can move quickly, the forces generated are strong (capable of lifting 1 kg) and the force can be precisely controlled. Movement of ~10% stroke can be achieved, with a controllable position. The force per unit area (i.e. pressure) per volt of CLMM is the best ever achieved for liquid-based actuators. The design is also simple to make using standard, commercially available 3D printers. This work also discusses the theory behind CLMM, characterises the force output with respect to time and distance moved, and determines the muscle's movement speed and controllability of force and position. Additionally, soft robotic elements and a damper are made using the artificial muscle.

4.2 Theory of CLMM and Initial Testing

LM has a variable interfacial tension. Without oxide, its interfacial tension is 500-650 mN/m, depending on the surrounding media [13, 14]. When immersed in NaOH solution, with a positive (oxidative) voltage applied to it relative to a counter electrode also in the solution, its interfacial tension drops to ~0 mN/m. In its high surface energy state, it will resist deformation. Whereas if oxidised, the oxide layer will dynamically form and dissolve, making the interfacial tension effectively lowered to ~0 mN/m to flatten the droplet [13] (Figure 4.1). Removing the oxide by applying a reductive potential to the droplet causes the interfacial tension to increase back to the original higher value. (NaOH also removes the oxide on its own, without any potential applied) [15]. The reaction time for interfacial tension change is <25 ms after voltage is applied (see section 4.5.4). Therefore, LM droplets can be used to generate force by applying a voltage to repeatedly alter their interfacial tension.

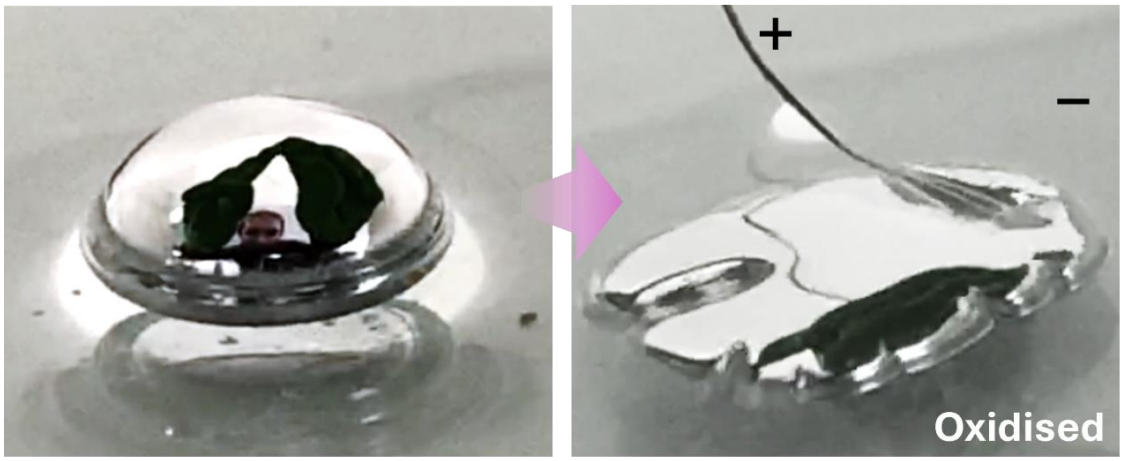

Figure 4.1 A LM droplet changes shape when oxidised due to the change in interfacial tension.

If liquid metal in its high interfacial tension state is attempted to be pushed into channels, it will require high pressure. This is because the LM's high interfacial tension means it takes a large amount of energy to increase its surface area However, in its low tension, oxidised state, LM can be easily pushed into small channels as its near zero interfacial tension requires a very small amount of energy to change its surface area. When the oxide layer of LM is removed to increase interfacial tension, it results in a dramatic increase in force, pushing the LM out of the channels (Figure 4.2). The channel design dramatically increases the output force and stroke possible from the change in interfacial tension of LM. The initial design used circular capillaries for liquid metal to be pushed in and out of.

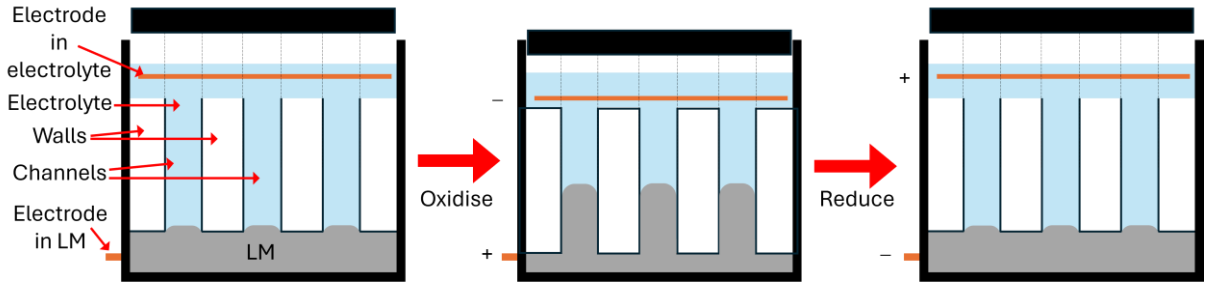

Figure 4.2 Diagram showing LM going in and out of channels.
To oxidise LM and lower the force/contract the CLMM, a positive potential is applied to the bottom electrode relative to the top electrode. To reduce LM and increase the force/extend the CLMM, a negative potential is applied to the bottom electrode relative to the top electrode.

4.2.1 Theoretical Force Change for CLMM with Circular Capillaries

The generated force for a given channel size and overall muscle diameter can be calculated by using the change in interfacial energy for the different states. See Figure 4.3 for the theory diagram.

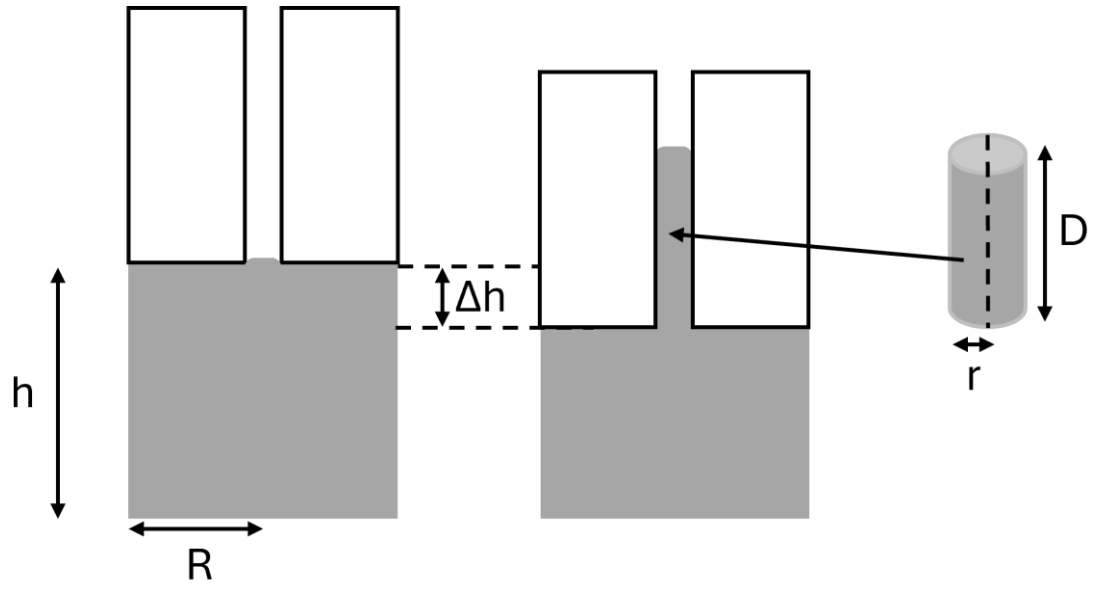

Figure 4.3 Theory diagram for the change in surface area of LM when pushed into a circular capillary.

For a cylindrical muscle, with overall diameter R and height of liquid metal h, it will have a volume, V of liquid metal of

$$V = \pi R^2 h \tag{4.1}$$

The surface area in this initial state is

$$SA_1 = 2\pi R^2 + 2\pi R h \tag{4.2}$$

If pushed down by distance Δh, it will move into circular channels (number of n) with radius r. The distance it will move into this channel is distance D. Overall volume must be unchanged, so

$$V = \pi R^2 (h - \Delta h) + n\pi r^2 D = \pi R^2 h \tag{4.3}$$

Rearranging and expanding the bracket gives

$$n\pi r^2 D = \pi R^2 h - \pi R^2 h + \pi R^2 \Delta h \tag{4.4}$$

Giving

$$nr^2 D = R^2 \Delta h \tag{4.5}$$

Therefore,

$$D = \frac{R^2}{nr^2} \Delta h \tag{4.6}$$

Surface area is changed in the second state, and is given by

$$SA_2 = 2\pi R^2 + 2\pi R(h - \Delta h) + 2n\pi rD \tag{4.7}$$

Change in surface area ΔSA is given by

$$\Delta SA = SA_2 - SA_1 = (2\pi R^2 + 2\pi R(h - \Delta h) + 2n\pi rD) - (2\pi R^2 + 2\pi Rh) \tag{4.8}$$

Which gives

$$\Delta SA = 2\pi R^2 - 2\pi R^2 + 2\pi Rh - 2\pi Rh + 2n\pi rD - 2\pi R\Delta h = 2n\pi rD - 2\pi R\Delta h \tag{4.9}$$

Substituting in for *D* gives

$$\Delta SA = 2n\pi r \frac{R^2}{nr^2} \Delta h - 2\pi R\Delta h = \left(2\pi \frac{R^2}{r} - 2\pi R\right) \Delta h \tag{4.10}$$

The change in interfacial energy ΔE is the interfacial tension, γ multiplied by the change in surface area

$$\Delta E = \gamma \Delta SA \tag{4.11}$$

Assuming Δh is infinitely small, the variation in force, *F*, is calculated by

$$F = \frac{dE}{dh} = \frac{\gamma dSA}{dh} = 2\pi\gamma R\left(\frac{R}{r} - 1\right) \tag{4.12}$$

Using this equation, for a given *R* and *r*, if the interfacial tension is varied from ~500 mN/m to ~0 mN/m [13], then the force due to interfacial tension will drop to zero. Maximum force can be increased by increasing overall *R* or by reducing *r*. Note that the force is not changed by increasing or decreasing the number of channels. Adding channels reduces the distance LM moves into the slits, *D*, and allows for greater stroke of the actuator.

As the predicted output force scales with the inverse of capillary radius, decreasing the size of the capillaries will have a dramatic effect on the performance of the muscle. Increasing the overall radius also boosts the predicted force quadratically. The predicted force for a 10 mm overall radius CLMM with varying capillary radius is shown in Figure 4.4.

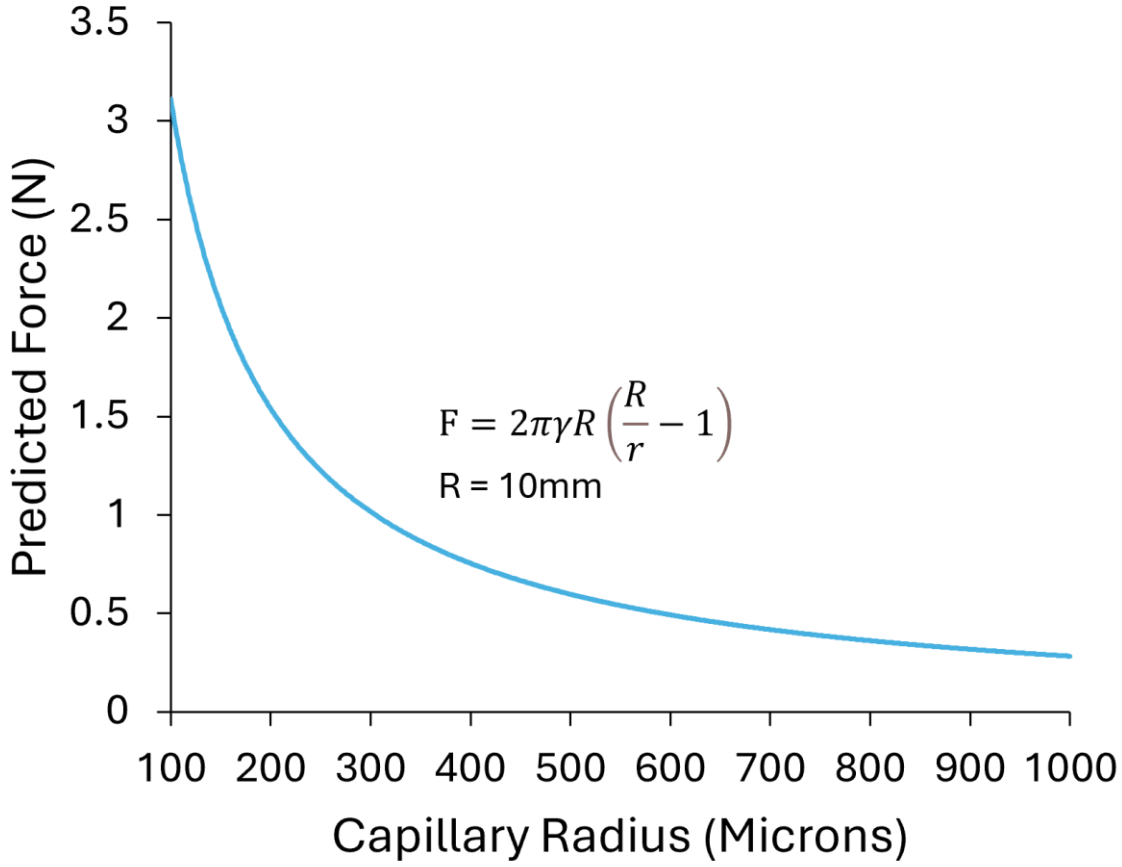

Figure 4.4 Predicted force with varying capillary radius for a CLMM with overall radius of 10 mm.

4.2.2 Creation of CLMM Using Fused Deposition Modelling 3D Printing

An initial design of CLMM for testing was created using an Ultimaker S5 fused deposition modelling (FDM) 3D printer. It printed a block of polylactic acid (PLA) circular capillaries and a container which was sized just larger (+0.5 mm diameter) so that the inside section could move freely (see Figure 4.5). This can be thought of as similar to a motor which has a moving part (rotor) and a stationary part (stator), as the block with capillaries in moves up and down while the overall container stays stationary. One electrode was wound around the top of the capillaries so it would be immersed in electrolyte. The other electrode was posted through one

of the capillaries so it could contact the LM directly, and was glued in place. The wire for contacting LM was transformer wire, so had a polymer insulating layer around it, this was scratched off at the bottom so it could easily form an electrical connection with the LM. A range of sizes were made with channel diameter from (0.5 – 1 mm) and overall radius of the actuator between 10 – 20 mm.

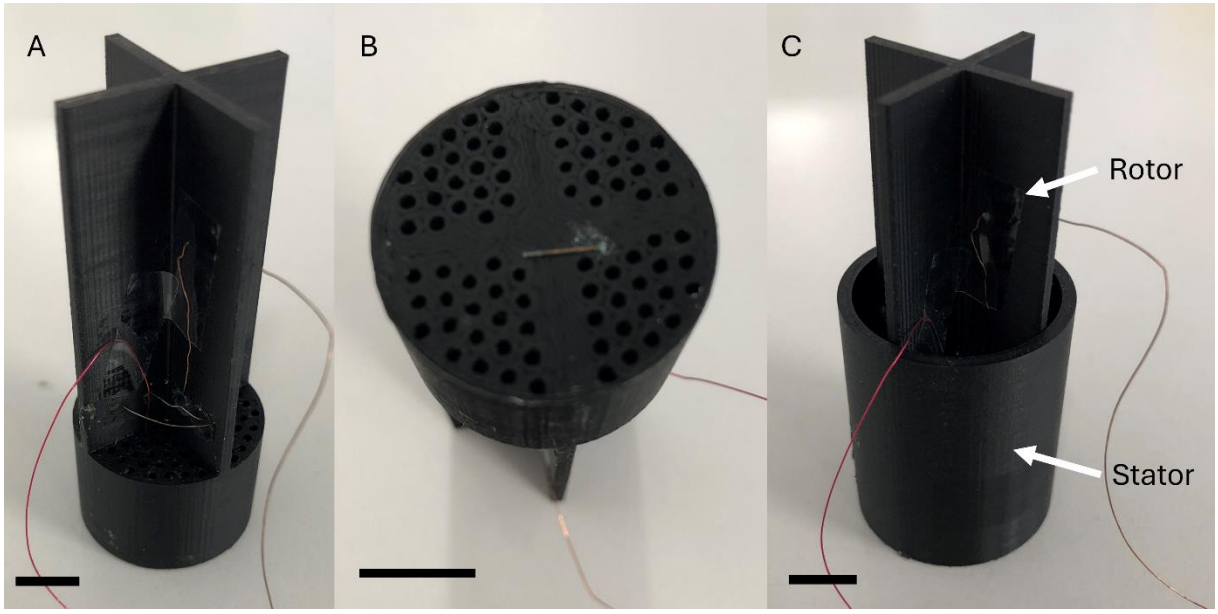

Figure 4.5 Pictures of a 3D printed CLMM.
(A) The rotor from above. (B) The rotor underneath, showing the capillaries and wire threaded through. (C) Rotor and stator fitting together. All scale bars are 10 mm.

4.2.3 Testing of FDM 3D Printed CLMM

Force testing was done on the manufactured CLMMs to compare with theory. Testing was done using a mechanical testing system (MTS, YK-Y0026, Dongguan Yaoke Instrument Equipment Co. Ltd., China). First, the muscle had LM and 0.5M NaOH solution injected into the bottom container. The amount of LM added was to give a depth of LM of ~10 mm (~3 mL LM for 10 mm R stator - ~13 mL LM for 20 mm R stator). The amount of NaOH added had to cover the

top electrodes when the top section was inserted (~10 mL for 10 mm R stator - ~40 mL for 20 mm R stator). The top section with capillaries was then put into the container. It rested on top of the liquid metal due to the LM high interfacial tension (and density). The wires were connected to a lab power supply set to max 7 V and max 0.06 A. The MTS then had its compression testing plate lowered to press the LM into the capillaries slightly, with the resultant force measured. The force measured by the MTS as it pushes down the rotor into the LM increases linearly over ~0.3 mm as LM is gradually pushed into all the slits. The increase in force then starts to level off when LM is in all the slits. The force test was done at this level of displacement. A test program was run on the MTS where it measured the force without moving, and oxidative voltage was repeatedly applied to the LM and then turned off. The results are shown in Figure 4.6 and Figure 4.7.

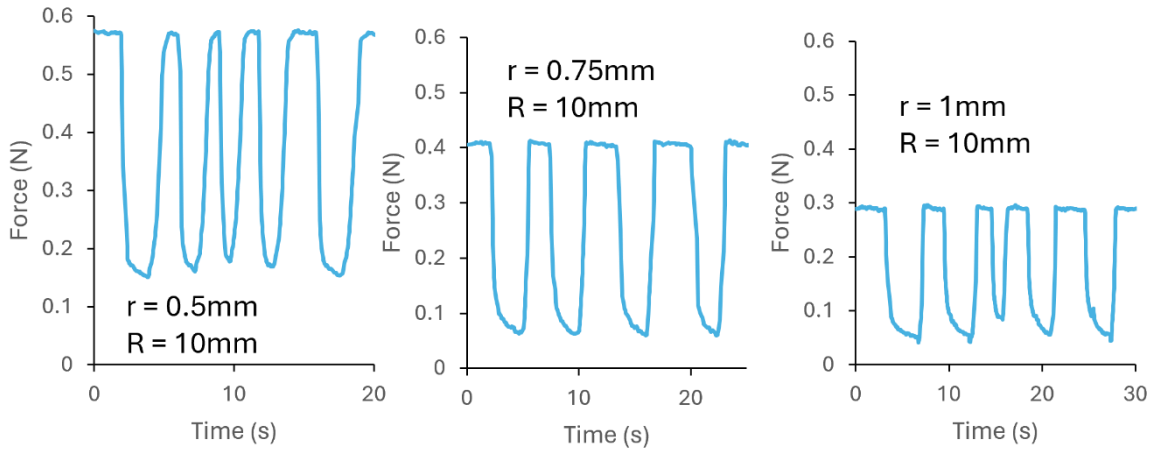

Figure 4.6 Measured force change for R = 10 mm CLMM for circular capillary radius ranging from 0.5 mm to 1 mm.

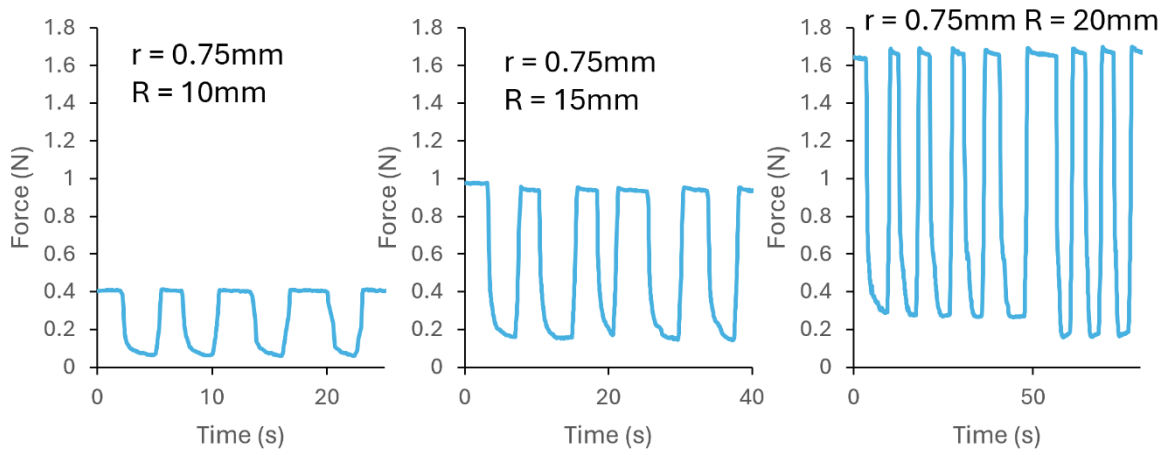

Figure 4.7 Measured force change for r = 0.75 mm CLMM with overall radius ranging from 10 mm to 20 mm.

Initial tests showed that the force variation was repeatable. The measured force started to decrease immediately after voltage was applied. Measured force decreased sharply initially, then started to level off when it got closer to the minimum value. When the power was turned off to remove the oxide on the LM, and increase its interfacial tension, the force started to increase. Force change was slightly faster when increasing force, <1 s, whereas to decrease the force, it typically took ~1.5 – 2s. The measured force change increased with decreasing capillary size and with increased overall radius as predicted.

The force change in the graphs does not drop to zero due to buoyancy of LM. If the force testing is conducted with the CLMM slightly less pressed down (so less LM displaced). The measured force drops to nearly zero (see Figure 4.8).

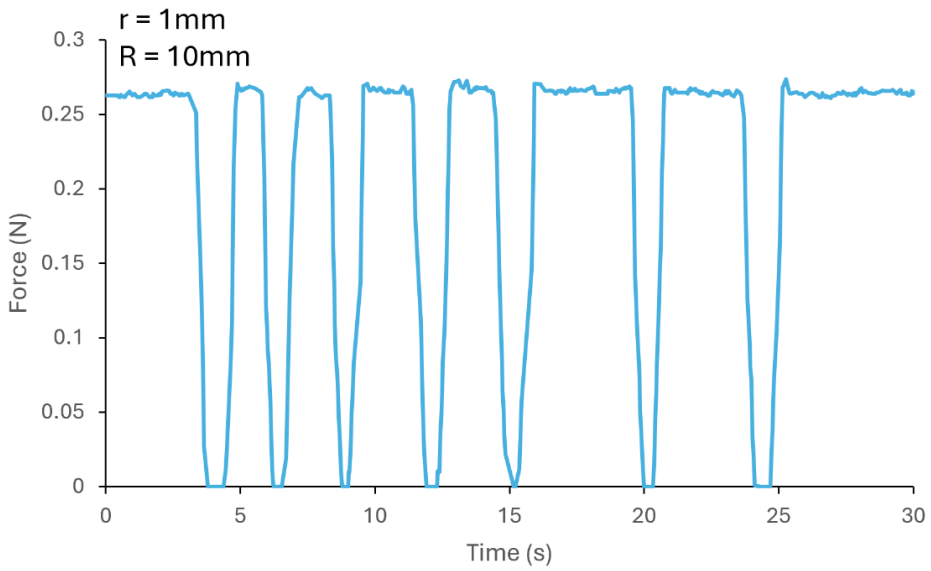

Figure 4.8 Measured force dropping to ~0 N during testing.

4.2.4 Comparison of Measured Results with Theory

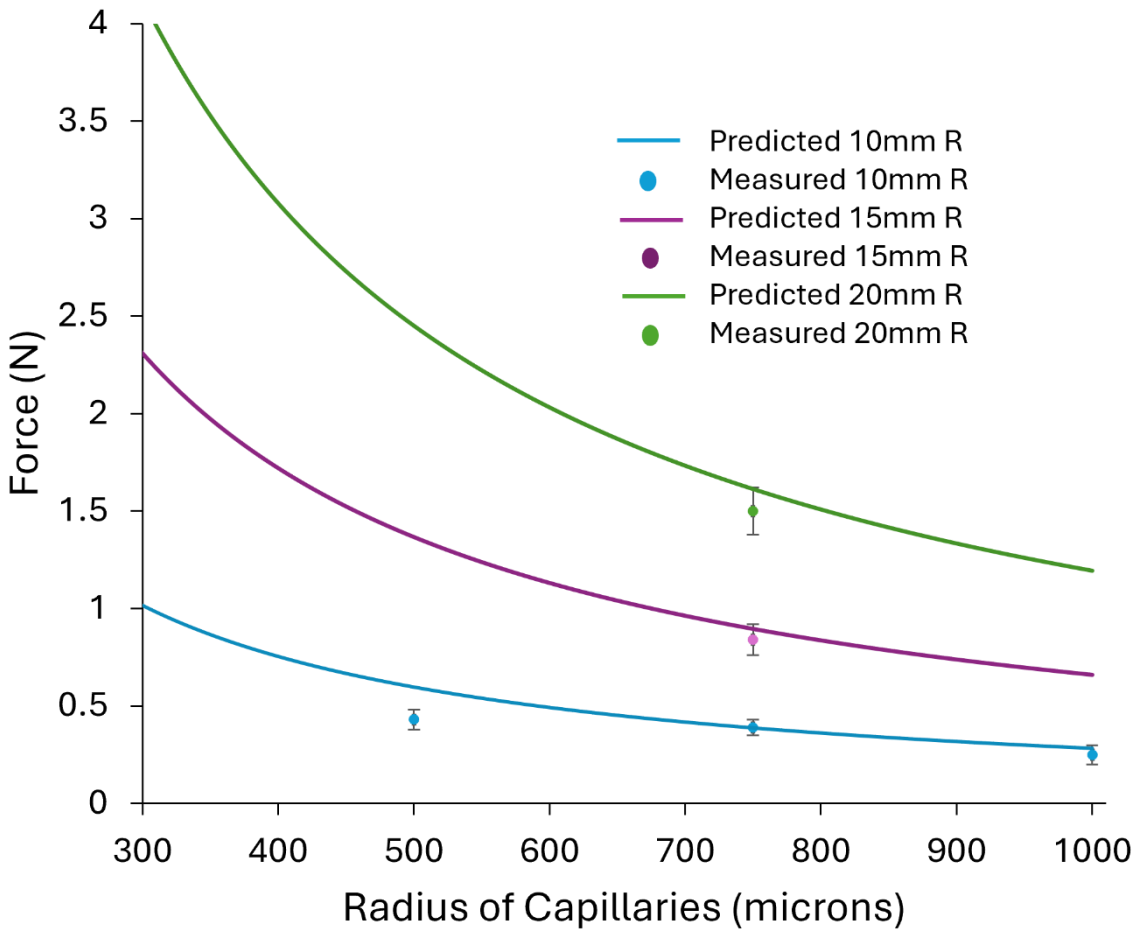

Figure 4.9 Predicted and measured force for varying capillary radius.
Error bars are given by the standard deviation of the measured force change.

The results were plotted against the predicted values for the different overall radius of muscle and with the variation in radius of the capillaries (Figure 4.9). Overall, the results are in line with those predicted by theory. The smallest radius capillary muscle has a lower change in force than predicted, this may be due to the size of the capillaries being different than that set on the CAD file. More power may have been required for the full force change also – the 15 mm and

20 mm *R* muscles both have slightly lowered measured than predicted values. A larger area will require more power to oxidise the LM.

4.3 Pillar Design of CLMM

In order to further optimise the CLMM, further decreasing the size of the channels which the LM travelled into seemed to be the key element. As the output force scales with the inverse of the channel size, decreasing the channel size to as small as possible will maximise the output force. However, other considerations must also be taken into account, such as the stroke of the muscle. Reducing the size of the channels will also mean that the channel gap percentage decreases (if channel wall thickness stays constant). For example, for a wall thickness of 0.5 mm, a 1 mm radius circular capillary has a gap percentage of 25%, but for a 0.5 mm radius circular capillary, it decreases to 11.1%. Therefore, the overall stroke of the muscle decreases as there is less volume for liquid metal to go into.

To mitigate the reduction in stroke with smaller channel size, a pillar design was conceived. This design consists of an array of pillars, equally spaced apart. LM and electrolyte can pass around each side of the pillar, meaning that greater stroke is available even at close pillar spacings.

4.3.1 Creation of the Pillar Design

In order to create the pillar design, it was decided to use a stereolithography (SLA) printer (Formlabs Form 3, used with clear resin v4), rather than the FDM type Ultimaker S5. The Formlabs printer offered higher resolution prints than could be done with the Ultimaker. Clear resin was used to be able to see inside the muscle during testing, and because it offered the best resolution. All prints with the Formlabs were done using its default settings, with 25 µm layer

height. Post print cleaning was done in an isopropanol (IPA) bath (Formlabs Form Wash) for ~20 minutes. After drying, it was postcured in the Formlabs Form Cure oven at 60 °C for 15 minutes with 405nm UV light exposure as well.

Before creating a muscle with the pillar design, a test print was done with the printer to see the best possible resolution and smallest pillar spacing. An array of 1 mm square pillars was made, with spacings of between 0.1 – 1 mm, in increments of 0.1 mm. Images of the test results are shown in Figure 4.10 - Figure 4.13.

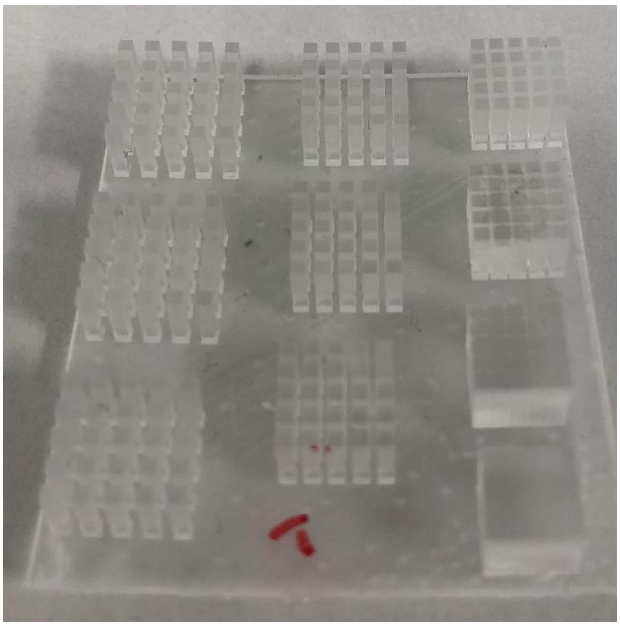

Figure 4.10 Photograph of the test print.

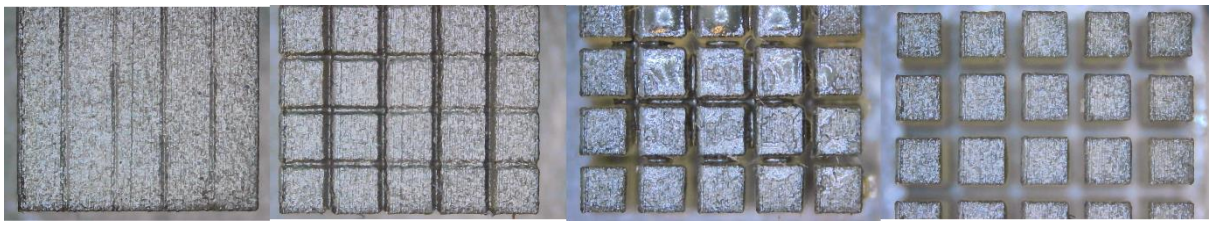

Figure 4.11 Microscope images of the 1mm width square pillars with spacings of (from left to right), 0.1, 0.2, 0.3 and 0.4 mm.

The gaps are completely blocked for 0.1 and 0.2 mm spacings and are mostly blocked for the 0.3 mm spacing print.

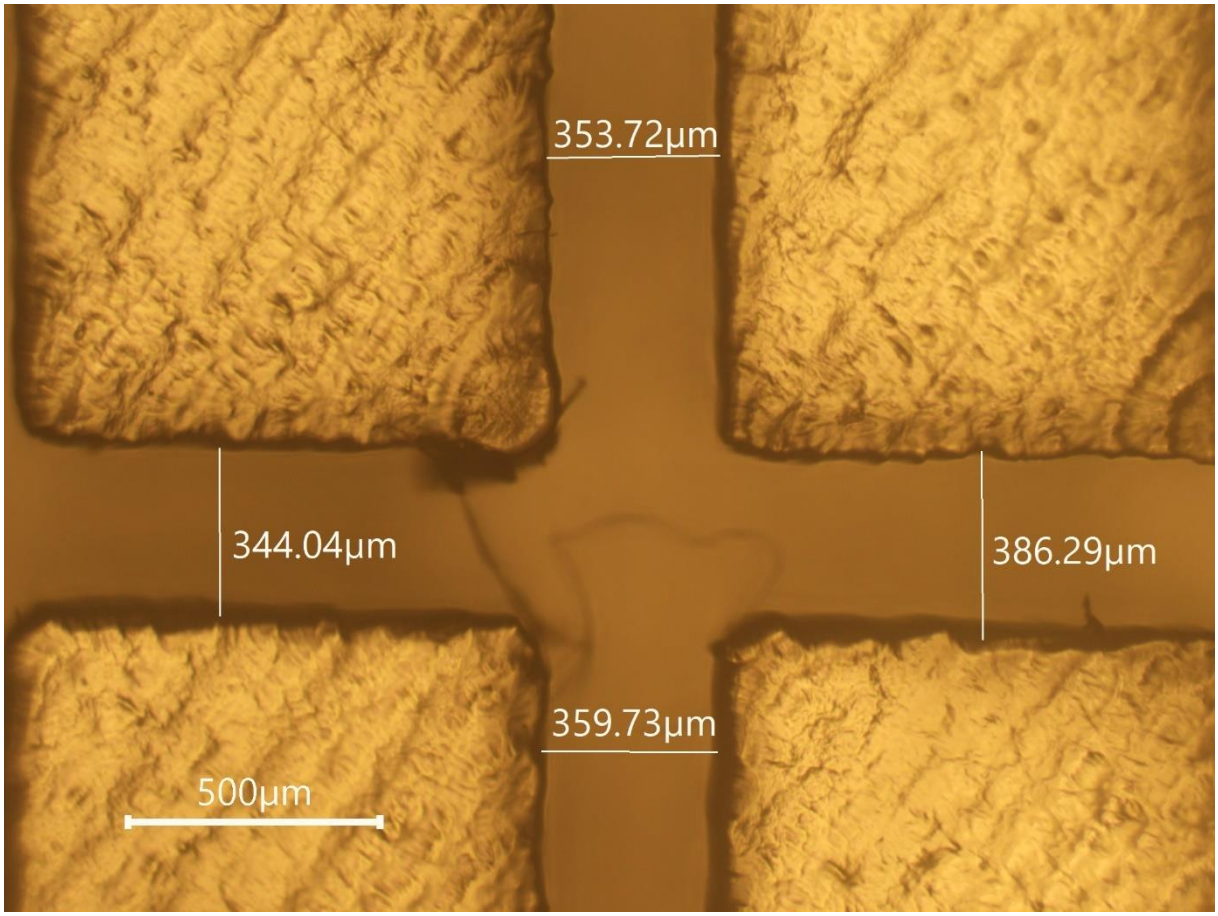

Figure 4.12 Microscope image of the 0.4 mm gap spacing print with measured lengths.

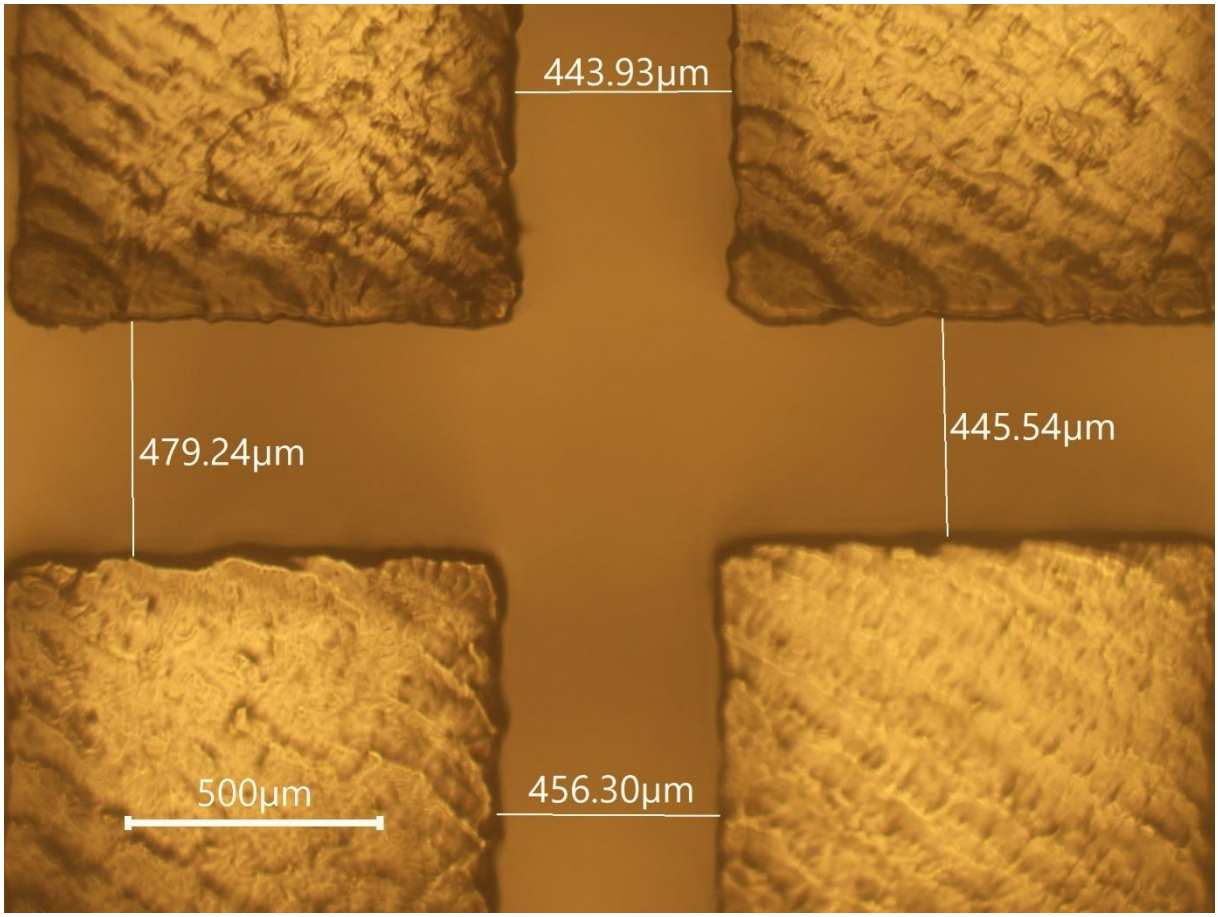

Figure 4.13 Microscope image of the 0.5 mm gap spacing print with measured lengths.

The test print revealed that prints with 0.1 and 0.2 mm spacings were completely filled with cured resin. The 0.3 mm spaced pillars also mostly had the spaces between them filled with resin. 0.4 mm spacing and above were printed well. The spacing between the pillars was also measured using a microscope (Nikon Eclipse TE2000-U)(see Figure 4.12 and Figure 4.13). The measurements show that the spacing between the pillars is less than set on the CAD file by 55-14 microns for the 400 micron width gaps and 56-21 microns for the 500 microns width gaps.

The reason for the infill between pillars and the smaller sized gaps is because the SLA printer uses resin to create the part. The resin is highly viscous, so when trying to print small gaps, the

liquid can remain trapped within the gap, causing it to become blocked. Overall, it was decided that the results of the print were satisfactory to create a pillar type CLMM with 0.5 mm gaps between pillars.

4.3.2 Pillar CLMM Creation and Testing

For the pillar type CLMM, the SLA printer created the pillars and the container. A small gap (0.8 mm diameter) was left in the container for a wire to be threaded through and glued sealed. Copper wire was threaded through the pillars at the top and pushed almost halfway down, where there was an alternating connection between the pillars which stopped the wire going down any further. Overall radius for the muscle was 10 mm, pillars were 1 mm square and the gap size was 0.5 mm. See Figure 4.14 for images of the pillar type CLMM.

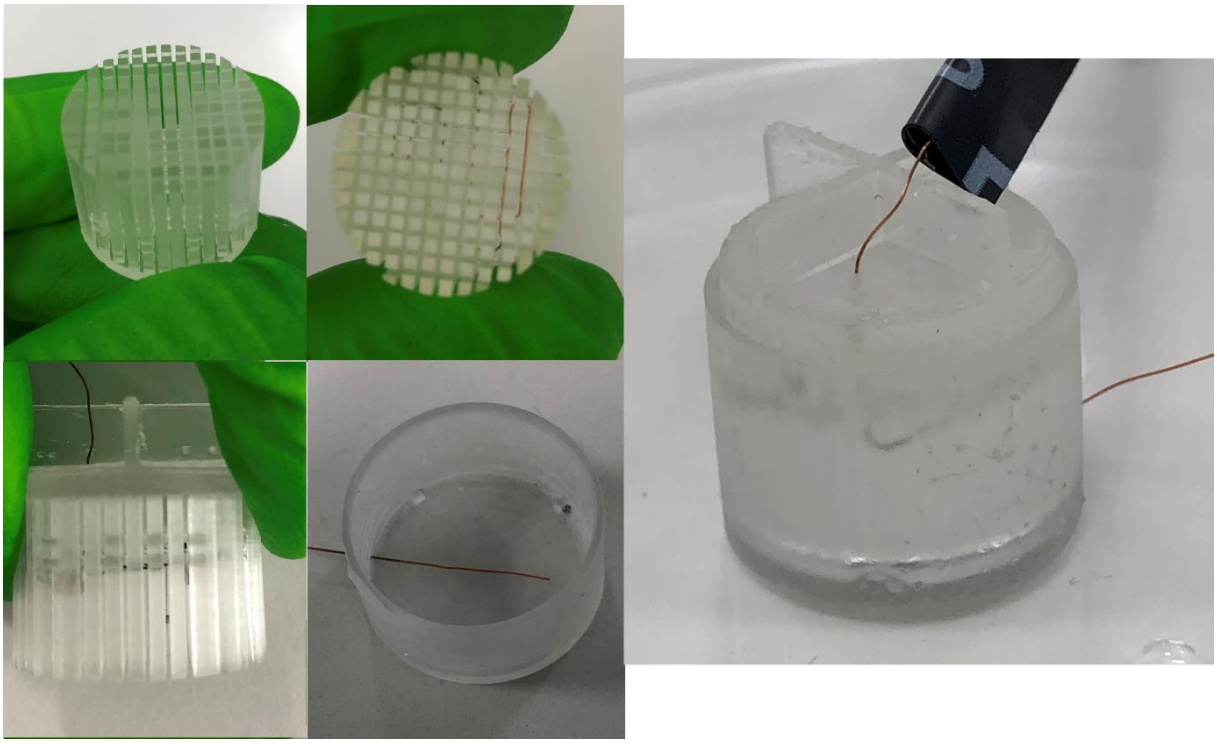

Figure 4.14 Pictures of (left) making the pillar type CLMM and (right), with LM and electrolyte added.

Testing was done in a similar way as previously, with the MTS used to measure the force change.

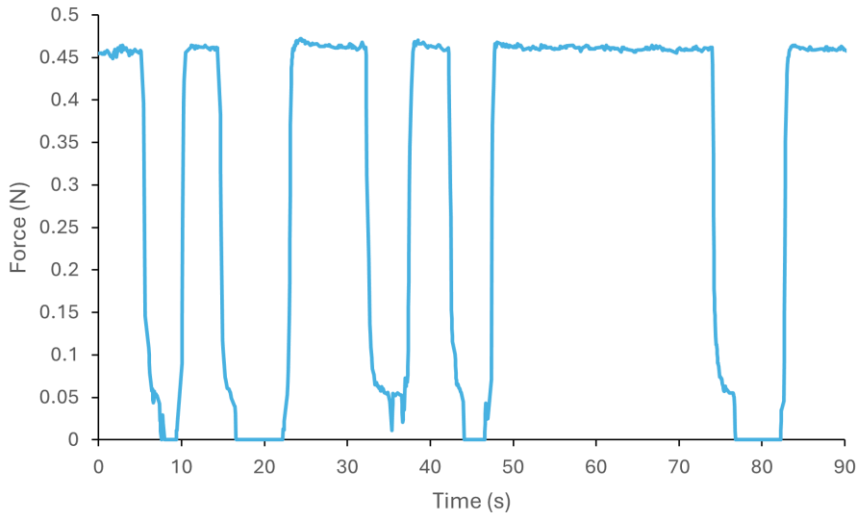

Figure 4.15 Measured force change with time for the pillar CLMM.

From the data shown in Figure 4.15, it can be seen that the pillar design exhibited repeatable force change, with overall performance similar to the previous circular capillary muscle.

4.3.3 Stacked Pillar Type CLMM

By stacking one LM muscle on top of another, it is possible to create an additive force. This enables greater force variation for the same overall footprint, as well as potentially easy control of the resultant force by just turning on one layer, or both layers. In order to test this, the tops of two LM muscles were made and joined together with columns, and two bottoms were also joined together (Figure 4.16). Enough space was left between the layers and at the side for the stacked muscle to be split apart after use by lifting the top section and moving it to one side.

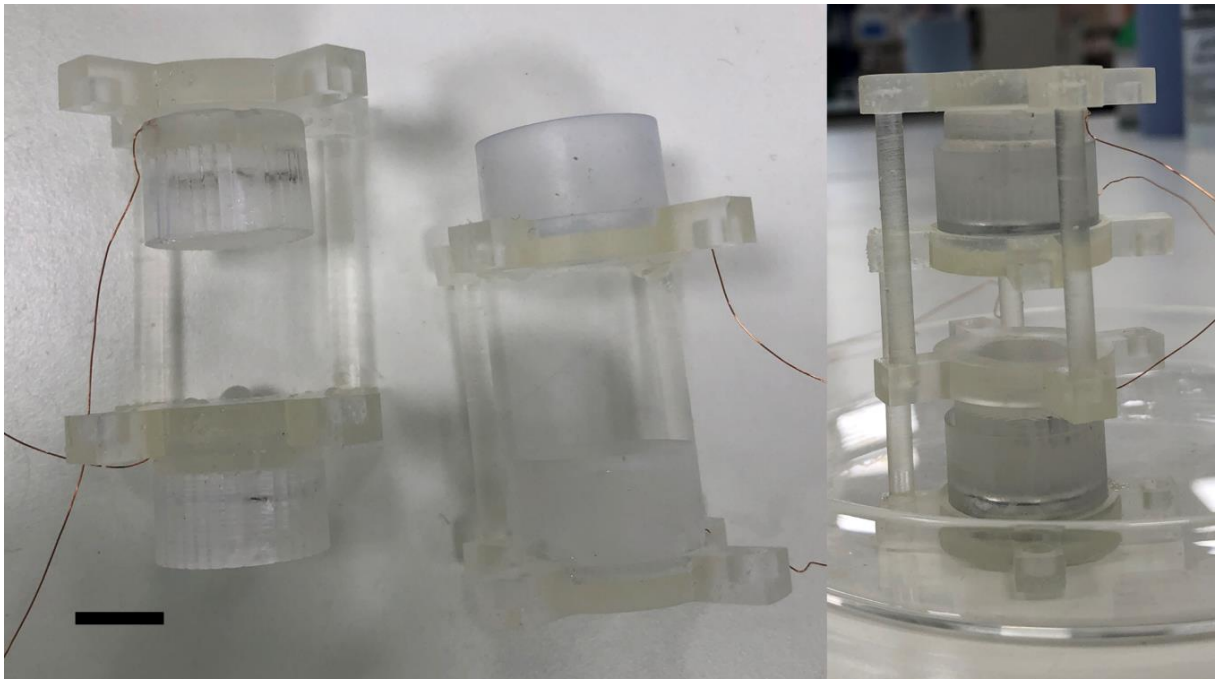

Figure 4.16 Pictures of the stacked pillar type CLMM disassembled (left) and assembled and filled with electrolyte (right).
The scale bar is 10 mm.

Before being assembled together, each layer was individually tested to check its force change characteristics (Figure 4.17).

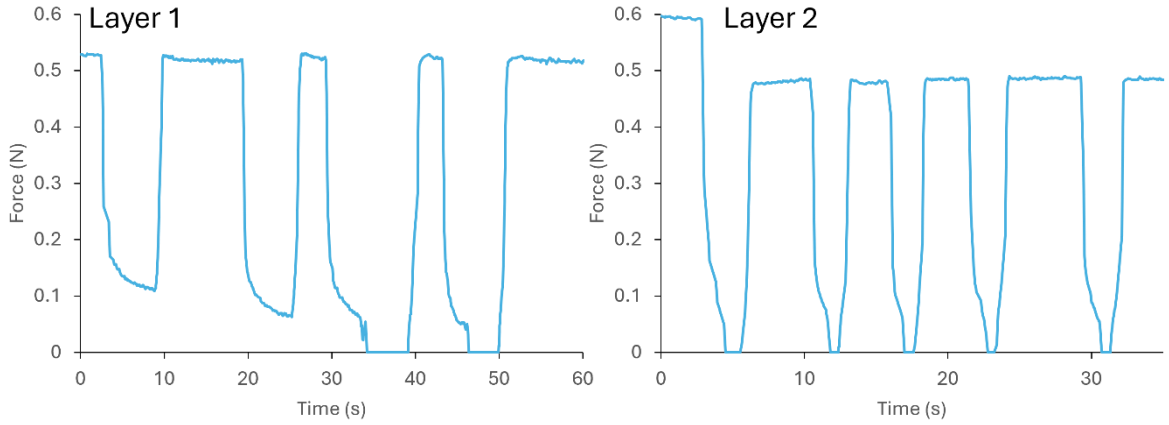

Figure 4.17 Force change for each of the individual layers of the stacked CLMM before being assembled together.

After assembling the stacked muscle, it was tested in combination, using separate power supplies for each half of the stacked muscle.

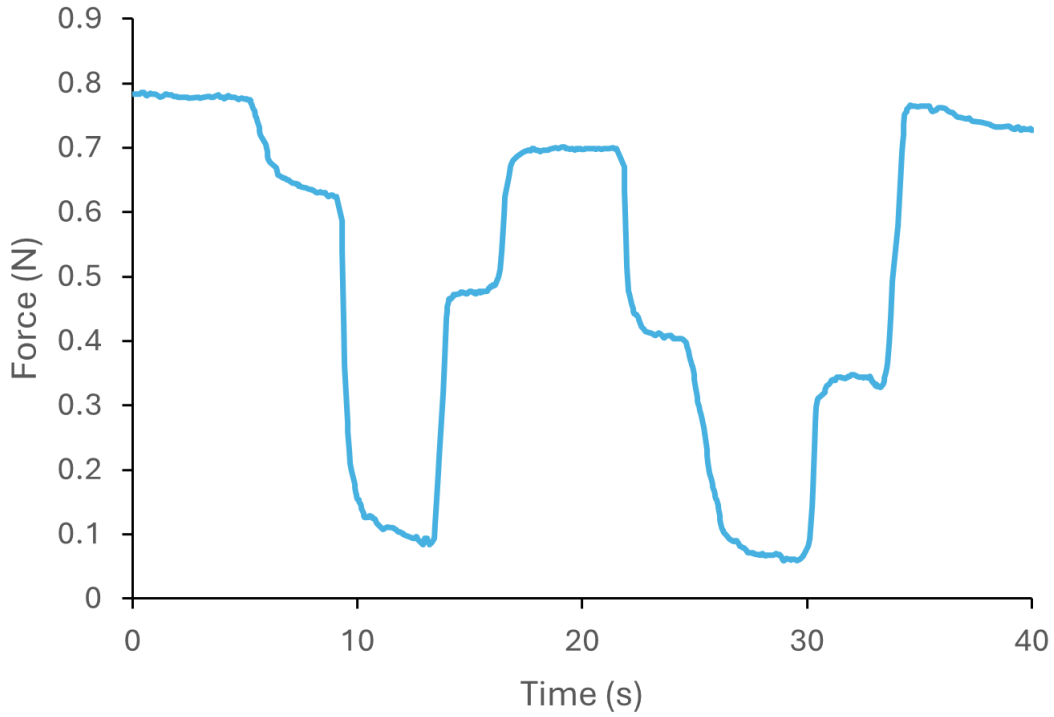

Figure 4.18 Force change for the stacked CLMM after assembly.

From Figure 4.18, the change in force for each layer is clear, as is the additive combination of both layers stacked together. The overall force is lower than for the individual layers added together. This is probably caused by some friction caused by a slight crookedness between the layers introduced during assembly.

4.3.4 Problems with Pillar Design

Overall, the pillar design worked well, however it also showed problems when pillar size was tried to be reduced below 1mm width square to increase the percentage stroke of the muscle.

For 0.5 mm square pillars, the muscle would work well initially (see Figure 4.19), however it would lose most of its force quickly during testing.

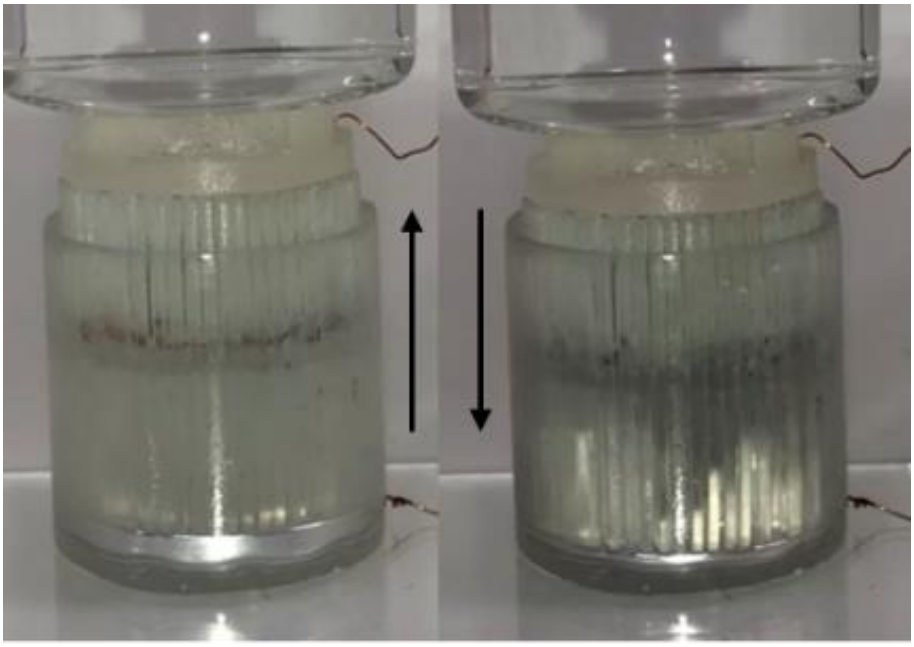

Figure 4.19 Pillar style CLMM with 0.5 mm width pillars lifting a ~25g mass.
The thin pillar designs would work well for a short period then deteriorate.

Reducing the thickness of the pillars weakened them. As their aspect ratio was high, they could be pushed from side to side easily. Pillars with a width below 1 mm always became pushed apart, which reduced the force of the muscle significantly. If a gap between pillars is slightly larger on one side than the other before testing, during testing, more LM goes into the larger gap. When reduced, the LM pushes the pillar towards the smaller gap side. This leads to bunching of the pillars, with large gaps between the bunches, as seen in Figure 4.20.

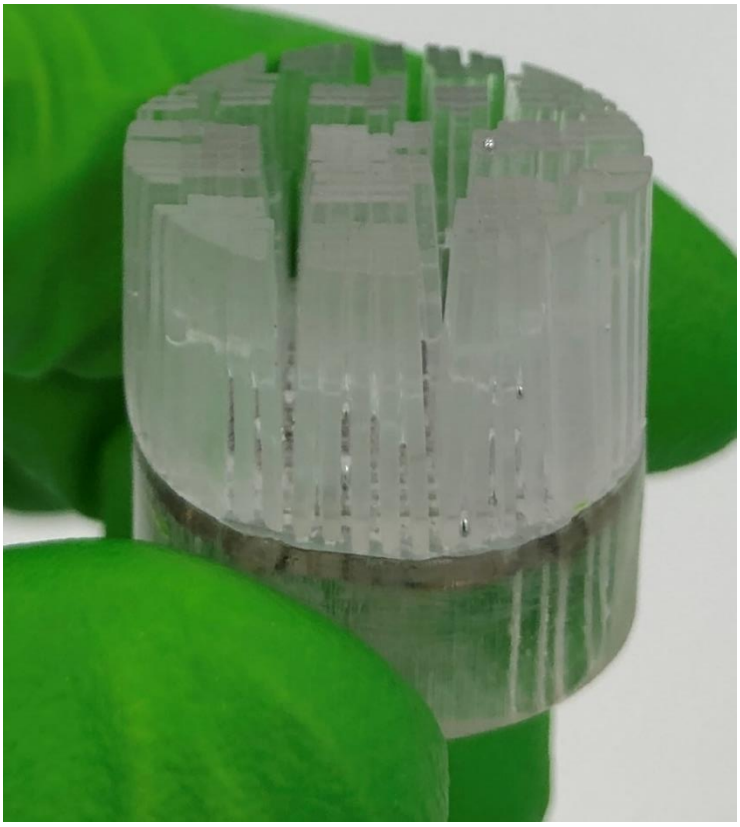

Figure 4.20 Bunching of thin (0.5 mm width) pillars in a CLMM.
The bunching weakens the force output of the CLMM.

4.4 Pillar with Cross Support LM Muscle

For the next iteration of the design, to rectify the problems of the pillars being pushed apart, cross support was added to the pillars. This was done in an alternating way so that LM could still move between the gaps effectively. See Figure 4.21 for a diagram of the updated design.

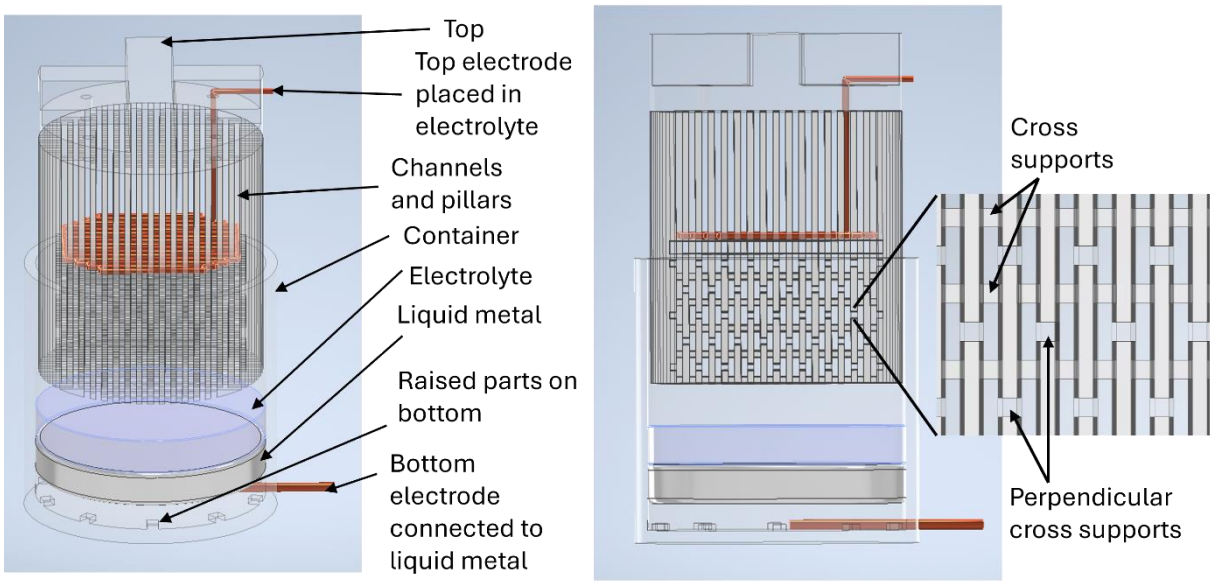

Figure 4.21 Exploded diagram of the pillars with cross support design of CLMM.
The cross supports alternate directions each layer as shown in the zoomed in view.

The design was printed using the SLA printer. Pillars were 0.5 mm square with cross supports also 0.5 mm square, and with gaps between pillars of 0.5 mm. Overall diameter of the inner section was 19.5 mm, the diameter of the inside of the container was set to 20 mm. After printing, the parts were washed in the IPA bath for ~2 hours, and were repeatedly taken out, squirted with IPA from a wash bottle, pressed dry with paper towel, before putting back into the wash station. The printed parts were rigid and robust so were able to be cleaned and pressed dry by wiping them with paper towels without sustaining any damage. Repeated washing and pressing dry was done to fully remove all resin from inside the channels. The small gaps in the design means that resin could remain there and block the channels if not thoroughly washed. The parts were then post-cured as with the previous settings.

For controlling the CLMM, an Arduino microcontroller (Arduino Due) was used with a motor controller (Deek-Robot motor shield). Supplied power to the motor controller was set to a

maximum of 17.5 V, 1 A using the lab bench power supply. Using the Arduino and motor controller meant that voltage could be turned on and off repeatedly at specified frequencies, and the applied voltage flipped to reduce or oxidise LM.

The new style CLMM was tested in the MTS with 0.5 M NaOH electrolyte added. The blocked force was measured for frequencies from 0.1 – 5 Hz. The motor controller was set to apply oxidative voltage to the LM for the first half of the period. It then applied 100 ms of reductive potential to the LM. It was then set to off for the rest of the period. Applying a brief reductive potential to the LM removes the oxide quickly, meaning that the CLMM can reach its maximum force as fast as possible. Frequencies from 0.1-1Hz were incremented in 0.1 Hz steps, from 1-5Hz, increments were in steps of 0.5 Hz. Cycles were for 60 s. A space of 5 s was left with the muscle off between each frequency cycle. Figure 4.22 shows the resultant data.

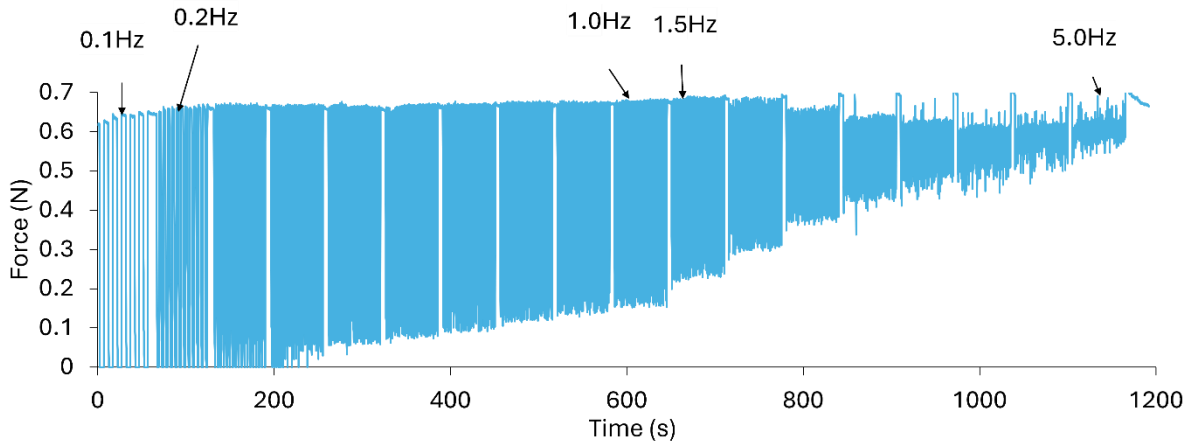

Figure 4.22 Force change testing for pillars with cross support CLMM for frequencies from 0.1-5 Hz.

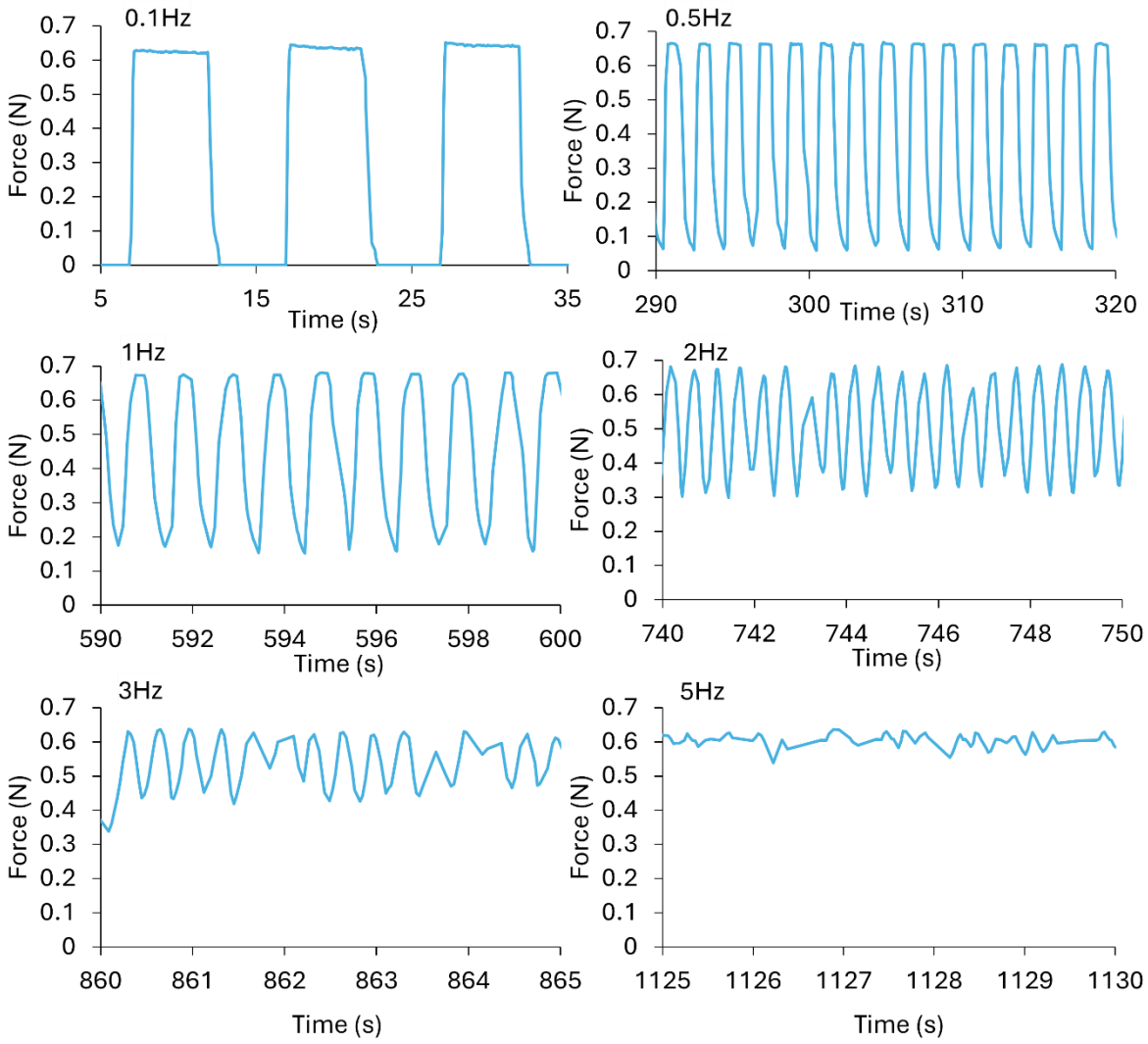

Figure 4.23 Zoomed in force measurement for various frequencies

From Figure 4.22 and Figure 4.23, the overall force can be seen to vary from a maximum of ~0.62 N down to ~0 N. The force change decreases with increasing frequency, with the minimum force increasing from 0 N at 0.4 Hz. At higher frequencies, there is still variation in blocked force, although at 5 Hz, its performance is very poor with only tiny variation in force.

4.4.1 Force Testing Using a Longer Reduction Time Period

The previous test used a reductive potential to more quickly remove the oxide and increase the force more rapidly. NaOH removes the oxide by itself, but applying a reductive potential speeds up the process. The previous test used a reductive potential application length of 100 ms, this length was chosen as it is roughly the same amount of time used for reduction in another LM muscle [12]. In order to see the effect of reductive potential application length on the performance of the LM muscle, another test was performed. This time, for each period, an oxidative potential was applied for the first half, and reductive potential applied for the second half. The frequencies tested were the same as previously. New 0.5 M NaOH was added to the muscle also. The resultant data is shown in Figure 4.24 and Figure 4.25.

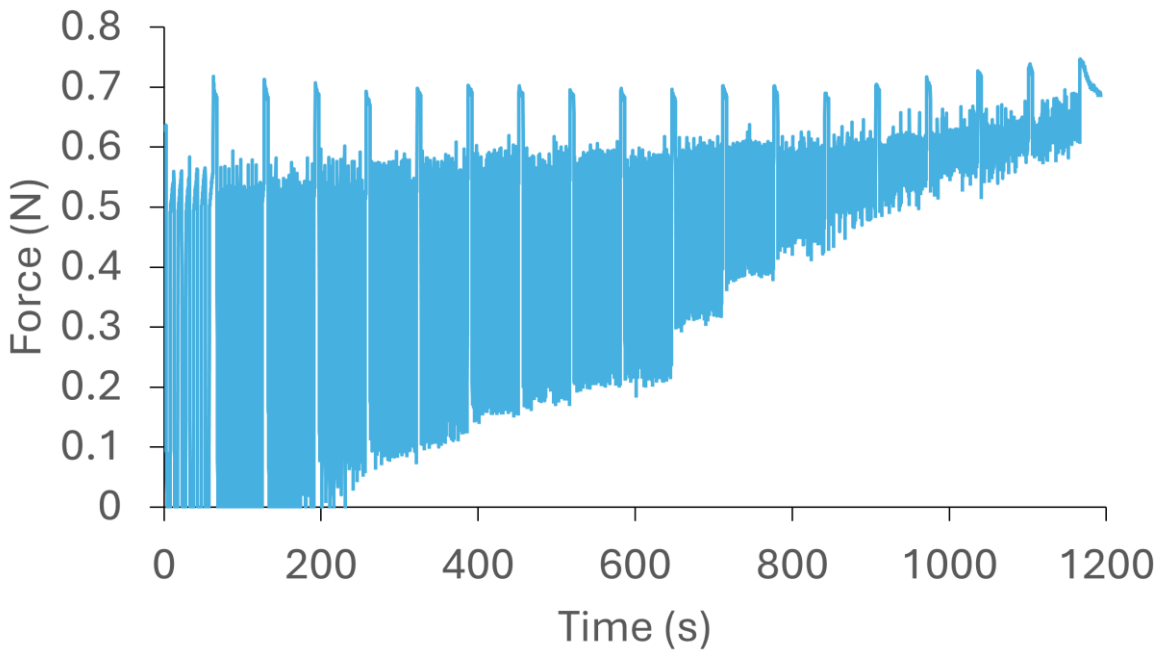

Figure 4.24 Force change with frequency for pillars with cross support CLMM with reductive potential applied for the second half of the period.

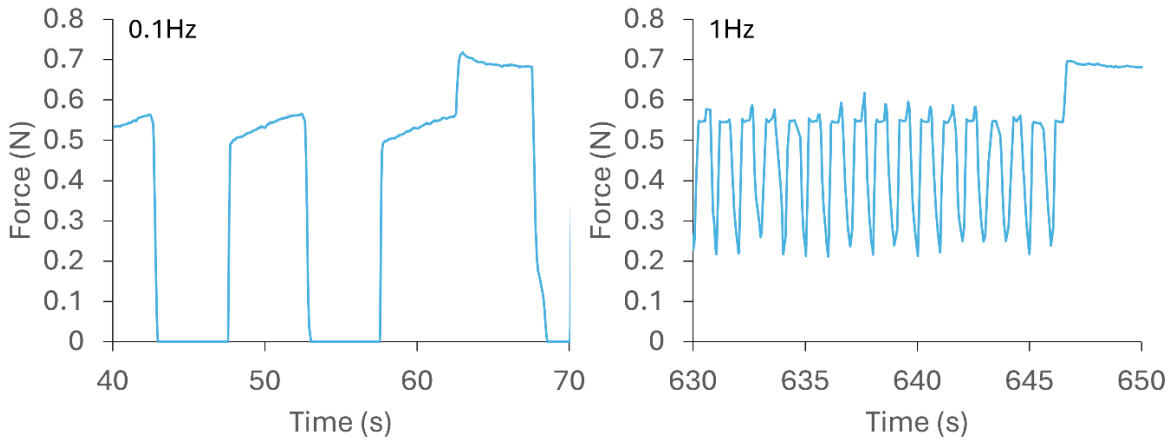

Figure 4.25 Zoomed in data for 0.1 Hz and 1 Hz.

The performance of the CLMM with extended reductive time length is significantly worse than that for 100 ms reduction. The overall force variation is lowered from 0.62 – 0 N for 100ms reduction to (0.5-0.56N sloping) – 0N for extended reductive potential applied. The measured force is also seen to increase sharply between frequency cycle blocks when the supplied voltage is turned off. There are also some sharp peaks in the 1 Hz data when the applied voltage to the LM is switching between negative and positive.

This lowered force and spiking force when the voltage is turned off is because of the electrocapillary effect of LM. Electrocapillarity is caused by the capacitance of the electrical double layer (EDL) that forms between the LM and the electrolyte [16]. The capacitive energy caused by the EDL lowers the effective interfacial energy of LM according to Lippman's equation

$$\gamma(V) = \gamma_0 - \frac{1}{2}C(V - V_0)^2 \tag{4.13}$$

where V_0 is the potential of zero charge, C is the capacitance of the EDL and γ_0 is the interfacial tension at the potential of zero charge [17].

The applied negative (reductive) voltage therefore lowers the interfacial tension of the LM, which results in a smaller measured force. When the applied negative voltage is turned off, the interfacial tension increases and so does the force.

4.4.2 Testing with No Reductive Potential Applied After Oxidation

Some reductive potential needed to be applied to the muscle after oxidation for it to work effectively. The NaOH electrolyte removes oxide by itself, however it cannot do that quickly enough for the muscle to work reliably. A test with no reductive potential applied, with frequencies from 0.1 – 1Hz in increments of 0.1 Hz is shown in Figure 4.26.

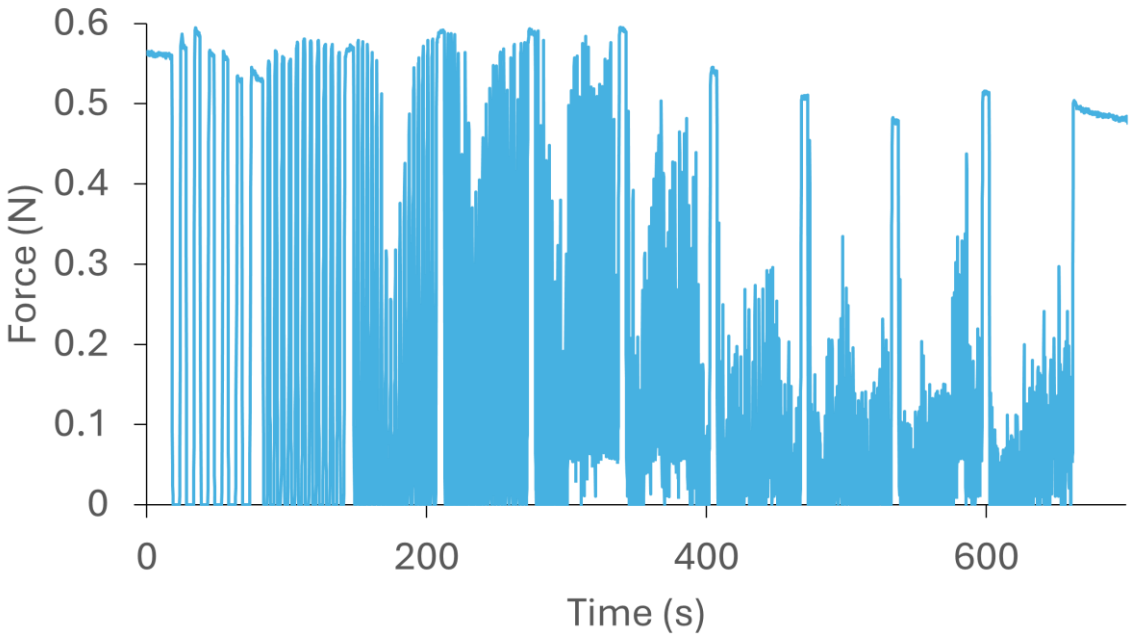

Figure 4.26 Measured force change for various frequencies for the pillars with cross support CLMM with no reductive potential applied after oxidation.

Force variation with no reductive potential applied is significantly less reliable, with frequencies of 0.7Hz-1Hz cycling below 0.3N due to oxide not being fully removed. The force

is seen to spike between frequency cycles as the NaOH has enough time to remove the oxide before the next frequency cycle begins.

4.4.3 Repeated Testing

For use in real world applications, an actuator must be capable of over hundreds of thousands of cycles without failure. Therefore, repeatability testing of the muscle until failure is important to see how many cycles it can do. The pillars with cross-support CLMM muscle was put in the MTS machine and was tested at an applied frequency of 0.5 Hz, with 100 ms reductive potential applied after oxidation. 0.5 M NaOH was used. The resulting data is shown in Figure 4.27 and Figure 4.28.

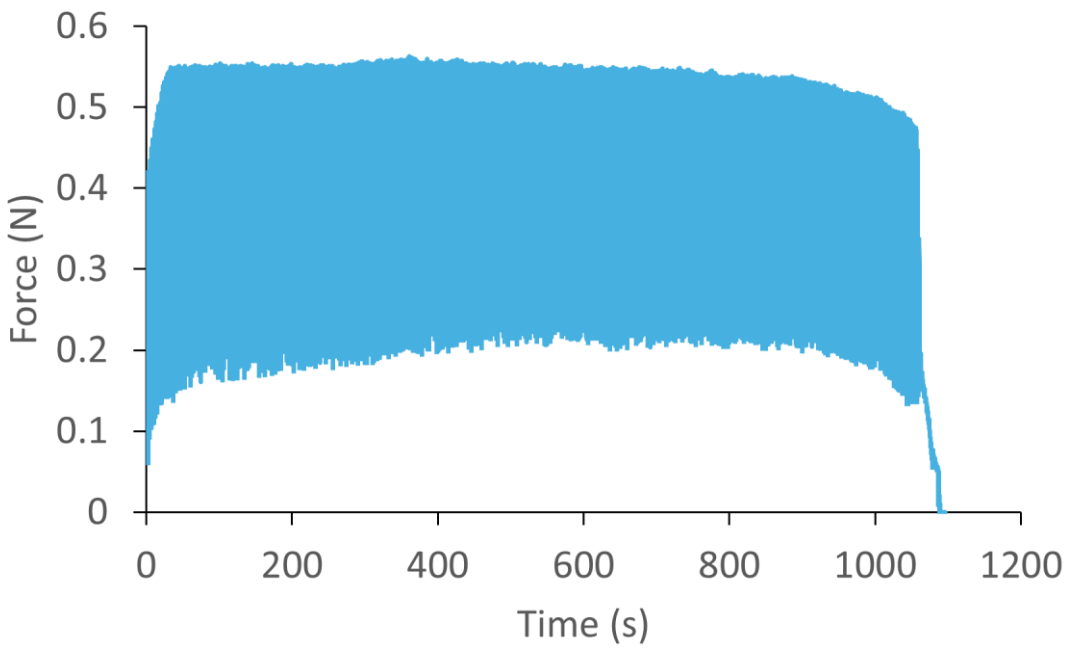

Figure 4.27 Repeated testing of pillar design with cross support CLMM until failure.

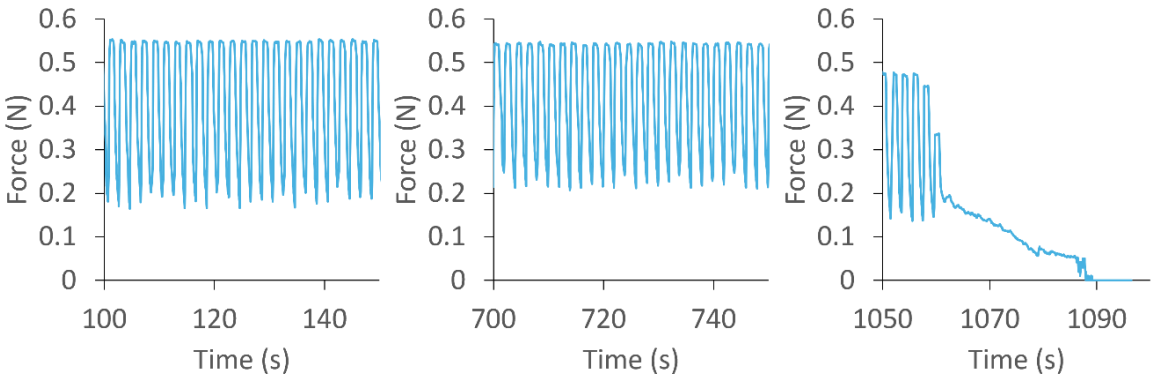

Figure 4.28 Zoomed in sections of repeated testing data.

The CLMM was able to change force repeatedly at 0.5 Hz for ~1060 s, or ~530 cycles. After 1060 s, it quickly deteriorated to 0 N, with no force change, and the test was stopped. Interestingly, the LM muscle can be made to work again by mixing the LM and electrolyte, then putting it back in the MTS for testing (Figure 4.29). No new LM or electrolyte was added to the muscle for the second test.

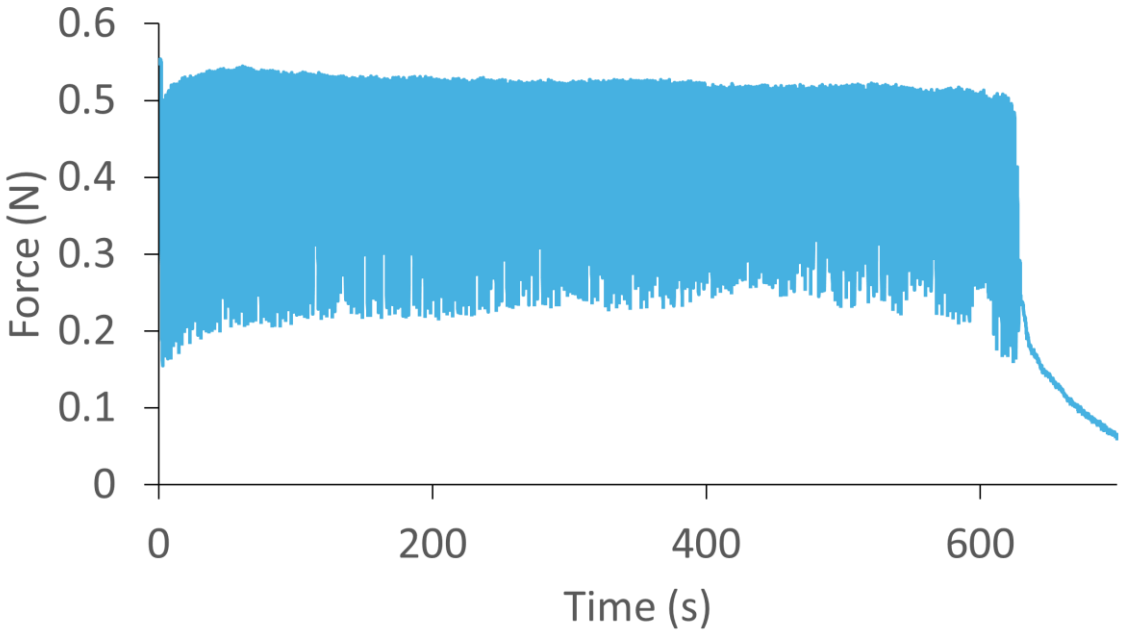

Figure 4.29 0.5Hz force variation of pillars with cross support CLMM after mixing.

The post-mixing test failed after ~600 s, which is over half the pre-mixing test. Overall force change characteristics were similar for the pre-and post-mixing tests. The post mixing test had a typical minimum force of ~0.23 N, whereas for pre-mixing typical minimum was ~0.2 N. Overall, this shows that the number of the cycles of the CLMM can be extended from its original failure point. Mixing may help by breaking up the surface of the LM and mixing it back in with the bulk. As Ga is used up in the reduction electrochemical reaction [15],

$$Ga_2O_3 + 2OH^- \rightarrow 2GaO_2^- + H_2O \tag{4.14}$$

over the course of many cycles, LM may form a surface layer with a higher wt% of In than at the eutectic point, which would then cause it to be less fluid at the surface. Mixing would equalise the concentration of Ga throughout the droplet and restore its ability to actuate effectively.

Previous liquid metal droplet-based muscles have shown thousands of cycles with no degradation [10, 11], so the decrease in force is not caused by the liquid metal itself. One potential option to extend the lifetime of the CLMM without manual mixing would be to add a small corkscrew-shaped element below the slits which would mix the LM when the slits move up and down.

4.4.4 Force control of the Pillars with Cross Support CLMM Using Voltage Change and Pulse Width Modulation

Being able to control the force exerted by the CLMM is very important for it to be useful. Stacking two muscles together meant force could be controlled in two steps, however, this

required two layers of muscle which increased the height and complexity. It would be better to be able to control the force output of each muscle.

The first test for force control of the CLMM involved changing the voltage applied to the LM. Lower applied voltage should lower the force as the oxide layer would not be formed as quickly. As the NaOH electrolyte used constantly acts to remove the oxide, tuning the voltage applied to add oxide more slowly will control the overall force. A test was done using the pillar with cross support CLMM. Voltage was applied with a lab bench power supply, and applied voltage was recorded with a Fluke 8845A digital multimeter connected via USB to a computer using Flukeview forms software. 0.5 M NaOH was used as electrolyte. The results are shown in Figure 4.30.

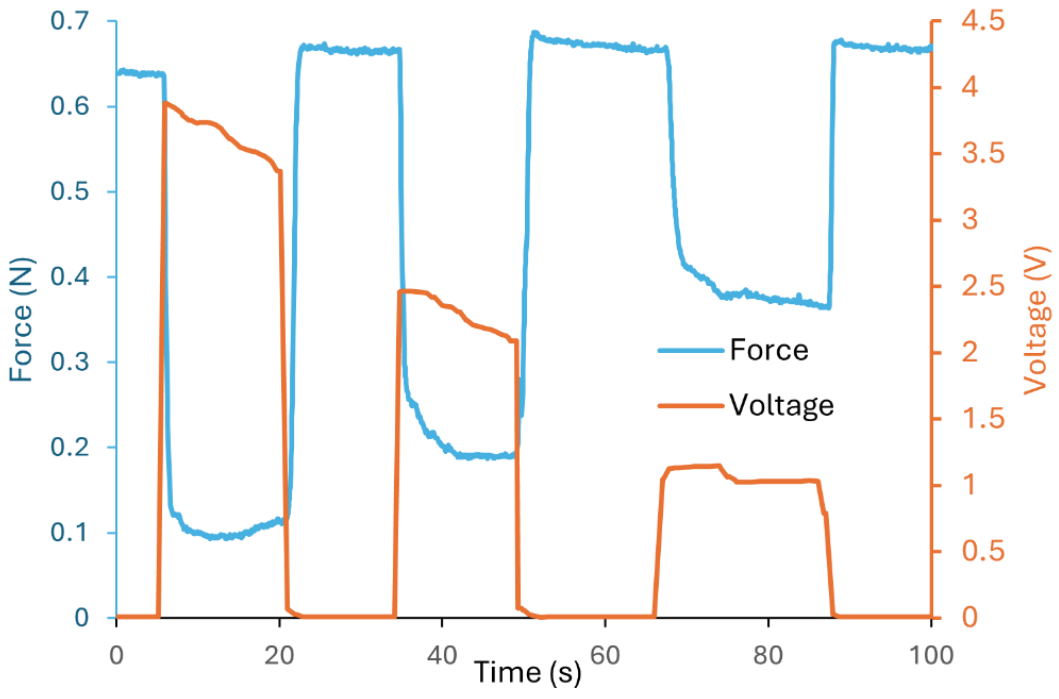

Figure 4.30 Control of force by changing the applied voltage.

Varying the voltage was found to have a controllable effect on the force of the LM muscle. Applying ~4 V oxidative to the LM resulted in the force dropping from 0.63 to 0.1N, whereas applying ~1 V oxidative resulted in a force of 0.4 N. This clearly showed that the force exerted by the LM muscle could be controlled dynamically. The force change when voltage was applied tended to drop quickly at first, then gradually reach an equilibrium point. Lowering the voltage after the initial application helps the force to stabilise faster.

Using pulse width modulation (PWM) duty cycle applied to the LM muscle can also control the output force. The motor controller used is able to apply multiple rapid voltage pulses every second, with a maximum switching frequency of 40kHz. The average voltage is then the result of the PWM duty cycle percent multiplied by the applied voltage per pulse. The Arduino was set to command the motor controller to apply PWM duty cycles of 100% - 0% in steps of 25%. This meant that the power supplied to CLMM varied between 0% to 100% in steps of 25%. The LM muscle tested was a pillar type muscle (no cross support). The results are shown in Figure 4.31.

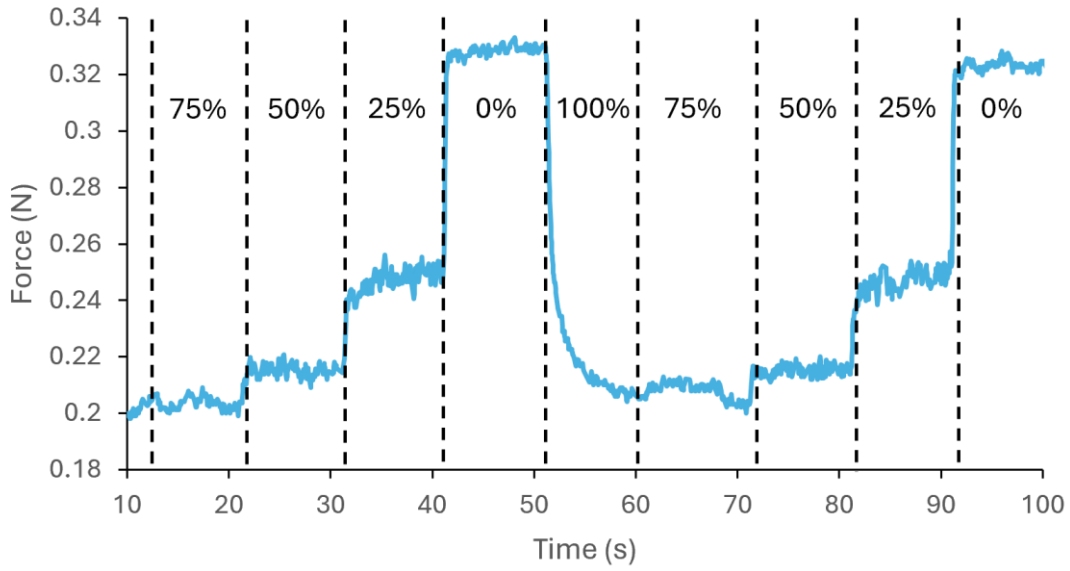

Figure 4.31 Control of force using duty cycle of PWM.

This method for force control was also successful, with the heights of the different duty cycles being different. The 25% duty cycle was furthest away from the other non-zero cycles, with 50% and 75% close together.

4.4.5 Electrolyte Testing

For testing so far, the only electrolyte used was 0.5 M NaOH. This continuously works to remove the oxide layer on the LM, which is useful for returning to a maximum force quickly. For a lot of applications, however, it would be better to lower the force of the muscle and keep it at a lower value without supplying any more power. Therefore, it was decided to try a different electrolyte to see if this could be achieved. Trisodium phosphate (Na_3PO_4) was chosen as an alternative electrolyte as it would work as a conductive liquid for the electrochemical reactions to occur, but also not remove the oxide continuously like NaOH. NaCl was not chosen to use as it would create chlorine gas during testing, which would quickly deteriorate the LM muscle.

The test was done using a pillar style (no cross supports) LM muscle with 0.5 mm gaps. 6 V was applied for 2 s and then turned off (no reducing potential applied). Data for 0.5 M Na_3PO_4 and 0.5 M NaOH are superimposed together in Figure 4.32.

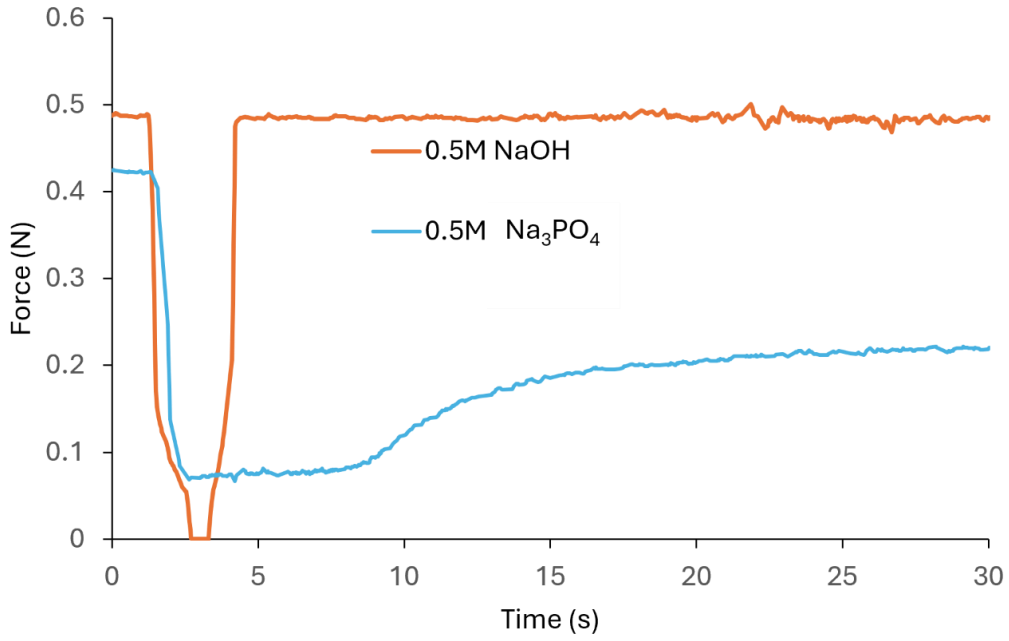

Figure 4.32 Force variation of CLMM for Na_3PO_4 and NaOH.

In the case of NaOH, it immediately starts to increase in force after the voltage is removed. For Na_3PO_4, it remains at a lowered force, only slightly increasing with time, from 0.07 N at 2.7 s to 0.09 N at 9 s. After this, its force increases slightly faster before levelling off again at 0.22 N, below its starting point of 4.2 N. Overall force change is lower for Na_3PO_4 however, only achieving a maximum of 0.42 N and a minimum of 0.07 N, compared to 0.49 – 0 N for NaOH in the same test.

To further test the use of Na_3PO_4 as an electrolyte, it was tested with a reductive potential applied to increase the LM force back to maximum. For testing, a 1 s oxidative voltage was applied, then for 9 s the power was turned off, then a 1s reductive potential was applied to the

LM, and then it was turned off for 9 s. This was then repeated. The results are shown in Figure 4.33.

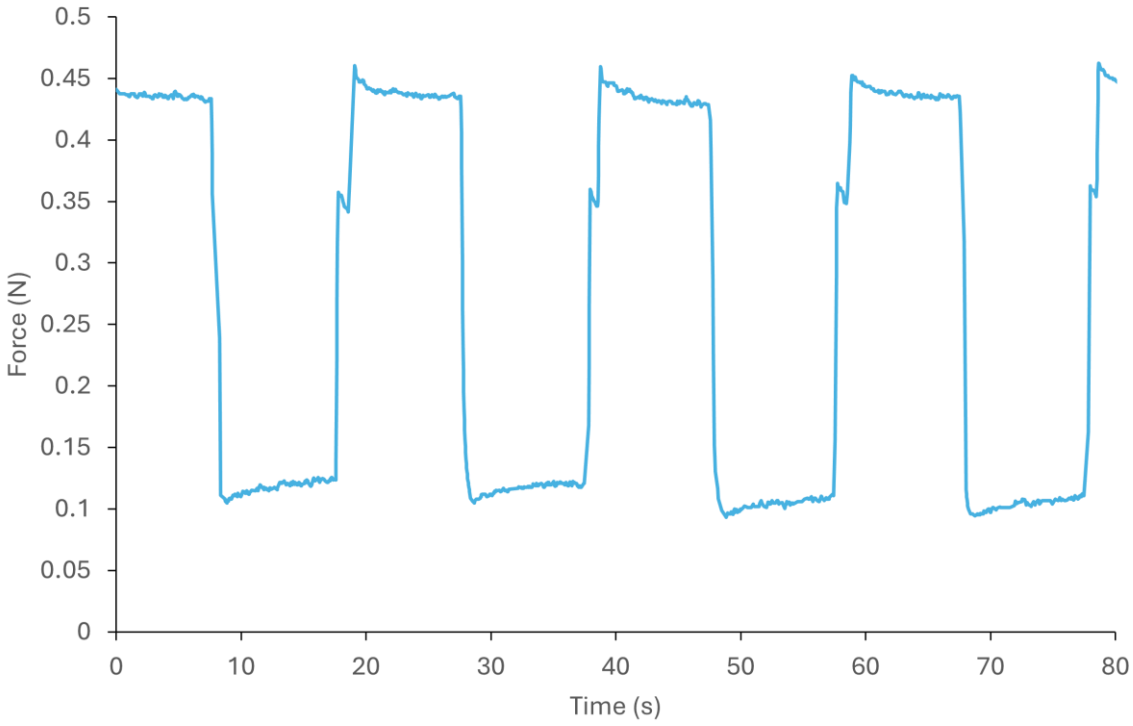

Figure 4.33 Force change of the CLMM using Na_3PO_4 as electrolyte with reductive potential applied to return force back to maximum.

The overall force change shape is similar to using NaOH as the electrolyte, however, no voltage needs to be applied to keep the force at the lowered value. The force rises by ~0.02 N while the power is turned off at the lowered force value. Applying a reductive potential causes the force to rise quickly as the oxide is removed. There is a notch shape in the rising force line caused by the electrocapillary effect of LM. Optimising the length of time a reductive potential is applied would remove the notch shape and make the force reach the maximum value more quickly. Overall, these tests show that Na_3PO_4 is a potentially valid electrolyte for use in the LM muscle for certain low power applications.

4.4.6 Force Change with Time For Different NaOH Concentrations

Optimising the concentration of NaOH for maximum speed of force change was also done. The same CLMM (pillars with cross support style) was loaded with LM and a certain concentration of NaOH for testing. After testing, it was washed with deionised water, dried, and then reloaded with the next concentration. Testing was done at 0.5 Hz with 100 ms reductive potential.

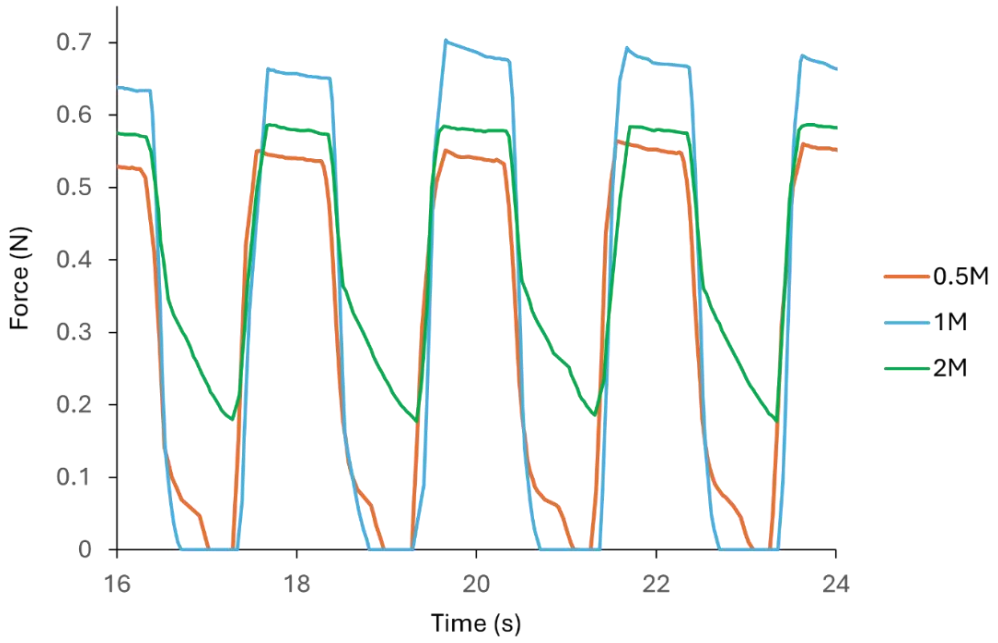

Figure 4.34 Force change versus time for the CLMM with different NaOH concentrations.

From Figure 4.34, 1M NaOH performed the best, with a higher maximum force of ~0.68N, and was quickest to reach 0 N. 0.5M NaOH was the next best performing, with the lowest measured maximum force of ~0.54 N, but its force variation was much higher than that for 2 M. 2 M NaOH performed the worst, with a max force (~0.58 N) in the middle of the other two concentrations, however, its minimum force achieved was only ~0.18 N. As NaOH continuously removes the oxide layer from LM, 2 M NaOH removes it too quickly for the force

variation to be maximised. After this experiment, it was decided to use 1 M NaOH for testing as this achieved the best performance.

4.4.7 Problems with Pillars with Cross Support Design

The LM muscle design of pillars with cross supports worked well for the most part, achieving variable and controllable force change. However, the cross supports introduced a problem of small droplets of LM breaking off and getting stuck behind the cross supports (Figure 4.35). The cross supports also reduced the percentage stroke as they were an additional wall where LM could not flow into. Therefore, a final iteration of the design was conceived – using slits as the channels for LM to travel into.

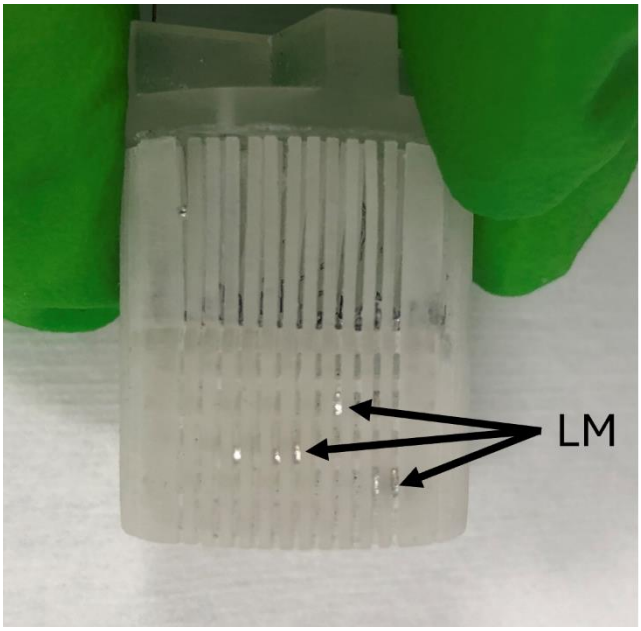

Figure 4.35 LM stuck behind pillar cross-supports.

4.5 Slit CLMM Design

Channels shaped as rectangular slits solved the problems of the previous designs. The cross support between rectangular channel walls means that the structure is strong and does not bend, which would lower its force output. The rectangular channels mean that there can also be a higher percentage stroke of the muscle as there is a greater volume for LM to flow into in comparison to circular capillaries. Also, there are no structures within the channels for LM to get stuck behind. An exploded diagram of the slit design CLMM is shown in Figure 4.36.

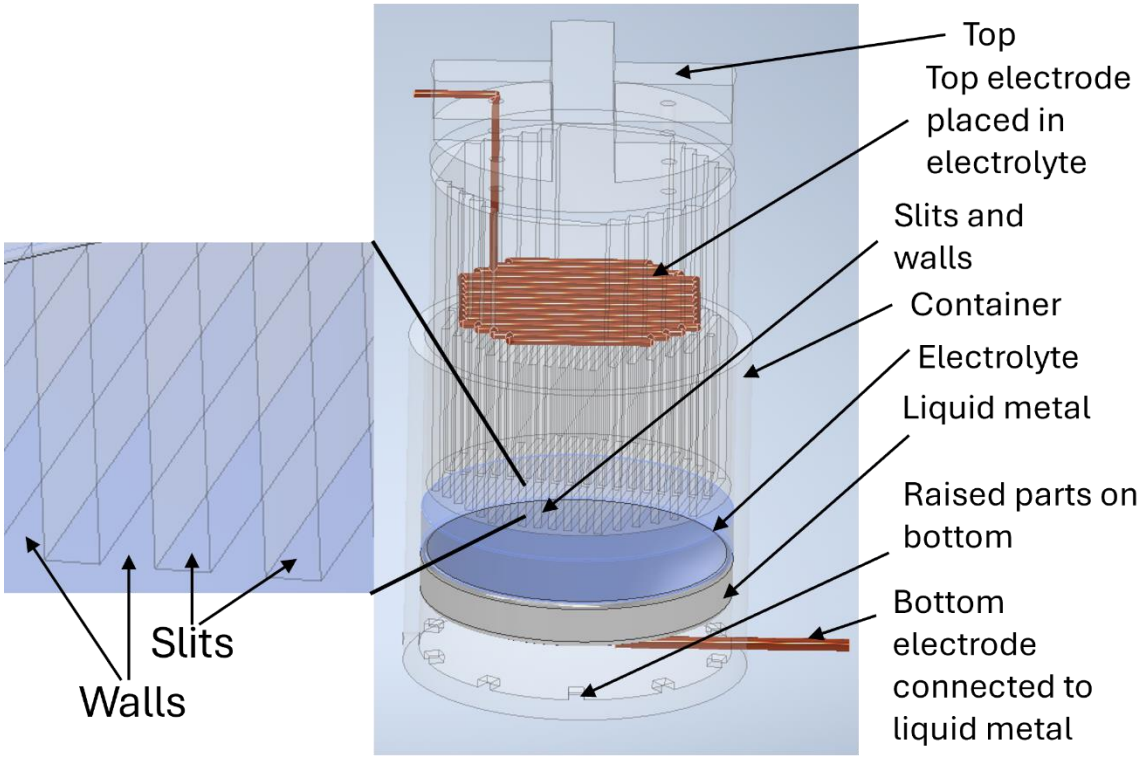

Figure 4.36 Exploded diagram of slit design CLMM

4.5.1 Making the Slit CLMM Design

The slit CLMM were made in a similar way to the previous pillar CLMM. An SLA printer (Formlabs Form 3) printed clear resin with a printing layer thickness of 25 microns. The walls of the muscle were 0.5 mm thick. The overall diameter of the muscle was 19.5 mm, this was 0.5 mm less than the inner diameter of the container so the muscle could move freely. The gap around the sides between the LM muscle and the container walls had to be lower than the slit width, otherwise, LM would preferentially be pushed around the sides of the muscle rather than within the slits. After printing, the slit design was washed for ~30 mins in the Formlabs IPA bath. The time to wash out the resin was lower for the slit design in comparison to the pillar with cross support design as liquid could flow more easily through the slits, so the resin was washed out quicker. The LM muscle was then post-cured as for the previous designs. A needle-hole type design was also implemented to thread copper wire through the top electrode (see Figure 4.37). This was then glued on top of the slit part of the muscle.

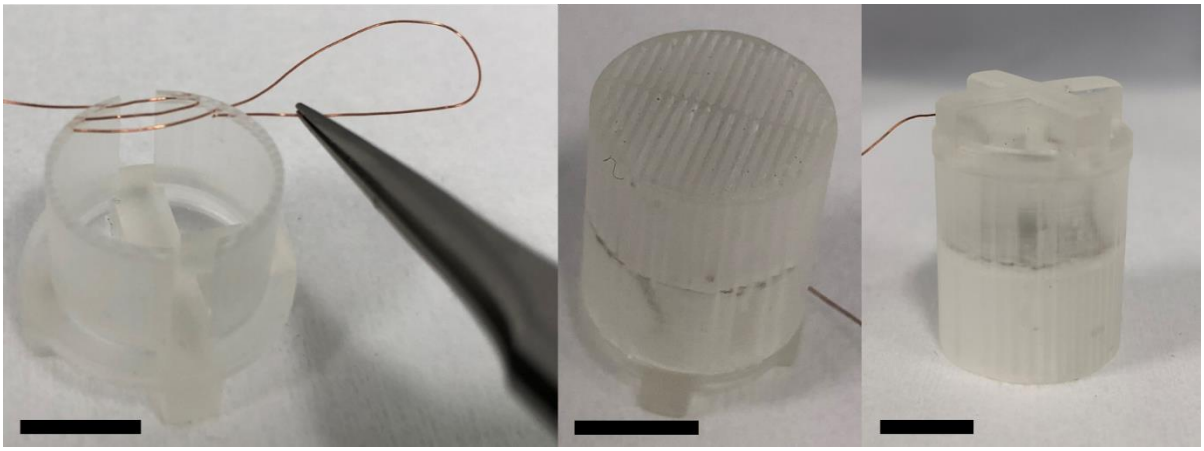

Figure 4.37 Making the slit CLMM.
Scale bars are 10 mm.

The walls between each of the slits were set to 0.5 mm thick on the CAD file as this was Formlabs' minimum recommended thickness for vertical walls. Thinner walls between the slits would increase the stroke of the CLMM as there would be less solid material and more channel space for LM and electrolyte to fill. Stroke would approach 33% of the maximum height of CLMM for infinitesimally thin walls.

The size of the slits and walls were also checked using the microscope (see Figure 4.38 and Figure 4.39). The measured wall thickness was consistently between 35-90 microns thicker than set on the CAD file. This in turn reduced the width of the slits slightly. For example, for 1 mm width slits, the wall thicknesses measured were 538 and 554 microns (it was set to 500 microns on the CAD print file). This, in turn, reduced the slit width to 966 microns (from the 1000 microns on the print file). For the 0.7 mm slit width print, the wall thicknesses were 584 and 570 microns, and the slit width measured was 625-652 microns. This increased wall thickness may be due to swelling of the resin during washing in the IPA bath [18]. However, the muscle also needs to be washed properly to remove any uncured resin from within the slits.

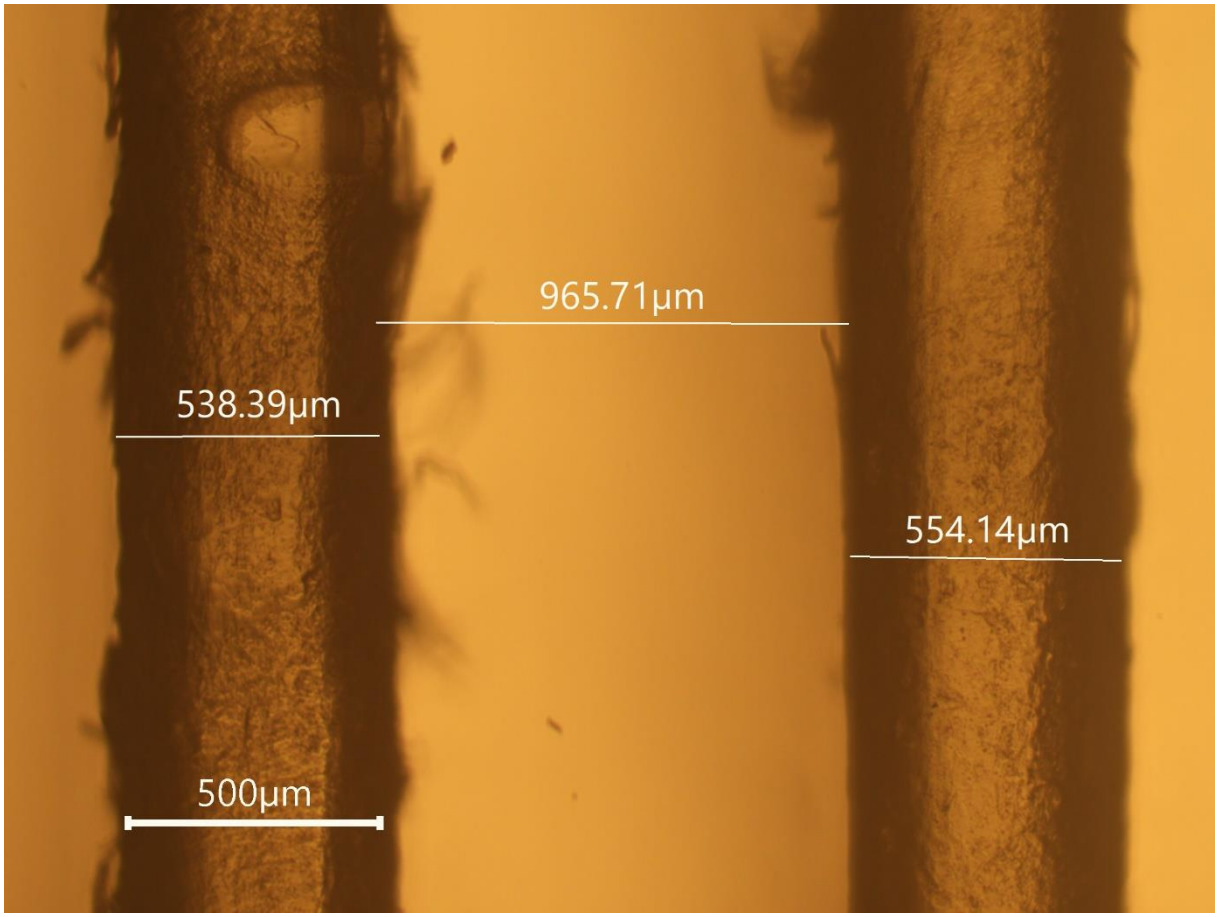

Figure 4.38 Microscope image of 1mm width slits.

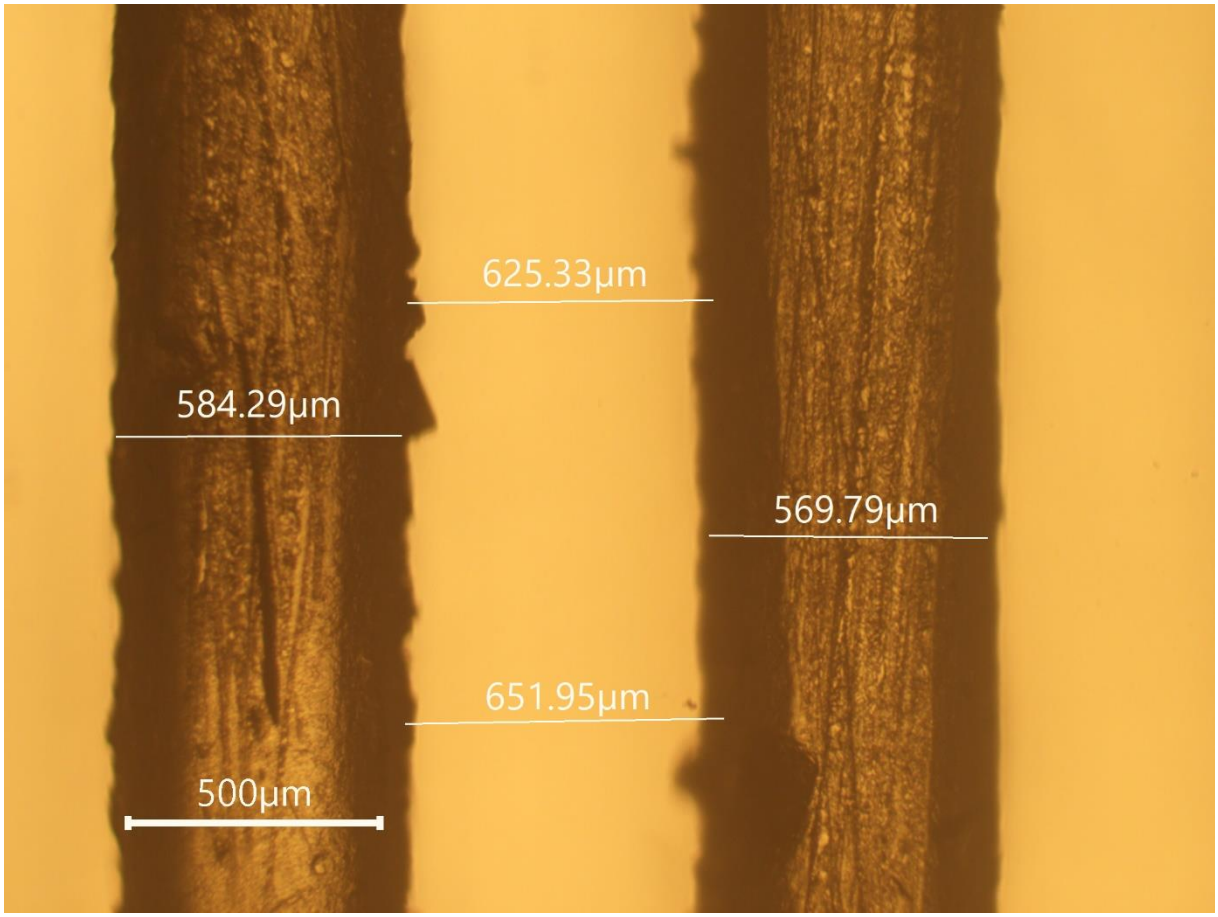

Figure 4.39 Microscope image of 0.7 mm width slits.

4.5.2 Calculating Force Using Change in Interfacial Energy for the Slit CLMM

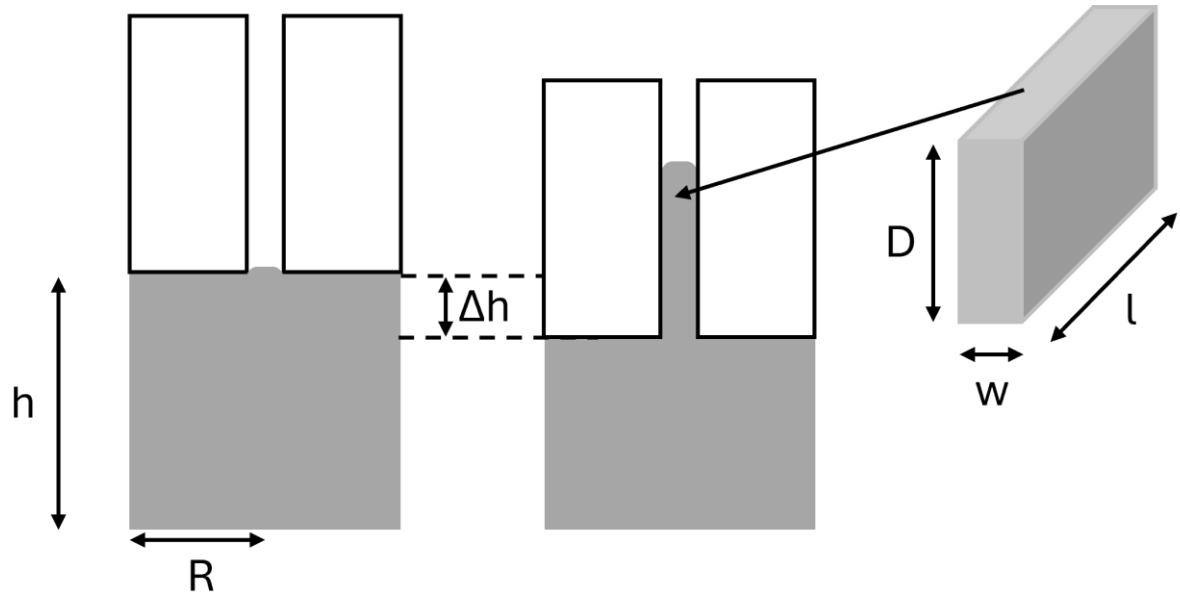

Figure 4.40 Theory diagram for slit CLMM

For a cylindrical muscle, with overall diameter *R* and height of liquid metal h (Figure 4.40), it will have a volume, *V* of LM of

$$V = \pi R^2 h \tag{4.15}$$

The surface area in this initial state is

$$SA_1 = 2\pi R^2 + 2\pi Rh \tag{4.16}$$

If pushed down by distance Δh , it will move into a rectangular channel with cross sectional width *w* and length *l*. The distance it will move into this channel is distance *D*. Overall volume must be unchanged, so

$$V = \pi R^2(h - \Delta h) + Dwl = \pi R^2 h \tag{4.17}$$

Rearranging and multiplying out the brackets gives

$$Dwl = \pi R^2 h - \pi R^2 h + \pi R^2 \Delta h \tag{4.18}$$

Therefore,

$$D = \frac{\pi R^2}{lw} \Delta h \tag{4.19}$$

Surface area is changed in the second state, and is given by

$$SA_2 = 2\pi R^2 + 2\pi R(h - \Delta h) + 2D(l + w) \tag{4.20}$$

Change in surface area is

$$\begin{aligned} \Delta SA = SA_2 - SA_1 &= \left(2\pi R^2 + 2\pi R(h - \Delta h) + 2D(l + w)\right) - (2\pi R^2 + 2\pi Rh) \\ &= 2D(l + w) - 2\pi R \Delta h \end{aligned} \tag{4.21}$$

Substituting in for *D* gives

$$\Delta SA = 2(l + w)\frac{\pi R^2}{lw} \Delta h - 2\pi R \Delta h = 2\pi R \left(\frac{R(l + w)}{lw} - 1\right) \Delta h \tag{4.22}$$

Therefore

$$\frac{\Delta SA}{\Delta h} = 2\pi R \left(\frac{R(l + w)}{lw} - 1\right) = \frac{2\pi R^2 l}{lw} + \frac{2\pi R^2 w}{lw} - 2\pi R = \frac{2\pi R^2}{w} + \frac{2\pi R^2}{l} - 2\pi R \tag{4.23}$$

For rectangular slits, $w \ll l$, so the $\frac{2\pi R^2}{l}$ term can be neglected, therefore

$$\frac{\Delta SA}{\Delta h} \approx \frac{2\pi R^2}{w} - 2\pi R = 2\pi R \left(\frac{R}{w} - 1\right) \tag{4.24}$$

The change in interfacial energy is the interfacial tension, γ multiplied by the change in surface area

$$\Delta E = \gamma \Delta SA \tag{4.25}$$

Assuming Δh is infinitely small, the change in force, *F*, is calculated by

$$\mathrm{F} = \frac{dE}{dh} = 2\pi\gamma R\left(\frac{R}{w} - 1\right) \tag{4.26}$$

Note that this is an identical equation as that for circular capillary channels, except with *w* replacing *r* (radius of the capillaries). As for the case of circular capillaries, the overall force is constant and is independent of the number of slits.

4.5.3 Improvements to Experimental Setup for Testing

For all previous force tests, the MTS had been used to record the force change with time. However, the maximum frequency of force measurement from the MTS is 30 Hz. For measuring force change of the LM muscle with a frequency of 5 Hz for example, the MTS would only record 6 data points. At higher frequencies, its performance would be even worse. Therefore, a different force sensor was chosen to be used (HX711 force sensor), which has a data acquisition rate of 80 Hz. The sensor was first calibrated. Calibration was achieved by zeroing the sensor reading with no weight placed upon it, then placing a known weight on the sensor. The sensor sent the Arduino a number which increased linearly based on the weight. A conversion factor to change the initial reading to the actual weight was added to the Arduino code, and a second known weight was placed on the sensor to test the measurement was correct. The MTS was still used to compress the LM muscle onto the new force sensor as the MTS offered a solid platform which could be raised or lowered easily. Force measurements during

testing were sent directly to the Arduino Due (which also controlled the muscle), and data was recorded using Putty serial monitor software. The difference between force measurements at 5Hz using the MTS and the new force sensor is shown in Figure 4.41.

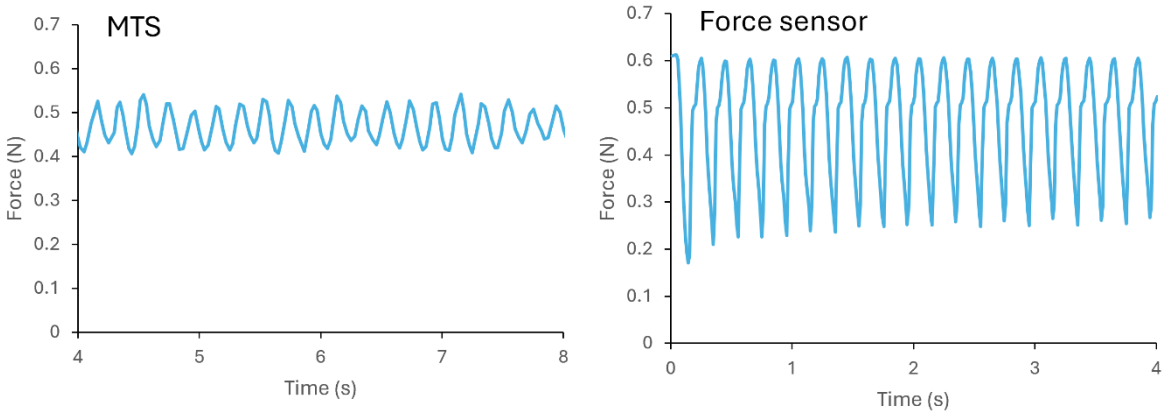

Figure 4.41 Measured force variation at 5 Hz using the MTS and the new force sensor.

Before each test, the force sensor reading was zeroed with the LM muscle in a fully oxidised position (see Figure 4.42). This was because when the Arduino program was started, the force sensor would measure 0 N for its first measurement (like turning on a scale with a weight already on it). Making the LM fully oxidised (so the force exerted by the LM muscle was 0 N) and then zeroing the scale, ensured the force sensor was making the correct reading.

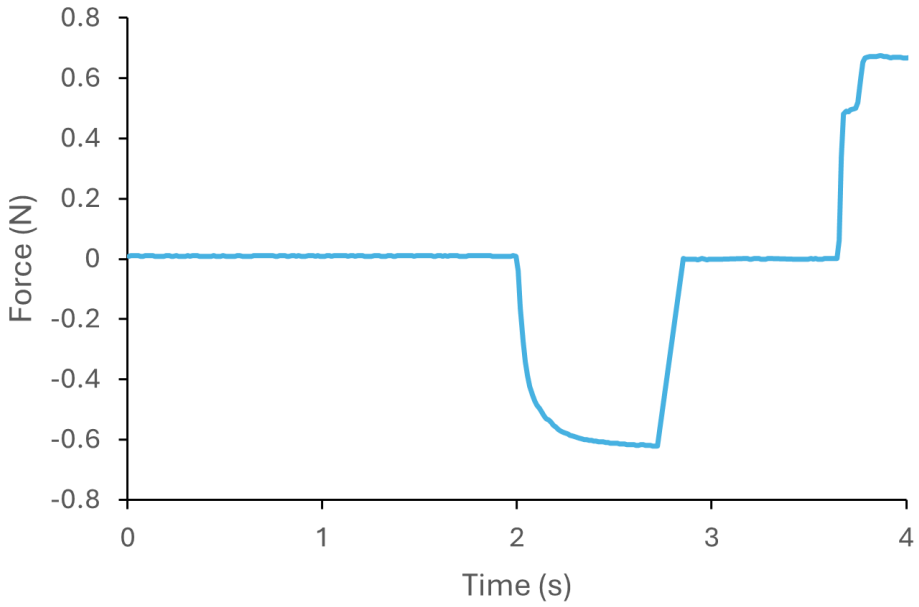

Figure 4.42 Resetting the force sensor reading.

Voltage and current sensing capabilities were also added to the experimental setup. Power sent to the LM muscle came from a motor controller (Deek-Robot motor shield) which was controlled by the Arduino. In order to measure and record the voltage sent from the motor controller, two voltage dividers were made, one for each polarity of the motor controller output. Each voltage divider stepped down the measured voltage to ~1/5 its initial value, and was made with 25.1 kOhm and 5.1 kOhm resistors. The voltage from each was then measured by the Arduino, at a resolution of 12 bits. As the Arduino Due has a maximum voltage of 3.3V, the step between each voltage reading is ~0.8 mV. The current was measured by adding a shunt resistor (0.083Ohm) in series with the LM muscle. The voltage across this was amplified (INA240A1PWR amplifier) and measured by the Arduino. Every ~1 ms, measured voltage values were sent as text to a computer and recorded (along with the force data at a rate of 80 Hz) using Putty serial interface.

4.5.4 Measurement of Force Change for Slit CLMM

The first measurements done for the slit CLMM were for blocked force change with frequency for a 0.5 mm slit width muscle. The frequencies tested were from 0.1-10 Hz. For 0.1-1 Hz, measurements were in increments of 0.1 Hz. From 1-5 Hz, the increments were 0.5 Hz, and between 5-10 Hz, the increments were 1 Hz. The applied reductive potential after oxidation was 100 ms for frequencies of 2 Hz and below. For frequencies greater than 2 Hz, reductive potential was applied for a quarter of the period. Force was measured using the HX711 sensor, and voltage and current were measured using the Arduino Due with the previously described circuit. Supplied power to the motor controller was set to a max of 17.5 V and 1 A from a lab bench power supply. Data is shown in Figure 4.43.

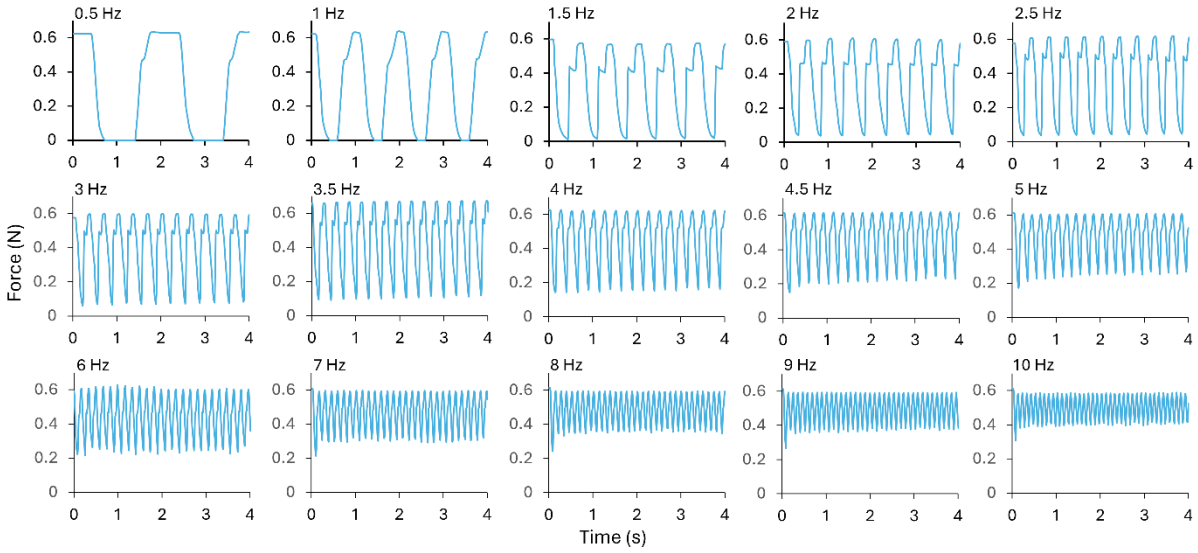

Figure 4.43 Force change with time for various frequencies for the 0.5 mm slit width CLMM.

Force change for a 0.5 mm slit width muscle is ~0.62 N at up to 1 Hz. From 1.5 Hz, the force change starts to decrease down to ~ 0.2 N at 10 Hz. The slight notch in the force increase line

is visible due to the continuous electrowetting effect, similar to in Figure 4.33. This can be eliminated by tuning the reduction time length so it is not too long.

The performance of the slit muscle is greatly improved over the pillars with cross support muscle, which had similar maximum force, but its force change decreased from the maximum at ~0.4 Hz see Fig. The force change with frequency for the slit LM muscle is shown in Figure 4.44, with error bars given by the standard deviation of the force change over 20 s (30 s for 0.1-0.9 Hz).

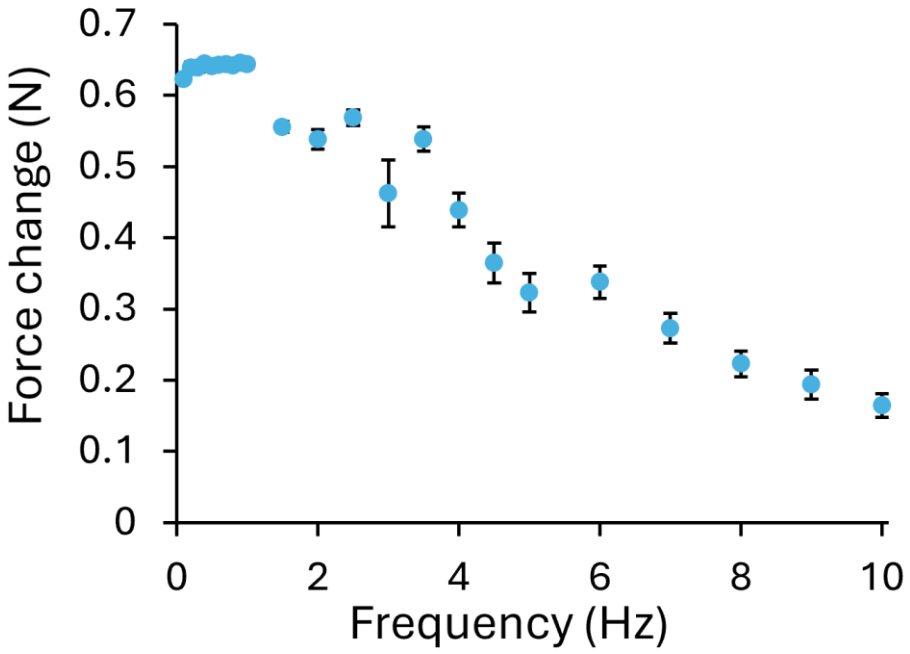

Figure 4.44 Force change for the 0.5 mm slit width CLMM with varying frequency. Error bars are given by the standard deviation of the measurements.

Force change tended to decrease slightly over the 20 s testing period for frequencies >1Hz. For example, for the case of 7 Hz, (Figure 4.45), force change decreased from ~0.29 N for the first few seconds, down to ~0.25 N towards the end of testing. This is thought to be because the resistance of the LM muscle increases slightly due to the gas bubble generation after

electrochemical reactions during actuation, so more power is required to achieve the same force change. Waiting a few seconds should restore the force change to its original state as the bubbles will have dissipated.

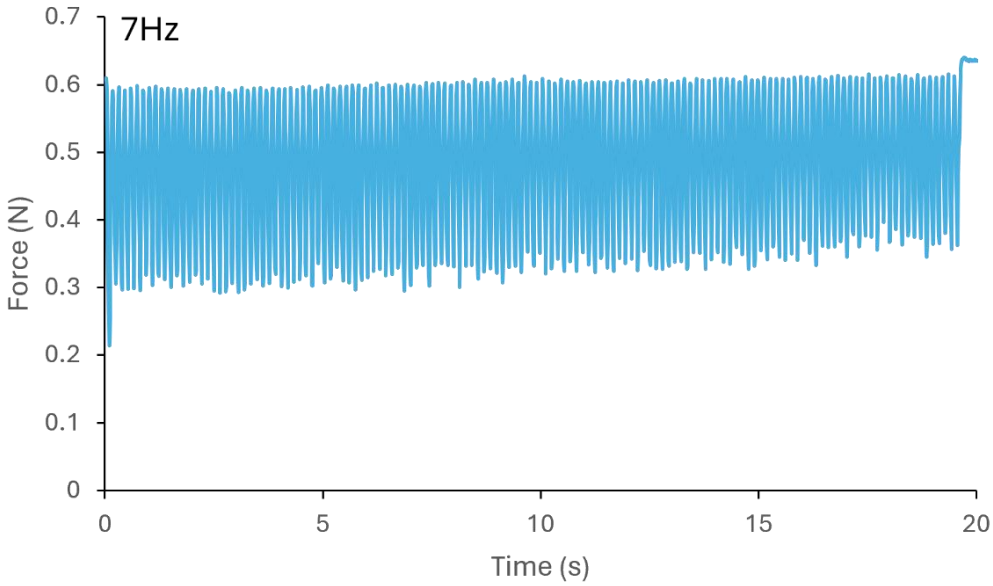

Figure 4.45 Measured force versus time for 0.5 mm slit width CLMM at 7 Hz.

For the higher frequencies measured (8-10 Hz), the data rate of the force sensor may affect the accuracy of the force measurements. The force data was measured by the HX711 sensor at a rate of 80 Hz- so for 10 Hz force variation, the sensor measured 8 points per cycle. This is comparable to the MTS sensor (30 Hz measurement) measuring 5 Hz force variation (so 6 data points per cycle), which had previously been shown (Figure 4.41) to be inaccurate. A higher data rate force sensor may therefore be required for accurate measurements for higher frequency actuation of the CLMM.

The force of the CLMM was also compared with that predicted by theory. Each thickness width of the slit was tested over 100 s at 0.5 Hz actuation (see Figure 4.46 and Figure 4.47).

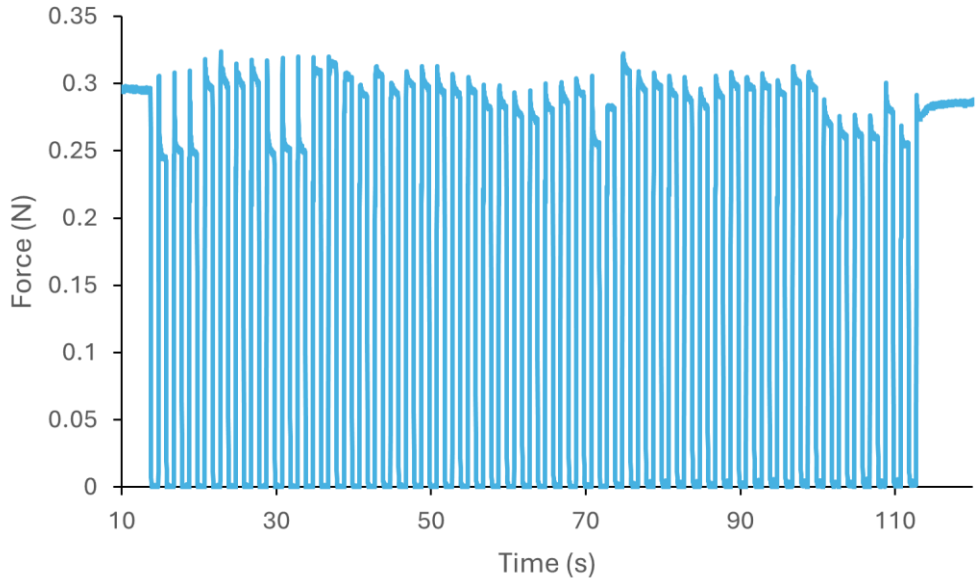

Figure 4.46 1 mm width slits CLMM force variation at 0.5 Hz.

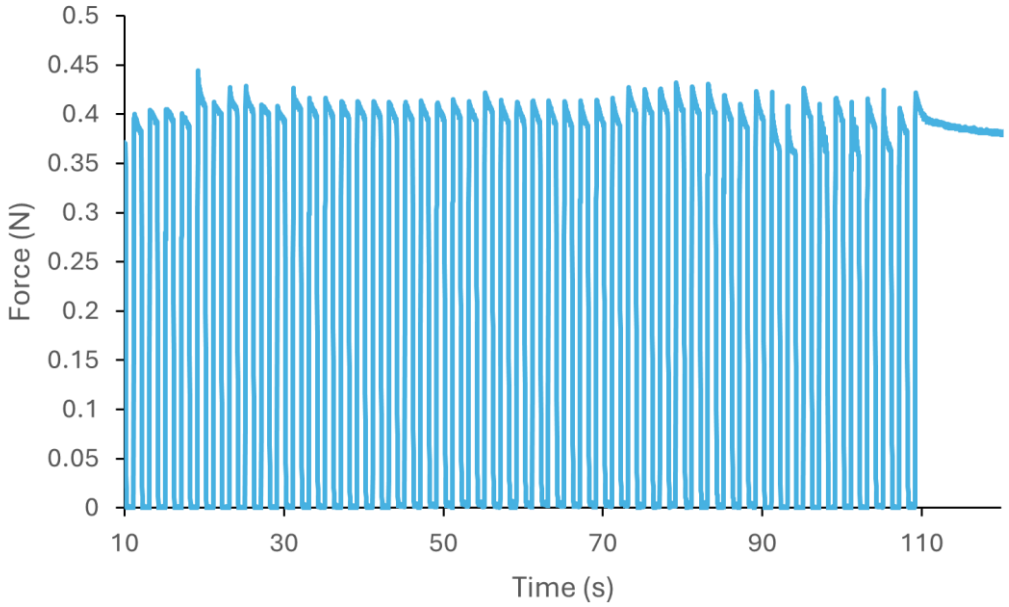

Figure 4.47 0.7mm width slits CLMM force variation at 0.5Hz

There are sharp peaks on some of the larger slit width curves. This is because the weight of the LM muscle top causes itself to move down during oxidation, and then during reduction, the top

quickly rises up and contacts the MTS top plate. Smaller width slits' top moves more slowly down during oxidation so does not move as quickly moving up during reduction and the peak is flatter.

The average force change was then plotted against that predicted by theory (Figure 4.48). Error is given by the standard deviation of the measurements. The measured values are in line with those expected by theory, with decreasing slit width leading to an increase in force.

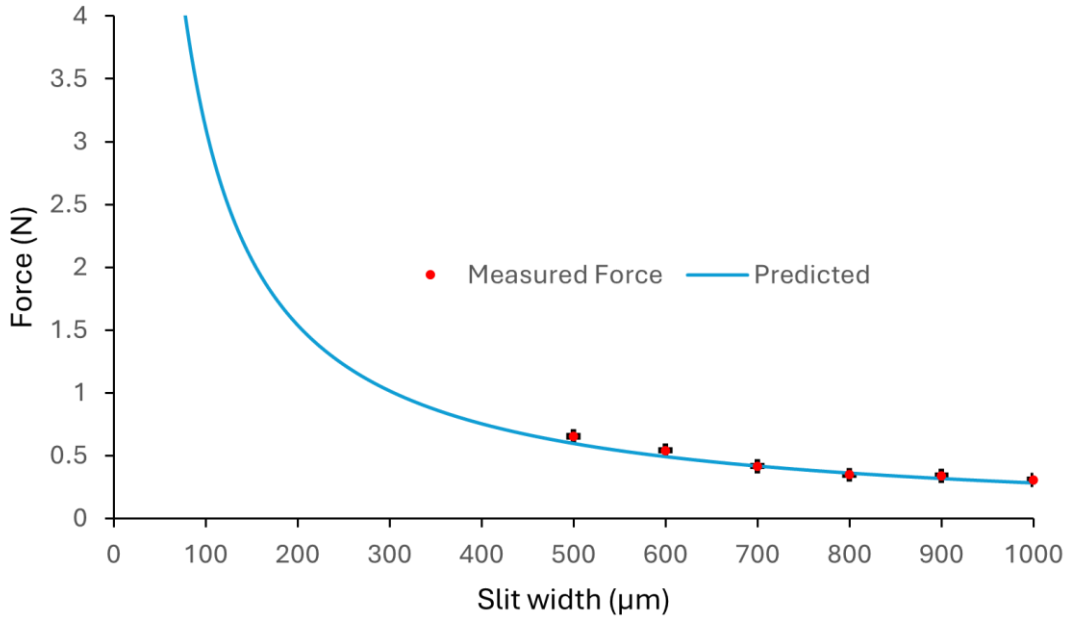

Figure 4.48 Measured force values with slit width variation plotted with the predicted force for 10 mm overall radius CLMM.

The reaction time for a 0.5 mm slit width LM muscle was measured using the voltage measurement in conjunction with the force sensor. Applying an oxidative voltage, and then measuring the time for force to decrease gives the reaction time. Likewise, the reaction time for when a reductive potential is applied can also be found (Figure 4.49).

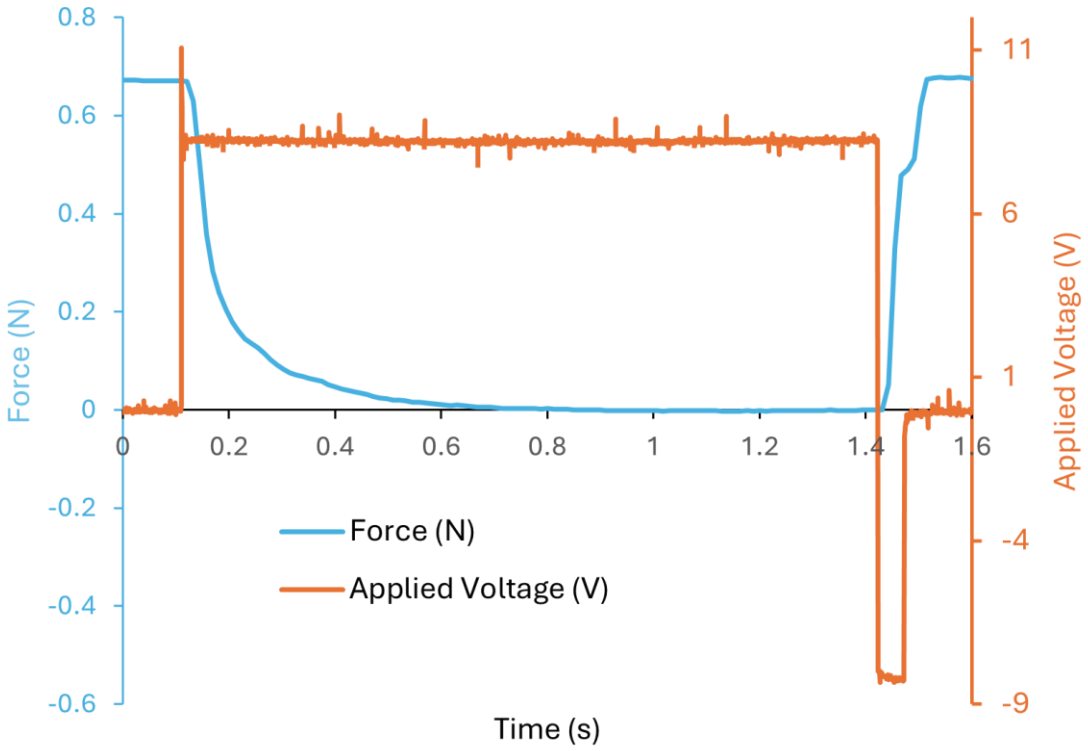

Figure 4.49 Reaction time of force change for CLMM.

It takes 0.62 s from when an oxidative potential is applied for the force to decrease to 0 N. The force change rate for reduction is much faster, reaching maximum force after 0.09 s. The reaction time for when force starts to change after the voltage is applied is shown in Figure 4.50 by zooming in on parts of the data.

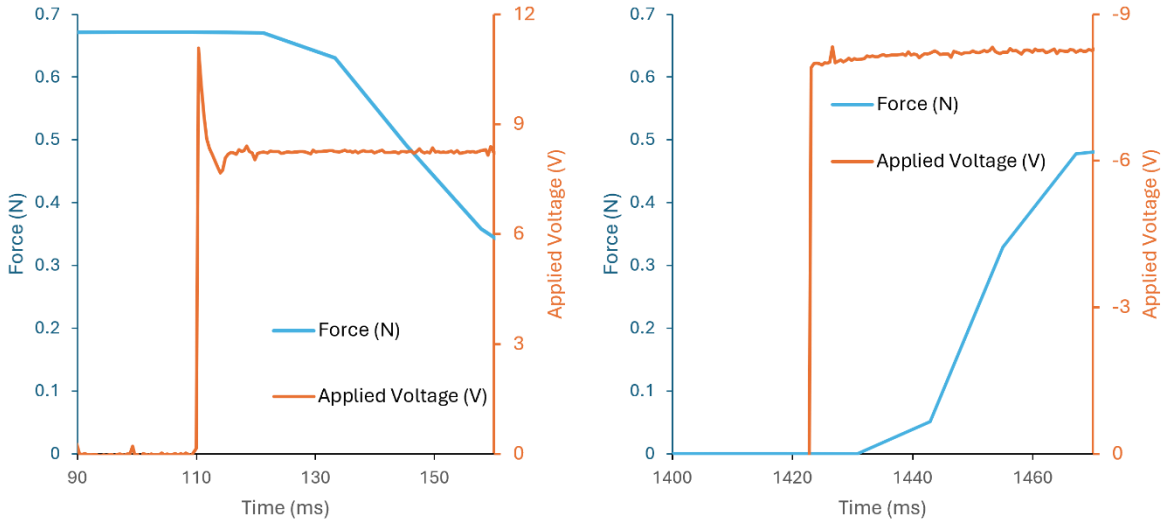

Figure 4.50 Zoomed in oxidative and reductive reaction times.
Note that applied voltage is flipped for the reductive graph to make it easier to see at what time it occurs.

From Figure 4.50, the reaction time for oxidation is ~23 ms. The oxidative voltage is applied at 110.4 ms, with a measured force of 0.671 N. The next measured force point is 121.2 ms, with a slightly lowered force of 0.670 N. After this, at 133.3 ms, the measured force dropped further to 0.630 N. The force sensor measures at a rate of 80 Hz, so the force value is recorded after every ~12.5 ms. This limits the accuracy of the reaction time measurement. For reductive reaction time, the reductive potential is applied at 1423.1 ms, force is shown to have increased to 0.051 N at 1442.9 ms, giving a reaction time of ~19.8 ms.

The force change rate for the muscle when no reductive potential was applied was also tested (Figure 4.51)

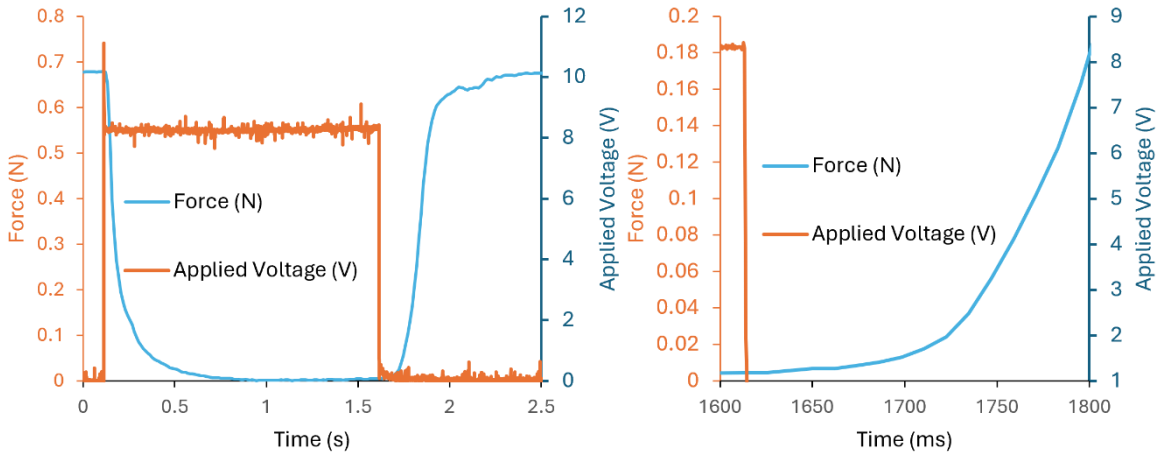

Figure 4.51 Reaction time for CLMM with no reductive potential applied.
Note the applied voltage on the right graph is shifted down by 1 V so force change is unobscured.

The time to reach maximum force from when the oxidative potential was turned off was measured to take 0.61 s, which is much longer than the case when the reductive potential was applied (0.09 s). This shows how effective the short burst of reductive potential is at improving force change rate as the oxide is removed more quickly, so the interfacial tension increases faster.

For the case of no reductive potential applied, the oxidative voltage was removed at 1614.5 ms, with a measured force of 0.005 N. At 1637.8 ms, force increased very slightly to 0.006 N, then at 1649.8 ms, it reached 0.007 N.

4.5.5 Feedback Force Control of CLMM

Previous tests (see Figure 4.30 and Figure 4.31) had shown it was possible to control the LM muscle force by changing the applied voltage, or by changing the PWM duty. However, the force could not be set to a specified level. Using the new force sensor, which was connected to

the Arduino, feedback control of the force could be achieved, enabling a chosen force level to be reached and maintained.

A proportional integral derivative (PID) controller was made using the Arduino, force sensor and motor controller. After an applied PWM signal came from the motor controller, the force change was measured by the force sensor and sent back to the Arduino. The PWM signal could then be changed based on the set force level to reach versus the current force measured, the rate of change of force, and the integral error of the force. The Arduino code enabled the PWM signal to be varied from 0-255, as well as flipping the voltage to reduce the LM. The PID controller kept the duty cycle around a certain level to maintain a specific force. The duty cycle was lowered to increase the force or vice versa. Applying a reductive potential was found to change the force too quickly to control.

A test of the force control was done using 0.5 mm width slit CLMM. Force levels to reach were 0.4, 0.3 and 0.2 N, going down then up in steps of 0.1N. The time for each step was 20 s. The resultant force control data is shown in Figure 4.52.

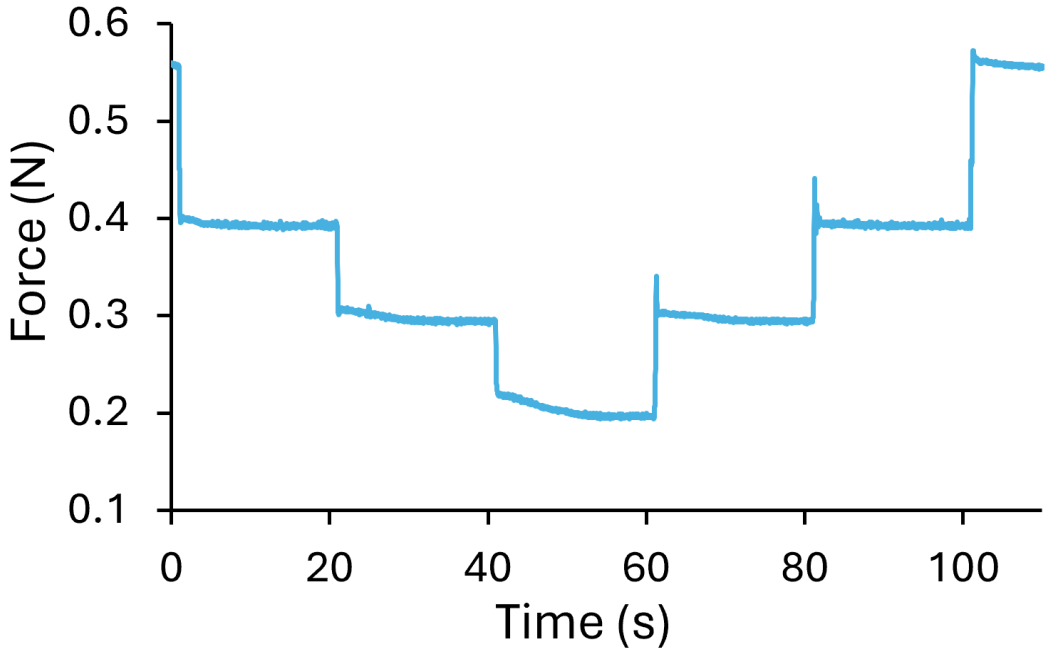

Figure 4.52 Force control of CLMM in steps of 0.1 N.

The force control results show a good level of control over the force, with each of the steps of force clearly visible. Downward steps have a higher degree of control than upward, as the upward steps tend to overshoot the desired level and then come back down. This is because for LM muscle it is faster to increase force than to decrease it. Better tuning of the PID controller or different parameters for increasing force than decreasing it would be able to stop the overshooting effect.

Each of the levels is relatively flat, showing the muscle can keep to a set level effectively. There is a slight downward slope of the 0.2 N level from 0.213-0.193 N, however, the measured force stops decreasing towards the end of the 20 s time period.

Another force control test was done to see the resolution of force control that could be achieved. Initially, the 0.5mm width slit LM muscle was set to 0.4 N for 10 s. It then moved down in

decreasing steps from 0.05 – 0.01 N, decreasing by 0.01 N each step. The measured results are shown in Figure 4.53.

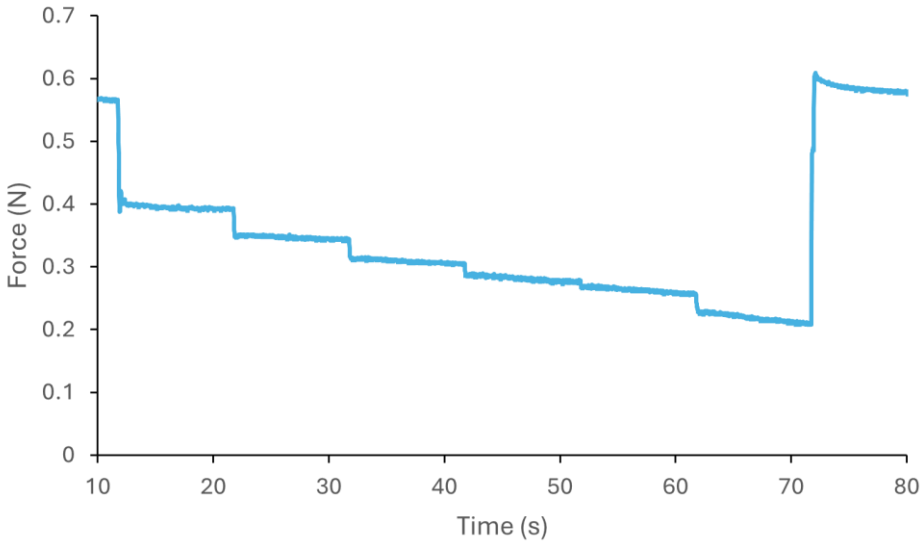

Figure 4.53 Force control of CLMM with decreasing steps.

Each of the steps from 0.05 – 0.01N can be seen, although the 0.01 N step is much larger than it should be, moving from 0.256 to 0.224 N. There is a slight downward slope again towards the lower force values.

Another test was done, with 0.03 N step size, down then up, starting at 0.4 N, lasting for 10 s per step. The results are shown in Figure 4.54.

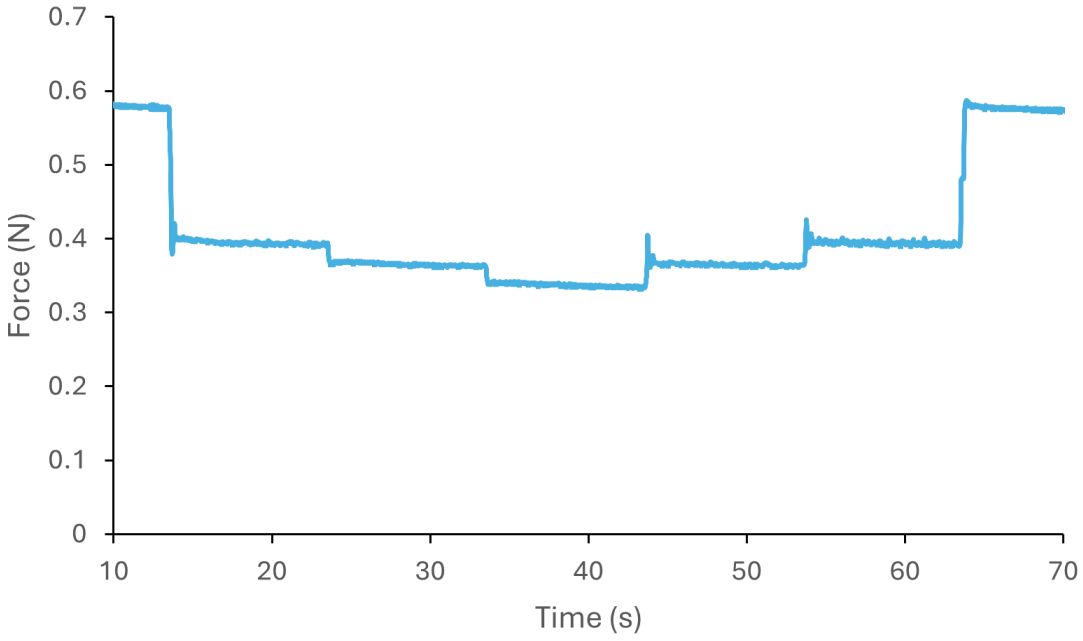

Figure 4.54 Force control with 0.03 N steps.

This force control graph is in line with previous measurements. There is a slight overshoot on the increasing force levels, however, it shows the LM muscle has a force control resolution of at least 0.03 N.

4.5.6 Measurement of Force of CLMM with Displacement

Blocked force measurements of the CLMM had so far only been done at one height level. Force of the CLMM varies with the height the top is pushed down by. When the top is resting on top of the LM, no LM is pushed into the slits, so there is no blocked force variation during oxidation. Pushing the top down slightly will increase the force as some LM enters into the slits a small amount. For full force change, LM should be pushed slightly into all the slits.

A test of force variation with displacement was done for a 1 mm width slit CLMM. The 1 mm width slit CLMM was chosen so that there could be a greater change in displacement over 0.5 mm slit width. The muscle was tested by moving the MTS down and then up at 1 mm s^{-1} to a

maximum displacement of 2 mm. The force from the muscle was varied at a frequency of 0.5 Hz. The starting point was set just above where the MTS measured an increase in force from the LM initially being pushed into the slits. The MTS was used to measure the force rather than the HX711 force sensor as the MTS was also measuring the displacement. The frequency chosen (0.5 Hz) meant that the 30 Hz refresh rate for force measurement from the MTS was not a problem. The resultant data is shown in Figure 4.55.

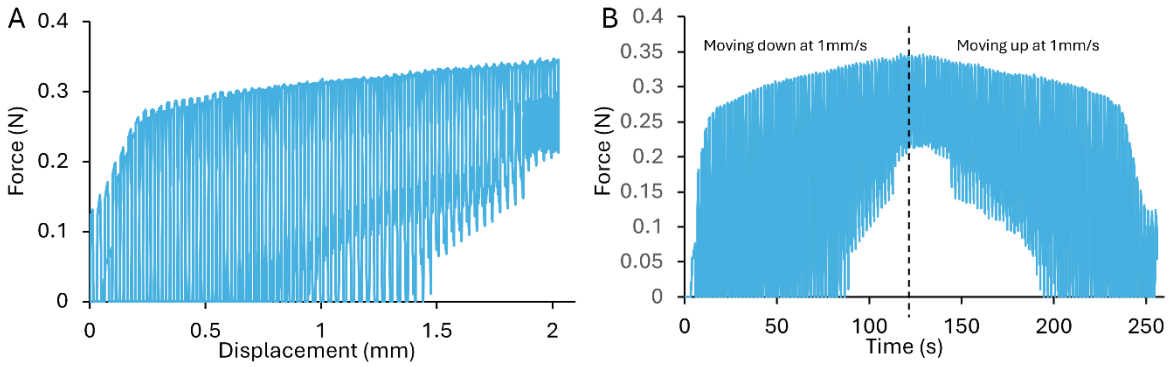

Figure 4.55 Measured force change of 1mm width slits CLMM with (A) displacement and (B) with time while constantly moving down then up at 1 mm s^{-1}.

Initially, force is seen to sharply rise with displacement, rising from 0 N at 0 mm displacement to 0.28 N at 0.3 mm displacement. This is as expected as the LM is pushed into the slits from just outside them. After this, maximum force rises still, but more slowly, reaching 0.34 N at 2 mm displacement. This may be caused by the buoyancy of the LM. From displacements above 1 mm, the minimum force starts to increase from 0 N. The minimum force is 0.21 N at 2 mm displacement, meaning variation in force is decreased from a maximum of ~0.3 to ~0.13 N. This decrease in minimum force is because the LM is pushed a large distance into the slits. When oxidised, the top part is oxidised as it is close to the counter electrode. LM within the slit

but further away has an unoxidized outer layer so has high interfacial tension still. Therefore, the force does not decrease to zero for lower displacements.

The time vs force graph shows that the force change is relatively symmetrical moving up and down, although for moving up, the minimum force drops at a later time than would be expected from the moving down data.

4.5.7 Repeated Force Test for Slit CLMM

A repeated force test had been done for the pillar with cross support CLMM previously. The same test was done for a 0.5 mm width slit CLMM, with 1 M NaOH. The results are shown in Figure 4.56.

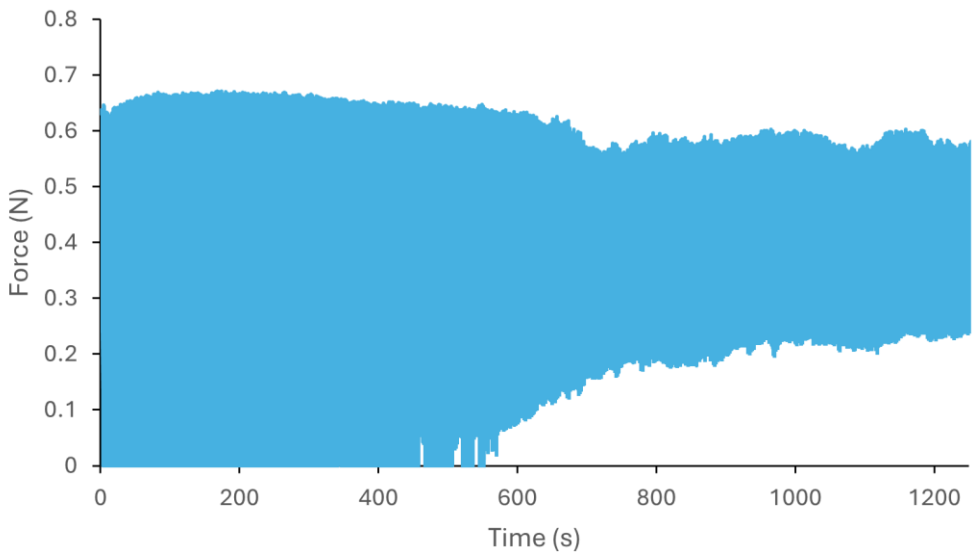

Figure 4.56 Repeated force test of 0.5 mm width slit CLMM at 0.5 Hz.

The minimum force starts to increase from 0 N at ~470 s, then consistently increases after 570 s, reaching 0.19 N at 800 s. Maximum force also decreases with time. This overall decrease in force may be caused by increased friction of the LM muscle due to heating from electrolysis.

Temperature was measured using a Tenma 72-7712 thermometer attached to the outer wall of the CLMM, with an increase from 22 °C (room temperature) to 58 °C after 10 minutes. The increased temperature causes the resin the LM muscle is made from to expand slightly, causing some friction. Leaving the muscle to cool for ~5 mins and then restarting the testing (no electrolyte added, no mixing of LM) resulted in the force change returning to the maximum for the first ~50 s, before lowering again (see Figure 4.57).

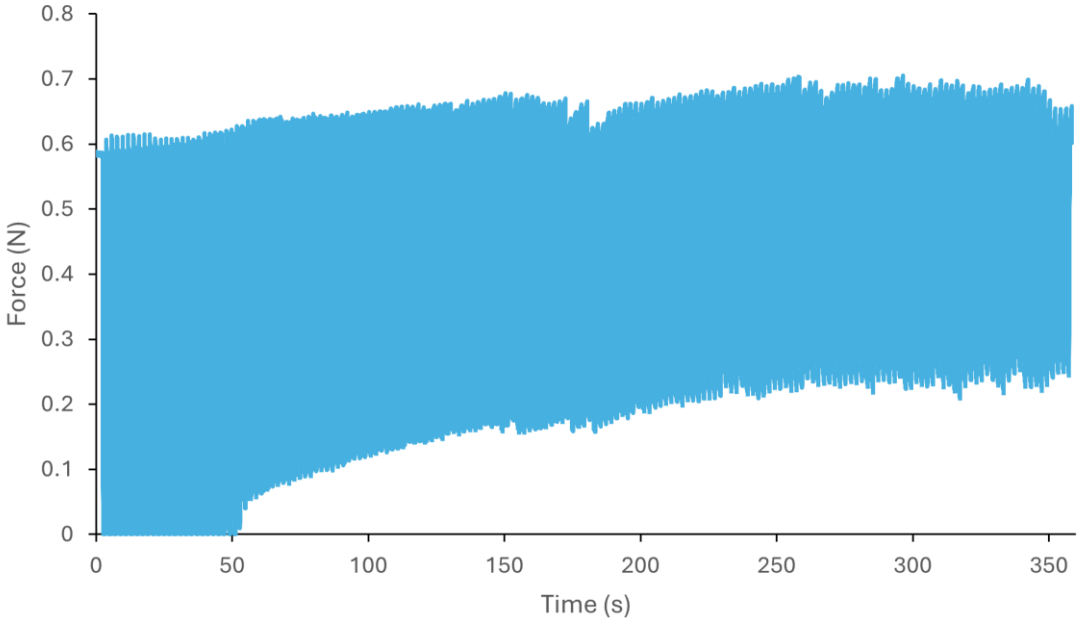

Figure 4.57 Repeated force test of 0.5mm width slit CLMM at 0.5Hz (continued after leaving to rest for ~5 mins).

Another test was done with 0.7 mm width slits. This LM muscle was a looser fit than the 0.5 mm width slit version. The gap around the side of the muscle top and the container must be smaller than the slit width otherwise LM will preferentially go around the sides of the LM muscle rather than into the slits. The looser fit meant that any expansion due to heating would have less of an effect. The resultant graph is shown in Figure 4.58.

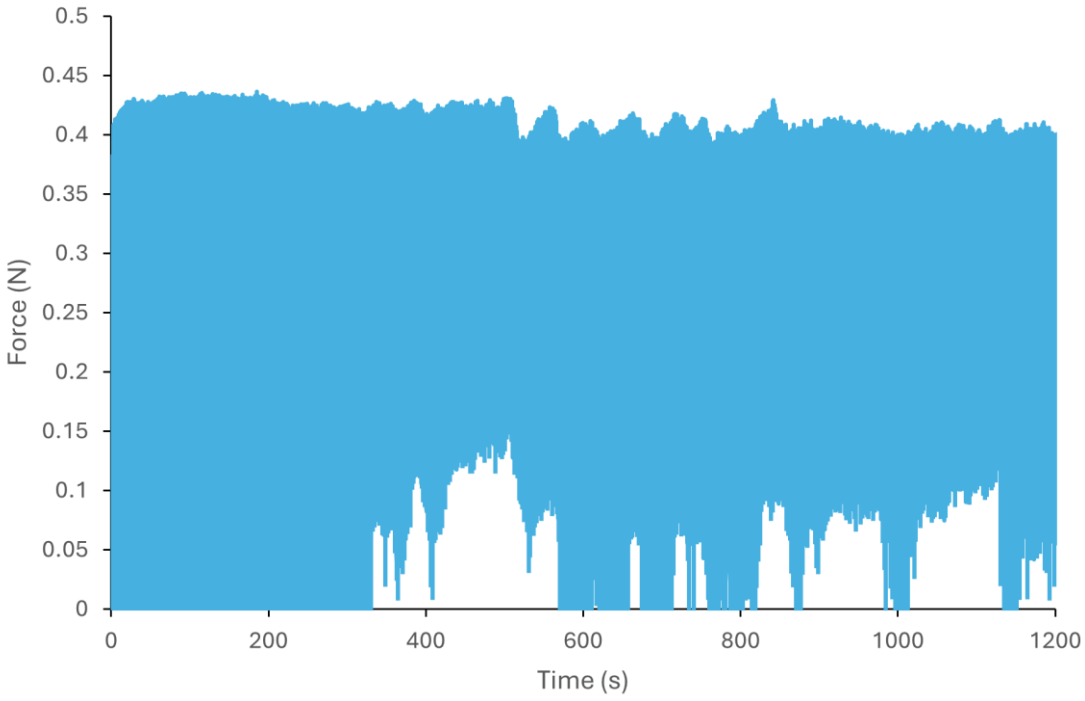

Figure 4.58 Repeated force test of 0.7 mm width slit CLMM at 0.5 Hz.

The 0.7 mm width slit minimum force repeatedly increases from 0 N, similar to the 0.5 mm width slit muscle. However, after a varying amount of time, it then returns to a minimum of 0 N, even after 1000 s (500 cycles). Maximum force decreases slightly from 0.43 to 0.40 N over the total time tested. These results may show that friction increase due to heating is the main cause of degraded LM muscle performance over repeated testing, as the looser fit muscle is less affected.

4.5.8 Displacement of CLMM and its Efficiency

When oxidised and then reduced with a mass payload on it, the LM muscle moves up and down (Figure 4.59). The lowered force during oxidation causes LM to be pushed into the slits by the weight. Then when reduction occurs, the force for LM to be within the slits increases quickly, so the mass is pushed up as the LM pushes itself out of the slits.

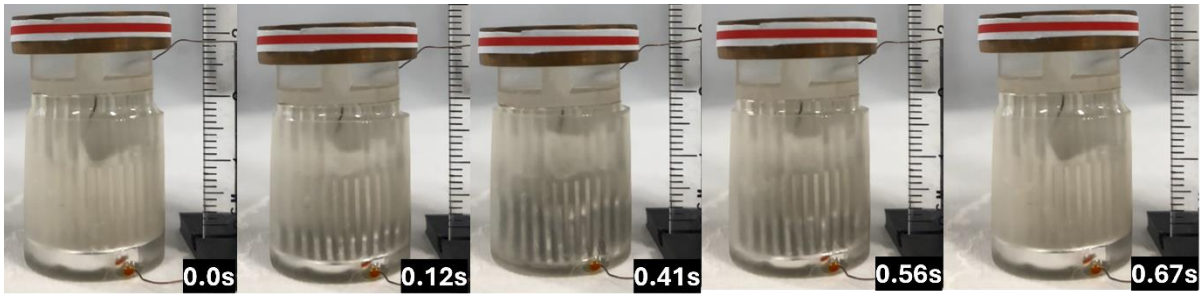

Figure 4.59 1Hz movement of 1 mm width slits CLMM with 20 g mass payload.

The movement of the LM muscle was measured for varying slit size, mass payload, and frequency. To measure the movement, a computer vision program was created based on OpenCV. The computer vision took a video of the muscle moving and was able to convert it into a comma separated value (csv) file of the vertical position with respect to time.

For filming, an iPhone 8 was used, placed on a tripod. Recording was done using 240 frames per second (fps), at 1080p for best results. A high fps was required for accurate tracking as this gave more data points per second and reduced motion blur. The height of the camera had to be level with the top of the muscle to reduce any artefacts caused by slight rocking of the top of the LM muscle. The payload weight was placed on top of the muscle, with a coloured band taped onto it. This was for the hue saturation value (HSV) mask to track a specific colour as it moved up and down. The HSV mask was set for a range of HSV values, and the computer vision program found each pixel that was within the range. The maximum area with values within the range (i.e. the coloured band) was what was tracked. Additionally, a ruler was placed next to the muscle. The computer program measured the number of pixels per cm, and was able to use this to accurately measure the distance the muscle moved. Every frame of the video was analysed and the distance moved from its initial position was determined with respect to time, which was then converted to a csv file and saved. See Figure 4.60 for snapshots of the program.

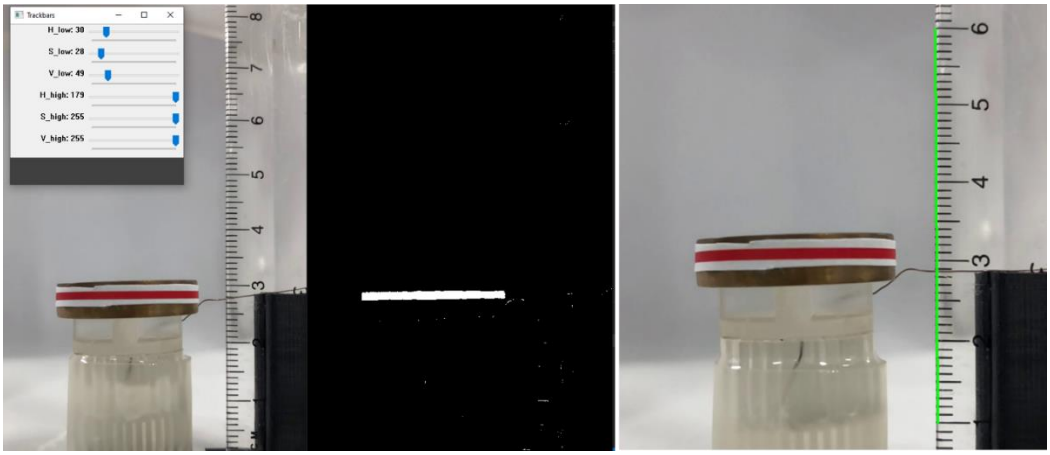

Figure 4.60 Mask (left) and measurement line (right) for tracking of CLMM movement.

Movement data for various slit widths, mass payloads and frequencies are shown in Figure 4.61.

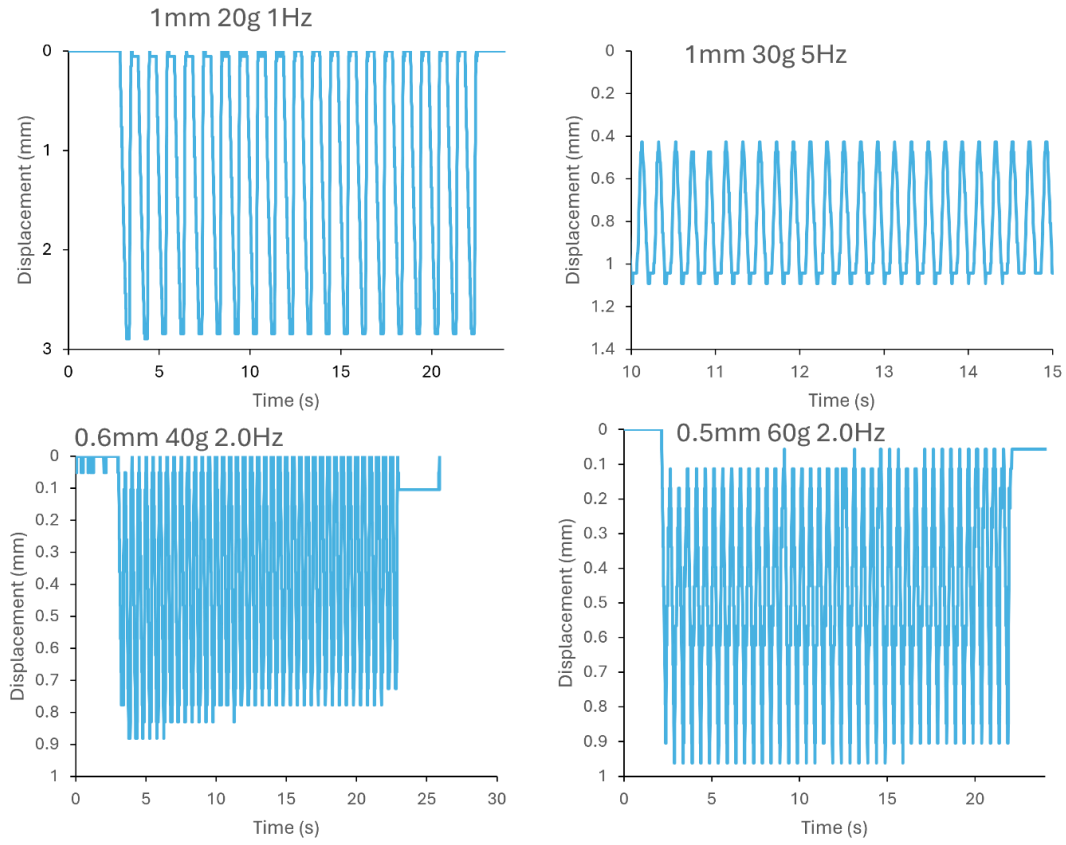

Figure 4.61 Displacement with time for CLMM with various slit widths, mass payloads and frequencies.

Movement is typically uniform, reaching the same displacement every cycle. A high frequency of movement of 5 Hz can be achieved. The LM muscle can also lift mass corresponding to its maximum force change (~0.3 N for 1 mm slits, lifting 30 g, ~0.62N for 0.5 mm slits, lifting 60 g). On some of the data, there is a slight dip between start and finish height. This is caused by the top of the muscle shifting in position slightly. This is perceived by the computer vision to be a lowered height, although that is not the case.

The speed of the muscle movement can be determined based on the position data (see Figure 4.62).

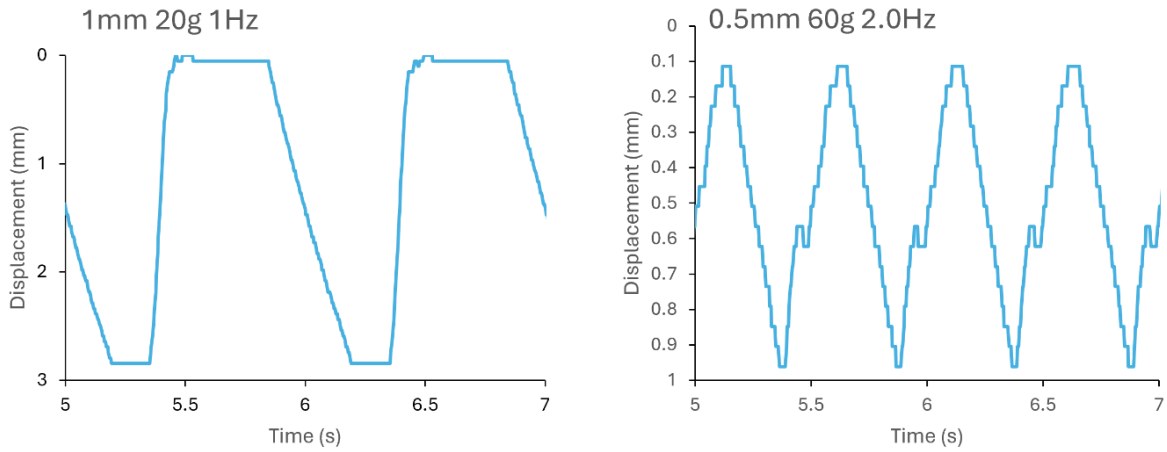

Figure 4.62 Zoomed in movement data to show the speed of the CLMM.

For a 1 mm width slit muscle, with a 20 g payload, its maximum speed is 36.3 mm s^{-1} moving up and 7.8 mm s^{-1} moving down. It is expected that moving down is slower than moving up as the force change for decreasing force is slower than for increasing. For the 0.5 mm width slit muscle, the max speed is 3.9 mm s^{-1} moving down and 6.8 mm s^{-1} moving up. The effect of a

slightly too long reduction can be seen on the rising line of the 0.5 mm slit data, showing the muscle briefly stops before continuing to move upwards.

Using the movement tracking data and the supplied energy, efficiency can be calculated. For 1 mm width slits with a 20 g payload, it repeatedly moves down and up by 2.85 mm. The total work done for lifting 20 g by 57 mm total is 0.011 J. Using data from the voltage and current measurement circuit, the total electrical energy used is 78J. The efficiency of the 1 mm slit width LM muscle is therefore 0.014%. This efficiency is very low, and is due to the electrolysis caused during oxidation and reduction, as this is wasted energy. Also, the continual removal of oxide by NaOH means continuous oxidative potential needs to be applied to lower the force or move the muscle down. Alternative electrolytes such as Na_3PO_4 may have greater efficiency. A lower voltage applied may improve the efficiency also as this would cause less electrolysis.

4.5.9 Control of CLMM Position

The CLMM is able to move quickly, and its force is also able to be controlled. Position control was the next element to work on.

The resistance of the muscle changes with position. As LM is pushed further into the slits, it is closer to the counter electrode and therefore the resistance is less. The resistance can be measured using the shunt resistor to determine the current and the voltage dividers to find the measured voltage. See Figure 4.63 for a graph of resistance and displacement measured with time.

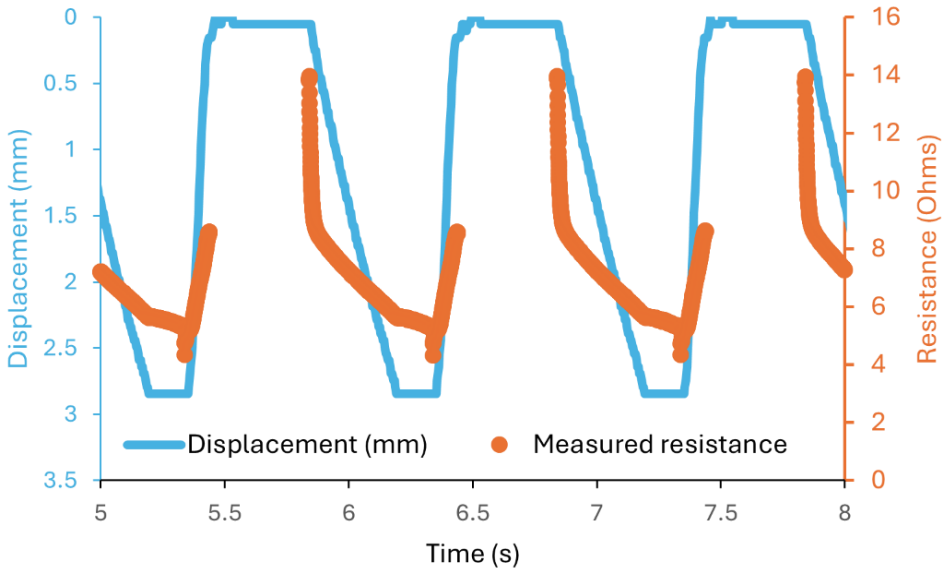

Figure 4.63 Measured resistance and displacement with time for 1mm width slits CLMM. There are gaps in the resistance measurements as the power is turned off every cycle after 100ms of reductive potential is applied to LM.

This variable resistance can therefore be used as feedback to control the height of the muscle when moving up and down. PID control was used to control the height of the muscle depending on the resistance measured. As the motor controller uses PWM, it sends bursts of voltage and current, then turns off for a short period, then sends another burst. Resistance therefore was checked by the Arduino for acceptable voltage and current measurement values before calculating the resistance. A circular buffer was used to keep the average of the resistance based on the last five measured values. This was used for the feedback. The average was used because it smoothed out the response of the muscle, although it meant it didn't respond to a change in resistance as quickly.

Oxidation of the LM was also a complicated matter for position control. The LM oxide was continuously being removed by the NaOH electrolyte, however, if a high power was applied for ~1 s (for example), then the LM muscle would move down as its force would decrease,

however, a thicker oxide layer than usual would be formed (due to the high power). Therefore, the measured resistance would increase, despite the muscle moving down, so it would get stuck in a positive reinforcement loop. This was avoided by tuning the PID to be less aggressive.

Displacement control for a 1mm width slit muscle with a 10 g payload is shown in Figure 4.64. The program was set to target resistances of 12, 10, and 9Ω, going down, then back up, holding for 10 s at each level.

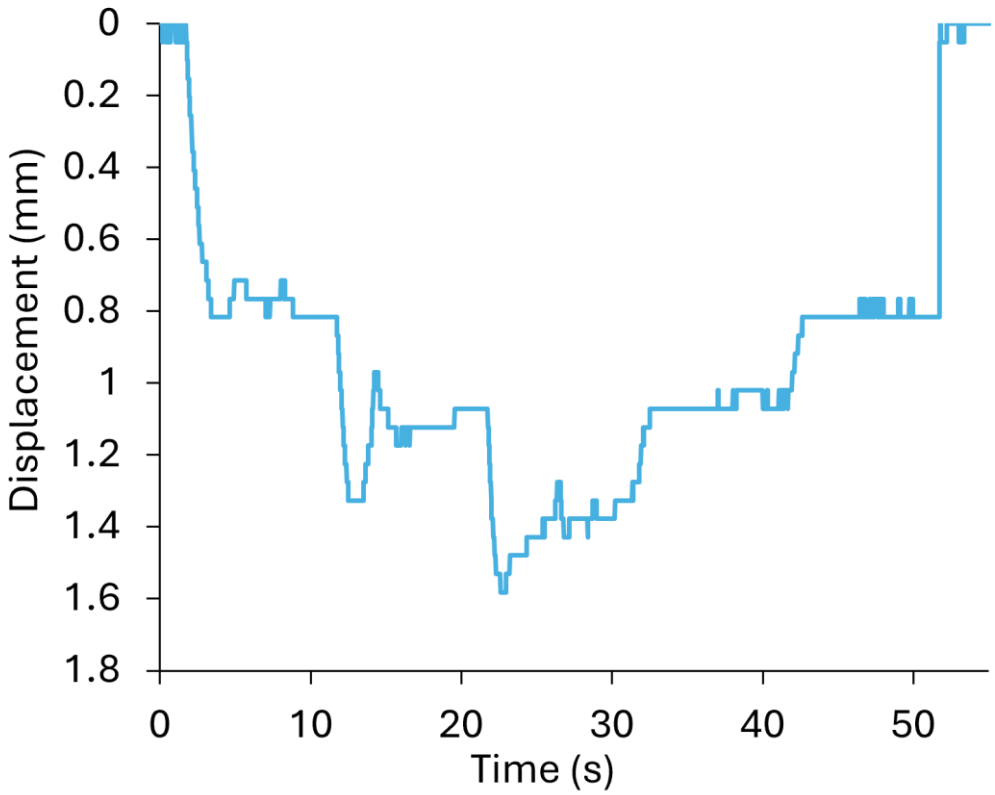

Figure 4.64 Displacement control of a 1 mm width slits CLMM with 10 g payload.

The position control is shown to be capable of repeatedly reaching a level and stabilising there for ~10 s. The muscle tends to overshoot coming down, then level out afterwards. Coming back

up, it is very flat and stable. This is the opposite of force control, where it tends to overshoot for increasing force.

The position was also held at a level for 60 s, for the same muscle with a 10 g payload (Figure 4.65).

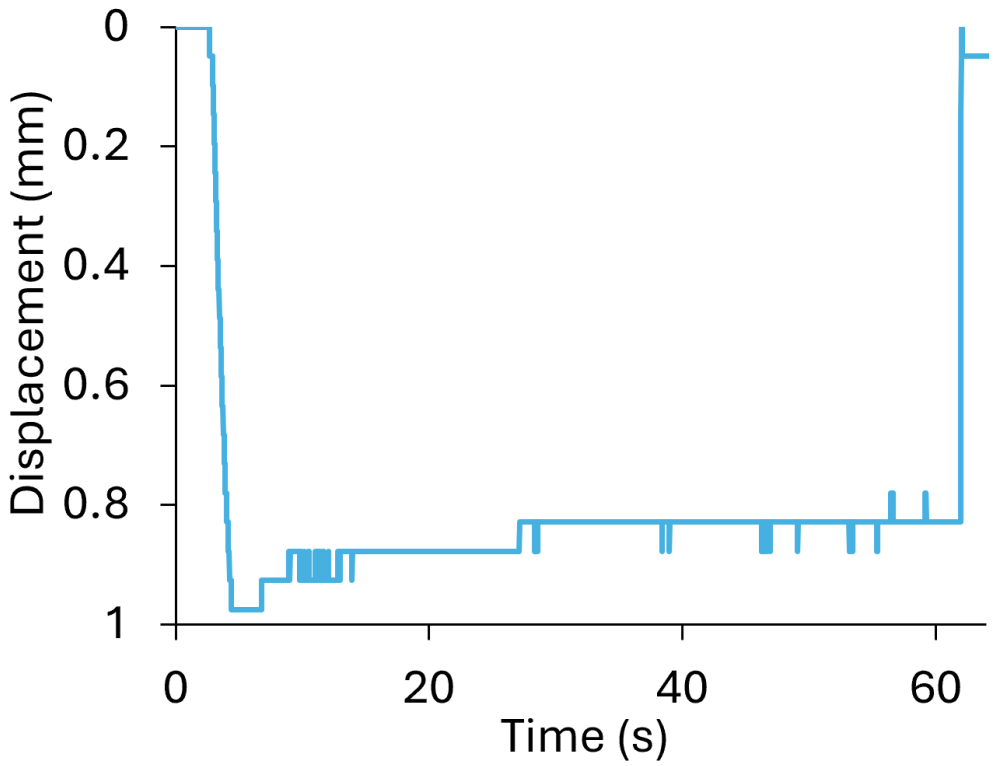

Figure 4.65 CLMM hold position for 60 s.

The position is seen to rise slightly over the 60s. The variation is between 0.97 and 0.78 mm, so less than 0.2 mm. Another position control test was done to determine the repeatability of multiple movements to a specific resistance (9Ω), with a short hold time of 5 s. The results are shown in Figure 4.66.

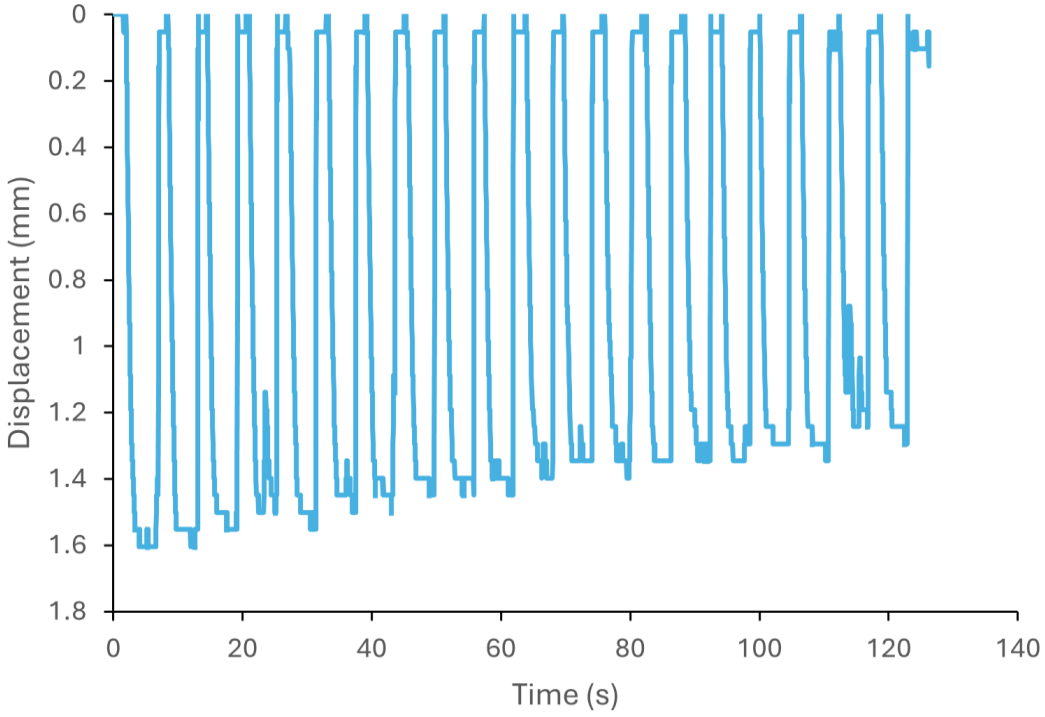

Figure 4.66 Repeated position control of CLMM.

The displacement reached varies from 1.60 to 1.24 mm, although there is also some fluctuations during the hold times. The maximum displacement reached gradually reduces with increased time.

4.6 Applications of the CLMM

4.6.1 Damping

The high force variability of the CLMM means that a potential application for it is as a variable damper, where it can be used instead of magnetorheological fluid dampers, which are bulky and require high magnetic fields [19].

The CLMM was tested as a variable damper. The MTS was used for compression of the muscle and data collection. The MTS moved down to compress the muscle by a maximum of 1mm

then lifted back up. It moved at a speed of 10mm min^{-1}. The muscle used for damping was a 1mm width slit muscle. The top of the muscle was also stuck to the top moveable plate of the MTS. In order to test its variable damping, the motor controller was used to change the PWM duty cycle so that the average voltage was 3.5V for 2 cycles, 2.5V for 2 cycles, and then was off for two cycles. The results are shown in Figure 4.67.

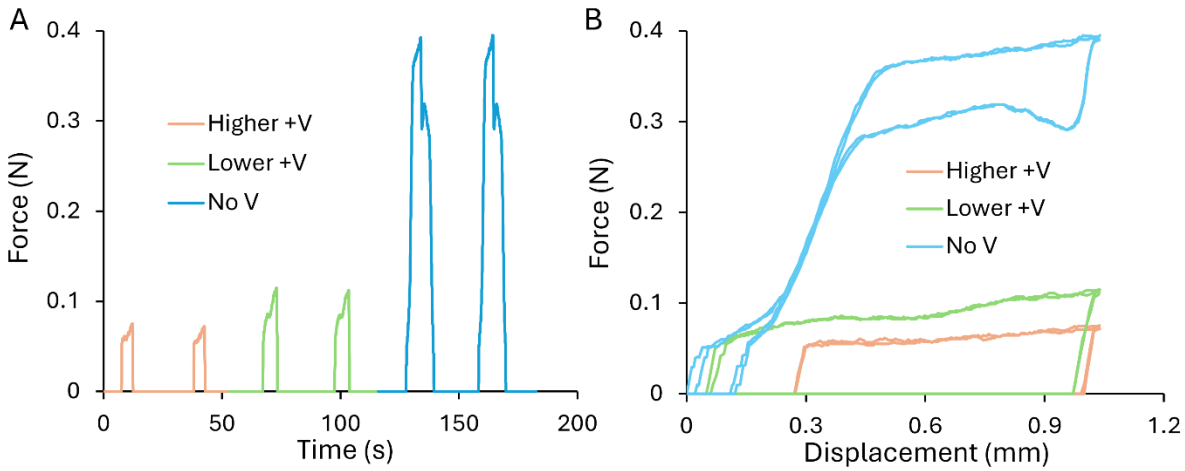

Figure 4.67 Force variation with (A) time and (B) displacement using 1mm slit width CLMM as a damper with differing oxidative voltages applied.

The variable voltage can be seen to have a clear effect on the damping force. In the case of no voltage applied, the damping force reaches a maximum of 0.39 N. This is lowered to 0.11 N for the 2.5 V average applied voltage and 0.07 N for the 3.5 V average. Additionally, the force measured with displacement graph shows that increased voltage results in measured force increasing from 0 N at later displacements (0.01 mm for 2.5 V and 0.28 mm for 3.5 V), meaning more movement can occur with no damping force.

4.6.2 Soft Diaphragm

The LM muscle also shows great potential for use in soft robotic applications due to its fluidic nature, ease of control and high force output.

In previous tests the top of the LM muscle was free to move, so LM could push it, and the measured force would change. A different design is possible, in which the slits are held in place and an outlet is connected to the bottom of the LM muscle container. The outlet is then connected to a soft robotic element (such as a diaphragm). By filling up the diaphragm with LM so it is under some pressure (but not too much) LM will want to go into the slits. If the pressure is right, it is not quite enough to push LM into the slits. Oxidising LM will mean the pressure required for LM to enter the slits is lowered, and the LM flows through the inlet/outlet into the slits. This causes the diaphragm to deflate. Reducing LM causes the pressure to keep it in the slits to increase, so it is pushed out the slits and through the outlet, inflating the diaphragm.

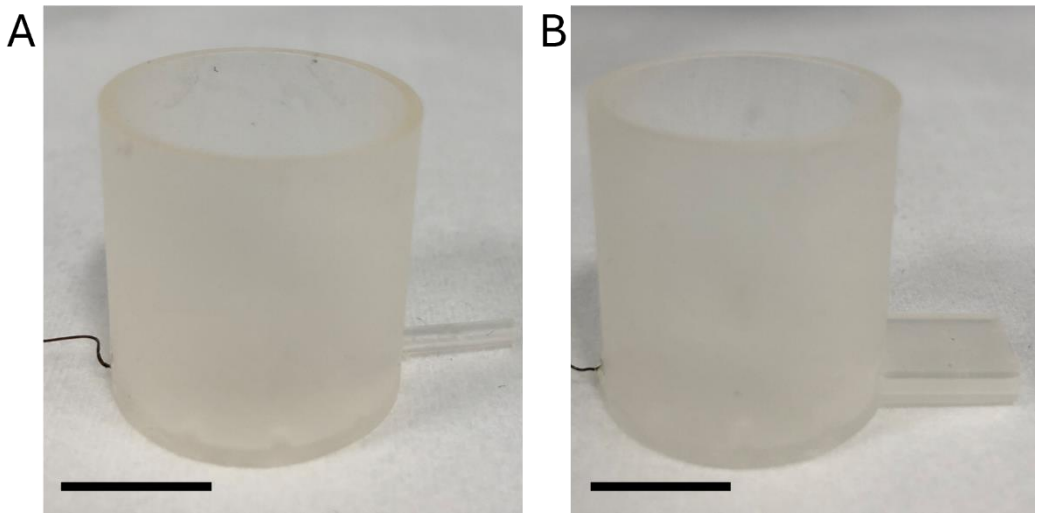

Figure 4.68 Container (A) with original outlet design and (B) with final design.
Scale bars are 10 mm.

The inlet/outlet needs to be relatively large so that the flow of LM is unimpeded (see Figure 4.68A). An initial test used a small (1mm inner diameter) outlet, however, LM did not move in and out of it as the pressure required to push it through the gap was too high. The final design used a rectangular outlet, 2 mm high and 5 mm wide, which LM could easily flow in and out of (Figure 4.68B).

To make a diaphragm for testing, Ecoflex 00-20 elastomer was used. Ecoflex elastomer is extremely soft and elastic, being able to be stretched over 200%. 50% Ecoflex part A and 50% part B were mixed by hand in a plastic cup, and then degassed in a desiccator. The mixture was then poured into two 3D printed moulds, one for the top, and one for the bottom. The mould shown has a chamber diameter of 15 mm. Thickness of Ecoflex top and bottom was 1mm. The Ecoflex was left to cure at room temperature for 2 hours. After peeling out of the moulds, the top and bottom layers were stuck together with fresh Ecoflex. On the bottom side, a layer of paper was added, with a small amount of Ecoflex coating it to stick it on. This is because paper cannot be stretched, so it prevents that side of the diaphragm from expanding as much. See Figure 4.69 for the finished diaphragm.

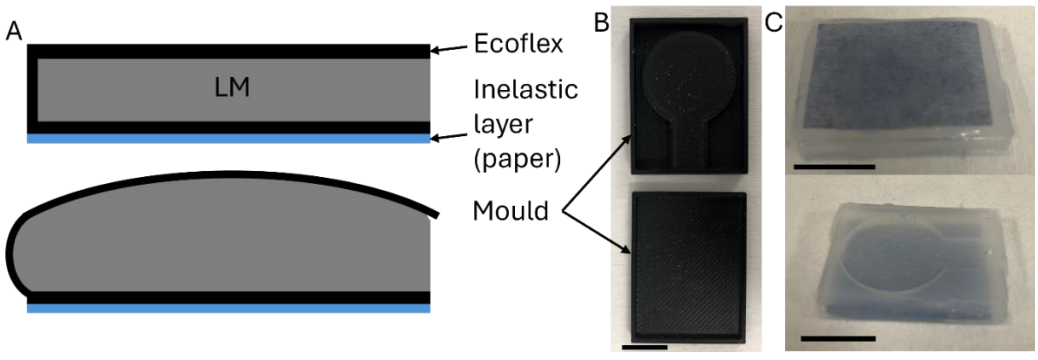

Figure 4.69 Soft diaphragm for expansion by CLMM. (A) Diagram of diaphragm expanding with increased pressure due to LM entering. (B) Diaphragm mould. (C) Completed diaphragm.
Scale bars are 10 mm.

The soft diaphragm was tested using a 0.5 mm width slit LM muscle, with the slits held in place. A custom clip was placed over the connection between the outlet and the diaphragm to prevent leaks of LM.

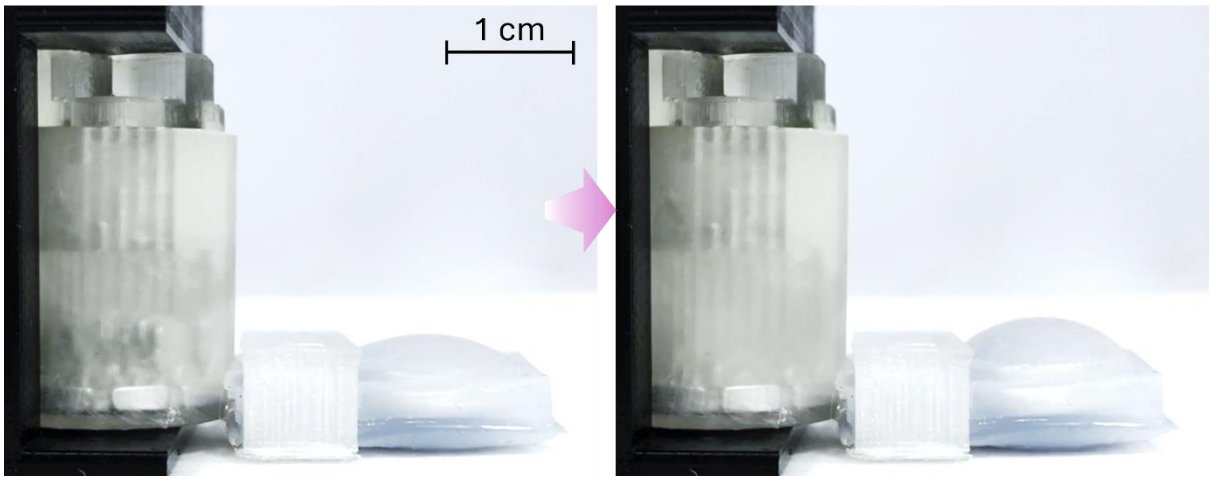

Figure 4.70 Soft diaphragm movement by oxidising and reducing LM in the CLMM.

The diaphragm can be seen to repeatedly inflate and deflate with applied potential to the LM muscle (see Figure 4.70).

4.6.3 Soft Robotic Finger

In addition to the diaphragm, a soft robotic finger was also created. The finger structure is made of a series of ridges which inflate with pressure. The other side has no ridges and does not expand, so the overall structure bends when pressure is increased.

The finger was more complex to make than the diaphragm. A diagram of how the finger moves and pictures of the moulds and the completed finger are shown in Figure 4.71. The ridge

structure requires a bottom and a top which fit together accurately so the ridges can inflate and push each other apart.

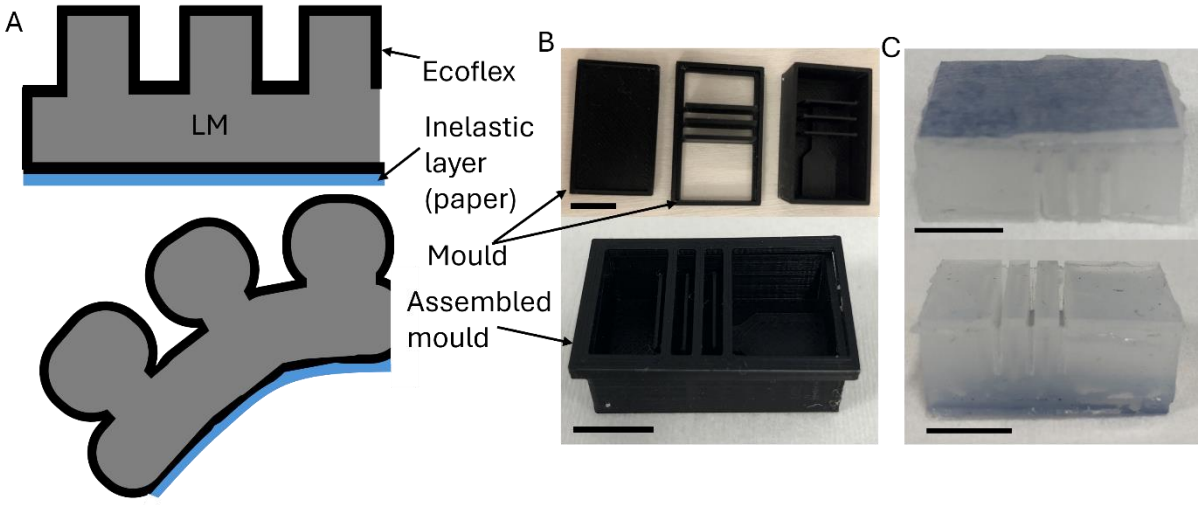

Figure 4.71 Soft finger actuated using CLMM. (A) Diagram of soft finger. (B) Moulds for making the soft robotic finger. (C) Completed soft finger
Scale bars are 10 mm.

Many iterations of the design were made to optimise the performance. As LM has a high density (6280 g L^{-1}) [20], it will weigh down the finger structure, so a lower amount of LM is preferable. However, the structure cannot be too small otherwise the LM will not generate enough force to inflate the finger. Different designs increased the width of the finger, the height and length of the ridges, and the number of ridges. The final design used ridges which were 2 mm high and 8 mm wide. The Ecoflex layer was 0.8 mm. If it was too thin it tended to break.

The final finger design was tested with 0.5 mm slit width muscle, with a large amount of movement when oxidised and reduced (Figure 4.72).

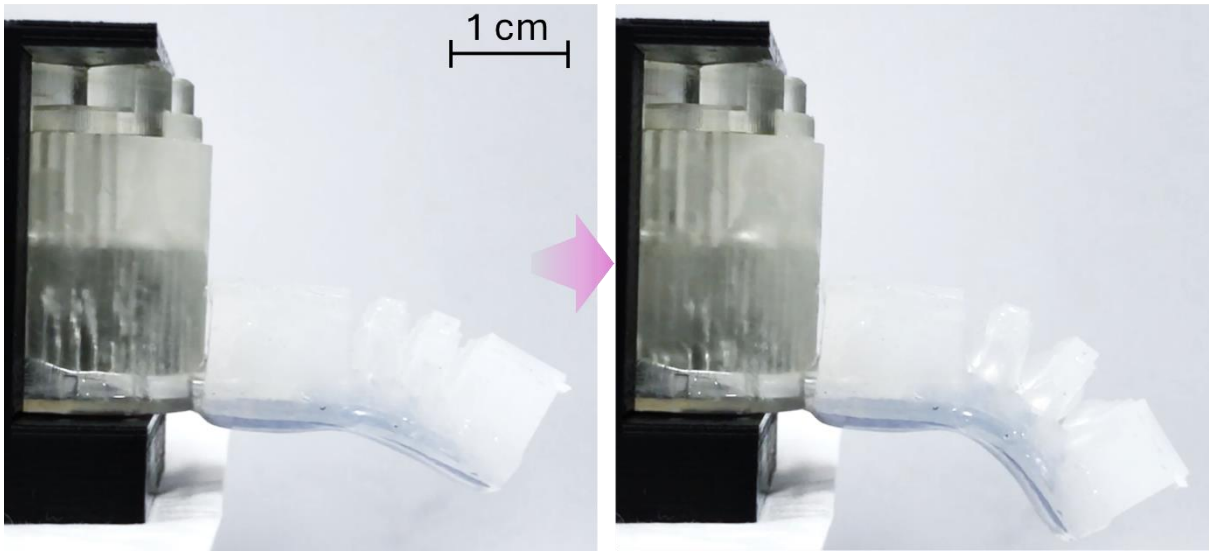

Figure 4.72 Movement of the soft robotic finger when LM in the CLMM is oxidised and reduced.

4.6.4 Gripper

Soft grippers are important for robotics applications as they can grasp delicate objects without damaging them. A soft gripper was made with the LM muscle, which utilised two diaphragms on either side of a gap. The diaphragms expanded when LM was in its high interfacial tension state and deflated when LM was oxidised. The soft gripper was shown to pick up an object, and then put it back down (see Figure 4.73).

Figure 4.73 A soft robotic gripper inflated and deflated by CLMM picking up and putting down an object.
Scale bar is 10 mm.

4.6.5 1Kg Lifting muscle

To fully demonstrate the potential strength of the CLMM, an extra large (100 mm diameter, slit width 0.6 mm) version was made. This was able to lift 1 kg (see Figure 4.74). This large muscle was made using the Ultimaker printer rather than the Formlabs as the prints failed for large diameters using the Formlabs.

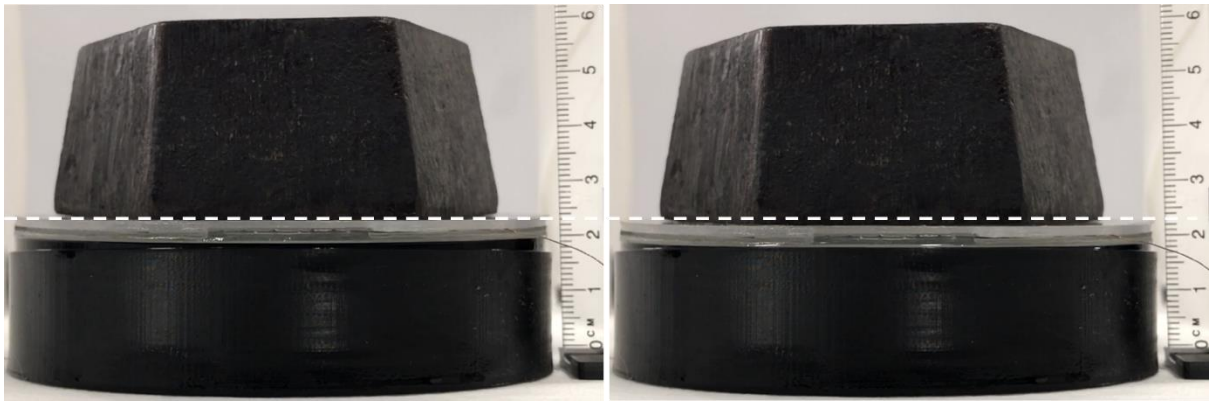

Figure 4.74 An extra large CLMM lifting 1 kg.

4.7 Reducing the Size of Slits Below 0.5mm for Greater Force

So far, the smallest size slit tested has been 0.5 mm wide. As the theoretical force scales with the inverse of slit width, it was desired to make LM muscles with even smaller slit sizes. The Formlabs printer got blocked at lower than 0.5 mm slit sizes due to the viscosity of the resin meaning that it remained in the slits. The Ultimaker S5 FDM printer could print slits with a minimum width of 0.3 mm, however, the printed PLA quickly weakened and broke when exposed to NaOH solution. Therefore, alternatives had to be tried.

A Boston Microfluidics S130 printer (resolution of 2µm) was used to print LM muscles with slit sizes of 100 and 300 microns. The radius of the muscles was smaller than for the others previously made, 6 mm rather than 10 mm. The height was 11 mm for the 100 micron slit width and 6mm for the 300 micron slit width version. This was so it was faster to print. A small container for testing was also made, which was set to be 100 microns in diameter larger than the outer radius of the LM muscle tops so it could move freely but also not have LM push around the sides of it. A small topper for threading the electrode was also made using the Formlabs printer. See Figure 4.75 for images of the extra small slit CLMM and top electrode.

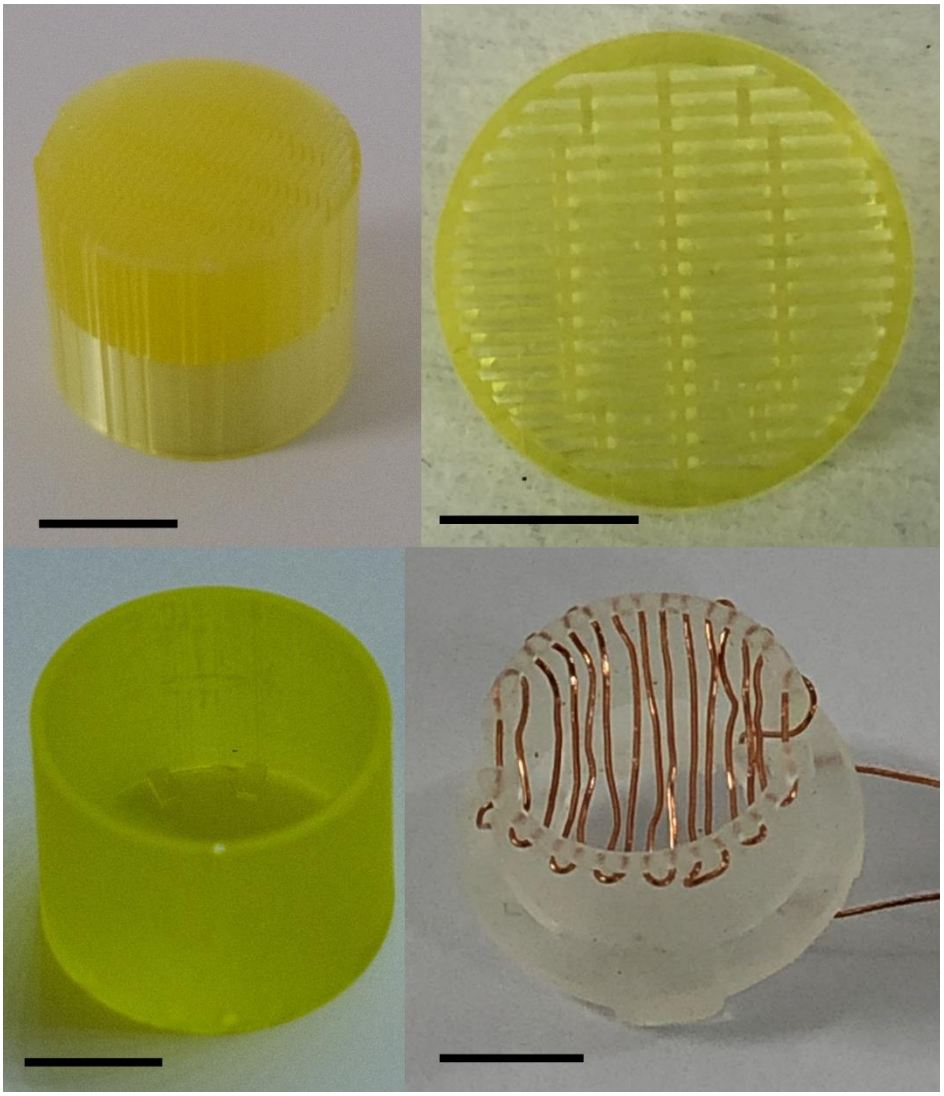

Figure 4.75 Pictures of the extra small slits CLMM and the manufactured top electrode. Scale bars are 5 mm.

The muscle was attempted to be tested, however, after putting the 100 micron slit width LM muscle top in the container with LM and electrolyte, it could not be moved up again. The very small gap <100 microns between the LM muscle top sides and the container's inner walls meant that it created a seal, so could not be moved upwards. It was able to be removed by taking out the wire from the container, however, that then split. An alternative method for testing was required due to the sealing effect.

4.7.1 Diaphragm for Testing Thin Slit Force Change

A diaphragm setup was devised to be able to test the force of the thin slit muscles. (See Figure 4.76). The CLMM slits were glued within a 3D printed polycarbonate (PC) tube, fully sealed around the edges. A wire was pushed through a gap in the side and sealed with glue. LM and electrolyte could then be added at the bottom, then a PDMS membrane was clamped onto it with another PC ring and bulldog clips.

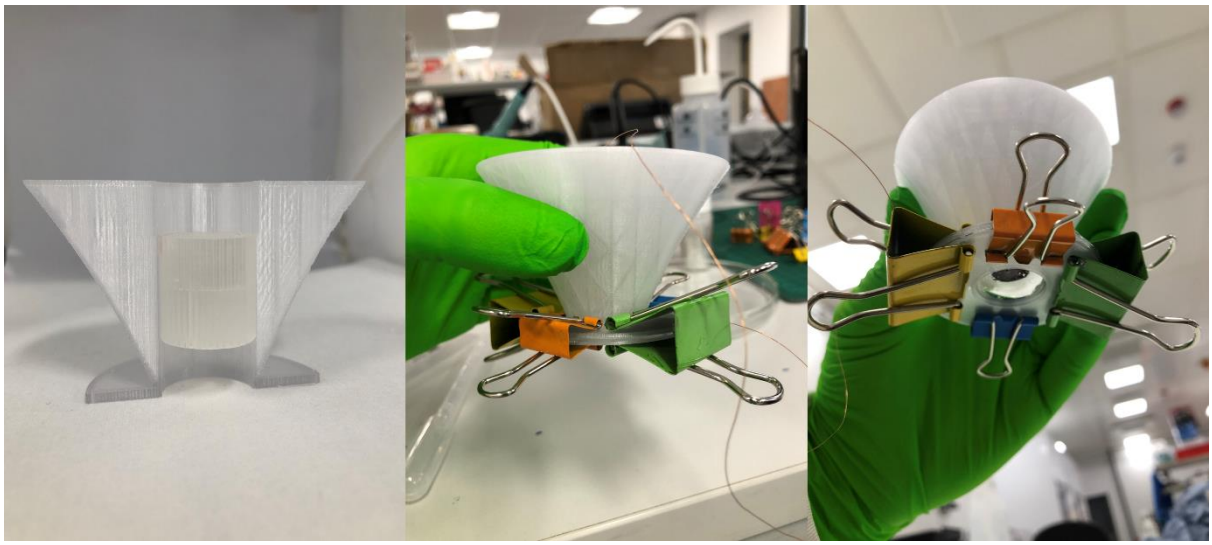

Figure 4.76 Creation of the diaphragm test setup and putting in LM and clamping with bulldog clips ready for testing.

The design was first tested with a spare 0.5 mm slit width CLMM to see if it worked. The top side of the device was stuck onto the bottom of the top plate of the MTS with double sided tape (Figure 4.77). A PC column pusher was used to compress the PDMS membrane, with the force measured by the MTS. The results are shown in Figure 4.78.

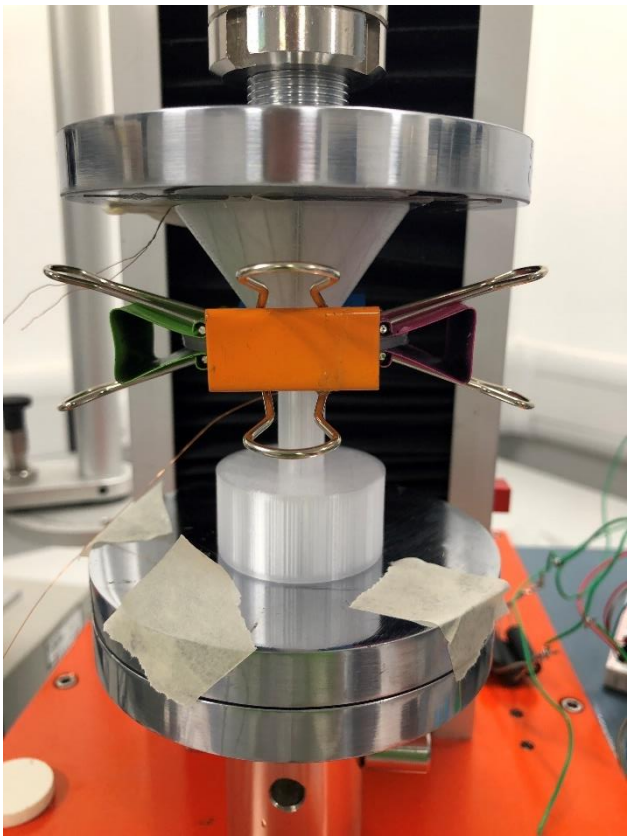

Figure 4.77 Diaphragm CLMM test setup.

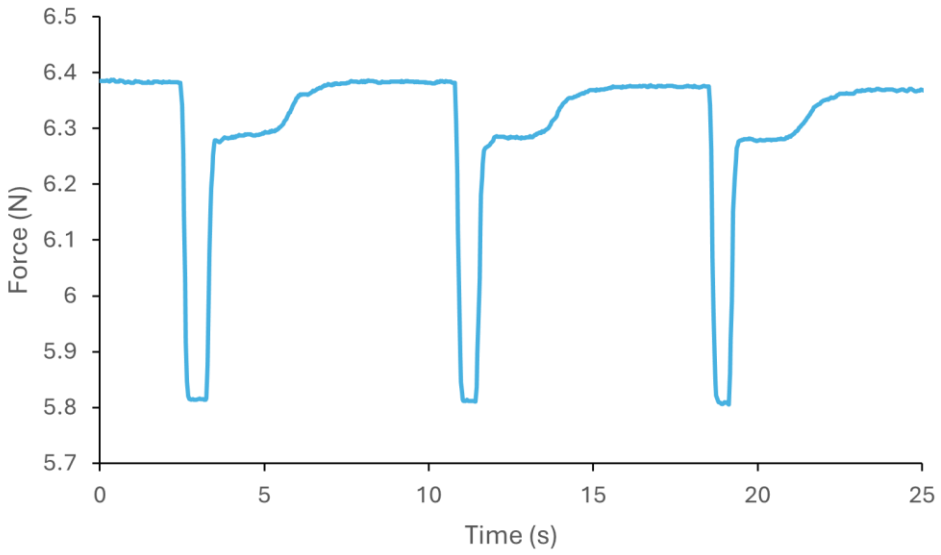

Figure 4.78 Force measurement for diaphragm test with 0.5 mm width slits.

The CLMM diaphragm is shown to lower in force when oxidised and increase again when reduced. The shape of the force change is different to that previously due to the elastic effects of the PDMS membrane. The overall force change measured is 0.58 N, compared to 0.62 N for the regular CLMM muscle with the same slit size. Therefore, there is some measured force loss due to the PDMS membrane but only ~5%. The measured force does not drop to zero as there needs to be some force to deform the PDMS enough to push LM into the slits.

After proving that the diaphragm design worked, the extra small slit width muscles were put into similar setups and tested. The results for both are shown in Figure 4.79 and Figure 4.80.

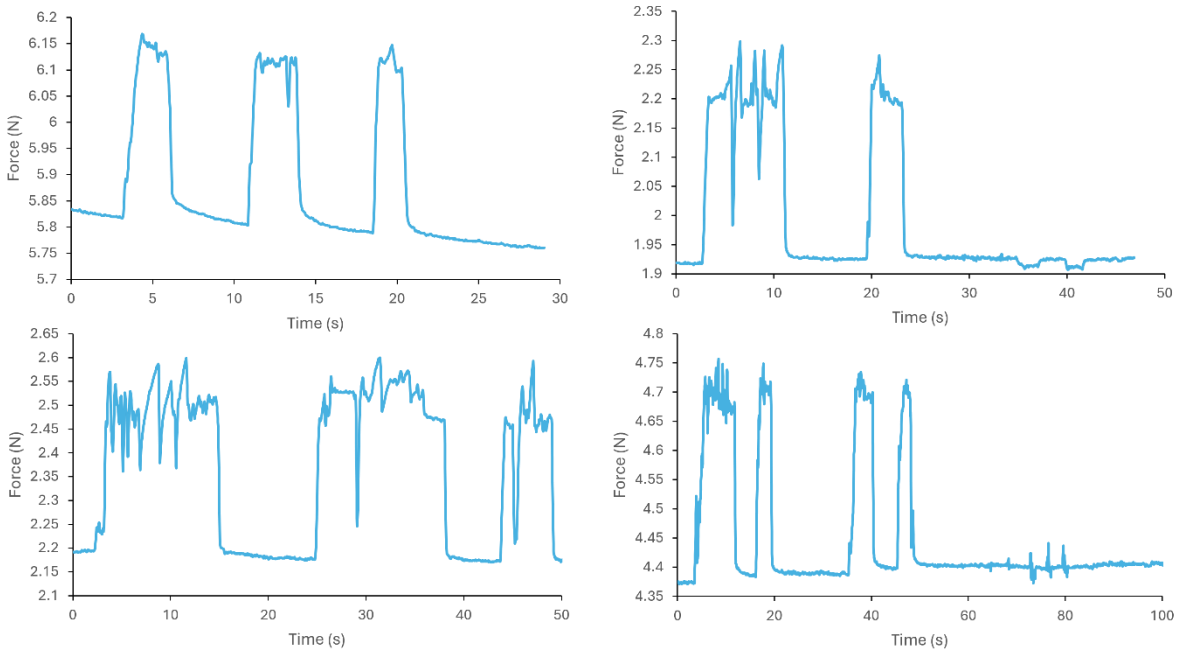

Figure 4.79 Force change measured for 0.3 mm slit width CLMM within diaphragm setup.

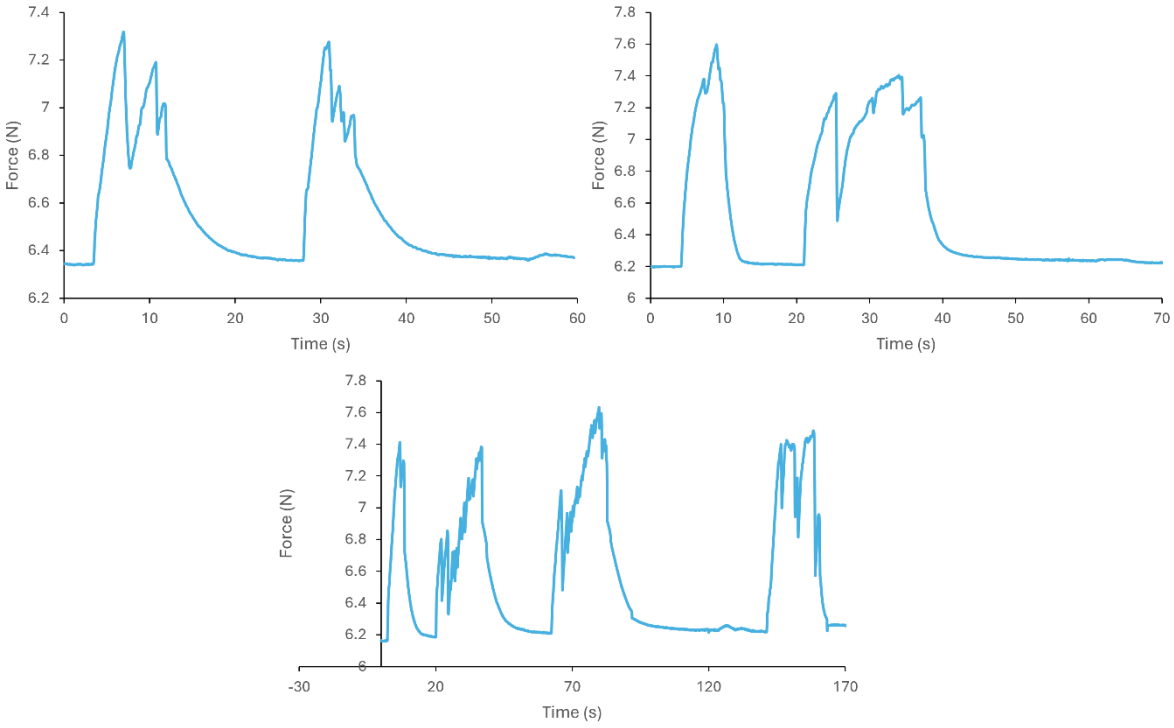

Figure 4.80 Force change measured for 0.1mm slit width CLMM within diaphragm setup.

Interestingly, the force of the small slit muscles does not decrease much when oxidised. The force increases dramatically when a reductive potential ~20 V is applied. Force increase is ~0.35 N for 0.3 mm width sits and ~1.2 N for 0.1 mm width slits. Note that as the radius of these LM muscles is 6 mm compared to 10 mm of previous designs, and as force scales with the square of the overall radius, this is the equivalent of 1 N and 3.3 N, respectively. The effects of oxidative potential on the measured force are very small, as seen on the right hand small dips on the top right graph of the 0.3 mm slits data.

The force increase may be due to LM moving into the small channels by electrocapillarity. Initially, the LM is just outside the slits. After a negative voltage is applied to LM, its effective interfacial tension at the entrance to the slits is lowered due to increased capacitance of the EDL between LM and the electrolyte [17]. This lowered interfacial tension results in a pressure

gradient between LM at the entrance to the slits and the bulk below which causes LM to enter into the slits [16, 21]. This results in increased force measured as LM within the slits still have a relatively high interfacial tension. Alternatively, it may be caused by increased pressure due to bubble generation during electrolysis.

For force to decrease during oxidation, LM must be pushed partway into the slits. For the thinner slits, their volume is much lower and the pressure required to push LM into them is greater. Therefore, LM may travel all the way through the slit to the other side rather than going partway in, so the force cannot be lowered by oxidation in the same way as for 0.5 mm + width slits. The height of the 0.1 mm and 0.3 mm slit muscles made (11 mm and 6 mm respectively) was much smaller than the others made (21 mm). Making the small slit designs taller may enable the oxidative force change to work.

4.7.2 Negative Voltage Applied Force Testing of 0.5mm Width Slit CLMM

The force change for LM reduction was tested for 0.5 mm width slits to compare with the force change by oxidation. The LM muscle was placed on the HX711 force sensor, and the MTS was lowered until just before LM was pushed into the slits (zero force from LM initially). Then a reductive potential was applied, and the force was measured. The results are shown in Figure 4.81.

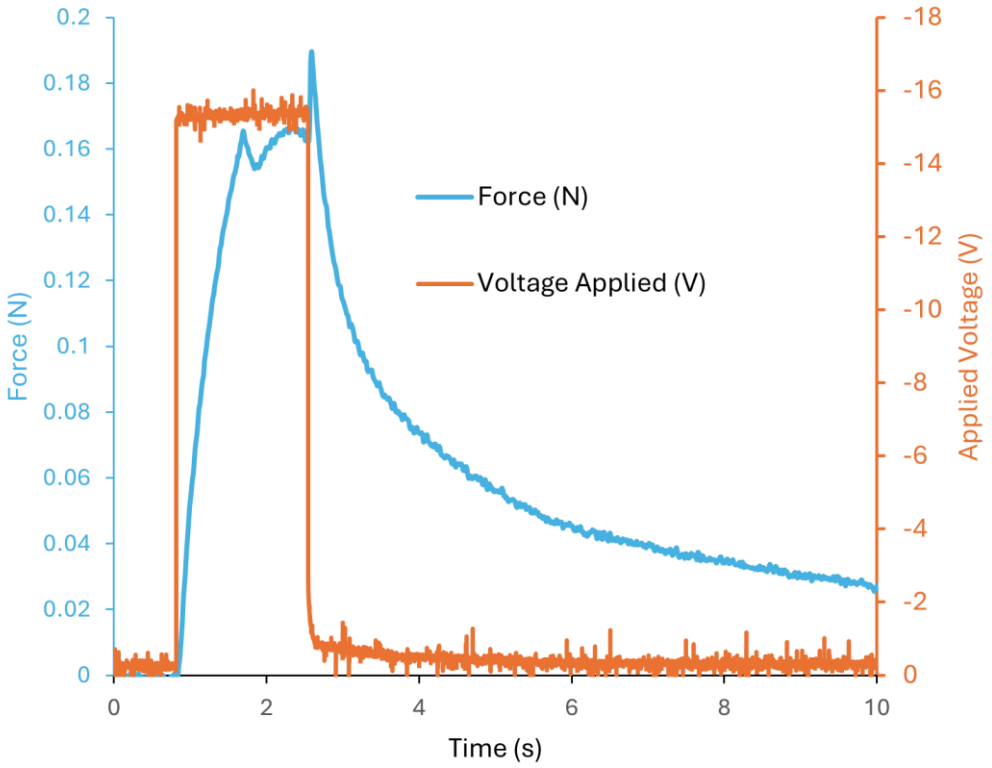

Figure 4.81 Negative voltage applied force change for 0.5mm width slit CLMM.

The force can be seen to rise, similarly to for the smaller slits. The force starts to increase when negative potential is applied to the LM, reaching a maximum of 0.19N (compared to 0.62N force variation for oxidative). The measured force is seen to spike briefly when the negative voltage is removed. This is because electrocapillarity lowers the interfacial tension of the LM slightly. When the voltage is removed, the interfacial tension increases to maximum so the force spikes. LM then starts to move out of the slits so the force drops.

Measured force change is much lower for reduction (0.19N) than for oxidation (0.62N) for 0.5mm width slits. Force change for thicker slits during reduction is lower as gravity means LM will only travel a small way into the slits, and the small part of LM that enters the slits has lowered interfacial tension also.

Force rise and drop is much slower for reductive force increase than oxidative force decrease. This may be because the increase in force is due to electrolysis bubble generation, which takes time to build up bubbles and then to dissipate when voltage is removed.

As a comparison, the force change for 0.5mm width slits muscle when reduced when already at maximum force was measured (see Figure 4.82).

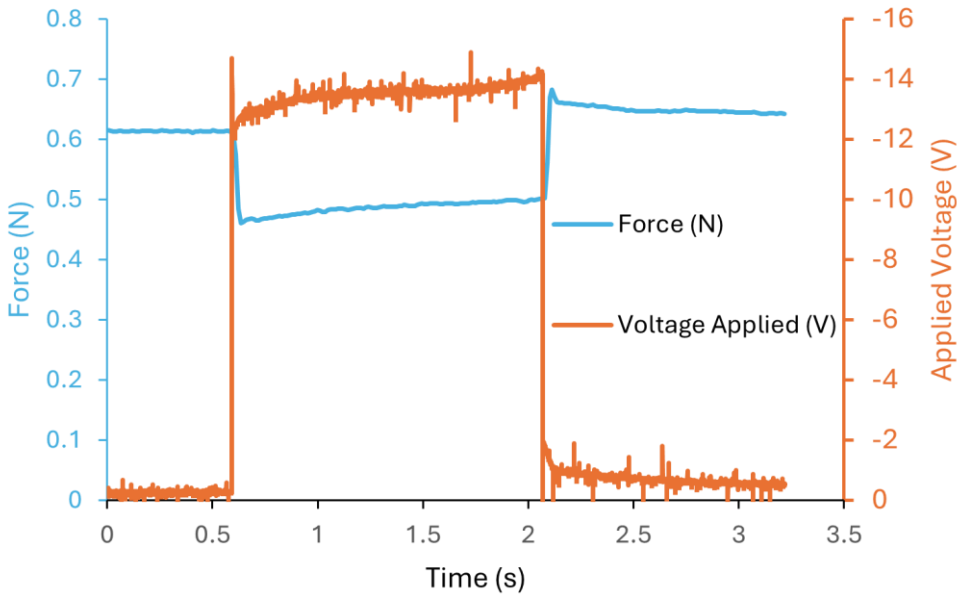

Figure 4.82 Negative voltage applied force change for a 0.5 mm width slit CLMM when already at maximum force.

It can be seen that the measured force drops when a reductive potential is applied and rises when the voltage is turned off. This is as expected as the interfacial tension of the LM is lowered with the applied reductive voltage due to electrocapillarity.

4.7.3 Comparison of All Thickness of Slits CLMM with Theory

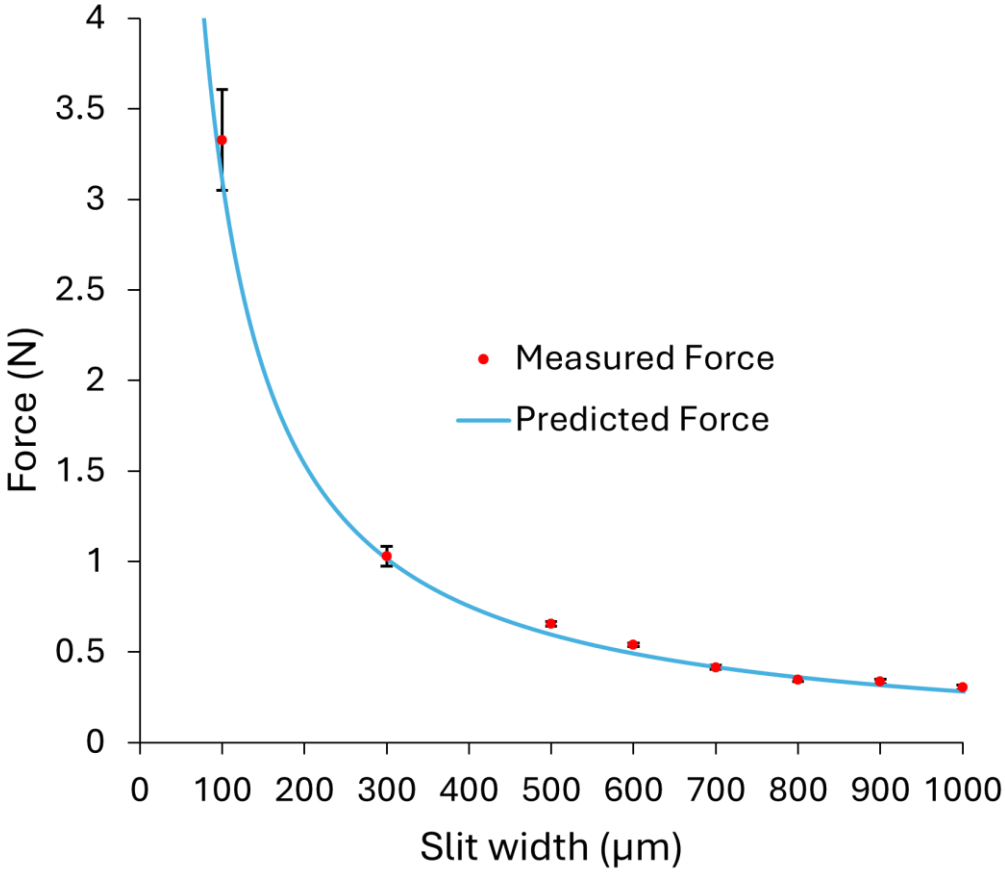

Figure 4.83 Measured and predicted force variation for a 10 mm overall radius CLMM with varying slit widths.
Error bars are from the standard deviation of the measurements.

The measured values for force variation for all slit sizes were plotted against that predicted by theory (Figure 4.83). The 0.3 and 0.1mm width slits force measurements were taken using the negative voltage applied force change, whereas for 0.5mm and up, oxidative force change was used. The measurements are seen to be in line with theory.

4.7.4 Comparison with Other Voltage Controlled Liquid Actuators

As the LM muscle is able to generate pressure by applying voltage, a comparison with other types of liquid actuators was made (Figure 4.84). Types of liquid based devices chosen were droplet based LM muscles, hydraulically amplified self-healing electrostatic actuators (HASEL), microhydraulic electrowetting, and electro conjugate force.

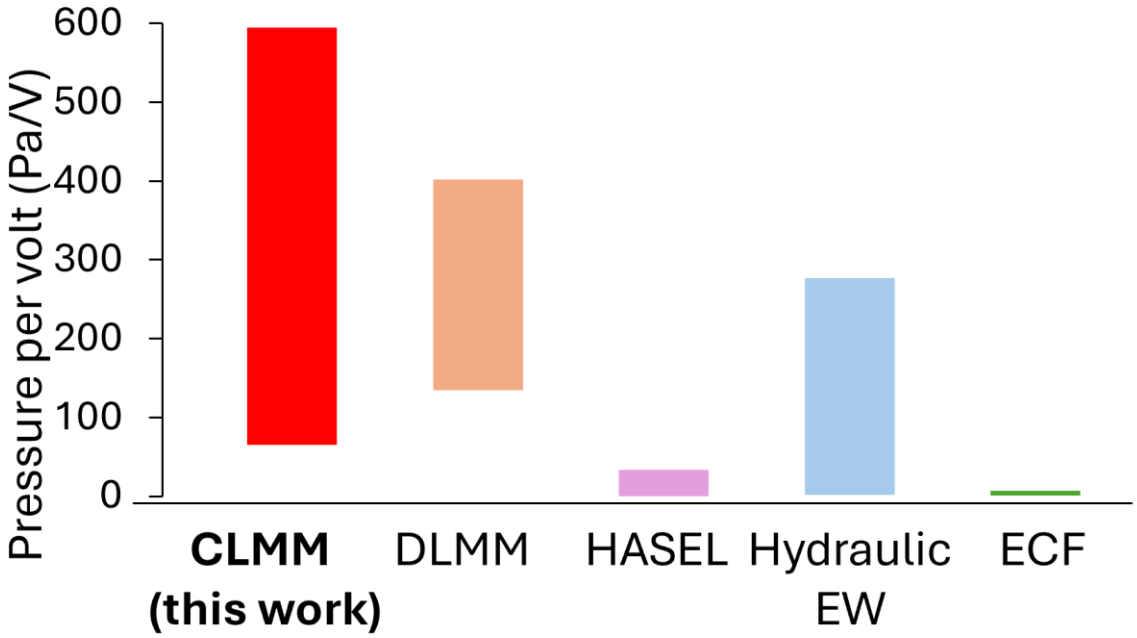

Figure 4.84 Comparison of pressure variation per volt applied for different liquid based actuators.
Data for comparison is taken from [5-12, 22-24].

This work was determined to have the greatest variation in pressure per volt applied over all of the compared works. This shows the great potential that the CLMM has for use in a wide range of applications, especially in cases where use of high voltages are not desired. Its force scaling with the inverse of channel width also means it could be used in more small-scale devices.

4.8 Summary

An all-new type of soft actuator has been created, which utilises the super-high change in interfacial tension of liquid metal and uses it to generate force and movement by confining it into small channels. The pressure that is required to push the liquid metal into the small channels increases with reducing the width of the channels. The voltage required to change force is relatively low (~10 V), force change occurs almost instantly (<25 ms reaction time) and force can be controlled with ~0.03N accuracy. The movement speed is fast (36.3mm s^{-1}) and position can be controlled based on the measured resistance. This new type of actuator can be used to create new and improved soft devices. Previous soft muscles often require the use of high voltages [9], or external pumps [2], which limits their usability. The CLMM requires neither of these. Its fluidic nature means that it can be used for a range of soft diaphragms and grippers. It is also relatively simple to manufacture, with most of the designs shown in this work made using commercially available 3D printers. Overall, the CLMM demonstrates an exciting new actuator type which can make a large impact in the soft robotics field.

4.9 References

1. Haines, C.S., et al., *Artificial muscles from fishing line and sewing thread.* science, 2014. **343**(6173): p. 868-872.
2. Doumit, M., A. Fahim, and M. Munro, *Analytical modeling and experimental validation of the braided pneumatic muscle.* IEEE transactions on robotics, 2009. **25**(6): p. 1282-1291.
3. Park, S.J. and C.H. Park, *Suit-type wearable robot powered by shape-memory-alloy-based fabric muscle.* Scientific reports, 2019. **9**(1): p. 9157.
4. Fan, J. and G. Li, *High performance and tunable artificial muscle based on two-way shape memory polymer.* RSC advances, 2017. **7**(2): p. 1127-1136.
5. Acome, E., et al., *Hydraulically amplified self-healing electrostatic actuators with muscle-like performance.* Science, 2018. **359**(6371): p. 61-65.
6. Nagaoka, T., et al., *ECF (electro-conjugate fluid) finger with bidirectional motion and its application to a flexible hand.* Smart Materials and Structures, 2019. **28**(2): p. 025032.

7. Yamaguchi, A., et al. *A robot hand using electro-conjugate fluid*. in *2011 IEEE International Conference on Robotics and Automation*. 2011. IEEE.
8. Kedzierski, J., et al., *Microhydraulic Electrowetting Actuators.* Journal of Microelectromechanical Systems, 2016. **25**(2): p. 394-400.
9. Rothemund, P., et al., *HASEL Artificial Muscles for a New Generation of Lifelike Robots-Recent Progress and Future Opportunities.* Adv Mater, 2021. **33**(19): p. e2003375.
10. Shu, J., et al., *A Liquid Metal Artificial Muscle.* Adv Mater, 2021. **33**(43): p. e2103062.
11. Liao, J. and C. Majidi, *Muscle-Inspired Linear Actuators by Electrochemical Oxidation of Liquid Metal Bridges.* Advanced Science, 2022. **9**(26): p. 2201963.
12. Liao, J. and C. Majidi, *Soft actuators by electrochemical oxidation of liquid metal surfaces.* Soft Matter, 2021. **17**(7): p. 1921-1928.
13. Khan, M.R., et al., *Giant and switchable surface activity of liquid metal via surface oxidation.* Proc Natl Acad Sci U S A, 2014. **111**(39): p. 14047-51.
14. Dickey, M.D., et al., *Eutectic Gallium-Indium (EGaIn): A Liquid Metal Alloy for the Formation of Stable Structures in Microchannels at Room Temperature.* Advanced Functional Materials, 2008. **18**(7): p. 1097-1104.
15. Yuan, B., Z.-Z. He, and J. Liu, *Effect of electric field on the wetting behavior of eutectic gallium–indium alloys in aqueous environment.* Journal of Electronic Materials, 2018. **47**: p. 2782-2790.
16. Eaker, C.B. and M.D. Dickey, *Liquid metal actuation by electrical control of interfacial tension.* Applied Physics Reviews, 2016. **3**(3): p. 031103.
17. Grahame, D.C., *The electrical double layer and the theory of electrocapillarity.* Chemical reviews, 1947. **41**(3): p. 441-501.
18. Ran, Y., et al., *Resin swelling in mixed solvents analysed using Hansen solubility parameter space.* Chemistry–A European Journal, 2019. **25**(19): p. 4951-4964.
19. Deng, H., X. Lian, and X. Gong, *A brief review of variable stiffness and damping magnetorheological fluid dampers.* Frontiers in Materials, 2022. **9**: p. 1019426.
20. Daeneke, T., et al., *Liquid metals: fundamentals and applications in chemistry.* Chem Soc Rev, 2018. **47**(11): p. 4073-4111.
21. Dacuycuy, S.J., W.A. Shiroma, and A.T. Ohta, *Electrocapillary actuation of liquid metal in microchannels.* Micromachines, 2022. **13**(4): p. 572.
22. Mitchell, S.K., et al., *An Easy-to-Implement Toolkit to Create Versatile and High-Performance HASEL Actuators for Untethered Soft Robots.* Adv Sci (Weinh), 2019. **6**(14): p. 1900178.
23. Wang, X., et al., *High-strain peano-HASEL actuators.* Advanced Functional Materials, 2020. **30**(7): p. 1908821.
24. Kellaris, N., et al., *An analytical model for the design of Peano-HASEL actuators with drastically improved performance.* Extreme Mechanics Letters, 2019. **29**: p. 100449.

5. Conclusion and Future Work

5.1 Conclusion

This thesis has explored the use of liquid metals and low melting point alloys in robotic systems in two different, complementary ways.

Firstly, different LM actuation types were detailed, including oxidation and reduction, continuous electowetting, electrocapillarity, electrowetting on dielectric, electrostatic and magnetic, and their relative performance compared.

Afterwards, an innovative, new smart material, Field's metal hybrid elastomer (FMHE) was created which is able to change stiffness and resistance in response to strain. It used the low melting point (62 °C) of Field's metal alloy to soften by 67%. The resistivity of the FMHE decreased by orders of magnitude when stretched or compressed due to the conductive filler network of nickel and Field's metal microparticles. When applying an electric potential across the composite while under strain, the composite is heated due to its high conductivity and Joule heating. This melted the Field's metal, softening the composite. Melting also caused the resistance to increase as the Field's metal particles moved away slightly from nearby conductive particles to relieve their stress. This then reduced the current through the composite and cooled it down. The FMHE was used for two different proof-of-concept applications - a compliance unit for a robotic gripper, and a resettable fuse.

FMHE offers researchers and industry a new, alternative means to accomplish strain sensing with stiffness changing capabilities. It is the first material of its kind which is able to change conductivity by several orders of magnitude, and also change stiffness by ~67%.

Secondly, a new type of actuator was created, the capillary liquid metal muscle (CLMM), which used the super-high change in interfacial tension of LM when oxidised to generate force and movement. The muscle design uses a series of channels for LM to flow into, which increases the force generated dramatically in comparison to droplets of liquid metal. The theory was analysed, showing that the force generated scales with the inverse of the width of the channels, and with the overall area of the device. The design of the muscle was optimised over multiple designs, with a final design using rectangular slits to achieve high force and stroke. Force change was tested for various slit widths and frequencies, and was found to be in line with that predicted by theory. The force generated could be controlled using PWM and feedback to a PID controller. The speed of movement of the muscle with a mass payload reached a maximum of 36.3 mm s^{-1}. The position of the muscle could be controlled by measuring the resistance change with height LM moved into the channels. Designs with slit widths as low as 0.1 mm were made and tested using a compressible PDMS diaphragm. The smaller slit designs showed the reverse of force change characteristics compared to those with 0.5 mm+ slit width. Force increased sharply for the smaller slits when reductive potential was applied to the LM, due to either the electrocapillarity effect or electrochemical bubble generation. Oxidation was seen to have little effect for the smaller slit designs, possibly because LM flows through the smaller size channels. The LM muscle was used for various proof of concept applications, such as damping, and soft robotic elements such as a gripper.

The CLMM uses an innovative channel type design to increase the output force of LM by several times over that reported for previous droplet-based muscles. CLMM offers a new means to achieve actuation in soft systems, driven by low voltages, and increasing in generated force for smaller channel sizes.

5.2 Future Work

Further work can be done on each of the projects detailed in this thesis.

5.2.1 FMHE

Changing the surface of the FMHE so it has a series of small pyramidal structures would concentrate the strain into small areas [1]. This could improve the sensitivity of the elastomer and enable the melting and softening of small zones.

Using two different sizes of Field's metal particles could eliminate the use of Nickel in the composite, allowing greater stiffness variation. Nickel microparticles of size between 2-5 μm were used in the FMHE, with Field's metal particles with an average size of 15-30 μm. Making a mixture containing smaller FM microparticles first, then adding the larger microparticles could mean Nickel microparticles are not needed for the improved piezoconductive effects when under strain.

5.2.2 CLMM

Future work on the CLMM can further reduce the channel size to determine the maximum possible force variation. It can also find if oxidative force change is possible for small slit designs. A simulation of LM changing interfacial tension when oxidised/reduced could be made also.

Using small slits, it should be possible to make an untethered soft robot at ~10 mm scale or smaller. The pressure change from LM could push a small joint to move from one position to another repeatedly, similar to spiders, which use hydraulic joints for their legs [2].

An all-soft LM muscle design could be made for soft robotics. Currently, channels and the container are made using hard resin. If they were made using PDMS, with an outlet for LM to flow in and out of, it would be completely soft. The PDMS would have to have a lot of cross supports between channels so it doesn't deform too much, however.

The efficiency of the muscle could also be improved by using different electrolytes or by lowering the voltage to reduce electrolysis.

As NaOH electrolyte was used in the CLMM to enable it to function by utilising electrochemical oxidation/reduction, this may limit the number of applications it can be used in. NaOH solution can cause skin irritation, depending on the concentration [3]. To increase the usability of CLMM, more alternative electrolytes can be tested in addition to the NaOH and Na_3PO_4 already tried. Additionally, a design which enables the CLMM to function and prevent leakage of LM and electrolyte would be required. However, batteries have electrolytes in them to facilitate their electrochemical reactions [4], and are used in a lot of consumer electronics- so use of electrolytes does not necessarily prevent CLMM from widespread use.

New designs of the CLMM are also possible, using thinner walls to increase the maximum stroke available. Multiple electrodes could be placed along the channel and turned on or off as LM neared it. This would further increase the possible stroke as there would be less electrolyte required.

Additionally, CLMM could be used in conjunction with variable stiffness composites such as FMHE to make smart soft robots with reconfigurable functionality.

5.3 References

1. Yun, G., et al., *Liquid metal hybrid composites with high-sensitivity and large dynamic range enabled by micro-and macrostructure engineering.* ACS Applied Polymer Materials, 2021. **3**(10): p. 5302-5315.
2. Landkammer, S., et al., *Biomimetic spider leg joints: a review from biomechanical research to compliant robotic actuators.* Robotics, 2016. **5**(3): p. 15.
3. SRIKRISHNA, V. and N.A. MONTEIRO-RIVIERE, *The effects of sodium hydroxide and hydrochloric acid on isolated perfused skin.* A Journal of Molecular and Cellular Toxicology, 1991. **4**(3).
4. Wang, Q., et al., *Progress of enhancing the safety of lithium ion battery from the electrolyte aspect.* Nano Energy, 2019. **55**: p. 93-114.